

# Microstructuur-gecorrleerde Eigenschappen van Conversielagen op Aluminium Legeringen

## Stellingen

1. Fenomenen op nano- en microschaal bepalen het microscopische elektrochemische gedrag van een systeem. Daarom moeten in het onderzoek ook technieken gebruikt worden met een resolutie gelijk aan de afmetingen van deze details.

*[This thesis, chapters 4, 5, 7, and 8]*

2. De SKPFM techniek verschaft nuttige en betrouwbare informatie betreffende de kathodische en anodische gebieden op een metaaloppervlak, hetgeen van belang is bij het bepalen van het elektrochemisch gedrag. Nochtans moeten de resultaten geïnterpreteerd worden met de nodige voorzichtigheid omdat het niet altijd duidelijk is hoe de experimentele omstandigheden de gemeten potentiaal beïnvloeden. Bijkomende beperkingen zijn er wanneer metingen uitgevoerd in lucht, gebruikt worden om fenomenen die plaatsvinden in oplossing te begrijpen.

*[This thesis, chapters 5, 7, and 8;*

*V. Guillaumin, P. Schmutz, G.S. Frankel, "Characterization of Corrosion Interfaces by the Scanning Kelvin Probe Force Microscopy Technique", J. Electrochem. Soc. 148 (2001) B163]*

3. Vanweg het beperkte frequentie gebied gebruikt bij EIS metingen is het meest geschikte equivalente circuit om het impedantie gedrag van het bestudeerde systeem te modelleren, dat circuit dat alleen de elementen meeneemt die binnen zo'n range vallen en niet een circuit dat alle mogelijke elementen beschouwt.

*[This thesis, chapter 6]*

4. De studie van de beschermende eigenschappen van organische deklagen wordt aanzienlijk verbeterd, wanneer men complementair aan de impedantiemetingen, meetmethoden toepast zoals ATR-FTIR spectroscopie voor de studie van wateropname in de film en op het grensvlak. Dit is beter dan koste wat kost berekeningen uit te voeren aan de kwantitative modellering van de impedantiemetingen om de graad van coating-delaminatie te bepalen.

*[L. Philippe, Novel Spectroscopic Techniques for studying Protective Organic Coatings, PhD Thesis at the Corrosion and Protection Center UMIST, University of Manchester, 2002*

*E.P.M. van Westing, Determination of Coating Performance with Impedance Measurements, PhD Thesis at TUDelft, 1992*

*F. Mansfeld, C.H. Tsai, Corrosion, 42 (1991) 12]*

5. Elk experiment, zelfs de visuele observatie, veroorzaakt veranderingen in het bestudeerde systeem. Dit ligt aan de basis van iedere meting, omdat datgene dat wordt waargenomen, de respons is van het systeem op externe interacties, in plaats van het systeem zelf. Daarom kan een correcte interpretatie van experimentele resultaten slechts plaatsvinden wanneer de opgewekte veranderingen bekend of verwaarloosbaar zijn.

*[D. Chidambaram, G.P. Halada, C.R. Clayton, Development of a Technique to Prevent Damage of Chromate Conversion Coatings during X-ray Photoelectron Spectroscopy Analysis", Applied Surface Science 181 (2001) 283]*

6. De aanwezigheid van intermetallische deeltjes aan het aluminium oppervlak is niet een noodzakelijke voorwaarde voor corrosie langs de korrelgrenzen. Daar de zwakte van de natuurlijke aluminiumoxidelaag langs de korrelgrenzen en de verarming of verrijking van de legeringselementen aldaar, de initiatie en propagatie van de corrosie langs de korrelgrenzen veroorzaakt, kunnen de intermetallische deeltjes slechts dit effect bevorderen.

*[J.R. Flores, H. Terry, J.H.W. de Wit, "Intergranular Corrosion of AA2024-T3 Initiation and Propagation" in the Proceedings of the Conference of Metallurgists COM2002, 10-16 August 2002, Montreal, Canada]*

7. Een gelijke naamgeving voor een zelfde entiteit zou de interactie tussen wetenschappers met een verschillende opleiding sterk verbeteren.

*[This thesis, chapter 4, section 4.2]*

8. Een nieuw figuur aan een oud artikel toevoegen maakt het geen nieuw artikel. Dit zou het aantal artikelen per auteur sterk reduceren.

9. Europeanen, in ieder geval die van de huidige generaties, zullen zich altijd eerder Italiaans, Duits, Frans, Nederlands, Belgisch, Spaans, etc. dan Europees voelen. Het bestaan van landspecifieke euromunten is daar het bewijs van.

10. Internationale mobiliteit behoort nog niet tot de normale mentaliteit: degene die het niet vanzelfsprekend vindt naar het geboorteland terug te keren, wordt als vreemd ervaren.

11. Het opmerken van verschillen tussen menselijke rassen is geen activiteit van een racist, het prioriteren van de verschillen is echter de basis van racisme.

12. Als je schreeuwt, word je gehoord, maar dat betekent nog niet dat er naar je geluisterd wordt.

13. De enige mensen die werkelijk van levensbelang voor je zijn, zijn je ouders, en aan de andere kant ben jij alleen voor j ou kinderen van levensbelang.

14. De tijdsduur van een avondmaal, doelend op de sociale gebeurtenis in plaats van op het simpelweg nuttigen van eten, is omgekeerd evenredig met de geografische breedtegraad.

3938

780361

312545

**Microstructure-related  
Quality of Conversion Coatings  
on Aluminium Alloys**

TR 3938

**Microstructuur-gecorreleerde  
Eigenschappen van Conversielagen  
op Aluminium Legeringen**



**Netherlands Institute**  
*for Metals Research*

# **Microstructure-related Quality of Conversion Coatings on Aluminium Alloys**

Proefschrift



Ter verkrijging van de graad van doctor  
aan de Technische Universiteit Delft,  
op gezag van de Rector Magnificus Prof. dr. J.T. Fokkema,  
voorzitter van het College voor Promoties,  
in het openbaar te verdedigen op woensdag 16 oktober 2002 om 13:30 uur

door

Paola CAMPESTRINI

Ingenere dei Materiali  
Università degli Studi di Trento, Italië  
geboren te Trento (Italië)

Dit proefschrift is goedgekeurd door de promotoren:

Prof. dr. J.H.W. de Wit

Prof. dr. ir. H. Terryn

Samenstelling promotiecommissie:

Rector Magnificus	voorzitter
Prof. dr. J.H.W. de Wit	Technische Universiteit Delft, promotor
Prof. dr. ir. H. Terryn	Vrije Universiteit Brussel, promotor
Prof. dr. P.L. Bonora	Università degli Studi di Trento, Italië
Prof. dr. L. Fedrizzi	Università La Sapienza, Roma, Italië
Prof. ir. L. Katgerman	Technische Universiteit Delft
Prof. dr. I.M. Richardson	Technische Universiteit Delft
Dr. ir. E.P.M. van Westing	Netherlands Institute for Metals Research, Delft

This research was carried out under the project number ME97025 in the framework of the Strategic Research Program of the Netherlands Institute for Metals Research (NIMR) in The Netherlands.

*Published and distributed by:* DUP Science

DUP Science is an imprint of

Delft University Press

P.O. Box 98

2600 MG Delft

The Netherlands

Telephone: +31 15 27 85 678

Telefax: +31 15 27 85 706

ISBN: 90-407-2342-7

Keywords: Aluminium, Corrosion, Conversion Coating

Copyright © by P. Campestrini, 2002

All rights reserved. No part of the material protected by this copyright notice may be reproduced or utilized in any form or by any means, electronic or mechanical, including photocopying, recording or by any information storage and retrieval system, without written permission from the publisher: Delft University Press.

Printed in The Netherlands

# Contents

<b>1. Introduction</b>	<b>1</b>
1.1 Background and general introduction	1
1.2 Outline of the thesis	3
1.3 References	4
<b>2. Corrosion of aluminium and its alloys</b>	<b>5</b>
2.1 Introduction	5
2.2 Localized corrosion	6
2.2.1 Pitting	6
2.2.2 Intergranular	10
2.2.3 Exfoliation	10
2.2.4 Filiform	11
2.2.5 Other forms of localized corrosion	12
2.3 Localized corrosion and alloy microstructure	12
2.3.1 2xxx series: Al-Cu system	13
2.3.2 1xxx series: pure aluminium	19
2.3.3 3xxx series: Al-Mn system	19
2.3.4 5xxx series: Al-Mg system	20
2.3.5 6xxx series: Al-Mg-Si system	21
2.3.6 7xxx series: Al-Zn-Mg system	22
2.4 Conclusions	23
2.5 References	23
<b>3. Surface treatments of aluminium and its alloys</b>	<b>27</b>
3.1 Introduction	27
3.2 Chromate conversion coatings (CCC)	28
3.2.1 Formation, morphology and composition	29
3.2.2 Mechanisms of corrosion protection	34
3.2.3 Chromate conversion coatings and microstructure	37
3.3 Cerium-based conversion coatings	40
3.3.1 Formation, morphology and composition	41
3.3.2 Mechanisms of corrosion protection	47

3.3.3 Cerium-based conversion coatings and microstructure	48
3.4 Conclusions	50
3.5 References	51
<b>4. Microstructure and corrosion – Use of the SKPFM technique</b>	<b>55</b>
4.1 Introduction	55
4.2 Principles of the SKPFM technique	57
4.3 Experimental procedure	63
4.3.1 Materials	63
4.3.2 Microstructural investigation	63
4.3.3 Electrochemical investigation	64
4.4 Results and discussion	66
4.4.1 Microstructural investigation	66
4.4.2 Electrochemical investigation	75
4.5 Conclusions	80
4.6 References	81
<b>5. Microstructure and chromate conversion coatings - Alclad 2024</b>	<b>83</b>
<b>I. Characterization</b>	
5.1 Introduction	83
5.2 Experimental procedure	84
5.2.1 Materials and treatments	85
5.2.2 Surface analysis investigation	87
5.3 Results and discussion	89
5.3.1 Surface morphology and microstructure	89
5.3.2 Nucleation and growth of the CCC: effect of the surface preparation	96
5.3.3 Morphology and composition of the CCC: effect of the surface preparation	103
5.3.4 Morphology and composition of the CCC: effect of the chromate bath pH	113
5.4 Conclusions	120
5.5 References	120
<b>6. Microstructure and chromate conversion coatings - Alclad 2024</b>	<b>123</b>
<b>II. Corrosion protection</b>	
6.1 Introduction	123



6.2 Experimental procedure	124
6.2.1 Electrochemical impedance spectroscopy (EIS)	124
6.2.2 Electrochemical noise (EN)	125
6.3 Results and discussion	128
6.3.1 Choice of a suitable equivalent circuit	129
6.3.2 Corrosion protection provided by the CCC: effect of the surface preparation	135
6.3.3 Corrosion protection provided by the CCC: effect of the chromate bath pH	147
6.4 Conclusions	154
6.5 References	155
<b>7. Microstructure and chromate conversion coatings - Bare 2024</b>	<b>157</b>
7.1 Introduction	157
7.2 Experimental procedure	158
7.2.1 Materials and treatments	158
7.2.2 Surface analysis investigation	159
7.2.3 Electrochemical investigation	159
7.3 Results and discussion	159
7.3.1 Surface morphology and microstructure	160
7.3.2 Nucleation and growth of the CCC: effect of the intermetallics	169
7.3.3 Nucleation and growth of the CCC: effect of the Cu-rich smut	177
7.3.4 Morphology of the CCC: effect of the surface preparation	183
7.3.5 Corrosion protection provided by the CCC: effect of the surface preparation	186
7.4 Conclusions	193
7.5 References	194
<b>8. Microstructure and cerium-based conversion coatings - Bare 2024</b>	<b>195</b>
8.1 Introduction	195
8.2 Experimental procedure	196
8.2.1 Materials and treatments	196
8.2.2 Surface analysis investigation	198
8.3 Results and discussion	198
8.3.1 Surface morphology and microstructure	198
8.3.2 Formation of the cerium-based conversion coating: effect of the intermetallics	204

8.3.3 Formation of the cerium-based conversion coating: effect of the Cu-rich smut	210
8.4 Conclusions	229
8.5 References	230
<b>Summary</b>	<b>231</b>
<b>Samenvatting</b>	<b>235</b>
<b>Acknowledgements</b>	<b>239</b>
<b>Curriculum Vitae</b>	<b>243</b>
<b>List of publications</b>	<b>245</b>

## Introduction

### 1.1 Background and general introduction

Aluminium when alloyed with small amounts of other materials is an essential and valuable metal in the aerospace, architectural, transportation, packaging and manufacturing industries because of its high specific strength. Other interesting properties of aluminium alloys include high thermal and electric conductance, especially in relation with their low specific weight, high ductility and resultant low working cost [1].

As concern the corrosion behaviour, aluminium and its alloys show a relative good corrosion resistance in chloride-free environments with pH ranging from 4 to 8.5, due to the formation of a thin oxide film when exposed to air. However, this natural oxide layer is amphoteric, i.e. dissolves both in strong acid and strong alkaline media, and contains flaws and defects, the concentration of which increases with the concentration of alloying elements and through which aggressive species can reach the metal surface leading to corrosive attack [2]. Therefore, the natural aluminium oxide film does not provide adequate corrosion protection in many conditions and has to be replaced by a layer having better corrosion resistance, a so-called conversion layer. This layer is meant also to enhance the paint adhesion through the generation of mechanical (micro-pores) and chemical (reactions with the organic coating) bonds.

The conversion treatments are usually distinguished in chemical, which consist of immersion in a bath containing oxidizers without the use of external current, and electrochemical, which require an external current or voltage source [1]. The conversion processes, either chemical or electrochemical, involving the use of chromates and dichromates are generally considered to provide the best corrosion protection for aluminium and its alloys. Only films formed in chromate solutions meet the stringent corrosion resistance requirements of the military specifications MIL-C-81706 [3]. Besides, the chemical chromate conversion treatment is quick, cheap, and simple and forms a layer able to withstand forming operations, which is the main requirement for use in coil coating processes. For these reasons, chromate-based treatments, especially the chemical ones, have been widely used for the corrosion protection of Al alloys for more than 40 years [4]. However, the production, storage, and application of chromate solutions cause large environmental and health related problems, since they contain hexavalent chromium compounds that have a wide range of toxic effects [5]. As a consequence, governments have lowered exposure limits and tightened control resulting in increase of the costs of

processes using chromate species. The position taken by the industries with respect to this problem is different depending on the area. For example, the automotive industry decided to restrict the use of hexavalent chromium species in the car body, which includes pigments, conversion layers on Al, Mg and Zn, inhibitors, etc. to less than 2 g/m<sup>2</sup> per car starting from 1 July 2003, whereas the building and aerospace industries have not yet shown such concrete will of replacing these toxic compounds. Nevertheless, it is expected that soon or later all the industrial areas will follow the example of the automotive industry. Therefore, several attempts have been made to find alternative systems able to reproduce the excellent properties of the chromate treatments but with a less detrimental impact on health and environment. This growing interest on chromium-free treatments has involved not only the industrial world but also the academic world, as is evident from the large amount of papers on this topic presented in several conferences during the last few years [6, 7]. Different types of chromium-free conversion processes have been developed using a variety of chemical compounds: molybdates, rare earth metal salts, zirconium and titanium fluoride, lithium salts, permanganate, silanes, cobalt, silicon and/or zirconium and/or yttrium and/or cerium oxide sol-gel. Nowadays, most of these treatments are still in the experimental phase and not yet suitable for industrial application, however some examples of companies that have replaced the chromate treatment with a chromium-free one, as that based on zirconium and titanium compounds, do exist.

Similar to the corrosion processes that can take place at the aluminium surface, the formation of some of the conversion layers, either chromate or alternative systems, involves the occurrence of electrochemical reactions, i.e. cathodic reduction of oxidizing species and anodic attack of aluminium. Therefore, the presence of local anodic and cathodic sites on the aluminium surface may be expected to play a very important role not only in the type and rate of corrosion but also in the nucleation, growth and final properties of the conversion films. Local anodes and cathodes in the aluminium alloys are mainly related to the intermetallic particles, which are distinguished in constituent particles or inclusions, dispersoids, and strengthening precipitates depending on their size [8]. Anyway, all three types of intermetallics give rise to galvanic coupling with the Al matrix since they have a different chemical composition and as a consequence a different surface potential in comparison with the Al matrix. The strong influence of the composition, size and distribution of intermetallics on the corrosion behaviour of different aluminium alloys has been widely investigated by many researchers. In general, the intermetallics rich in elements that are more noble than aluminium, such as copper, iron and silicon, behave as cathodic sites and therefore in contact with aggressive species lead to local dissolution of the aluminium matrix in their proximity, whereas the intermetallics rich in elements less noble than aluminium, as magnesium and zinc, act as anodic sites and then dissolve during exposure in aggressive environment. Therefore, from a corrosion point of view while the anodic intermetallics are almost non-influential, since once dissolved they do not affect anymore the corrosion behaviour of aluminium, the presence of cathodic intermetallics is extremely deleterious. Indeed, many authors have found that the intermetallics that act as local cathodes are

preferential nucleation sites for pitting and enhance the susceptibility to both intergranular and filiform corrosion.

On the other hand, the effect of the intermetallic particles on the nucleation, growth and final properties of conversion coatings has started to be considered only in the last few years. As concern the chromate film, although Brown *et al.* [9] at the beginning of the nineties highlighted the important role in the growth of the chromate coating played even by minor surface heterogeneities in aluminium (99.98% pure) associated with grain or cellular boundaries, the first study mentioning the influence on the chromate film properties, in particular the thickness, of much more evident heterogeneities, as the intermetallics, is dated 1994 [10]. After this work, as far as we know, only at the end of the nineties, beginning of the new century the effect of the intermetallic particles on both the final properties and the nucleation, growth of the chromate layer has been considered by some research groups, who proposed different and sometimes contradicting theories. Regarding the innovative chromium-free treatments, only the cerium-based processes, both the one developed by Mansfeld in US [11] and that developed by Hinton in Australia [12], have been investigated taking into account the influence of the intermetallics on the formation and as a consequence on the morphology and composition of the conversion film, whereas for all the other alternative systems a uniform and homogeneous formation of the film has always been supposed.

However, the comprehension of the exact role played by the intermetallic particles on the formation of conversion layers on Al alloys is a necessary condition both for a better understanding of the mechanisms of nucleation, growth and corrosion protection of the chromate conversion coating and for finding out what could be done to improve the chromium-free systems. Besides, a better understanding of the chromate corrosion inhibition is a prerequisite for the development and improvement of alternative chromium-free systems, as highlighted by a recent view of the aircraft coating technology [13].

## 1.2 Outline of the thesis

This thesis deals with the correlation between the microstructure, in particular the intermetallic particles, and the electrochemical behaviour of aluminium alloy 2024-T3, both clad and bare. Two aspects related to the electrochemical behaviour are considered, that is the corrosion attack occurring in aggressive environments and the formation of conversion layers, either chromate and alternative systems. Amongst the proposed chromium-free processes, the cerium-based conversion coating is studied, since it is very interesting both from an industrial point of view, due to its promising properties, and from an academic point of view, since its formation consists of a redox process and then a comparison with the chromate treatment is a valid approach of investigation.

Chapters 2 and 3 review the corrosion and the surface treatments of aluminium alloys, respectively. Regarding the corrosion, the attention is mainly focused on the local type of attack caused by the presence of intermetallic particles at the surface, and for the surface treatments the chromate and the cerium-based ones are those discussed in more detail. In the other chapters the experimental results and their interpretation are reported. Chapter 4

deals with the influence of small changes in the heat treatment procedure on the microstructure and as a consequence on the corrosion resistance of bare 2024 aluminium alloy. Besides, in this chapter the use of the SKPFM technique and its applicability for the study of the micro-electrochemical behaviour of aluminium alloys are discussed in detail. Chapters 5 and 6 focus on the effect of the intermetallic particles on the formation and corrosion resistance, respectively, of the chromate conversion coating formed on Alclad 2024 alloy. In chapter 7 the nucleation, growth and final properties of the chromate film are considered in the case of bare 2024 alloy. In particular, the role of both the intermetallics and that of the Cu-rich smut, which can eventually form during the surface preparation procedure, is discussed and the differences of the chromate layers formed on the bare and the clad alloys are also reported and related to their different microstructure. Finally, chapter 8 deals with the influence of the same microstructural features, i.e. intermetallics and Cu-rich smut, on the formation of the cerium-based conversion coating on bare 2024 aluminium alloy.

### 1.3 References

- [1] S. Wernick, R. Pinner, *The Surface Treatment and Finishing of Aluminium and its Alloys*, 5<sup>th</sup> edition, Finishing Publication, Teddington UK (1986)
- [2] H.Habazaki, K.Shimizu, P.Skeldon, G.E.Thompson, G.C.Wood, X.Zhou, *Trans. Inst. Met. Finish.* 75 (1997) 18
- [3] Military Specification MIL-C-81706, *Chemical Conversion Materials for Coating Aluminium and Aluminium Alloys*
- [4] *Metals Handbook: Surface Cleaning, Finishing and Coating*, vol. 5, 9<sup>th</sup> edition, American Society for Metals
- [5] L. Friberg, G.F. Nordberg, V.B. Vouk, *Handbook of Toxicology of Metals*, Vol. II, Elsevier, Amsterdam NL (1986)
- [6] 2<sup>nd</sup> *International Symposium on Aluminium Surface Science and Technology (ASST 2000)*, 21-25 May 2000, UMIST, Manchester, England, UK
- [7] *Eurocorr 99*, August 30 to September 2 1999, Aachen, Germany
- [8] M.S. Hunter, A.M. Montgomery, G.W. Wilcox, *Aluminum: Physical Properties and Metallurgy*, 6<sup>th</sup> edition, J.E. Hatch (ed.), Metals Park, OH (1984)
- [9] G.M. Brown, K. Shimizu, K. Kobayashi, G.E. Thompson, G.C. Wood, *Corros. Sci.* 33 (1992) 1371
- [10] P.L. Hagans, C.M. Haas, *Surf. Interface Anal.* 21 (1994) 65
- [11] F.B. Mansfeld, Hong Shih, You Wang, *Method for Creating a Corrosion Resistant Aluminium Surface*, US Patent 51 94138
- [12] B.R.W. Hinton, D.R. Arnott, N.E. Ryan, *Mater. Forum* 9 (1986) 16
- [13] Report by the Air Force Blue Ribbon Advisory Panel on Aircraft Coatings (1995)

# Corrosion of aluminium and its alloys

### 2.1. Introduction

Corrosion is usually defined as the destruction or deterioration of a material because of its reaction with the environment, which in the case of metals involves anodic oxidation of the metal itself and cathodic reduction of oxidizing species [1]. Corrosion is a spontaneous phenomenon and then is always governed by energy changes, that means the corrosion process is always occurring with a release of free energy [2]. Since the nature tends to minimize energy, higher is the amount of free energy realised in the oxidation reaction of a metal higher is its tendency to undergo corrosion. From this thermodynamic point of view aluminium should be a very active metal towards corrosion, second only among the structural metals to magnesium, beryllium and zinc. However, aluminium generally shows a good corrosion resistance in natural atmosphere, fresh waters, many soils and chemicals [3]. This is due to the fact that the result of the high oxidation reactivity of aluminium is not the dissolution of the metal but the formation of a thin oxide film on its surface, which is able to protect the aluminium substrate against corrosion in many environments. Indeed, it is recognized that the air-formed amorphous oxide film on aluminium, of thickness dependent on the formation conditions and in the range of 1-10 nm, has a relative high band gap ( $\approx 3$  eV) and acts as a poor electron conductor [4]. Besides, if damaged this thin film re-forms immediately in most environments and continues to protect the aluminium from corrosion. In dry air the natural aluminium oxide film consists only of a pores-free barrier layer of a thickness dependent solely on the temperature of the environment, whereas in normal atmospheres on top of this barrier layer a thicker and more permeable layer of hydrated oxide develops. Two different forms of aluminium hydroxide are observed: bayerite,  $\text{Al}(\text{OH})_3$ , and boehmite,  $\text{AlO}(\text{OH})$ , predominant at low ( $< 70^\circ\text{C}$ ) and high temperature ( $> 100^\circ\text{C}$ ), respectively. In addition, during the complex course of the aging of aluminium hydroxide another trihydrated aluminium oxide, named gibbsite or hydrargillite, can form [3].

The extent of protection against corrosion provided by the natural oxide film to the aluminium substrate is determined mainly by two factors: the type and aggressiveness of the environment and the chemical, metallurgical properties and mechanical conditions of the aluminium [5]. First of all, aluminium oxide/hydroxide is amphoteric, that means it is thermodynamically unstable either at low ( $< 4$ ) or at high ( $> 8.5$ ) pH. Therefore, the aluminium oxide film dissolves when exposed to non-oxidizing strong acid media, such as phosphoric acid, and particularly to strong alkaline media, such as sodium hydroxide. Once

the oxide layer is removed the aluminium can undergo corrosive attack leading to the formation of  $\text{Al}^{3+}$  and  $\text{AlO}_2^-$  ions in acid and alkaline media, respectively. Usually, in these conditions of oxide film instability general corrosion of aluminium takes place, which is a type of corrosion that involves the occurrence of cathodic and anodic reactions all over the entire surface without spatially well-defined and distinguished anodic and cathodic areas. On the other hand, in environments with a pH in the range between 4 and 8.5 where the oxide film is thermodynamically stable, localized corrosion is more probable to occur. In this type of corrosion the anodic oxidation of aluminium and the cathodic reduction of other species, usually  $\text{O}_2$  and  $\text{H}^+$ , take place preferentially at different locations on the aluminium surface.

The occurrence of localized attack even in conditions where the oxide film should be stable is due to the fact that this film is far from perfect and contains several defects and flaws, which are weak spots where film breakdown can take place especially in presence of aggressive species as chloride ions. In most cases, the defects in the aluminium oxide film are related to microstructural aspects, as intermetallic particles, grain boundaries, etc., which are determined by the chemical composition and the thermo-mechanical history of the aluminium alloy. Localized corrosion can occur in different forms, which are described in detail in the next section, depending again on the environment and especially on the microstructure of the alloy. This last very important aspect is addressed in section 2.3, where the localized corrosion is discussed for different families of aluminium alloys in relation with the properties of the intermetallics and the grain boundaries.

## 2.2. Localized corrosion

Localized corrosion results from the formation of local electrochemical cells, where anode and cathode are spatially separated, due to differences either in the alloy surface, e.g. in the chemical composition, or in the environment, e.g. oxygen concentration profile. Due to the separation of anodic and cathodic reactions, significant local changes take place in both the solution and the surface as a function of time. Thus, localized corrosion on aluminium alloys is a highly time dependent phenomenon. Generally, it occurs in an environment where the oxide film is insoluble and it takes one of the forms described in the following sections.

### 2.2.1 Pitting

Pitting is one of the most destructive and insidious forms of corrosion since it is difficult to detect, while perforation of the structure can occur with only a small overall weight loss; therefore it often results in extreme sudden failures. For aluminium, pitting is most commonly provoked by halide ions, of which chloride is the most frequently encountered in service [1, 3]. Figure 2.1 shows the typical active-passive behaviour of aluminium alloys characterized by a passive range, where the current density is low and almost constant with the potential, followed by a strong and sudden increase in current when the alloy is polarized above a certain potential, which is called pitting potential ( $E_p$ ) and depends on parameters relative both to the substrate (type of alloy, presence of conversion layers, etc.) and to the environment (pH, T, presence of aggressive species, presence of inhibitors, etc.). This



sudden increase in current is the result of the on-setting of stable pit growth, whereas metastable pits form also below  $E_p$ . It is important to note that  $E_p$  can be reached not only by

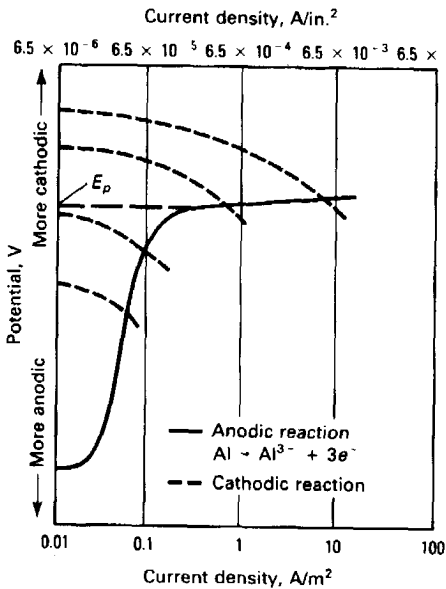


**Figure 2.1:** Anodic polarization curve of Al alloy 1100 immersed in neutral de-aerated NaCl solution free of cathodic reactant [Ref. 3].

application of an external potential to the sample, but also by addition of oxidizing species ( $O_2$ ,  $H_2O_2$ , etc.) that enhance the cathodic reaction rate (dashed lines in Figure 2.1) and shift the open circuit potential (OCP = interception between anodic and cathodic curves) to a value close to or higher than  $E_p$ . Therefore, it is believed that the resistance to pitting corrosion of Al is truly represented by the passive range ( $\Delta_{pas} = E_p - OCP$ ) rather than by the solely value of pitting potential.

When discussing the mechanism of pitting it is necessary to distinguish between initiation of the pit, which can occur also at potential lower than  $E_p$ , and propagation of the pit, which takes place in conditions where  $E$  is higher than  $E_p$ . The initiation of a pit is caused by the local breakdown of the oxide film on the aluminium surface that is a multi-step process [6]. All the prevailing

theories claim that the first step consists of adsorption of aggressive anions, in most cases  $Cl^-$ , on the passive Al surface due to the relative high isoelectric point (9.5) of aluminium oxide [6-8]. Indeed, the isoelectric point corresponds to the pH of zero charge ( $pH_{zc}$ ) of a surface, which is the pH of the aqueous solution at which the hydroxyl groups present on the outermost surface of the oxide film remain undissociated. At pH lower than the isoelectric point the hydroxyl groups are protonated and the surface acquires a positive charge, whereas at pH higher than the isoelectric point the hydroxyl groups are de-protonated and the surface acquires a negative charge. Therefore, in an environment with  $pH < 9.5$  the aluminium oxide surface is positively charged and tends to adsorb anions. Analytical techniques such as auto-radiography [9] and X-ray photoelectron spectroscopy [10] have revealed the adsorption of  $Cl^-$  ions on Al oxide film at the open circuit potential as well as at applied anodic potentials. Besides, the adsorption of the aggressive ions is assumed to be localized at the location of *active centers*, as flaws and defects in the oxide film, which can be mechanical flaws due to scratches and crystallographic asymmetry or residual flaws originating from intermetallic particles [11].

The pit initiation, which leads to the final attack propagation of the exposed metal, has been described using various theories:

- ✓ **Formation of soluble complexes:** many authors have concluded that after the adsorption of aggressive anions intermediate soluble complexes are formed between aluminium

and halides, especially in the case of  $\text{Cl}^-$  that is the most widely investigated situation [12-14]. One of the more often proposed mechanisms is a stepwise chlorination of aluminium hydroxide, which leads to the formation of transitory compounds,  $\text{Al}(\text{OH})_2\text{Cl}$  and  $\text{Al}(\text{OH})\text{Cl}_2$ , and to aluminium chloride,  $\text{AlCl}_3$ . Since these compounds are soluble, a thinning of the aluminium oxide takes place at the weakest spots of the film where  $\text{Cl}^-$  ions have been adsorbed.

- ✓ Penetration of aggressive species: this theory suggests that  $\text{Cl}^-$  ions incorporate into and migrate through the passive film resulting in film breakdown. The diameter of chloride ions is 0.36 nm [15] and it is then conceivable that they can penetrate through the defective sites of the aluminium oxide film with relative ease. Natishan *et al.* [16, 17] have actually shown by means of XPS and XANES techniques the incorporation of  $\text{Cl}^-$  in the Al oxide film, which was attributed by the authors to migration of these species from the solution/film interface to the interface of the metal with the passive film. Different mechanisms have been suggested to explain how penetration of  $\text{Cl}^-$  ions can lead to oxide film breakdown. One of these is the point defect model, which explains the growth kinetics of a passive film and was extended to account for the chemical breakdown of the film [18]. One assumption of this model is the diffusion of metal cations from the metal/film to the film/solution interface, which causes the formation of metal vacancies at the metal/film interface that tend to submerge into the bulk of the metal. However, the penetration of chloride ions in the passive film enhances the metal cations diffusion rate, which becomes higher than the submergence of the metal vacancies, and as a consequence the metal vacancies start piling up and form voids at the metal/film interface that can in turn lead to local collapse of the oxide film. A different mechanism was suggested by Burstein and Souto [19], who stated that when  $\text{Cl}^-$  ions reach the metal/film interface islands of  $\text{Cl}^-$  or  $\text{Cl}^-$ -containing compounds may nucleate and grow leading to internal stresses, which can exceed a critical fracture stress of the Al oxide film and thus causing film ruptures.
- ✓ Chemico-mechanical theory: this theory postulates that the adsorption of chloride ions onto the film/solution interface results in "peptization" due to mutual repulsion of the adsorbed charged species. When the repulsive forces are sufficiently high, the breakdown of the film occurs [20, 21]. This approach has not been further considered in recent years.
- ✓ Crack healing mechanism: according to Richardson and Wood [11], the natural oxide film on aluminium surfaces contains flaws, which are caused by mechanical damages and by microstructural heterogeneities. During exposure, depending on the environmental conditions, two possible events can occur: the flaw either is repaired or becomes a nucleation site for pitting. The presence of chloride ions, which preferentially adsorb into these flaws, render the second possibility the predominant one inhibiting the repair of the defect in the film.

The most probable mechanism is likely a combination of soluble complex formation and  $\text{Cl}^-$  ions penetration, leading to the result that the aluminium oxide film is locally thinned and/or damaged and therefore a direct attack of the aluminium substrate can take place. At this

moment, the initiation of the pit is concluded and the pit can either repassivate (metastable pit) or propagate (sometimes called "stable" pitting).

After pitting has been initiated, the process propagates by anodic dissolution of aluminium in the occluded pit environment and cathodic reactions on the surface adjacent to the pit [1], as schematically shown in Figure 2.2. According to Hagyar and Williams [22] inside the pit, after the rapid ionisation of Al to  $Al^{3+}$  the following reactions occur:



From these reactions it appears clear that pitting is an autocatalytic process, i.e. is producing by itself the conditions necessary to propagate. Indeed, the dissolution of Al tends to produce an excess of positive charge inside the pit (reaction 2.1) leading to inward migration of chloride ions, which in turn form compounds with Al (reaction 2.2) that hydrolyse and decrease the pH of the solution inside the pit (reaction 2.3). The high concentrations of  $H^+$  and  $Cl^-$  in the occluded pit environment enhance the anodic dissolution rate inside the pit itself and enable its propagation.

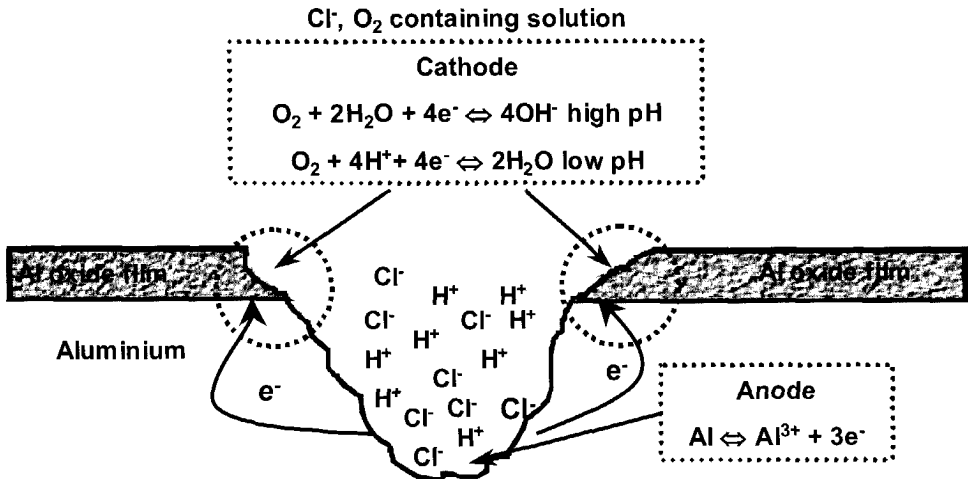


**Figure 2.2:** Schematic representation of pitting propagation on aluminium in chloride aerated solution.

Besides, since the solubility of oxygen in highly concentrated solution, as that present in the pit, is very low a differential aeration cell is created between the pit, which is oxygen-free and acts as anode, and the areas adjacent to the pit, which are oxygen-rich and act as cathode. Since aluminium oxide is not a good conductor, the extension of the cathodic area is very limited and located nearby the pit, where the oxide film is damaged and the necessary pathway for the electrons is present (Figure 2.2). During the propagation of the pit corrosion products can deposit and form a cap that completely or partially covers the pit mouth.

However, it is obvious that a pit will develop only when the low pH and high  $Cl^-$  concentration are maintained within the pit. A first criterion for stable pit propagation was

proposed by Galvele [23], who suggested that a pit would grow continuously if a critical value of the parameter  $x \cdot i$  (pit depth times pit current density) were exceeded. More recently, Pride *et al.* [24] have found that stabilization of the pit occurs on aluminium when the ratio between the current within the pit and the radius of the pit ( $I_{\text{pit}}/r_{\text{pit}}$ ) is greater than  $10^{-2}$  A/cm. Both criteria are based on the ability of keeping a sufficient low pH inside the pit, which leads to high Al dissolution rate and results also in the deposition of aluminium/chloride salts inside the pit that are stable only at very low pH. As a consequence, any phenomenon that leads to dilution of the pit electrolyte, as the rupture of the cap of corrosion products due to hydrogen evolution or osmotic pressure, can cause the repassivation of the pit that stops to grow.

### 2.2.2 Intergranular

Intergranular corrosion is a localized attack at and adjacent to grain boundaries accompanied by little or no corrosion of the grains themselves, which can in the worst case drop out from the surface. This form of localized corrosion arises from potential differences, i.e. local electrochemical cells, between the grain and the grain boundaries area. The formation of these local cells at the grain boundaries can have different causes: presence of impurities, segregation of alloying elements, precipitation of intermetallic particles, depletion of some elements in a band along the grain boundaries [1, 3]. Similarly to pitting corrosion, two stages, i.e. initiation and propagation, can be distinguished in the intergranular attack.

The initiation stage consists, as in all forms of localized corrosion, of local breakdown of the passive film on the aluminium surface, which occurs in a similar way as described in the previous section for pitting and is favoured by the presence of halide species in the environment. It has been shown that grain boundaries and especially triple point boundaries of the grains are locations of flaws and defects in the oxide film [25, 26]. Therefore, the breakdown of the Al oxide film is more probable to take place at these sites, exposing grain boundary areas to the aggressive environment. Whether this results in propagation of the anodic dissolution along the grain boundaries, i.e. intergranular attack, or formation of a pit depends on the nature and reactivity of the grain boundaries themselves, i.e. on the presence or absence of strong galvanic couples. It has been often observed that first a pit is formed as a consequence of the passive film breakdown and afterwards intergranular attack starts to develop from either the bottom or the walls of the pit. Intergranular corrosion penetrates more quickly than pitting but reaches a self-limiting depth due to limited transport of oxygen and aggressive species down the narrow corrosion path [5].

### 2.2.3 Exfoliation

Exfoliation, also called layer corrosion or lamellar corrosion, is a form of selective subsurface attack that proceeds along narrow strata parallel to the external surface [3, 5]. Usually, it takes place along the grain boundaries, and then is often ascribed as a special case of intergranular corrosion that occurs in relatively thin products characterized by a highly worked and directional microstructure, e.g. rolled sheets. However, exfoliation can also result from intragranular corrosion along a layer associated with a high density of

intermetallics, which have been lined up during the thermo-mechanical treatments undergone by the aluminium product. Also in the case of exfoliation the attack starts with the breakdown of the passive film, usually at the sheared edge of the piece rather than at the rolled or extruded surface, afterwards the corrosion process continues in the direction parallel to the external surface due to the presence of galvanic cells lined up along this direction, either at the grain boundaries or inside the grains. Alternate layers of thin, relatively uncorroded metal and thicker layers of corrosion products characterize a sample observed in cross section after the occurrence of exfoliation. Since the layers of corrosion product occupy a larger volume than the original metal, their formation leads to swelling of the metal itself.

### 2.2.4 Filiform

Filiform corrosion occurs on aluminium surfaces coated with a thin organic film and is characterized by the appearance of fine filaments emanating from one or more sources with semi-random directions [5]. The initiation stage involves the formation of a differential aeration cell due to the presence of a defect in the organic film, which can either be originated mechanically, i.e. scratches, or chemically, i.e. osmotic blistering.

Indeed, at the location of the defects in the organic coating water and aggressive species can reach the aluminium passive film and cause its breakdown, as described before in the case of pitting, leading to corrosion attack. Since in this situation the main oxygen transport path is through the aluminium corrosion products, a differential aeration cell is created where oxygen is mainly reduced at the center of the blister and aluminium is mainly dissolved at the edges. Once a differential aeration cell is established, the corrosion attack underneath the coating can propagate and a transition from a circular to a uni-directional filament growth may take place [27, 28].

The mechanism of filiform corrosion propagation on aluminium is anodic undermining, which consists of anodic dissolution of aluminium occurring at the head of the filament and cathodic reactions, mainly oxygen reduction, taking place at the back of the head or at the front of the area where corrosion product are deposited (Figure 2.3). This spatial separation of the anodic and cathodic sites, which is due to the differential aeration cell, results in acidification and increase in chloride concentration at the head of the filament, similarly to the occluded solution in a pit. This provides the necessary conditions for breakdown of the passive film and further corrosion attack to continue in the head of the filament, and

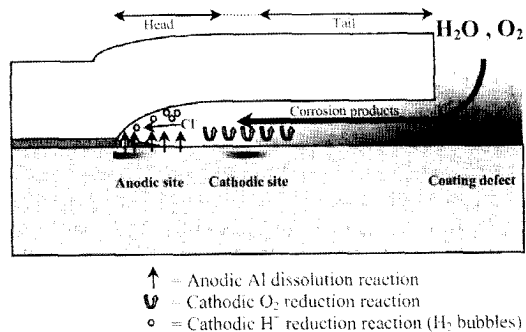


Figure 2.3: Propagation mechanism of filiform corrosion on aluminium [Ref. 27].

and

therefore for the propagation of the filiform corrosion. However, entrapment of chloride in the corrosion products and decrease of the oxygen concentration gradient promote a stagnation of the filament growth after considerable exposure time [27].

### 2.2.5 Other forms of localized corrosion

Localized corrosion can occur when an electrolyte is present in a crevice formed between two facing aluminium surfaces, or between an aluminium surface and a non-metallic material, as a gasket, sand or dirt deposit, etc. This form of localized attack is called crevice corrosion and takes place in many mediums, although it is more intense in those containing chloride [1, 3]. The corrosion attack is located inside the crevice due to the formation of an occluded solution that is enriched in  $H^+$  and  $Cl^-$  ions and depleted in oxygen. Indeed, once the reduction reaction has consumed all the oxygen inside the crevice a differential aeration cell is created between the crevice, where diffusion of oxygen is hindered, and the areas adjacent to it. This results in the spatial separation of the anode, located inside the crevice, and the cathode, located outside the crevice. In the case of aluminium, the cathodic area is small and very nearby the crevice, since aluminium oxide is a poor conductor. Inside the crevice dissolution of aluminium to  $Al^{3+}$  continues and this leads to migration of chloride in order to maintain the charge balance, which in turn enhances the corrosion attack in the crevice. Actually, the propagation mechanism of crevice corrosion is virtually identical to that of pit, since the pit itself can be considered as a crevice.

Galvanic corrosion occurs when two metals or alloys with a different surface potential are connected in the same electrolyte [1, 3]. The extent of the attack depends on the value of the potential difference, which is the driving force for the anodic reactions to take place on the less noble metal and the cathodic reactions on the more noble metal of the couple. This form of corrosion can be localized, as in the case of coupling between aluminium matrix and intermetallic particles that leads to local dissolution either of the matrix near the cathodic intermetallics or of the anodic intermetallics.

Selective leaching is the removal of the less noble element from a solid alloy as a result of corrosion processes [1]. This form of attack can occur also in the intermetallic particles present in aluminium alloys when these are formed by elements with strong difference in corrosion potential, as copper and magnesium.

Stress corrosion cracking (SCC) refers to sub-critical propagation of cracks caused by the simultaneous presence of tensile stress and a specific corrosive environment, which have a synergetic effect [1, 3]. During this type of attack the aluminium is virtually uncorroded over most of its surface, while fine cracks progress through it generally along the grain boundaries.

### 2.3. Localized corrosion and alloy microstructure

In aluminium alloys the intermetallics, which are classified as constituent particles or inclusions, dispersoids, and strengthening precipitates depending on their size [29], strongly influence the localized corrosion behaviour of the alloy especially when they are sufficiently large in size or when they are concentrated by preferential precipitation on boundaries [30].

Although it is recognized that also the alloying elements in solid solution affect the localized corrosion process, the attention in the literature survey was principally focused on the role of the intermetallics since it is of main interest for this work.

Intermetallic particles play a fundamental role both in the initiation and in the propagation of localized attack. Indeed, the presence of intermetallics, either cathodic or anodic to the Al matrix, favours the aluminium oxide film breakdown, which is the initiation step for all forms of localized corrosion, since they are sites of flaws and defects in the oxide film. In the case of cathodic intermetallics the effect on the breakdown process is even worse due to alkalisation of the electrolyte in their proximity, which renders the aluminium oxide less stable, and due to the polarization of the matrix around them to a potential close to its pitting potential. Moreover, the formation of galvanic cells between the intermetallics and the matrix provides the driving force for the electrochemical reactions involved in the propagation of the localized corrosion. In the remainder of this section the role played by the intermetallics in the different forms of localized attack will be described and discussed for the different families of aluminium alloys with major attention for AA2024, as it is the material used in this study.

### 2.3.1 2xxx series: Al-Cu system

In the alloys of 2xxx series a heterogeneous microstructure is intentionally developed by addition of large quantities of copper to optimise the mechanical properties. Among the alloys of this family, AA2024 is the most investigated one since it is widely used in the aircraft industry for numerous applications, like as fuselage, door skin, dorsal fin, bottom wing skin, stringers, and trailing edge panels, due to its high strength-to-weight ratio, good damage tolerance, and low cost. The typical composition of AA2024 is, on a weight percentage basis, as follows: 90-93% Al, 3.8-4.9% Cu, 1.2-1.8% Mg, 0.5% Si, 0.5% Fe, 0.3-0.9% Mn, 0.25% Zr, 0.15% Ti, 0.1% Cr, and 0.15% others, including Ni. The intermetallics present in this alloy can be classified into three general categories: Al-Cu, Al-Cu-Mg, and Al-Cu-Fe-Mn containing particles [31-34]. Differences in apparent composition are often observed amongst particles with the same elemental constituents and in some cases even amongst different regions of the same intermetallic. However, generally the Al-Cu and Al-Cu-Mg containing intermetallics are assigned to the  $\text{Al}_2\text{Cu}$  ( $\theta$ -phase) and  $\text{Al}_2\text{CuMg}$  (S-phase) chemical type, respectively. On the other hand, the assignment of the Al-Cu-Fe-Mn containing intermetallics is more difficult since different chemical phases are thermodynamically and kinetically possible:  $\text{Al}_6(\text{Cu,Fe,Mn})$ ,  $\text{Al}_7\text{Fe}_2\text{Cu}$ ,  $\text{Al}_{20}\text{Mn}_3\text{Cu}_2$  and  $(\text{Al,Cu})_6\text{Mn}$  that in some cases are enriched in silicon.

Amongst the coarse intermetallics, which are very large in size (up to 30  $\mu\text{m}$ ), the most heavily populated category is the round-shaped Al-Cu-Mg particles followed by the irregularly shaped Al-Cu-Mn-Fe ones, whereas the Al-Cu category is not always present. The smaller intermetallics are needle shaped  $\text{Al}_2\text{CuMg}$  and  $\text{Al}_2\text{Cu}$  strengthening particles, which can precipitate both inside the grains and preferentially at the grain boundaries and provide the increased strength performance of the alloy. A further improvement of the mechanical properties is obtained by the addition of small amount of elements, as Cr, Zr,

and Mn, which causes the precipitation of dispersoids, like as rod shaped  $\text{Al}_{20}\text{Mn}_3\text{Cu}_2$  small intermetallics, that act as grain refiners retarding the recrystallisation kinetic [31].

All categories of coarse intermetallics strongly affect the pitting corrosion behaviour of AA2024, but in different way and extent:

- ✓ Al-Cu-Mn-Fe coarse intermetallics have been shown to have in air a more noble Volta potential in comparison with the Al matrix [35], in good agreement with the corrosion potential value measured for a bulk precipitate in chloride solution [36]. Therefore, these intermetallics act as cathodic sites and promote the dissolution of the matrix around them (Figure 2.4) that results in formation of pits, as observed by many authors after exposure to chloride-containing electrolyte at neutral pH [33, 37-39]. Dissolution of the matrix continues as long as the intermetallic retains electrical contact with the matrix and is cathodically controlled due to the smaller area represented by the cathodic intermetallic. In addition, the cathodic nature of the Al-Cu-Mn-Fe intermetallic particles leads to rapid reduction of oxygen with consequent increase of the pH in their proximity (see  $\text{O}_2$  reduction reactions in Figure 2.2). This in turn causes alkaline attack of the Al adjacent to these intermetallics, resulting in a trench-like attack morphology, which often forms a perimeter around the particle [34, 38]. This is in agreement with Missert and co-workers [40], who found that a highly alkaline solution environment with consequent deposition of corrosion products is created in proximity of engineered copper islands in Al thin films, which were used to model the cathodic intermetallics in AA2024.

However, the behaviour of Al-Fe-Cu-Mn intermetallics upon immersion in chloride

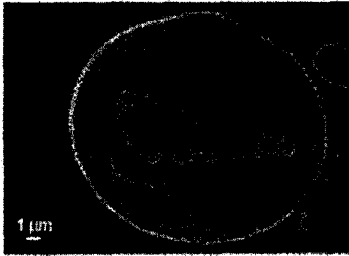


**Figure 2.4:** Al matrix dissolution around an Al-Cu-Fe-Mn intermetallic [Ref. 39].

Mn-Fe intermetallics that results in non-uniform dissolution of the intermetallic in concentrated chloride media [35, 41]. Suter and Alkire [42] also observed preferential dissolution of iron and manganese during anodic polarization, especially at the edges of the particle, which gives rise to a spongy structure. In addition, as the high local pH in proximity of these intermetallics stabilizes, it induces the hydrolysis of dissolved iron cations, resulting in an iron oxide/hydroxide deposition on their surface [43]. Nonetheless, the main effect of Al-Fe-Cu-Mn intermetallic particles is to induce breakdown of the passive film on the surrounding matrix and consequent Al dissolution due to galvanic coupling and alkanisation of the electrolyte.

solution is not as simple as this model system. First of all, a secondary effect of their cathodic nature is the reduction at their location of  $\text{Cu}^{2+}$  ions dissolved in solution, which leads to nodular Cu deposits, as observed by Chen *et al.* [37]. Besides, in some cases a dispersoid-free zone was observed around these intermetallics, which is supposed to enhance even more the dissolution of the Al matrix around them [33]. Another important aspect is the presence of lateral Volta potential gradients in some Al-Cu-



- ✓ Al-Cu coarse intermetallics, which are less frequently encountered in AA2024, behave similarly to the Al-Cu-Mn-Fe particles. That means, they function as local cathodes and induce pitting at their periphery, assisted by the attack due to the alkaline conditions locally developed [44]. The cathodic trenching in standard corrosive solution (0.5M NaCl pH=6) caused by this category of intermetallics seems to be more severe and faster than in the case of Al-Cu-Mn-Fe containing particles [34]. Besides, they also undergo selective dissolution of the more active element, i.e. aluminium, leaving behind a Cu-enriched particle remnant. The dealloyed particle remnants are physically unstable and have been observed to coarsen and emit 10 to 100 nm metallic clusters into corrosion products and surface films, which in turn become more conductive [44].
- ✓ Al-Cu-Mg coarse intermetallics are expected to preferentially dissolve, since the corrosion potential of a bulk Al-Cu-Mg sample in solution has been found to be 0.3-0.4 V lower than that of AA2024 [36]. However, the behaviour of this category of intermetallics is not so simple and changes from particle to particle and even from region to region of the same particle. Indeed, different phenomena have been observed to occur depending on the conditions of exposure, but even simultaneously in the same sample on different Al-Cu-Mg intermetallics: selective dissolution of Al and Mg in different extents leaving behind a spongy structure enriched in copper [32, 33, 37, 38, 42, 43], complete dissolution of the intermetallic [33, 37, 39, 41, 45], preferential dissolution of the surrounding matrix [32, 33, 38, 39, 42, 43]. The first two phenomena would suggest an anodic nature of the intermetallic particles, whereas the later would indicate that these intermetallics serve as cathodic sites. In addition, Al-Cu-Mg intermetallics often undergo both dealloying with formation of a porous system and dissolution of the Al matrix, suggesting a reversal of the galvanic couple matrix-intermetallic during exposure. Indeed, the common theory concerning the corrosion mechanism associated with Al-Cu-Mg intermetallics states that these intermetallics are initially active with respect to the matrix and are partly dissolved by dealloying resulting in a copper-rich remnant, which then behaves as a cathodic site and induces peripheral matrix pitting.

Although this theory explains most of the phenomena observed, it does not take into account that in some cases intact Al-Cu-Mg particles with a pit in the surrounding matrix are observed, which suggests that matrix dissolution occurs before any evident dealloying process has taken place due to exposure to the electrolyte [32, 33]. To explain all these observations we believe that a multi-step mechanism (Figure 2.5) for the corrosion processes related to Al-Cu-Mg intermetallics must be considered. Before immersion the Al-Cu-Mg intermetallics have a more noble surface potential with respect to the Al matrix, as shown by Schumtz *et al.* [35], due to the presence of a quite dense surface layer enriched in copper, which is itself catalytic for reduction reactions and inhibits dissolution of the underlying material (step I in Figure 2.5). The cause of the formation of this layer, which can be considered as a pseudo-passive film, is not yet completely clear. However, considering the high reactivity of the Al-Cu-Mg intermetallics [37, 46, 47] it can be supposed that partial dealloying of the outermost surface layer can occur even during exposure in humid air, and afterwards this layer becomes dense as a

result of the superficial cold-work caused by mechanical treatments, as rolling, polishing, etc. [33].

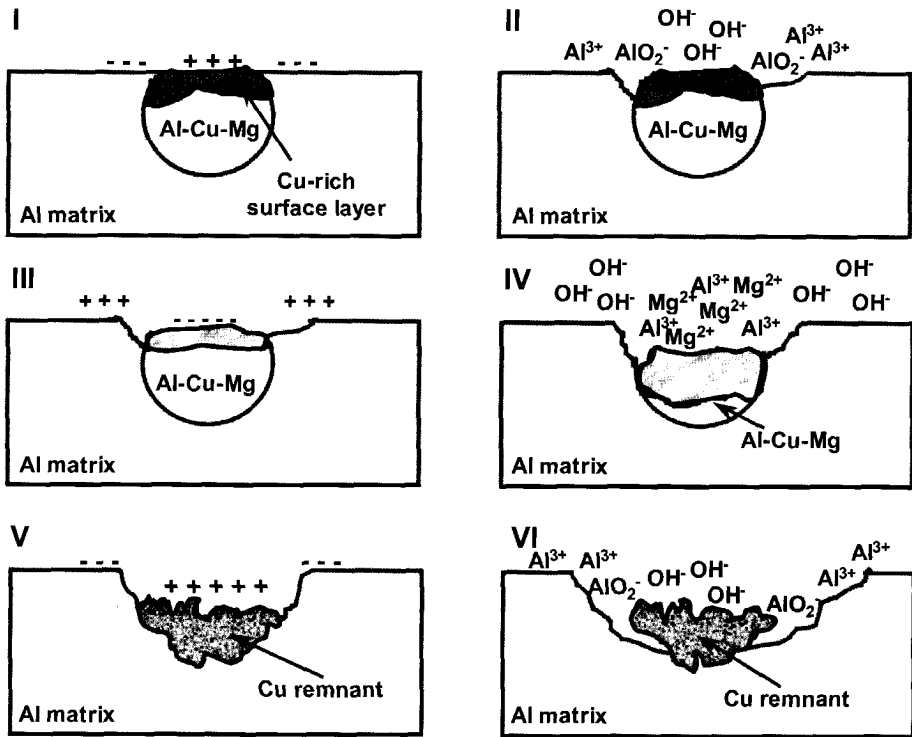


**Figure 2.5:** Schematic representation of the corrosion mechanism associated with Al-Cu-Mg intermetallic particles.

Besides, also the polishing process can give rise to selective dissolution phenomena, in accordance with the findings of Shimizu et al. [48], who observed the preferential dissolution of Al during electropolishing leading to a few nanometers thick layer enriched in copper even on the surface of pure aluminium containing only 30 ppm of Cu. Another cause of the copper-rich film on the surface of Al-Cu-Mg intermetallics could be the diffusion of copper from the bulk of the intermetallic towards the external surface. Anyway, this copper-rich film on top of the Al-Cu-Mg intermetallics is an effective local cathode capable of inducing dissolution of the surrounding matrix via galvanic coupling and alkalinisation of the solution (step II in Figure 2.5). In addition, destabilization and breakdown of this modified surface layer can also occur during immersion in the aggressive solution leading to exposure of the underlying Al-Cu-Mg intermetallic, which acts as a local anode and undergoes selective dissolution of Al and Mg starting from the edges (steps III and IV in Figure 2.5). Obviously, anodic polarization [33, 42] speeds up the breakdown of the Cu-rich surface layer and based on the findings of Schumtz and Frankel [41] mechanical interactions, as rastering with the tip of the AFM, seem to have a similar effect.

After the dealloying has taken place, a spongy structure enriched in copper is left behind, which serves again as cathodic site and further enhances the Al matrix local dissolution (steps V and VI of Figure 2.5). It is important to note that the time extent of the different steps can vary from particle to particle and even from area to area of the same particle, depending on the stability of the pseudo-passive Cu-rich layer, thus explaining the very different morphologies of attack observed by many authors. Indeed, when the Cu-rich layer is very stable it is possible that steps I and II last for the complete immersion time resulting in an intact Al-Cu-Mg particle with a dissolved zone at its periphery, whereas when the Cu-rich film is very instable steps I and II are extremely short, or even absent, and severe dissolution of the intermetallic occurs. Finally, in intermediate situations of stability of this layer the duration of the different steps is similar leading to both local matrix dissolution and dealloying of the intermetallic. It is reasonable to think, even if not yet proved experimentally, that the stability of the Cu-rich layer is function of the exposure conditions (T, pH, chloride concentration, etc.) and of the intermetallic properties (amount of Mg, crystallographic structure, etc.). As a consequence, since in one sample a range of different Al-Cu-Mg intermetallics exists, exposure to a certain solution causes a range of different types of corrosion attack to these intermetallics, from negligible to complete dissolution.

An important phenomenon associated with the corrosion process of Al-Cu-Mg intermetallics is the copper redeposition observed at cathodic sites of the surface, as Al-Fe-Mn-Cu particles. Buchheit and his co-workers extensively investigated this aspect [36, 44, 49]. They suggested that the porous copper remnant coarsens to reduce its surface energy and as a consequence clusters of metallic Cu, 10 to 100 nm in diameter, become detached, are captured in the corrosion product gel and move away due to mechanical transport related either to growth of the corrosion products or to solution movement. This non-faradic detachment electrically isolates the copper clusters from the substrate and therefore their potential rises from the OCP of the Al alloy to the OCP of Cu enabling the oxidation of copper. Then copper ions are liberated into the solution and can reduce at cathodic sites forming a copper deposits. A similar phenomenon was found to occur during the corrosion process at  $\text{Al}_2\text{CuLi}$  intermetallics present in Al-Cu-Li alloys [44]. The redeposition of copper further decreases the resistance to localized attack of AA2024, especially when together with chloride ions also sulfate ions are present since they are aggressive species for copper and lead to micropits in the proximity of the copper deposits [45, 50].

The pitting susceptibility of AA2024 is determined not only by the chemical composition and size of the intermetallic particles but also by their distribution. If the intermetallics are distributed in clusters and bands, as it is often the case for rolled products, the localized corrosion in proximity of an intermetallic can expose subsurface intermetallics to the electrolyte enhancing the pit growth in depth through further nucleation and coalescence of pits [37, 39]. As pitting proceeds, the acidified local environment promotes also pit growth in the classical sense, but the galvanic coupling between matrix and intermetallics is expected to be a major contributor to the growth of the pit. Besides, it has

been recently shown that the concentration and distribution of cathodic intermetallics on the surface of a coated AA2024 plays a very important role in the propagation of filiform corrosion [27].

As concern the intergranular form of localized corrosion, it is generally accepted that the most important microstructural aspect is the formation of a copper-depleted zone adjacent to the grain boundaries during the precipitation of copper-containing intermetallics along the grain boundaries themselves [51]. Indeed, a galvanic coupling between this copper-depleted zone (anode) and the aluminium matrix (cathode) exists and results in preferential dissolution along the grain boundaries. This mechanism of intergranular corrosion is confirmed by the fact that the intergranular attack is reduced by thermo-mechanical treatments that decrease the heterogeneity in copper concentration in solid solution [38, 52, 53], such as rapid quench, which limits the grain boundary precipitation and therefore the extension of the depleted area, and artificial aging, which reduces the solid solution copper concentration in the body of the grain. The influence of the intermetallics on the extent of intergranular attack is considered to be only secondary and related to their tendency to precipitate at the grain boundaries. As an example, the Al-Li alloy AA2090 was found to be more susceptible to intergranular attack than AA2024 because the  $\text{Al}_2\text{CuMg}$  phase of AA2024 has a lower tendency to concentrate on boundaries than the  $\text{Al}_2\text{CuLi}$  phase of AA2090. On the other hand, Robinson *et al.* [54] attributed a more important role to the type of intermetallics present at the grain boundaries. Indeed, these authors claimed that the faster intergranular corrosion shown by AA2024 in comparison with AA2014 should be attributed to the precipitation at the grain boundaries of  $\text{Al}_2\text{CuMg}$  intermetallics, which undergo anodic dissolution, in the former and of  $\text{Al}_2\text{Cu}$  intermetallics, which are not dissolved, in the later. However, keeping in mind the very complex behaviour of Al-Cu-Mg intermetallics discussed above it appears evident that the role of these intermetallics in enhancing intergranular attack is not so simple and straightforward.

In addition, it is well known that the parameters of the heat treatments, which are always carried out on AA2024 in order to optimise its mechanical properties, strongly influence the susceptibility of the alloy to all types of localized corrosion. Generally, the heat treatment involves a solution treatment at a temperature within the range 460-530°C, followed by quenching into water and then either aging at room temperature (natural aging) or artificially aging at temperatures up to 190°C [55]. Quenching and specifically the cooling rate, is the most critical step in the sequence of heat treatment operations not only to obtain the best combination of strength and toughness, but also to limit the corrosion susceptibility [29]. It has been shown that the cooling procedure after solution treatment and also the aging procedure after quench result in drastic changes in the corrosion behaviour of AA2024 [56, 32] due to the precipitation of intermetallics that differ in size, shape, and distribution. In particular, the quench rate and the temperature and time of aging have been found to affect the pitting susceptibility [57], the intergranular and exfoliation corrosion extent due to modifications of the grain boundary region [52, 58, 59], and the stress corrosion cracking

resistance due to changes in the type of intermetallic/matrix interface, i.e. coherent, semi coherent, incoherent [60].

### 2.3.2 1xxx series: pure aluminium

This family includes super-purity aluminium (Al = 99.99%) and the various grades of commercial-purity aluminium (Al  $\geq$  99%) with a percentage of impurity up to 1%. Typical applications are lithographic products, chemical process equipment, heat exchangers, electrical conductors, capacitors, and packaging foils. Their corrosion resistance is relatively high, but it decreases with increasing the impurity content, especially iron. It is well known that commercial aluminium contains Fe impurities in the range of 0.3-0.7%, which leads to the formation of Fe-containing intermetallics during solidification due to the extremely low solubility of Fe in Al (0.004% at 400°C). Depending upon the melt composition and especially the cooling rate different types of intermetallics can form: the equilibrium phase Al<sub>3</sub>Fe, the metastable phases Al<sub>6</sub>Fe, Al<sub>x</sub>Fe, Al<sub>2</sub>Fe<sub>9</sub>, and the Si-rich phases  $\alpha$ -Al-Fe-Si,  $\beta$ -Al-Fe-Si, Al<sub>3</sub>FeSi, Al<sub>4</sub>FeSi<sub>2</sub> when silicon is present [61]. Anyway, all the iron-rich intermetallics have been found to be more noble than the aluminium matrix and as a consequence to enhance the susceptibility of aluminium to pitting corrosion [62] in a similar way as the Al-Cu-Mn-Fe intermetallics in AA2024, i.e. dissolution of the matrix in their surroundings due to the weaker oxide film, the galvanic coupling and the alkalisation of the solution. Besides, the Fe-containing intermetallics can undergo preferential dissolution of Al during exposure and become enriched in Fe, as observed by Nisancioglu [63] for Al<sub>3</sub>Fe in NaOH solution near the corrosion potential. This phenomenon enhances the cathodic nature of the intermetallics with consequent increase of matrix dissolution at their periphery.

### 2.3.3 3xxx series: Al-Mn systems

The microstructure of this series of aluminium alloys, widely used for packaging applications, is characterized by the presence of two main categories of intermetallics: Si-free Al<sub>6</sub>(Mn,Fe) phase and Si-containing  $\alpha$ -Al-(Mn,Fe)-Si phase, often identified as  $\alpha$ -Al<sub>12</sub>(Mn,Fe)<sub>3</sub>Si. Both intermetallic particles are cathodic with respect to the aluminium matrix, but on different extent. Indeed, it was found that the Si-containing intermetallics are more noble than the silicon-free ones [64]. On the other hand, Nisancioglu [65] suggested that the main factor in determining the electrochemical properties of these intermetallics is the iron content rather than the presence of silicon. Anyway, the cathodic nature of these intermetallics leads to pits nucleation at their location through preferential dissolution of the surrounding aluminium matrix (Figure 2.6), with a mechanism similar to that observed for Al-Cu-Mn-Fe intermetallics in AA2024 and described above [66].

Since manganese is less active than aluminium but more active than iron, the potential difference between the intermetallics and the matrix, i.e. the driving force for the corrosion process, is decreased by the increase of the amount of manganese content in solid solution either in the matrix or in the intermetallic phase [67]. Therefore, the Mn content in solid solution together with the density, size and distribution of intermetallic particles is expected to strongly affect the resistance of these aluminium alloys to localized corrosion. Afseth *et al.*

[66, 68] have recently carried out an extensive work on the influence of heat-treatments on the filiform corrosion susceptibility of AA3005. They found that annealing at temperature > 350°C results in a significant increase of filiform corrosion with a change of the morphology from a successive pitting type to a highly superficial attack.

The detrimental effect on filiform corrosion was attributed to the precipitation in the highly deformed surface layer of a fine dispersion of  $Al_{12}(Mn,Fe)_3Si$  intermetallics during the heat treatment, which simultaneously leads to a depletion of the matrix in noble alloying elements. This high density of small intermetallics provides both a larger area for the cathodic reactions and a high density of potential corrosion initiation sites that are both negative for the filiform corrosion resistance, and for the localized corrosion resistance in general. It is worthwhile to note that the formation of an active surface layer has been observed in other families of alloys after different mechanical processes, i.e. rolling, extrusion, etc., bringing in the foreground that the electrochemical properties of the bulk are extremely different than those of the surface.



**Figure 2.6:** Crystallographic pit around a large intermetallic on the surface of AA3005 after 15 minutes of immersion in 5 wt.% NaCl pH=3 solution [Ref. 66].

### 2.3.4 5xxx series: Al-Mg systems

These aluminium alloys, where the main alloying element is magnesium, find their principal applications in the building, marine and automotive industries. The typical intermetallic compounds encountered in Al-Mg alloys are coarse  $Al_6(Mn,Fe)$  constituent particles, whose amount depends on the manganese and iron content of the alloy, and small, discretely distributed  $\beta$ -phase particles, which are usually given as  $Al_3Mg_2$  or  $Al_6Mg_5$ . The former is however outside the limit of existence, whereas the latter fits the composition of the solid phase and most of the proposed structures [69]. Independently from the exact composition, the  $\beta$ -phase is strongly anodic to the Al-Mg solid solution matrix in the presence of many electrolytes [70, 71]. In contrast, as already observed for Al-Mn alloys, the coarse  $Al_6(Mn,Fe)$  intermetallics serve as cathodic sites and therefore pitting starts preferentially at their locations due to both the galvanic coupling and the local alkalisation of the solution [72].

Besides, precipitation of  $\beta$ -phase intermetallics has been observed to occur at the interface of  $Al_6(Mn,Fe)$  intermetallics and the Al matrix [70] resulting in a stronger local potential difference, which can be expected to enhance the pitting susceptibility of the alloy. However, it is generally accepted that the main role of the  $\beta$ -phase in the corrosion behaviour of Al-Mg alloys is to decrease the resistance to intergranular corrosion and stress corrosion cracking (SCC) [70, 71, 73, 74]. This is due to the fact that it forms initially at grain boundary triple points and then along the grain boundaries. In particular, when the alloy

contains an amount of Mg higher than 3.5% and is exposed to temperatures ranging from 50° to 200°C for sufficient time, a continuous band of the  $\beta$ -phase along the grain boundaries is formed that anodically dissolves if exposed to an aggressive environment and as a consequence causes severe intergranular corrosion and SCC when a stress is applied. The strong influence of the presence of  $\beta$ -phase at the grain boundaries on the susceptibility to SCC is confirmed by the observation that crack growth rate velocity increases with increasing the volume of this phase [74]. It was suggested that the crack propagation is enhanced not only by the anodic dissolution of the  $\beta$ -phase but also by the formation of hydrogen during the corrosion process, which can be adsorbed in the alloy resulting in brittle crack advance. In addition, recently a more fundamental role of magnesium segregation at the grain boundaries, which also would rapidly dissolve in contact with the solution, has been proposed [70].

Another remarkable aspect from a corrosion point of view of the high magnesium content in solid solution of this family of alloys is its tendency to oxidize and incorporate into the surface oxide layer. Afseth *et al.* [75] have shown that after heat treatment on the surface of AA5754 the oxide film consists of crystalline and amorphous separate phases and is strongly enriched in magnesium, especially in the crystalline oxide particles. Such a film is thought to be responsible for the observed increase in filiform corrosion susceptibility, since it is less protective and has lower adhesion to organic coatings than the pure aluminium amorphous oxide layer.

### 2.3.5 6xxx series: Al-Mg-Si systems

The aluminium alloys of this family are extensively used as extruded and rolled products for construction, transport industries and architectural applications. The strengthening particle  $\beta$ -Mg<sub>2</sub>Si, which forms during aging, characterizes the microstructure of these alloys. When copper is added in quantities higher than 0.25 wt.% (e.g. 6061, 6056, 6013 aluminium alloys) other strengthening intermetallics can precipitate, such as Al<sub>2</sub>Cu and Al<sub>5</sub>Cu<sub>2</sub>Mg<sub>8</sub>Si<sub>6</sub> [76-78]. Besides, different types of coarse insoluble intermetallics are observed in the aluminium alloys of 6xxx series: Al<sub>3</sub>Fe, Al<sub>6</sub>Fe, Al<sub>8</sub>Fe<sub>2</sub>Si, Al-Si-Mn-Fe and Al-Mg-Si-containing particles [76,79]. Blanc and Mankowski [80] have found that even when the copper content is relatively high (0.8 wt.%) as in AA6056 the coarse intermetallics are not enriched in this element. The strengthening particles mainly affect the intergranular corrosion behaviour of the alloys, whereas the bigger coarse intermetallics have a more significant influence on the pitting susceptibility. During aging the  $\beta$ -Mg<sub>2</sub>Si phase, which has a more active potential with respect to the Al matrix, precipitates preferentially at the grain boundaries creating a zone along the grain boundaries depleted in silicon. Although, the anodic dissolution of  $\beta$ -Mg<sub>2</sub>Si intermetallics resulting in lined up pits along the grain boundaries can enhance the intergranular corrosion, the main cause of the increase in intergranular corrosion susceptibility with aging time until the peak strength is ascribed to the formation of the Si-depleted zone, similarly to the Cu-depleted zone in 2xxx series alloys. Indeed, this area along the grain boundaries is anodic with respect to the rest of the grain and therefore preferentially dissolves during exposure to aggressive media [78, 79, 81].

Several observations confirm the predominant role played by the depleted zone in the intergranular corrosion process. When Si is in excess of the stoichiometric composition for the formation of  $\beta$ -Mg<sub>2</sub>Si, Si particles, which act as cathodic sites, tend to segregate at the grain boundaries enhancing both the depletion extent and the galvanic coupling and as a consequence resulting in more severe intergranular corrosion [79, 81]. The addition of copper in the alloy has a similar effect since it enables the formation of cathodic intermetallics (Al-Cu-Si and Al-Cu-Mg-Si) at the grain boundaries [76, 77]. Therefore, a reduction of the potential difference between the depleted zone adjacent to the grain boundaries and the grain center should be able to improve the intergranular corrosion resistance. This has been shown by many authors and can be obtained either by limiting the preferential precipitation at the grain boundaries and then the formation of the depleted zone, through the addition of Cr [81] or the formation of a grain structure with low angle boundaries [82], or by inducing the formation and growth of strengthening intermetallics inside the grain through an over-aging treatment [83].

In these alloys is often observed that pitting and intergranular corrosion are dependent upon each other since intergranular attack often initiates at the pit walls [77, 83] due to the more aggressive environment formed inside the pit. On the other hand, the principle sites of pit initiation and growth are the coarse intermetallics. In particular, the Al-Mg-Si ones undergo selective dissolution of Al and Mg during exposure and are very deleterious for pitting corrosion, whereas the Al-Si-Mn-Fe intermetallics serve as cathodes and induce matrix dissolution at their periphery, whose extent depends on both the electrolyte and the aging conditions [76, 80, 83]. The Fe-rich intermetallics, i.e. Al<sub>3</sub>Fe, Al<sub>6</sub>Fe, show a similar cathodic behaviour and lead to pitting of the surrounding matrix due to galvanic coupling and alkalinisation of the solution at their location [84].

### 2.3.6 7xxx series: Al-Zn-Mg systems

These aluminium alloys find application in the aircraft structural components and other high-strength products, like military vehicles. The strengthening particle of the Al-Zn-Mg alloys is the  $\eta$ -MgZn<sub>2</sub> phase, which develops during aging and preferentially precipitates at the grain boundaries. Since the MgZn<sub>2</sub> intermetallics are less noble with respect to the aluminium matrix, their precipitation at the grain boundaries results in the formation of an anodic path along the grain boundaries themselves, which in turn is responsible for the susceptibility to intergranular corrosion, or intergranular stress-corrosion cracking in the presence of tensile load, of this family of aluminium alloys [85]. However, the intergranular corrosion is not caused only by the precipitation of MgZn<sub>2</sub> intermetallics but also by the segregation of solute atoms (Zn and Mg) at the grain boundaries, which enhances their anodic nature, and by the formation of a precipitate-free zone near the grain boundaries, which increases the difference in potential between the matrix and the grain boundaries [86].

Since iron is always present as impurity in commercial aluminium, also the 7xxx aluminium alloys are characterized by the presence of Fe-rich coarse intermetallics, as Al<sub>3</sub>Fe, Al<sub>23</sub>CuFe<sub>4</sub>, Al<sub>7</sub>Cu<sub>2</sub>Fe, which serve as cathodic sites and have been observed to be preferential nucleation sites for pitting [87, 88]. Benedetti *et al.* [88] have found that the



presence of iron causes, in addition to the precipitation of cathodic intermetallics, a decrease of the growth of  $MgZn_2$  intermetallics leading to a matrix richer in Zn and Mg and therefore more anodic. This makes Fe even more deleterious for the resistance to pitting corrosion of Al-Zn-Mg alloys since the galvanic coupling between matrix and iron-containing intermetallics becomes stronger giving rise to a higher dissolution of the aluminium in proximity of these intermetallics.

## 2.4. Conclusions

The literature survey discussed in this chapter clearly shows the fundamental role played by the microstructure of aluminium alloys on their susceptibility to localized corrosion. On the other hand, it is well known that the microstructure is strongly affected by the heat and mechanical treatments undergone by the alloy. Even very small changes in the heat treatment procedure, which can easily occur during industrial practice, have drastic effects on the microstructure and as a consequence on the corrosion behaviour of aluminium alloys. Therefore, it is very important for both the producers and the users of aluminium alloys to be aware of the influence of the different heat treatment parameters on the microstructure of the aluminium alloys in order to avoid sudden product failures resulting from unexpected high localized corrosion. Thus, a part of this PhD work, which is discussed in Chapter 4, has been dedicated to the investigation of the influence of the time spent in air before water cooling, referred to as quench delay time, on the microstructure and the corrosion resistance of AA2024. The attention has been focused on this alloy because it is of interest from both an industrial and an academic point of view. Indeed, 2024 aluminium alloy is widely used for aircraft applications, where often the exposure conditions are quite severe and therefore the corrosion resistance of this alloy is an important issue. On the other hand, the microstructure of AA2024 is complex, especially in regard with the electrochemical behaviour of the intermetallics, and further investigations are required to completely understand the relation between microstructure and localized corrosion in this alloy.

## 2.5. References

- [1] M.G. Fontana, *Corrosion Engineering*, 3<sup>rd</sup> edition, McGraw-Hill Book Company (1986)
- [2] K.R. Trethewey, J. Chamberlain, *Corrosion for Science and Engineering*, 2<sup>nd</sup> edition, Longman Scientific & Technical, Essex, England (1995)
- [3] *Corrosion of aluminium and aluminium alloys*, J.R. Davis (ed.), Materials Park: ASM International (1999)
- [4] G.E. Thompson, G.C. Wood, *Corrosion: Aqueous Processes and Passive Films*, Academic Press, London (1982)
- [5] *Special Metals Handbook: Aluminium and Aluminium Alloys*, J.R. Davis (ed.), Materials Park: ASM International (1994)
- [6] R.T. Foley, *Corrosion* 42 (1986) 277
- [7] E. McCafferty, *J. Electrochem. Soc.* A46 (1999) 2863
- [8] Z. Szklarska-Smialowska, *Corros. Sci.* 41 (1999) 1743
- [9] A. Berzins, R.T. Lowson, K.J. Mirans, *Aust. J. Chem.* 30 (1977) 1891

- [10] J. Augustynski, *Proceedings of the Fourth International Symposium on Passivity*, R.P. Frankenthal, J. Kruger (eds.), The Electrochem. Soc., Pennington, NJ (1978) 989
- [11] J.A Richardson, G.C. Wood, *J. Electrochem. Soc.* 120 (1973) 193
- [12] Z.A. Foroulis, M.J. Thubrikar, *J. Electrochem. Soc.* 122 (1975) 1296
- [13] T.H. Ngyen, R.T. Foley, *J. Electrochem. Soc.* 127 (1980) 2563
- [14] R. Li, M.G.S. Ferreira, *Mater. Sci. Forum* 192-194 (1995) 237
- [15] *CRC Handbook of Chemistry and Physics*, R.C. Weast (ed.), Boca Raton: CRC Press (1989-1990)
- [16] P.M. Natishan, W.E. Grady, E. McCafferty, D.E. Ramaker, K. Pandya, A. Russell, *Proceedings of the Electrochemical Society Meeting: Passivity and its Breakdown*, Paris, France (1997)
- [17] S.Y. Yu, W.E. Grady, D.E. Ramaker, P.M. Natishan, *J. Electrochem. Soc.* 147 (2000) 2952
- [18] L.F. Lin, C.Y. Chao, D.D. MacDonald, *J. Electrochem. Soc.*, 128 (1981) 1194
- [19] G. Burstein, R. Souto, *Electrochim. Acta* 40 (1995) 1881
- [20] L. Liepina, V. Kadek, *Corros. Sci.* 6 (1966) 177
- [21] T. P. Hoar, *Corros. Sci.* 7 (1967) 355
- [22] T. Hagyar, J. Williams, *Trans. Faraday Soc.* 57 (1961) 2288
- [23] J.R. Galvele, *J. Electrochem. Soc.* 123 (1976) 464
- [24] S.T. Pride, J.R. Scully, J.L. Hudson, *J. Electrochem. Soc.* 141 (1994) 3028
- [25] G.E. Thompson, P.E. Doherty, G.C. Wood, *J. Electrochem. Soc.* 129 (1982) 1515
- [26] G.E. Thompson, *Mater. Sci. Forum* 217-222 (1996) 95
- [27] J.M.C. Mol, PhD Thesis, TUDelft, The Netherlands (2000)
- [28] M.H.M. Huisert, PhD Thesis, TUDelft, The Netherlands (2001)
- [29] M.S. Hunter, A.M. Montgomery, G.W. Wilcox, *Aluminium: Physical Properties and Metallurgy*, 6<sup>th</sup> edition, J.E. Hatch (ed.), Metals Park, Ohio, US (1984)
- [30] R.G. Buchheit, J.P. Monar, G.E. Stoner, *Corrosion* 46 (1990) 610
- [31] L. Mondolfo, *Aluminium Alloys: Structure and Properties*, Butterworths, London (1976)
- [32] R.G. Buchheit, R.P. Grant, P.F. Hlava, B. McKenzie, G.L. Zender, *J. Electrochem. Soc.* 144 (1997) 2621
- [33] V. Guillaumin, G. Mankowski, *Corros. Sci.* 41 (1999) 421
- [34] O. Schneider, G.O. Ilevbare, R.G. Kelly, J.R. Scully, *Proceedings of the Electrochemical Society Meeting: Corrosion and Corrosion Prevention of Low Density Metals and Alloys*, Phoenix, Arizona, US (2000) 87
- [35] P. Schumtz, G.S. Frankel, *J. Electrochem. Soc.* 145 (1998) 2285
- [36] R.G. Buchheit, *J. Electrochem. Soc.* 142 (1995) 3994
- [37] G.S. Chen, M. Gao, R.P. Wei, *Corrosion* (1996) 8
- [38] T. J. Warner, M.P. Schmidt, F. Sommer, D. Bellot, *Z. Metallkd.* 86 (1995) 494
- [39] C. M. Liao, J.M. Olive, M. Gao, R.P. Wei, *Corrosion* 54 (1998) 451
- [40] N. Misset, R.G. Copeland, J.C. Barbour, J.E. Mikkalson, H. Isaacs, *Proceedings of the Electrochemical Society Meeting: Corrosion and Corrosion Prevention of Low Density Metals and Alloys*, Phoenix, Arizona, US (2000) 239
- [41] P. Schumtz, G.S. Frankel, *J. Electrochem. Soc.* 145 (1998) 2295
- [42] T. Suter, R.C. Alkire, *J. Electrochem. Soc.* 148 (2001) B36
- [43] A. Kolics, A.S. Besing, T. Suter, H. Böhni, C.H. Paik, R.C. Alkire, A. Wieckowski, *Electrochemical Society Proceedings* 23 (2000) 11
- [44] R.G. Buchheit, *Mater. Sci. Forum* 331-337 (2000) 1641
- [45] Ch. Blanc, B. Lavelle, G. Mankowski, *Mater. Sci. Forum* 217-222 (1996) 1559

- [46] R.G. Buchheit, F.D. Wall, G.E. Stoner, J.P. Moran, *Corrosion* 51 (1995) 417
- [47] J.R. Scully, D.E. Peebles, A.D. Romig, D.R. Frear, C.R. Hills, *Metall. Trans.* 23A (1992) 2641
- [48] K. Shimizu, H. Habazaki, P. Skeldon, G.E. Thompson, G.C. Wood, *Proceedings of the 2<sup>nd</sup> International Symposium on Aluminium Surface Science and Technology*, Manchester, England, UK (2000) 578
- [49] R.G. Buchheit, M.A. Martinez, L.P. Montes, *J. Electrochem. Soc.* 147 (2000) 119
- [50] Ch. Blanc, G. Mankowski, *Corros. Sci.* 40 (1998) 411
- [51] H.P. Godard, W.B. Jepson, M.R. Bothwell, R.L. Kane, *The Corrosion of Light Metals*, J. Wiley and Sons Inc., New York (1967) 70
- [52] J.W. Evancho, J.T. Staley, *Metall. Trans.* 5 (1974) 43
- [53] T.D. Burleigh, R.C. Rennick, F.S. Bovard, *Corrosion* 49 (1993) 683
- [54] M.J. Robinson, N.C. Jackson, *Br. Corros. J.* 34 (1999) 45
- [55] *Heat Treater's Guide*, H. Chandler (ed.), Materials Park: ASM International (1996)
- [56] Internal Fokker Aircraft report
- [57] C.S.M. Lombardi, E.M. Cintho, L.V. Ramanathan, *Proceedings of the 13<sup>th</sup> International Corrosion Congress (ICC)*, Paper 388
- [58] B.W. Lifka, D.D. Sprowls, *Localised Corrosion-Cause of Metal Failure*, in: ASTM STP 516, ASTM, Philadelphia, PA (1972) 120
- [59] S.J. Ketcham, *Corros. Sci.* 7 (1967) 305
- [60] L. Schra, W.G.J. 't Hart, *Effect of Cooling Rate on Corrosion Properties of High Strength Aluminium Alloys under Atmospheric Conditions*, NLR Technical Publication, TP 90138 L
- [61] P. Skjerpe, J. Gjønnes, *Ultramicroscopy* 22 (1987) 239
- [62] W.K. Johnson, *Br. Corros. J.* 6 (1971) 200
- [63] K. Nisancioglu, *J. Electrochem. Soc.* 137 (1990) 69
- [64] E.V. Koroleva, G.E. Thompson, G. Hollrigl, M. Bloeck, *Corros. Sci.* 41 (1999) 1475
- [65] K. Nisancioglu, *J. Electrochem. Soc.* 137 (1990) 69
- [66] A. Afseth, J.H. Nordlien, G.M. Scamans, K. Nisancioglu, *Corros. Sci.* 44 (2002) 145
- [67] M. Zamin, *Corrosion* 37 (1981) 627
- [68] A. Afseth, J.H. Nordlien, G.M. Scamans, K. Nisancioglu, *Corros. Sci.* 43 (2001) 2093
- [69] W.D. Fei, S.B. Kang, *Scr. Mater.* 34 (1996) 357
- [70] D.R. Baer, C.F. Windisch, M.H. Engelhard, M.J. Danielson, R.H. Jones, J.S. Vetrano, *J. Vac. Sci. Technol.* A18 (2000) 131
- [71] M.C. Carroll, P.I. Gouma, M.J. Mills, G.S. Daehn, B.R. Dunbar, *Scr. Mater.* 42 (2000) 335
- [72] M. Bethencourt, F.J. Botana, J.J. Calvino, M. Marcos, J. Perez, M.A. Rodriguez, *Mater. Sci. Forum* 289-292 (1998) 567
- [73] S.L. Searles, P.I. Gouma, R.G. Buchheit, *Proceedings of the Electrochemical Society Meeting: Corrosion and Corrosion Prevention of Low Density Metals and Alloys*, Phoenix, Arizona, US (2000) 344
- [74] R.H. Jones, D.R. Baer, M.J. Danielson, *Proceedings of the Electrochemical Society Meeting: Corrosion and Corrosion Prevention of Low Density Metals and Alloys*, Phoenix, Arizona, US (2000) 322
- [75] A. Afseth, J.H. Nordlien, G.M. Scamans, K. Nisancioglu, *Corros. Sci.* 43 (2001) 2359
- [76] V. Guillaumin, G. Mankowski, *Corros. Sci.* 42 (2000) 105
- [77] T.D. Burleigh, E. Ludwiczak, R.A. Petri, *Corrosion* 51 (1995) 50
- [78] R. Dif, B. Bes, J.C. Ehrstrom, C. Sigli, T.J. Warner, Ph. Lassince, H. Ribes, *Mater. Sci. Forum* 331-3237 (2000) 1613

- [79] A.K. Bhattamishra, K. Lal, Z. Metallkd. 89 (1998) 11
- [80] C. Blanc, G. Mankowski, Corros. Sci. 39 (1997) 949
- [81] A.K. Bhattamishra, K. Lal, Mater. Des. 18 (1997) 25
- [82] T. Minoda, H. Yoshida, Mater. Sci. Forum 331-337 (2000) 1689
- [83] V. Guillaumin, G. Mankowski, Corrosion 56 (2000) 12
- [84] J.O. Park, C.H. Paik, Y.H. Huang, R.C. Alkire, J. Electrochem. Soc. 146 (1999) 517
- [85] G. Dehais, S.B. Newcomb, Mater. Sci. Forum 331-337 (2000) 1635
- [86] S. Maitra, G.C. English, Metall. Trans. A 12A (1981) 535
- [87] R. P. Wei, C. M. Liao, M. Gao, Metall. Mater. Trans. A 29A (1998) 1153
- [88] A.V. Benedetti, P.L. Cabot, J.A. Garrido, A.H. Moreira, J. Appl. Electrochem. 31 (2001) 293

# Surface treatments of aluminium and its alloys

### 3.1 Introduction

The susceptibility to corrosion of aluminium alloys, described in the previous chapter, can be significantly reduced by the use of an appropriate finishing process, which consists of a conversion treatment usually, but not always, followed by the application of an organic coating (primer and topcoat). Therefore, the conversion treatment should first of all provide a good corrosion protection to the aluminium substrate and in many applications promote also a strong and durable adhesion to the organic coating. One of the qualification tests for commercial application of conversion coatings on aluminium is the ASTM-B117 salt spray testing in a chamber fogging with 5% NaCl at 38°C for 336 hours.

The surface conversion coatings for aluminium alloys are usually divided into two main categories: chemical and electrochemical, or anodic, conversion layers [1]. The former involve the use of a chemical solution without the application of any external current and are of great industrial significance, both in unpainted condition and as pre-treatment for organic coatings. The latter are obtained by making the aluminium surface anodic in an appropriate electrolyte and find a wide range of applications due to their properties, such as high corrosion resistance, good paint adhesion, and resistance to wear. However, the anodizing treatments can decrease the fatigue resistance, leading to premature failure of aluminium components. In addition, the choice of the surface treatment is determined not only by the quantity of corrosion protection or paint adhesion required but also by the costs involved. As an example, on one hand the anodic layers provide the best corrosion protection for aluminium and its alloys, but on the other hand the investment cost for chemical conversion treatments is only a fraction of the cost of anodizing.

Since many decades, the chemical conversion treatments based on chromate or chromate/phosphate solutions are widely used, especially in the aircraft industry, owing to their excellent corrosion resistance together with relatively low cost of application. More recently, the interest for phosphate conversion coatings on aluminium alloys has increased mainly due to the automotive industry. Indeed, for "multi-metal cars" the aluminium car body panels should be treated similarly to galvanized steel, i.e. zinc-phosphated, in order to enable the use of the same existing paints line. Unlike the chromate layer, the main characteristic of the phosphate one is the paint adhesion rather than the corrosion protection. The anodic conversion process on aluminium and its alloys can be carried out in many different electrolytes [2]. The most popular one was a sulfuric acid solution, used by

about 99% of anodizers, particularly in the building industry. However, the retention of small quantity of  $H_2SO_4$ , which can occur in components of complicated shape and in welded or riveted assemblies also after a neutralizing rinse, results in corrosion. Therefore, the aircraft, automotive, and marine industries have started to use electrolytes, as chromic acid solution, that inhibit corrosion if retained on the aluminium surface [3]. The use of phosphoric acid anodizing for aluminium alloys is limited to specific applications, as structural adhesive bonding in the aircraft industry, which require excellent adhesion to organic coatings.

Nowadays, the surface conversion treatments, either chemical or electrochemical, based on the use of chromate species, i.e. chromate or chromate/phosphate conversion coatings and chromic acid anodizing, are still the most used, in particular in airframe structures, since they are considered to give the best improvement in corrosion behaviour of aluminium alloys. On the other hand, the production, transport, storage and application of hexavalent chromium bath pose an actual as well as long term risk, since  $Cr^{6+}$  ions have a wide range of toxic effects: allergic skin and asthmatic reactions, ulcerations on the skin and in the mucous membranes, lung cancer due to inhalation [4]. As a consequence, several treatments for aluminium surfaces, which do not contain hexavalent chromium, are currently under development. The early attempts to find alternative non-toxic systems focused on metal oxianions analogous to chromate, as molybdates, tungstates, vanadates and permanganates [5]. These compounds can form oxide/hydroxide films on the aluminium surface similarly to the chromate species, but they provide lower corrosion protection. Other chromium-free processes, based on the use of zirconium and/or titanium fluorides complexes, are starting to be used in the packaging and automotive industries [6, 7]. More recently, new environmentally friendly chemical conversion coatings have been investigated, which are formed by immersion in solution containing rare earth metal chlorides [8]. Further studies involved the search for other film forming compounds suitable for aluminium, among which are cobalt salts [9], lithium salts [10, 11], silanes [12, 13], other sol-gel systems [14, 15], and self-assembled films [16, 17].

The following of this chapter deals with a more detailed literature survey on both the chromate and the cerium-based conversion coatings, since they are the surface treatments investigated in this PhD project.

### **3.2 Chromate conversion coatings (CCC)**

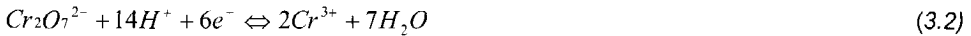
Two main conversion treatments are based on hexavalent chromium-containing solution: the chromate and the chromate-phosphate conversion coating, named yellow and green chromate layers, respectively. Both processes are carried out using an acid solution, which contains one or more sources of hexavalent chromium and fluorides. In the case of the chromate-phosphate conversion treatment, phosphoric acid is also added in the solution at a concentration ranging between 20 and 100 g/l. Different application methods are commonly used for these conversion layers: dipping, spraying, and no-rinse process. In the following of the section the attention will be focused on the yellow chromate conversion coating applied by dipping the aluminium substrate in an appropriate bath, since it is of particular interest for this study.

### 3.2.1 Formation, morphology and composition

Nowadays, chromate conversion coatings on aluminium alloys are obtained by contact of the metal surface with a chromic acid ( $\text{CrO}_3$ ) solution containing fluoride compounds, generally  $\text{NaF}$ , and  $\text{K}_3\text{Fe}(\text{CN})_6$ , added as accelerator. The pH of the bath is lowered to a value in the range 1.5-2. At this pH and at the relatively high concentration of  $\text{CrO}_3$  used in the bath, the chromic acid exists in solution as either the chromate  $\text{HCrO}_4^-$  or the dichromate  $\text{Cr}_2\text{O}_7^{2-}$ . Both these hexavalent chromium [Cr(VI)] compounds are excellent oxidizing agents and therefore the formation of the chromate film occurs via a redox process involving the oxidation of aluminium:



by the reduction of the Cr(VI) species:



The evolution of reactions 3.2 and 3.3 together with the reduction of hydrogen ions, as secondary cathodic reaction, results in an increase of the pH of the chromate solution in proximity of the aluminium surface to a value high enough to enable the precipitation of a gel of chromium hydroxide:



The addition of fluoride species to the chromate solution is a necessary condition for the formation of the chromate film, since they strongly activate the aluminium surface, especially in acid solutions, by partial or complete chemical dissolution of the natural aluminium oxide film during the first seconds of immersion and prevent the repassivation of the surface by forming soluble complexes with aluminium [18, 19]:



Goeminne *et al.* [20, 21] have extensively studied the role of fluoride species on the nucleation and growth of both chromate and chromate/phosphate conversion coatings on Al. They found that the increase in HF concentration in the chromate bath gives rise to a stronger and faster activation of the surface and then a thicker chromate film is formed after the same conversion time. However, when the quantity of HF exceeds a certain value the etching of the aluminium surface becomes too strong and the deposition of chromium hydroxide does not take place. Based on their numerous results, these authors concluded that the activation of the surface by the fluoride species dominates the electrochemistry of the conversion process. However, the role of the fluoride compounds is not limited only to the initial activation of the surface but continues also during the coating growth process [22]. Indeed, due to the increase of pH in proximity of the surface caused by the reduction reactions not only the chromium ions (reaction 3.4) but also the aluminium ions ( $\text{Al}^{3+}$ ) tend to react with water and to form aluminium hydroxide, however due to the presence of fluoride species other reactions become preponderant that give rise to the formation of soluble aluminium fluorides:





Therefore, the presence of fluoride species in the chromate bath strongly decreases or even eliminates the co-precipitation of aluminium oxide/hydroxide in the chromate conversion coating.

At the end of the seventies, Katzman and Malouf [22] proposed a first detailed mechanism of formation of the chromate conversion coating on aluminium alloys. They stated that in order for the film deposition to start the chromate solution must directly contact the aluminium metal, i.e. the aluminium oxide must be completely removed. Afterwards, the chromium hydroxide film precipitates on the Al surface and as the coating continues to grow the aluminium metal is oxidized at the metal/film interface and the  $Al^{3+}$  ions diffuse through the film to the interface with the solution, where they dissolve as fluoride compounds.

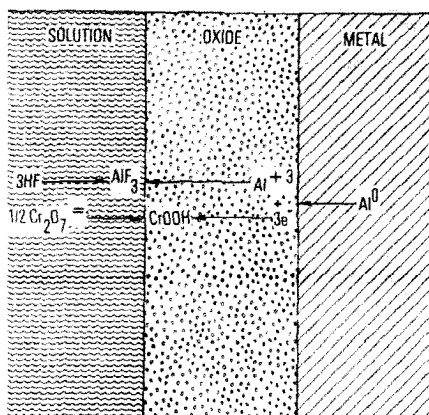
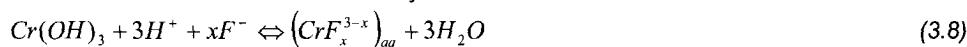


**Figure 3.1:** Mechanism of the chromate conversion coating growth [Ref. 22].

Simultaneously, the electrons are also drawn through the film to the film/solution interface, leading to the reduction of the chromate species (reactions 3.2 and 3.3) adsorbed on the surface (Figure 3.1). After a certain time of immersion, the thickness of the chromate coating reaches a constant value, i.e. a steady-state condition of the film growth is established. The authors foresaw two possible causes. One is that the electronic resistivity of the coating reaches a value high enough that the oxidizing power of the chromate solution is not longer felt at the metal/film interface. The other is related to the fact that chromium hydroxide is somewhat soluble in presence of fluoride species, even if

in much lower extent than aluminium hydroxide:



Therefore, when the chromate film dissolves at the same rate as it precipitates a steady-state value of its thickness is reached.

Although the mechanism described above explains several experimental observations, it does not consider the formation of defects, flaws and thickness inhomogeneities always encountered in chromate layers deposited on aluminium alloys and even on high purity aluminium. More recently, Brown and co-workers [23, 24] developed a model of chromate film growth based on spatial separation of the cathodic and anodic reactions on the aluminium surface, which accounts for both the cellular-like structure and the holes characteristic of chromate conversion coatings on Al. The principal assumption of this model is that the natural oxide covering the aluminium surface is not completely removed by chemical dissolution in HF but thinned until appreciable tunnelling of the electrons becomes possible (Figure 3.2). In the case of high purity aluminium [24], where the amount of minor surface heterogeneities is very low, the formation of spatially separated cathodic and anodic



sites is caused by the non-uniform decrease of the thickness of the Al oxide on the whole surface due to concentration gradient of both  $F^-$  and  $H^+$  ions. Indeed, since the electron tunnelling increases exponentially with the thinning of the oxide [25], at areas where the oxide film is thinner the tunnelling probability is higher and as a consequence the reduction of the chromate species (reactions 3.2 and 3.3) and deposition of chromium hydroxide (reaction 3.4) start at these locations. These local regions covered by the  $Cr(OH)_3$  are protected from further attack by fluoride species and then act only as cathodic sites during the subsequent growth of the chromate film. The deposition of chromium hydroxide results in an increase of the potential of the aluminium substrate, which in turn leads to a thickening of the aluminium oxide in areas not yet covered by the chromate film. Therefore, these regions, characterized by a negligible electron tunnelling, remain free of chromate deposit and act as fixed and persistent anodic sites. On the other hand, the precipitation of hydrated chromium oxide continues laterally and perpendicularly to the surface in the surrounding cathodic areas, resulting in the formation of a relatively uniform conversion coating that contains holes, corresponding to the anodic regions.

When less pure aluminium (99.98%) is considered, the presence of surface heterogeneities associated with grain boundaries or metal ridges plays a dominant role in the separation of the cathodic and anodic sites on the surface [23]. Indeed, at their locations the natural aluminium oxide is thinner and contains flaws and thus the electron tunnelling with subsequent deposition of chromium hydroxide occurs more easily. Therefore, the surface heterogeneities act as preferential cathodic sites, whereas the anodic sites lie between the metal ridges. The faster formation of the chromate film at the grain boundaries and metal ridges leads to a cellular-like structure of the conversion coating. These studies of Brown and co-workers brought in the foreground the strong influence of minor surface heterogeneities on the chromate layer nucleation and growth. It is logical to expect that when more evident heterogeneities are present, as intermetallic particles in aluminium alloys, the microstructure will play a dominant role in the nucleation, growth and final properties of the chromate conversion coating. This is discussed in more detail in section 3.3.

None of the two mechanisms previously discussed considers the role of the ferricyanide ( $Fe(CN)_6^{3-}$ ) that is used as accelerator in commercial chromate solution formulations since the 1960s. Despite the long history, the exact role of this component of the chromate bath in film formation has not yet been completely clarified. Treverton and Davies [26], based on XPS results, assumed that the chromate film consists of microcrystalline particles of mainly chromium oxide covered with an adsorbed layer of

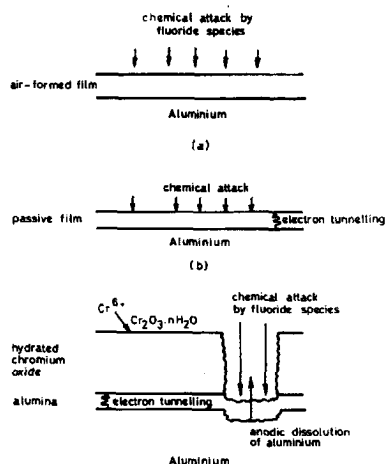


**Figure 3.2:** Model of the development of the chromate conversion coating on high purity aluminium (99.9996%) [Ref. 24].

ferricyanide ions. They concluded that the adsorption of ferricyanides on the surface prevents or reduces the adsorption of chromate ions and thus the concentration of chromates free to react is higher and this in turn speeds up the coating growth. This mechanism is supported both by the observation of a higher concentration of chromate ions in film formed without the use of ferricyanide compounds [27] and by the detection of high proportions of Fe, C, and N in the outer regions of the coating [28, 29]. Other authors hypothesised, however without any experimental evidence, the possibility of complex formation between Al and ferricyanide, which would accelerate the aluminium dissolution and as a consequence the chromates reduction and  $\text{Cr}(\text{OH})_3$  deposition [30]. Recently, at the Ohio State University a detailed Raman and infrared investigation was carried out with the aim of elucidating the structure of cyanide species in the CCC and their role in the coating growth [31]. The principal conclusion was that the chromate film contains  $\text{Fe}(\text{CN})_6^{3-}$  ions, hydrogen bonded to Cr-OH groups together with Berlin green, a complex hydrolysis product formed by  $\text{Fe}^{3+}$  bridged by  $\text{CN}^-$  groups. The results also established that the ferricyanide can act as a redox mediator: the reduction of ferricyanide ( $\text{Fe}(\text{CN})_6^{3-}$ ) to ferrocyanide ( $\text{Fe}(\text{CN})_6^{4-}$ ) speeds up the aluminium oxidation and then the re-oxidation of the ferrocyanide greatly increases the reduction of  $\text{HCrO}_4^-$  and  $\text{Cr}_2\text{O}_7^{2-}$  enabling a faster formation of the CCC.

Initially, the characterization of the structure, i.e. morphology and chemical

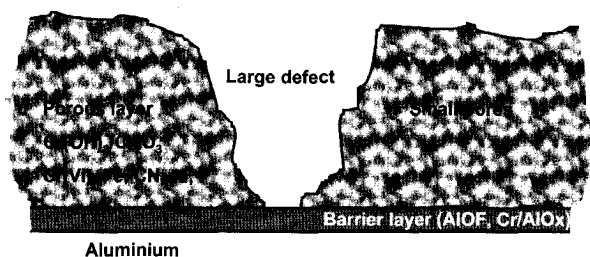


**Figure 3.3:** Schematic illustration of the structure of the chromate conversion coating on aluminium alloy.

composition, of the chromate conversion coating on aluminium was made difficult by the amorphous nature of the film, which prevents its characterization by traditional methods of analysis, such as X-ray diffraction. In the last 20-25 years, however, modern sensitive techniques, as XPS, AES, FTIR, SIMS, and XAS, together with electron spectroscopy (SEM and TEM) have contributed specific details concerning elemental distribution and morphology of the layer. It is well accepted that CCC has a duplex layered structure: a relatively thick porous layer containing small pores and large defects separated from the aluminium substrate by a thin and dense barrier layer (Figure 3.3). The thickness of both layers depends of course on the treatment conditions, as temperature, time, and pH of the chromate bath. As concern the chemical composition of the barrier film, the presence of either aluminium oxy-fluorides [18, 20, 29, 32] or a mixed aluminium/chromium oxide has been proposed [22]. An important feature of this layer consists of its presence also at the bottom of the large defects, cracks, which are caused by internal stresses developed during drying of the CCC [33]. A high resolution SEM study, carried out by Treverton and Amor [34], showed that the thick external porous layer is formed by small spherical particles with a diameter varying from 50 to 60 nm down to 10 nm.

Variations in particle size can be related to variations in local conditions of either the chromate bath or the aluminium surface. The authors highlighted the importance of this high degree of nano-roughness for the adhesion properties of the CCC. Indeed, it results in a high extension of the contact area between the organic coating and the substrate surface with consequent high probability of interfacial bond formation.

Regarding the chemical composition of the porous layer, there is a general agreement that the main component is chromium hydroxide ( $\text{Cr}(\text{OH})_3$ ), which partially dehydrates and transforms in chromium oxide ( $\text{Cr}_2\text{O}_3$ ) during drying. Nonetheless, more controversial results are reported concerning the minor chemical components present inside the chromate film. Although many authors have detected both Al and F in the CCC and proposed the presence of aluminium oxy-fluoride as a separate phase amongst the chromium hydroxide particles or incorporated within the particles themselves, the measured quantities varied considerably, from 0.4% to over 8% [26, 28, 29, 35]. In addition, the incorporation of the ferricyanide accelerator has also been observed during many investigations carried out in different groups. However, several possible different cyano compounds have been proposed to be present in the chromate conversion coating formed on aluminium alloys: physisorbed  $\text{Fe}(\text{CN})_6^{3-}$  on  $\text{Cr}(\text{OH})_3$ , Berlin Green [31], free  $\text{CN}^-$ , copper cyanides, chromium cyanides [36], chromium iron mixed cyanides [37, 38].

Finally, it has often been suggested the presence of hexavalent chromium [ $\text{Cr}(\text{VI})$ ] in tetrahedral coordination in addition to the trivalent chromium [ $\text{Cr}(\text{III})$ ] in octahedral coordination, which form the  $\text{Cr}(\text{OH})_3$  matrix of the film. However, due to difficulties in measuring  $\text{Cr}(\text{VI})$ , the presence and amount of  $\text{Cr}(\text{VI})$  in the chromate film is still a controversial topic. Indeed, a wide range of  $\text{Cr}(\text{VI})$  compositions is reported in literature, from 0 to 90% (as a percentage of all chromium species present) but most commonly from 15 to 35%. Using XPS, different authors have measured levels of  $\text{Cr}(\text{VI})$  in chromate films formed on aluminium varying from 0% up to more than 33% [22, 26, 34, 39]. These differences could be related to variations in the parameters of the chromate process; however the XPS results should be considered with caution. Indeed, it has been demonstrated that  $\text{Cr}(\text{VI})$  undergoes during XPS analysis, even if Ar sputtering of the surface is not performed, thermal breakdown and especially photo-induced reduction in presence of hydrocarbon species, which can be introduced in the high-vacuum chamber from the pumping system [40, 41]. Recently, Chidambaram *et al.* [42] have developed a method of liquid nitrogen cooling and hydrocarbon-free pumping for XPS instrumentation that, although does not completely eliminate the reduction of  $\text{Cr}(\text{VI})$ , it does stop the process at intermediate species, i.e.  $\text{Cr}(\text{IV})$ . This enables to determine the original amount of  $\text{Cr}(\text{VI})$  by just summing the measured  $\text{Cr}(\text{VI})$  and  $\text{Cr}(\text{IV})$  percentages. With this modified XPS system, the authors found that 50% of the total Cr species in a medium weight CCC on AA2024-T3 is formed by hexavalent chromium. Other researchers tried to overcome the disadvantages of XPS using XANES, since the measurements are performed under ambient pressure and utilize higher energy photons that induce less photo-reduction [28, 43, 44]. The level of hexavalent chromium detected with this technique ranges from 20 to 30%. Although, this lower value in comparison with that obtained with the modified XPS system could be due to differences in

the film preparation, it suggests that some photo-induced reduction of Cr(VI) occurs also during XANES measurements. Anyway, independently from the exact amount it is evident that Cr(VI) species are somehow incorporated in the growing chromium hydroxide layer.

Xia and co-workers [45, 46] proposed a model based on reversible adsorption and desorption from the CCC of Cr(VI) species ( $\text{HCrO}_4^-$ ,  $\text{Cr}_2\text{O}_7^{2-}$ ), with adsorption favoured at low pH. The authors considered the insoluble hydrated Cr(III) oxide to have many surface hydroxyl groups that act as sites for adsorption of Cr(VI) by means of the reversible formation of a covalent Cr(III)-O-Cr(VI) bond during the deposition of the CCC in the low pH solution used for the chromate process (Figure 3.4). On the other hand, the sol-gel model for the formation of the CCC developed by Osborne [33] considers the appreciable amount of Cr(VI) present in the film as a result of occlusion of chromate solution dried into the xerogel film. In any case, the presence of Cr(VI) species in the chromate conversion coating formed on aluminium is thought to be the key feature for the unique excellent corrosion protection provided by this film. This is extensively discussed in the next section.

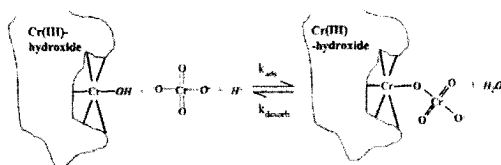


**Figure 3.4:** Model for adsorption of Cr(VI) to Cr(III) hydroxide [Ref. 46].

3.2.2 Mechanisms of corrosion protection

Several theories exist regarding the mechanism of corrosion protection provided by the chromate conversion coating to the aluminium and its alloys. The predominant one is based on the dynamic repair of defects in the film, a so-called “self-healing” behaviour, due to the presence of Cr(VI) species in the film itself. The self-healing model of the corrosion resistance of CCC assumes that during exposure to the aggressive environment the Cr(VI) species leach from the film, diffuse to the weak spots, as holes, flaws, etc., which are preferential sites of attack, and then either are reduced to Cr(III) and precipitate or adsorb on the walls of the defects (Figure 3.5).

### 3.2.2 Mechanisms of corrosion protection

Several theories exist regarding the mechanism of corrosion protection provided by the chromate conversion coating to the aluminium and its alloys. The predominant one is based on the dynamic repair of defects in the film, a so-called “self-healing” behaviour, due to the presence of Cr(VI) species in the film itself. The self-healing model of the corrosion resistance of CCC assumes that during exposure to the aggressive environment the Cr(VI) species leach from the film, diffuse to the weak spots, as holes, flaws, etc., which are preferential sites of attack, and then either are reduced to Cr(III) and precipitate or adsorb on the walls of the defects (Figure 3.5).

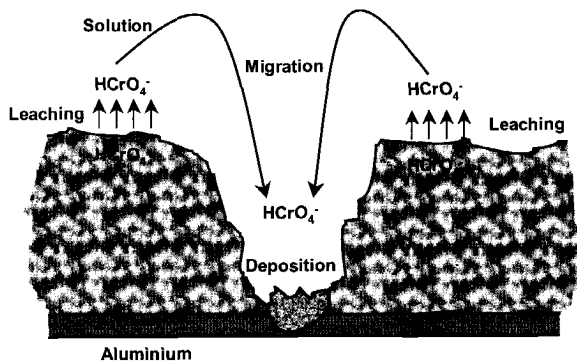


**Figure 3.5:** Schematic illustration of the “self-healing” behaviour of the chromate conversion coating.

Different research groups have found several confirmations of this theory. As previously reported, Xia *et al.* [46] explained the adsorption of Cr(VI) in the chromate film by means of the formation of a reversible covalent bond with the Cr(III) hydroxide. As a consequence, the Cr(VI) species can be also leached, especially at not too low pH as often

is the case in field conditions. These authors, using UV-vis absorption analysis, showed the occurrence of the leaching of Cr(VI) from a CCC immersed in solution and the increase of the rate of such leaching when chloride ions were present. The same group of researchers claimed a diffusion control for the release of Cr(VI) species, that means the release of chromates is not determined by their concentration in solution but by their diffusion in the film [47]. According to the authors this model would explain also the following phenomena that are often observed: enhance of the leaching of Cr(VI) when chloride species are present in the environment, decrease of the quantity of Cr(VI) leached from the film after a certain aging of the coating, especially if exposed to high temperature (50°C) [46, 47]. Indeed, they suggested that on one hand the Cl<sup>-</sup> ions inhibits the reversible binding of Cr(VI) to chromium hydroxide increasing then the diffusivity of Cr(VI), and on the other hand the reduction in hydration of the film and/or the structural rearrangement occurring during the aging of the film lowers the mobility of the Cr(VI) species.

XANES measurements carried out on the CCC before and after exposure to an electrolyte also indirectly prove the leaching of Cr(VI) from the film, since the ratio Cr(VI)/total Cr in the CCC decreases as a consequence of the exposure [28, 43, 44].

The "self healing" mechanism assumes that once leached from the CCC the Cr(VI) species selectively diffuse to the preferential sites of attack in the coating. This was indirectly demonstrated by Zhao et al. [48] using an "artificial scratch cell", in which an untreated and a

chromate-treated sample are positioned with a 1.8 mm layer of solution (0.1M NaCl) between them. Indeed, the XPS and Raman results clearly showed that chromate species migrate from the CCC to the initially unprotected surface and that a product chemically similar to the original CCC forms in or near previously active corrosion sites, i.e. pits. The deposition of chromate species leached from the film seems to be quite selective for corrosion sites and provides good corrosion protection, as shown by visual and electrochemical results. The same group at the Ohio State University [49]

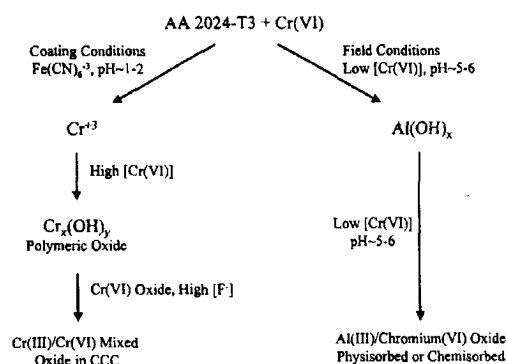


**Figure 3.6:** Formation process for Cr(III)/Cr(VI) mixed oxide in a CCC under coating conditions and Al(III)/Cr(VI) mixed oxide in field conditions [Ref. 49].

used Raman spectroscopy to further investigate the structure and composition of the deposit, which was named *chromate corrosion product (CCP)*, formed by interaction of Cr(VI) species with actively corroding pits on aluminium. It was found that while the CCC is a Cr(VI)/Cr(III) mixed oxide the CCP is an Al(III)/Cr(VI) mixed oxide. This difference was ascribed to the different conditions of formation of the CCP in comparison with the CCC, i.e. much lower concentration of Cr(VI) and absence of the  $\text{Fe}(\text{CN})_6^{3-}$  accelerator, which do not enable the rapid deposition of polymeric Cr(III) hydroxide, absence of fluoride and higher pH, which do not enable the dissolution of aluminium oxide/hydroxide (Figure 3.6).

The main conclusion is that Cr(VI) species in low concentration, as when leached from chromate films, diffuse to actively corroding spots of the film and form a physisorbed or chemisorbed mixed oxide with  $\text{Al}(\text{OH})_3$ , which prevents further attack of the aggressive environment and then drastically increases the corrosion protection provided by the CCC.

A simple explanation for the inhibition of corrosion caused by the deposition of CCP is the plugging of the defects of the chromate film. However, it is likely that part of the Cr(VI), which at low concentration and pH below 6 is mainly present in the form of  $\text{HCrO}_4^-$ , is reduced to Cr(III) via the reaction 3.3 near or in the pits. This leads to an increase of the pH, which in turn results in the repassivation of the pit [49, 50]. Sharman [50] considered this mechanism as the dominant one and he concluded that the pit repassivates in the normal way, due to the reduction in acidity, rather than because a deposit of chromium/aluminium oxide is formed in the pit, which occurs as a consequence of the increase in pH and then after the repassivation has taken place. In addition, a secondary effect is the formation and precipitation of chromium-chloride complexes, which reduce the  $\text{Cl}^-$  concentration and favours the repassivation of the pit. A third effect of the migration of Cr(VI) species at the active corroding spots of the CCC consists in the decrease of the surface charge and the pH of zero charge ( $\text{pH}_{\text{zc}}$  defined in chapter 2) resulting in a lower chloride adsorption [51, 52].

According to Ilevbare and co-workers [53], a weak point of the previously exposed theory involving leaching, diffusion and deposition of Cr(VI) is the very low amount of leached Cr(VI), far below the level necessary to be effective in corrosion inhibition of bare aluminium. These authors proposed a modified "self-healing" model, where a considerable amount of Cr(VI) incorporated in the film is not leached into the solution but remains within the pores and cracks and reaches the sites of attack by ionic mobility inside the chromate coating itself. It is thought that the relatively shorter distances the chromate ions have to travel compensate their lower mobility in the solid film in comparison with an aqueous solution. On the other hand, while it is true that the leached amount of Cr(VI) is very small, it should be taken into account that the quantity of Cr(VI) necessary to protect a limited number of weak spots in the CCC is much lower than that required to protect an uncoated aluminium surface. Therefore, the leached Cr(VI) is likely sufficient to provide corrosion inhibition to aluminium surfaces covered by a CCC and on the other hand the very low rate of leaching would explain the long term corrosion protection shown by the CCC.

Although the incorporation of Cr(VI) species in the chromate film is considered the main reason for the unique corrosion resistance shown by the CCC, the presence of a layer of chromium oxide/hydroxide obviously contributes to the protection of the aluminium substrate from the environmental attack. First of all, the film represents a barrier against aggressive species due to its insolubility in many media and its strong adhesion to aluminium, which is likely related to the similarity in ionic radii between  $\text{Al}^{3+}$  and  $\text{Cr}^{3+}$ , 0.5 and 0.53 Å, respectively [22]. The barrier properties of the film, which depend on the thickness and amount of cracks and defects, are responsible for the very low anodic current observed during polarization of chromate conversion coated aluminium alloys [54]. Another important aspect of the chromium oxide/hydroxide film is the development, due to a long range

ordering during the first 24 hours of aging, of a high hydrophobicity that in turn improves its corrosion resistance [29] and especially its adhesion to organic coatings [55]. In addition, it was thought that the chromium oxide/hydroxide film can have a cathodic inhibition action by limiting the kinetic of the oxygen reduction reaction (ORR), which results in the decrease of the free corrosion potential below the potential of stable pitting [48, 50]. Indeed, the presence of an inert film, such as the chromate coating, can decrease either the electron transfer rate or the  $O_2$  mass transport. At the University of Virginia the ORR kinetics were investigated both on high purity aluminium and on bulk synthesized analogues of Al-Cu, Al-Cu-Mg, and Al-Cu-Fe-Mn intermetallic phases in uncoated condition and after the deposition of a chromate film [56]. It was found that while the CCC does not reduce the rate of oxygen reduction on aluminium, it does limit it on intermetallic phases. In relation to this, Kendig and Jeanjaquet [57] claimed that even the simple adsorption of Cr(VI) species is capable to strongly decrease the ORR rate on copper. This suggests that either the deposition of the chromate film or the adsorption of Cr(VI) on intermetallic particles of aluminium alloys significantly decreases their activity leading to an excellent corrosion resistance because of the removal of local galvanic couples on the aluminium surface. Besides, Kolics *et al.* [58] have observed that the deposition of a Cr(III)/Cr(VI) mixed oxide on the Al-Cu-Mg intermetallics of AA2024 strongly retards the selective dissolution of magnesium and reduces the formation of copper deposits, which are extremely deleterious for the corrosion resistance of this alloy. The effect of the intermetallic particles on the formation and final properties of the CCC is further described in the following section.

### 3.2.3 Chromate conversion coatings and microstructure

The first study considering the role played by the microstructure on the nucleation and growth of chromate films was carried out at the beginning of the nineties by Brown *et al.* [23], who showed that the CCC preferentially nucleates at the location of minor heterogeneities,

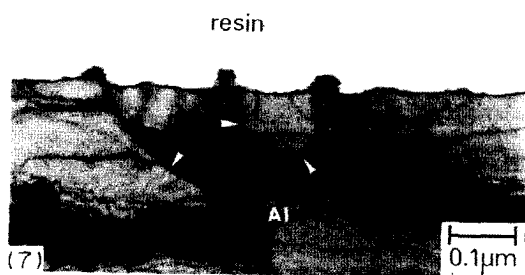


**Figure 3.7:** TEM micrograph of the ultramicrotomed cross section of the aluminium substrate after 5s of immersion in the chromate-fluoride bath, indicating the deposition of hydrated chromium oxide at the sites where the cellular boundaries (indicated by the arrows) intersect the external surface [Ref. 23].

i.e. grain or cellular boundaries, on the surface of 99.98% pure aluminium (Figure 3.7). Based on this, a strong interest has grown concerning the effect of the much more complex microstructure of commercial aluminium alloys on the formation and as a consequence on the final properties of the chromate forces to treat the aluminium surfaces with a chromate conversion film, often together with an organic coating.

The same authors have recently moved their interest from pure aluminium to AA2024 performing a detailed investigation on the nucleation of the CCC on fresh, clean alloy specimens prepared using the ultramicrotome technique [59]. After immersion for 5 seconds in a chromate-fluoride solution, they observed similarly to the case of pure aluminium a non-uniform formation of the film on the aluminium matrix caused by the presence of highly orientated microstructural deformities associated with distorted grain and cellular boundaries that are aligned along the rolling direction. However, the main heterogeneities in the nucleation and growth of the CCC were found in proximity of the intermetallic particles. Based on AFM and SEM results, it was concluded that the film starts to form either as discrete nodules on the Al-Cu-Mn-Fe intermetallics, identified as  $Al_6(Cu, Fe, Mn)$  and  $(Al, Cu)_6Mn$ , and on the Al-Cu-Mg particles only after the preferential dissolution of magnesium has occurred, or as halos of materials over the outer lying alloy matrix region surrounding the intermetallics. The preferential precipitation on the Al-Cu-Mn-Fe intermetallic particles and on the copper remnants, which form from the selective dissolution of Mg from the Al-Cu-Mg intermetallics, was related to their cathodic nature, which favours the reduction of the chromate species to a hydrated chromium oxide (reactions 3.2, 3.3, and 3.4). In addition, these reactions are sped up also by the presence in proximity of the intermetallics of a natural aluminium oxide layer being thinner and containing a large number of defects and flaws. On the other hand, the presence of halos of chromium hydroxide deposits around some intermetallics was explained taking into account the formation of a copper-depleted zone in the periphery of some intermetallics, which is anodic in comparison with not only the intermetallic itself but also the external matrix. Therefore, the cathodic reactions with subsequent deposition of chromium hydroxide take preferentially place above the intermetallics and also above the matrix surrounding the copper-depleted zone, which in turn anodically dissolves.

The higher reactivity, associated with a more noble surface potential, of the intermetallic particles present in AA2024 towards the reduction of chromates and the deposition of the chromium hydroxide film was confirmed by other studies, which have shown that by addition of small amount of  $Na_2CrO_4$  to a chloride-containing solution a chromate film precipitates first and faster on top of the intermetallics, both the Al-Cu-Mn-Fe and the Al-Cu-Mg [58, 60]. A further confirmation of the dominant role played by the electrochemical properties of the intermetallics in the nucleation mechanism of the CCC on AA2024 comes from the AFM investigation carried out by Waldrop and Kendig [61]. After immersion for 10 seconds in a commercial chromate bath (Alodine 1200S) cooled below  $5^\circ C$ , the chromate film deposition was found to be considerably faster on the Al-Cu-Mn-Fe intermetallics than on the Al matrix, whereas on the Al-Cu-Mg ones it was observed to be considerably slower, in contrast with the results reported previously. Therefore, it seems that while the Al-Cu-Mn-Fe intermetallic particles are clearly preferential nucleation sites for the CCC, the behaviour of the Al-Cu-Mg intermetallics is more complex due to a less well-defined electrochemical (cathodic or anodic) nature that can change from particle to particle and even between different regions of the same particle, as discussed in section 2.3.1 of chapter 2.



On the other hand, several studies have raised serious doubts on the preferential formation of the chromate layer at the location of the intermetallic particles. Hagans and Haas [62] found by AES and XPS investigation that upon immersion for 1.5 or 3 minutes the chromate film deposition rate proceeds in the following order: matrix > Al-Cu-Mg intermetallics > Al-Cu-Mn-Fe intermetallics. They suggested that this behaviour is related with the reaction of copper of the intermetallics with ferrocyanide species, which result from the reduction of ferricyanide compounds added as accelerator in the chromate bath, leading to the deposition of insoluble precipitates, as  $\text{Cu}_4\text{Fe}(\text{CN})_6$  and  $\text{Cu}_2\text{Fe}(\text{CN})_6$ . This theory has been further developed by McGovern *et al.* [63], who investigated the CCC formation on AA2024 and on a polyphase  $\text{Al}_x\text{Cu}_y\text{Mg}_z$  ingot. It was found that on AA2024 after 5 minutes of immersion in the chromate bath the deposition of the film is inhibited above the Cu-containing intermetallics and that on the polyphase ingot, after either a short (3 seconds) or long (5 minutes) immersion time, the thickness of the CCC is inversely proportional to the copper-content of the phase. Based on this, the authors claimed that the ferricyanide species adsorb on copper-rich regions, such as intermetallics, with some decomposition to form a Cu-CN linkage or a Fe-CN-Cu bridging group. The resulting deposits inhibit the electron transfer and the redox mediation of the ferricyanide species thus decreasing the Cr(III) generation and the film formation (Figure 3.8).

Nevertheless, the formation of Cu-CN bonds on the surface of the intermetallic particles is in disagreement with the presence of C and N homogeneously distributed in the whole thickness of the CCC formed at their location, which was found by Hagans and Haas themselves [62], since this suggests that the cyanide species do adsorb inside the chromate film but do not concentrate at the interface

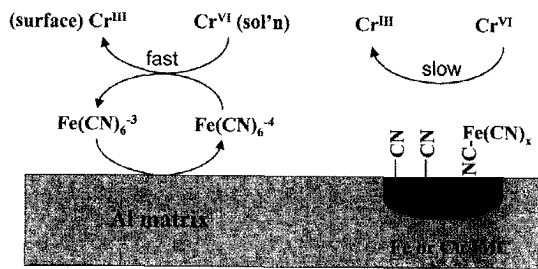


**Figure 3.8:** Schematic illustration of the possible inhibition of the CCC formation over Cu-rich intermetallics of aluminium alloys [Ref. 63].

film/substrate via formation of complexes with copper. The observation that cyano compounds are irregularly distributed over the alloy matrix and are absent at the location of the intermetallics brings further evidence of the fact that the interaction between Cu-rich intermetallic particles and the accelerating species of the bath is unlikely [64]. Therefore, the limited growth of the CCC on top of the intermetallics, which has been highlighted also by other authors [64, 65], can not be explained with the formation of copper-cyanide deposits that render the particles less active.

Based on the results of an RBS study on the formation of the CCC on macroscopic galvanic couples, consisting of an intermetallic phase (5 mm in diameter) surrounded by pure aluminium, Juffs and co-workers [65] assumed that the presence of a thick aluminium oxide above the intermetallic phase hinders the chromate film nucleation and growth. The authors considered that the thick aluminium oxide film is a result of fluoride attack and

oxygen reduction reaction on the surface of the intermetallic phase, which would make the surface conditions more alkaline and suitable for the precipitation of hydrated aluminium oxide. However, also this explanation appears to be quite unlikely, since the presence of fluoride leads to dissolution of the aluminium oxide film especially in proximity of intermetallic particles, where a higher concentration of flaws and defects in the oxide film is present.

In conclusions, the role of the intermetallic particles on both the nucleation and growth of the CCC on aluminium alloys, in particular AA2024, is not yet clearly understood. The apparent contradiction of the results reported by different groups can be related either to differences in the film formation conditions, as immersion time, composition, temperature, and pH of the treatment bath, or to lack of resolution of certain analytical tools. In addition, it should be noted that the methods used for sample preparation and surface pre-treatment prior to the conversion coating significantly influence the mechanisms of nucleation and growth of the CCC, since they can lead to both modifications of the intermetallic properties and redistribution of alloying elements. In most of the published studies polished samples without any pre-treatment are considered, which are not really representative for alloy surfaces of practical importance that are usually pickled and/or desmutted before immersion in the chromate solution. Besides, also the use of polyphase ingots or intermetallic analogs to reproduce the behaviour of the intermetallic particles on a macroscopic scale can lead to wrong conclusions, since the small and numerous galvanic couples, which are fundamental in determining the electrochemical behaviour of the aluminium alloys surface, are absent in these models. This is confirmed by various experimental observations: different effect of a pre-treatment process on the subsequent formation of the CCC on AA2024 and on intermetallic polyphase [63], different reactivity towards ferricyanide species of thin film analogs and the intermetallics of AA2024 [64, 66], different film growth kinetics in some cases between intermetallic analogs and particles in AA2024 [66].

Therefore, further investigations are needed to clarify the role of the intermetallics on the formation of the chromate conversion coating on aluminium alloys, to distinguish their effect on the nucleation and on the growth of the film, and to understand how they affect the corrosion resistance provided by the layer. This is very important, since it has been shown that the deterioration of the chromate coating during exposure to aggressive environments starts at the location of the intermetallics [67]. A large part of this PhD work has been dedicated to the study of the influence of the intermetallic particles on the nucleation, growth, and final properties of the CCC on both Alclad 2024 and bare 2024 aluminium alloy that will be discussed in chapter 5, 6, and 7.

### 3.3 Cerium-based conversion coatings

Lanthanides ions, as  $\text{Ce}^{3+}$ ,  $\text{Y}^{3+}$ ,  $\text{La}^{3+}$ ,  $\text{Pr}^{3+}$ ,  $\text{Nd}^{3+}$ , forming insoluble hydroxides, have a low toxicity and their ingestion or inhalation is not considered harmful to health [68]. In addition, lanthanides are economically competitive products, since some of them, in particular cerium, are relatively abundant in nature [69]. Therefore, this family of compounds has been investigated during the last two decades as possible alternative to chromate in developing corrosion protection systems. The pioneering studies concerning the application

of lanthanide compounds as corrosion inhibitors for aluminium alloys were carried out by Hinton, Arnott and Ryan at the Aeronautical Research Laboratory of Australia [8, 70]. They found that additions of 1000 ppm  $\text{LaCl}_3$ ,  $\text{YCl}_3$ ,  $\text{PrCl}_3$ ,  $\text{NdCl}_3$ , or  $\text{CeCl}_3$  to 0.1M NaCl solution induce a decrease in the corrosion rate of AA7075, in some cases of more than a factor of ten. The best degree of inhibition is achieved with  $\text{Ce}^{3+}$  ions when added as chloride compounds [71]. The corrosion protection provided by the addition of cerium chloride to the sodium chloride solution is attributed to the formation of a compact film of cerium oxides and hydroxides that replaces the natural oxide film on the surface of the alloy [72]. This explains the low inhibition provided by cerium nitrate and cerium sulfate compounds, since they are very stable complexes as a result of the oxygen-donor ligand and the Ce cation interaction, which limits the amount of  $\text{Ce}^{3+}$  ions available for hydrolysis and as a consequence the cerium hydroxide produced.

### 3.3.1 Formation, morphology and composition

Based on the above mentioned film forming properties of cerium chloride and the corrosion protection provided by such films, different treatments have been proposed in order to develop cerium oxide conversion coatings on aluminium alloys. The first attempt made by Hinton *et al.* [70] consisted in full immersion of AA7075 in a cerium chloride solution for a long period of time, in the order of days. Similarly, Mansfeld and co-workers [73] proposed a full immersion method, based on the exposure to a solution containing 1000 ppm  $\text{CeCl}_3$  open to air and at room temperature for 7 days, to form cerium oxide films on alloys AA2091 and AA6061 and on metal matrix composites. Exposure of AA7075 to the NaCl- $\text{CeCl}_3$  leads to the formation of a cerium hydroxide layer, whose cerium content and thickness increase over a 20 days exposure period [71]. Indeed, the film deposited after several days of immersion consists almost entirely of hydrated cerium oxide with virtually no aluminium oxide and has a thickness in the range of 200-500 nm. SEM micrographs showed the presence of a finely particulate background film together with single crystalline particles with lateral dimensions up to several microns [71, 74].

As concern the oxidation state of cerium in the conversion coating, different results have been reported. On one hand, XPS studies indicate that the cerium-rich film is formed by a mixture of oxide/hydroxide of trivalent [ $\text{Ce(III)}$ ] and tetravalent [ $\text{Ce(IV)}$ ] cerium, as  $\text{CeO}_2$ ,  $\text{Ce(OH)}_4$ , and  $\text{Ce(OH)}_3$  [74, 75]. On the other hand, a XANES investigation by Davenport *et al.* [76] has shown that 5 days of exposure to the

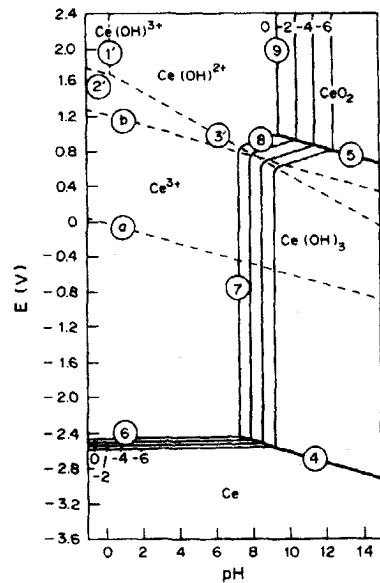


**Figure 3.9:** Potential-pH (Pourbaix) diagram for the cerium-water system at 25°C [Ref. 76].

CeCl<sub>3</sub> solution results in the formation of a layer containing trivalent cerium whereas 7 days of exposure leads to a film containing tetravalent cerium.

These apparently contradicting results are due to the high sensitivity of the valence state of cerium towards the level of aeration and solution pH. While under de-aerated conditions very little film deposition occurs and the cerium is in the trivalent state, when oxygen is present the amount of cerium oxide precipitated strongly increases and the cerium is mainly in the tetravalent state, especially after long exposure time. Two different theories have been developed to explain the formation of a mixed Ce(III)/Ce(IV) hydrated oxide in the presence of oxygen:

- ✓ The increase in pH caused by the oxygen reduction reaction enables the precipitation of solid Ce(III) hydroxide, which is stable at lower pH than tetravalent cerium oxide as can be seen from the Pourbaix diagram (Figure 3.9) [76, 77]. Once deposited, Ce(OH)<sub>3</sub> may become oxidized to hydrated CeO<sub>2</sub> (ceria) through the following reaction:



This explains the conversion of any Ce(III) to Ce(IV) during long term exposure of the aluminium samples to NaCl solution observed by Davenport and co-workers [76]. However, reaction 3.9 should not occur on aluminium substrate, since its open circuit potential is significantly below the potential of thermodynamic equilibrium between Ce(OH)<sub>3</sub> and CeO<sub>2</sub> at any solution pH (line 5 in the Pourbaix diagram of Figure 3.9). This suggests that the cerium-containing oxides are electrical insulators and may enter into chemical redox processes that are not in equilibrium with the metal substrate. Another possible explanation takes into account the fact that the reduction of oxygen can follow either a four-electron or a two-electrons pathway depending on the nature of the alloy substrate [78]:



When the two-electron pathway is followed hydrogen peroxide is formed, which acts as a stronger oxidizing species than O<sub>2</sub> through the following reaction:



and will readily oxidize Ce(OH)<sub>3</sub> to CeO<sub>2</sub> at all pH values for which Ce(OH)<sub>3</sub> exists.

- ✓ Aldykiewicz *et al.* [78], based on rotating disk measurements on copper and gold, postulated that the first step of film deposition involves the oxidation of Ce(III) to Ce(IV) in solution. The valence state of cerium in solution is determined by the line 3' in the Pourbaix diagram of Figure 3.9, which corresponds to the reaction:



The equilibrium potential ( $E^0$ ) of this reaction is sensitive to the anion present in solution [79]. In particular, chloride ions lower  $E^0$  by 400 mV allowing the oxidation of Ce(III) to Ce(IV) by oxygen to take place more readily. The critical pH for  $[\text{Ce(OH)}_2^{2+}]/[\text{Ce}^{3+}] = 1$  was found to be 8.7 at a partial oxygen pressure of 0.2 and the pH at the substrate surface during diffusion-controlled oxygen reduction was estimated to be 10.5 and 10.8

for the two and four-electrons reduction reactions, respectively. Therefore, in proximity of the surface the dominant cation species in solution is  $Ce(OH)_2^{2+}$ , which can in turn precipitate as insoluble  $CeO_2$  due to the local pH increase:



Considering the strong dependence of all the reactions described above on the pH reached at the substrate surface, it is likely that both processes, i.e. precipitation of Ce(III) hydroxide and subsequent oxidation or oxidation of Ce(III) in solution and subsequent precipitation of Ce(IV) oxide, occur during the immersion in the  $CeCl_3$  bath depending on the experimental condition used, as type of substrate, pH, temperature, time, etc. Davenport *et al.* [76] observed that since Ce(III) is less soluble than Ce(IV) in the pH range 8-10, they will precipitate at different locations. Indeed, in the pH and oxygen gradient, which is formed adjacent to the metal surface, while Ce(III) is more likely to precipitate before it reaches the surface, Ce(IV) is sufficiently soluble to reach the surface and afterwards precipitate. Recently, it has been experimentally shown by means of AFM *in situ* investigation on gold substrate that the immediate result of the electrochemical and chemical reactions involved in the process is the formation of an intermediate cerium gel rather than direct precipitation of solid deposits [80]. Following the formation of the gel precursor, true deposition of the film proceeds via a nucleation mechanism, i.e. microscopic cerium oxide nuclei crystallize from the gel and act as sites for deposition. In the later stages, nucleation and growth continue on the deposited material enabling formation of a relatively thick film.

In spite of the simplicity of the immersion process for the formation of cerium oxide coatings, commercially it is unattractive because of the long time, in order of several days, required. A first attempt to lower the duration of the process was based on electrolytic activation method, which consists of galvanostatically polarizing the aluminium surface in 1000 ppm  $CeCl_3$  bath at cathodic current densities of around 1 A/m<sup>2</sup> for 30 minutes [70]. The application of a cathodic current enhances the reduction reactions ( $H_2$  evolution and  $O_2$  reduction), which in turn rapidly generate alkaline conditions at the metal surface and accelerate the deposition of cerium compounds. The film formed under these conditions contains cerium predominantly in the trivalent state [76], since even if Ce(III) is oxidized in solution to Ce(IV) via reaction 3.13 at the cathodically polarized surface it is likely reduced back to Ce(III) prior to precipitation. This would also explain the higher proportion of Ce(IV) in the film electrochemically deposited on copper with respect to that deposited on aluminium [76]. Indeed, during the process the higher potential of the Cu electrode (-0.3 V in comparison with -1.4 V for the Al electrode) does not provide a sufficiently strong over-voltage for the electrochemical reduction of Ce(IV) to Ce(III) and therefore the cerium is incorporated in the film as Ce(IV). The 30 minutes of cathodic polarization leads to a mixed cerium and aluminium oxide layer with an average thickness of 50 nm, containing blister-like features. These defects are likely caused by hydrogen evolution during the treatment and result in a loss of protective properties of the film [70]. This problem was overcome by electro-deposition from a solution of cerium salts in organic solvents, which gives rise to a thicker film (150-500 nm) exhibiting a continuous network of random cracks resulting from

the combination of shrinkage during drying and low ductility of the film [81, 82]. Although the corrosion resistance of the conversion layer is improved, also due to a higher portion of Ce(IV) oxide that is more stable and less soluble than Ce(OH)<sub>3</sub>, the requirement of high DC potentials in conjunction with a volatile organic solvent makes the industrial application of this method difficult.

Another way to decrease the time necessary to form a cerium oxide film on aluminium is based on increasing the temperature of the cerium salts bath. Immersion for 2 hours at 100°C in 5mM Ce(NO<sub>3</sub>)<sub>3</sub> solution followed by 2 hours at 100°C in 5mM CeCl<sub>3</sub> solution was found to lead to a Ce(III) hydroxide film with a thickness of about 100-150 nm [83]. Mansfeld and Wang [84, 85] had previously proposed the immersion in boiling aqueous baths of cerium salts in combination with an anodic treatment in 0.1M Na<sub>2</sub>MoO<sub>4</sub> as a suitable method to produce a Ce-rich oxide film on aluminium alloys, which provides high corrosion protection due to a synergetic effect of cerium and molybdenum. AES investigation showed large amounts of Ce in the film, while the concentration of Mo is lower and likely located in the outermost layers. It is worthwhile to note that there is an important difference between this treatment and those described above. The Ce-Mo process causes the oxidation of the aluminium alloy due to exposure to aqueous solutions at high temperature and subsequent

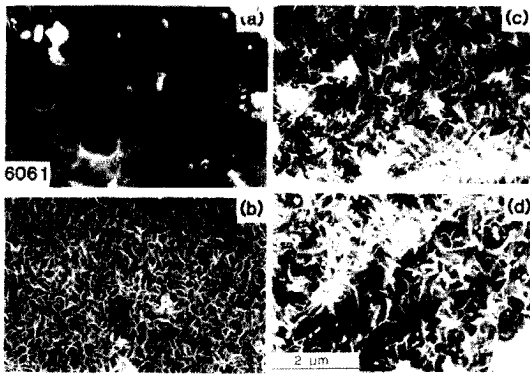


**Figure 3.10:** SEM micrographs of the AA6061 surface after each step of the Ce-Mo process: (a) 24h in air saturated with water vapour at 100°C, (b) 2h in Ce(NO<sub>3</sub>)<sub>3</sub> bath at 90°C, (c) 2h in CeCl<sub>3</sub> bath at 90°C, (d) 2h anodic polarization in Na<sub>2</sub>MoO<sub>4</sub> [Ref. 86].

incorporation of cerium in the oxide film, whereas the immersion in the cerium chloride bath at room temperature leads to the precipitation of ceria gel onto the surface of the alloy as a result of reactions in solution.

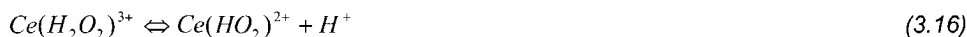
A detailed investigation of the evolution of the oxide film during each step of the Ce-Mo treatment was carried out by Hughes and co-workers [86]. During the immersion in the first cerium bath (10mM Ce(NO<sub>3</sub>)<sub>3</sub>, 2h, 90°C) a crazed oxide structure covers the Al matrix (Figure 3.10-b) and a dense oxide containing large amounts of cerium deposits on the intermetallics. Additional Ce is incorporated on the surface during the second step of the treatment, i.e. immersion in 10mM CeCl<sub>3</sub> solution for 2h at 90°C. In particular, coarsening of the crazed oxide structure takes place together with the formation of small particles of hydrous Ce(IV) oxide (Figure 3.10 c). Finally, during the anodic polarization in the Na<sub>2</sub>MoO<sub>4</sub> bath, Mo is incorporated both as MoO<sub>4</sub><sup>2-</sup> ions in the crazed oxide and as cerium molybdate in the cerium containing particulates on the surface. While the corrosion protection provided by this conversion treatment is quite good, its realization at industrial

scale is complicated by both the use of boiling baths and the additional cost coming from the anodic step.

A simple method, consisting of addition of hydrogen peroxide to the cerium chloride bath, to form a cerium oxide/hydroxide film on copper-rich aluminium alloys in very short time (about 10 minutes) has been developed and patented by Wilson and Hinton [87]. The pH of the  $\text{CeCl}_3$  (0.035M) and  $\text{H}_2\text{O}_2$  (0.12M) solution is lowered to a value close to 2 by means of HCl addition in order to avoid deposits formation inside the solution instead of on the aluminium surface, and the bath is heated to about 43°C. Hydrogen peroxide, even when present in small amount derived from the 2-electrons reduction of  $\text{O}_2$  (reaction 3.11), was found to increase the efficiency of film formation [78]. The acceleration effect of  $\text{H}_2\text{O}_2$  could be simply related to the rapid increase in pH caused by its reduction (reaction 3.12) that favours the precipitation of cerium oxide/hydroxide. An additional consequence of  $\text{H}_2\text{O}_2$  is the enhancement of the oxidation of Ce(III) to Ce(IV) ions in solution (reaction 3.13), which results in a hydroxide film containing cerium mainly in the 4-valent state, as observed by XPS studies [88]. However, Hughes *et al.* [89] proposed a different sequence of reactions in comparison with that occurring in the cerium bath without hydrogen peroxide. The authors observed the necessity of 30 minutes aging of the solution to achieve full activity. It is thought that during this time, hydrogen peroxide substitutes water reversibly in the coordination sphere of the Ce(III) ions creating a peroxo complex:



Afterwards, in the thin solution film in proximity of the metal substrate, where the reduction reactions have increased the pH, partial deprotonation of the Ce(III) peroxo species takes place followed by oxidation with  $\text{H}_2\text{O}_2$  to a Ce(IV) peroxo complex  $\text{Ce}(\text{O}_2)^{2+}$ , which then undergoes reduction to hydrated  $\text{CeO}_2$ :



Anyway, the final result is the formation of hydrated Ce(IV) oxide at the cathodic sites, where reduction reactions and pH increase occur, while at the anodic sites in addition to aluminium dissolution undesirable oxidation of  $\text{H}_2\text{O}_2$  is likely to take place:



Indeed, during immersion in the  $\text{CeCl}_3$ - $\text{H}_2\text{O}_2$  bath gas evolution, identified by burning taper test as  $\text{O}_2$ , was always observed [88].

The coating formed with this method on the copper-rich alloys (AA2024 and AA7075) is not uniform in thickness across the surface and has a layered structure. XPS and SEM results showed the presence of an outer layer of Ce(IV) hydrated oxide (up to 30 nm) over a layer of mixed Ce(III) and Ce(IV) hydrated oxides (around 120 nm), which is separated from the substrate by a thin layer enriched in copper [88].

Recently, a further decrease of the time, from 10 to 2-4 minutes, necessary to deposit a relatively thick and more protective cerium oxide film on copper-rich Al alloys has been

obtained using a cerium-based deoxidiser (sulphuric acid solution of Ce(IV)) to prepare the surface before the immersion in the  $\text{CeCl}_3\text{-H}_2\text{O}_2$  bath [90]. This led to the development of a "Cerate" coating process consisting in several steps, i.e. Ce-based deoxidising treatment, immersion in the cerium chloride-hydrogen peroxide bath, sealing in silicate solution, which greatly improves the corrosion resistance of AA2024 [91].

The Ce(IV) oxide film formed after the pre-treatment in the Ce-based deoxidiser is homogeneously deposited on the surface with some cracks and local changes in morphology [90]. XPS depth profile showed that it is 100-200 nm thick and possibly bilayered, with a cerium-rich layer over a hydrated Al oxide film. The layered structure of the conversion coating was confirmed by TEM investigation (Figure 3.11), which indicated the presence of an aluminium oxide layer (50-100nm thick) adjacent to the substrate surface with possible Cu-enrichment at the metal/oxide interface.

On top of this Al oxide film a cerium oxide layer comprised of nanocrystallites (2-3 nm) of  $\text{CeO}_2$  with a fluorite structure is deposited [89].

The standard  $\text{H}_2\text{O}_2$ -assisted solution for deposition of cerium-based conversion coatings resulted to be effective only for Cu-rich aluminium alloys, i.e. 2xxx and 7xxx series. Thus, different types of accelerators have been investigated in order to obtain satisfactory coating formation also on other families of aluminium alloys, as 3xxx, 5xxx, and 6xxx series. While there are a number of possible accelerated solutions, the following composition was found to perform well for many alloys: 0.035M  $\text{CeCl}_3$ , 0.12M  $\text{H}_2\text{O}_2$ , 1mM  $\text{Cu}(\text{glycinate})_2$ , 1mM  $\text{Ti}(\text{O}_2)^{2+}$  operated at pH 2 and 45°C [92]. The two accelerators added are thought to play different roles in the acceleration of the cerium oxide film deposition [89]. On one hand, it is suggested that the presence of copper in solution results in the deposition of metal crystallites on the aluminium surface via the following reaction:



The addition of a complexing agent for Cu, as glycine, renders the reduction of Cu slightly less favourable, and leads to a more fine dispersion of copper crystallites, which are cathodic with respect to the aluminium matrix and then enhance the reduction reactions kinetic and as a consequence the cerium oxide/hydroxide precipitation. On the other hand, the  $\text{Ti}(\text{O}_2)^{2+}$  species is supposed to increase the concentration of reactive Ce(III) peroxo complex:



$\text{Ti}^{4+}$  is unstable and may precipitate via hydrolysis to hydrated  $\text{TiO}_2$ , as confirmed by the detection of significant quantities of titanium in the cerium oxide film formed from the accelerated  $\text{CeCl}_3\text{-H}_2\text{O}_2$  solution. Indeed, the film deposited after immersion in this solution

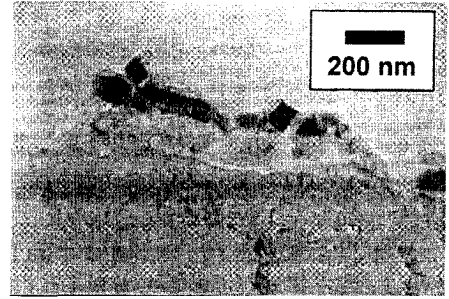


**Figure 3.11:** TEM micrograph of the coating deposited from the  $\text{H}_2\text{O}_2$ -accelerated cerium chloride solution after the Ce-based deoxidising treatment [Ref. 89].



consists of an amorphous mixed Ce-Ti-Al oxide on top of an aluminium oxide layer with areas of Cu-enrichment at the metal/oxide interface.

### 3.3.2 Mechanisms of corrosion protection

Since the first investigation of the use of lanthanide compounds as corrosion inhibitors for aluminium alloys, it was pointed out that the corrosion protection provided by  $Y^{3+}$ ,  $Pr^{3+}$ ,  $Ce^{3+}$  additives to an aerated sodium chloride solution follows from a strong suppression of the oxygen reduction reaction, as can be seen from the shift of the cathodic branch of the polarization curves in Figure 3.12 [8, 71]. Other works showing a strong decrease of the current density together with a fall in the open circuit potential confirmed the behaviour of cerium ions as cathodic inhibitors [93, 94]. A reduction of the rate of the cathodic reactions by inhibitor compounds is generally related to the precipitation of an insoluble film at the cathodic sites. Indeed, the suppression of the cathodic oxygen reduction reaction was found to be the principal mechanism of corrosion protection provided by the cerium oxide film

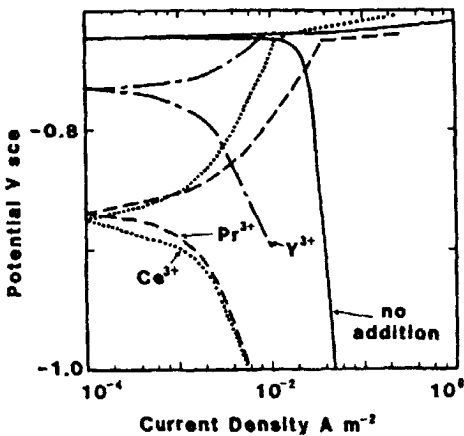


**Figure 3.12:** Polarization data for AA7075 conducted in 0.1M NaCl with or without additions of 1000 ppm  $CeCl_3$ ,  $PrCl_3$ ,  $YCl_3$  [Ref. 71].

independently on the preparation method [72, 75, 81-84, 95, 96]. This suppression is believed to occur because the cerium-based conversion coating provides a barrier against both the passage of electrons and the diffusion of oxygen to the metal surface, which are both necessary reactants for the reduction of oxygen (reactions 3.10 and 3.11). Obviously, this strong limitation of the cathodic half of the corrosion reaction decreases the overall corrosion rate. As concern the effect of the cerium on the anodic reaction either as inhibitor or as conversion film, contradictory results are reported in literature. Some authors have found almost no influence on the rate of aluminium dissolution and on the value of pitting potential, which indicates that the improvement in corrosion resistance is exclusively due to a decrease in the cathodic reactions kinetic that lowers the open circuit potential leading to a large passive range (Figure 3.12) [8, 71, 75, 83, 95]. Whereas, in other works it has been shown that the deposition on the aluminium surface of a cerium-rich film, which, especially if consists of  $CeO_2$ , is very stable and insoluble in many media, results in a significant decrease in the rate of not only the cathodic but also the anodic reactions [82, 84, 96].

In section 3.2.2 the high importance of the "self-healing" mechanism in determining the excellent and unique corrosion protection properties of the chromate conversion coating was discussed. Regarding the cerium oxide film, this kind of corrosion protection mechanism could in theory also occur since, similarly to chromium, cerium has also two possible

oxidation states: Ce(III) and Ce(IV). Therefore, if Ce(IV) species, as  $\text{Ce}(\text{OH})^{3+}$ , were present in the oxide/hydroxide film, during exposure to the aggressive environment they could leach and diffuse at the weak spots of the coating, where redox reactions involving the reduction of Ce(IV) and the oxidation of Al could in principle occur. As a consequence a mixed Ce(III)/Al hydroxide could precipitate and repair the defect, similarly to what is suggested to take place in the chromate conversion coating. However, there is no published data relative to the incorporation of leachable form of Ce(IV) for the healing of the film. Even though several studies of cerium based conversion coatings, produced either by long immersion in  $\text{CeCl}_3$  solution or by short dipping in  $\text{CeCl}_3\text{-H}_2\text{O}_2$  bath, indicate that cerium is present in the tetravalent state, it is likely that most if not all of this cerium is immobilized in the fluorite lattice of  $\text{CeO}_2$  rather than adsorbed. Indeed, Hinton, Arnott and Ryan [8] during their early studies discounted the leaching of cerium from the Ce-based conversion coating by means of polarization tests on bare samples in a solution to which a coated sample had been previously exposed for hours.

Finally, it is suggested that the cerium oxide film reduces the susceptibility of aluminium alloys to pitting corrosion due to its deposition on top of intermetallic particles, which eliminates the local galvanic couples present on the surface and as a consequence limits the number of preferential nucleation sites for pitting [95, 93, 95, 97]. The role of the alloy microstructure, in particular the intermetallics, on the formation of the cerium-based conversion coating is discussed in the next section.

### 3.3.3 Cerium-based conversion coatings and microstructure

The deposition of cerium oxide/hydroxide on a metal surface has been demonstrated to be a cathodic process independently on the method used to form the film. As reported in section 3.3.1, the precipitation of either Ce(IV) or Ce(III) hydroxides occurs as a consequence of the increase in pH resulting from the cathodic reactions ( $\text{O}_2$  and/or  $\text{H}_2\text{O}_2$  reduction and hydrogen evolution). Therefore, since the first studies concerning the deposition of the cerium-based conversion coating the effect of the cathodic intermetallics, which due to their electrochemical nature enhance the rate of the cathodic reactions at their location, was considered [70, 72]. In these works it was suggested that the deposition on AA7075 of the cerium oxide film during prolonged immersion in  $\text{CeCl}_3$  solution starts at the cathodic areas, i.e. Cu-rich intermetallics, on the alloy surface and then proceeds via island growth from these locations.

The preferential precipitation of the Ce oxide layer on top of Cu-containing intermetallic particles has been observed in many other investigations. Aldykewicz, Isaac, and Davenport [93] showed that when AA2024 or an aluminium/copper galvanic couple are immersed in a sodium chloride solution containing small amount of  $\text{CeCl}_3$ , a hydrated cerium oxide film is formed only over the  $\text{Al}_2\text{Cu}$  intermetallics and the copper, respectively. Hughes *et al.* [89] found that dipping a macroscopic couple consisting in  $\text{Cu}_2\text{FeAl}_7$  phase (5 mm in diameter) surrounded by pure aluminium (AA1100) in  $\text{CeCl}_3\text{-H}_2\text{O}_2$  bath results in the formation of hydrated cerium oxide only on the intermetallic phase. Similarly, during the immersion in cerium salts solutions at high temperature a dense oxide containing large amount of cerium

covers all the large copper-rich intermetallics, as  $\text{Cu}_2(\text{Fe},\text{Mn})\text{Al}_7$  and  $\text{Al}_2\text{Cu}$ , of AA2024, whereas a crazed aluminium oxide is formed on the matrix [86].

Recently, based on XPS, SEM and EDX results a two-stage mechanism of cerium oxide film growth on AA2024 during immersion in the  $\text{H}_2\text{O}_2$ -accelerated cerium bath has been proposed [88], which considers the presence of Cu-rich intermetallic as a necessary condition for a rapid film deposition. During the first stage the film forms above the large Cu-rich intermetallics, which are the most noble sites on the surface of AA2024 and then have the highest cathodic efficiency for  $\text{H}_2\text{O}_2$  reduction (Figure 3.13-a). Afterwards, the coating deposition proceeds radially away from these intermetallics, i.e. island growth mechanism, under the influence of the local pH rise, which results from the cathodic reactions and is attenuated with increasing distance from the intermetallic particle due to mixing with the bulk solution.

The second stage of film growth begins between 6 and 10 minutes of immersion, when a golden coating develops above the whole surface. Deposition in this case is related to the dissolution of the aluminium passive layer, which activates other small cathodic sites on the aluminium surface, as dispersoid and hardening particles, alloying elements segregation at the grain boundaries, etc. (Figure 3.13-b). This leads to the formation of a thicker and more cracked layer on top of the Cu-rich coarse intermetallics and of a finely structured, amorphous, and thinner film above the rest of the surface, as observed by SEM investigation.

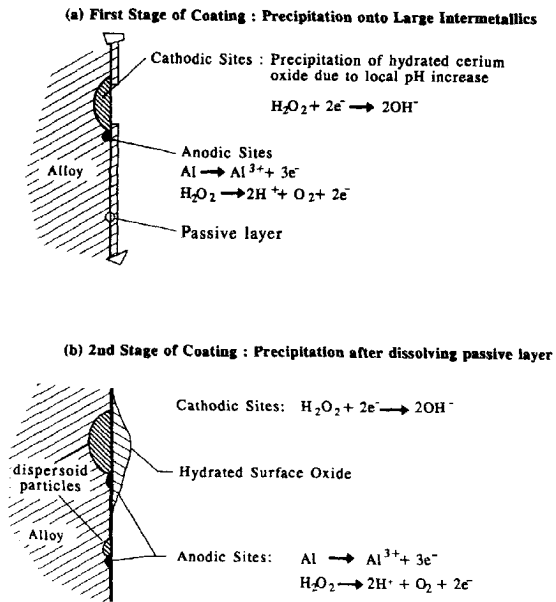


**Figure 3.13:** Model of the precipitation process of the hydrated cerium oxide coating on AA2024 [Ref. 88].

According to the authors, the much higher reactivity shown by the aluminium alloys belonging to the 2xxx and 7xxx series in comparison with all the other alloys (3xxx, 5xxx, 6xxx series) towards the formation of a cerium oxide film during immersion in  $\text{CeCl}_3\text{-H}_2\text{O}_2$  solution is mainly caused by the presence of Cu-rich intermetallics on the surface, which behave as very strong cathodes. However, this is in disagreement with several studies, where other intermetallic particles, which do not contain copper, do act as strong cathodic sites and do lead to the formation of a thick cerium oxide layer at their locations but do not cause a rapid deposition of this layer over the whole surface:  $(\text{Fe},\text{Cr})_3\text{SiAl}_2$  in AA6061 [83, 86],  $\text{FeNiAl}_9$  in AA2618 [83],  $\text{Al}_6\text{-(Mn,Fe,Cr)}$  on AA5083 [75, 97].

These controversial results suggest that other features typical of the aluminium alloys of the 2xxx and 7xxx series in addition to the Cu-containing intermetallics are responsible for the rapid growth of the cerium-based conversion coating on their surface. The high content of copper in solid solution can be one possibility. Indeed, copper could be redeposited on the external surface as small metal copper or copper oxide particles either during the cerium-based conversion treatment or during the previous surface preparation procedure. These Cu particles in turn act as small cathodic sites homogeneously distributed on the whole surface enhancing the rate of the cathodic reactions and as a consequence the increase in pH at the surface and the deposition of the film. The hypothesised acceleration effect of the copper particles would explain several experimental findings: the faster film formation induced both by the Ce-based deoxidiser treatment [90], which was found to cause considerable etching of the surface and generation of a copper dissolution product distributed as particulate matter on the surface [98], and by the addition of  $\text{Cu}(\text{glycinate})_2$ , which is supposed to lead to a fine dispersion of copper crystallites on the surface [89], the absence of film deposition on the matrix of AA2024 when no surface preparation treatment is carried out and/or the immersion in the  $\text{CeCl}_3$  bath is very short [93], which do not enable the surface copper redeposition to take place.

However, as far as we know there are no published studies focusing on the role of the copper redeposition on the nucleation, growth and final properties of the cerium-based conversion coatings. Therefore, it was felt that a more detailed investigation on the formation of the cerium oxide film on AA2024 is needed in order to single out the exact effect of the microstructure, in particular to distinguish between the roles played by the intermetallic particles and by the copper in solid solution, which are expected to influence also the degree of corrosion protection provided by the film. This knowledge is very important to further improve this alternative system and render it a valuable replacement for the chromate conversion coating.

### 3.4 Conclusions

The chromate conversion coating is still extensively used to improve the corrosion resistance and the paint adhesion of aluminium alloys, especially those used in aircraft applications, as Alclad and bare AA2024. Yet the mechanisms of formation and corrosion protection of such film are not completely understood. On the other hand, a promising alternative for the chromate treatments, which due to the presence of toxic and suspect carcinogenic substances need to be replaced, consists of the use of cerium salts solutions to form cerium oxide conversion coatings. However, this environmental friendly treatment can be further improved, either concerning the corrosion protection provided or the method of application. The literature review discussed in the present chapter has brought in the foreground the strong effect of the microstructure, especially the intermetallic particles and the alloying elements, on the nucleation, growth, and final properties of both types of conversion coating. However, controversial results are found on this topic and it appears clear that the exact role played by the different microstructural features of the aluminium surface is not yet understood.

Therefore, one of the main goal of this PhD study is a clarification of the influence of the aluminium alloy microstructure on the formation and final properties of the chromate and the cerium-based conversion coatings, since it is believed to be a necessary condition both for a better understanding of the chromate film system and for an improvement of the cerium-based system. In addition, a more exact and precise knowledge of the role played by the microstructure on the formation of the chromate film can help also the understanding of its effect in the case of the cerium-based process, since the nucleation and growth of both coatings involve redox reactions.

The investigation of these two treatments has been focused on Alclad and bare AA2024 since these alloys are of high interest for the aerospace industry, where a very good level of corrosion resistance is required and as a consequence the chromate conversion process is widely used and the development of an alternative system, able to provide similar level of protection, is becoming more and more a stringent priority.

### 3.5 References

- [1] S. Wernick, R. Pinner, *The Surface Treatment and Finishing of Aluminium and its Alloys*, 5<sup>th</sup> edition, Finishing Publication, Teddington, UK (1986)
- [2] *Metals Handbook: Surface Cleaning, Finishing and Coating*, Vol. 5, 9<sup>th</sup> edition, American Society for Metals (1978)
- [3] M. van Lancker, *Metallurgy of Aluminium Alloys*, Chapman and Hall (1967)
- [4] L. Friberg, G.F. Nordberg, V.B. Vouk, *Handbook of Toxicology of Metals*, Vol. II, Elsevier, Amsterdam (1986)
- [5] B.R.W. Hinton, *Met. Finish.* 89 (1991) 55
- [6] Pyrene Chemical Service, Ltd. Brit. Pat. 2.0145.617 (1979)
- [7] Amchem Products Inc., U.S. Pat. 4.313.769 (1980)
- [8] B.R.W. Hinton, D.R. Arnott, N.E. Ryan, *Metals Forum* 7 (1984) 211
- [9] M. Scriver, US Patent 5.298.092
- [10] C.M. Rangel, M.A. Travassos, *Corros. Sci.* 33 (1992) 327
- [11] R.G. Buchheit, M.D. Bode, G.E. Stoner, *Corrosion* 50 (1994) 205
- [12] Holmes-Farley, US Patent 5182143 (1993)
- [13] W.J. VanOoij, D.Q. Zhu, G. Prasad, S. Jayaseelan, Y. Fu, N. Teredesai, *Surf. Eng. (UK)* 16 (2000) 315
- [14] X.F. Yang, D.E. Tallman, V.J. Gelling, G.P. Bierwagen, L.S. Kasten, J. Berg, *Surf. Coat. Technol.* 140 (2001) 44
- [15] T.L. Metroke, R.L. Parkhill, *Prog. Org. Coat.* 41 (2001) 233
- [16] R. Feser, Th. Schmidt-Hansberg, *Proceedings of Eurocorr97*, Trondheim, Norway (1997) 291
- [17] G.M. Bommarito, A.V. Pocius, *Thin Solid Films* 327-329 (1998) 481
- [18] M.F. abd Rabbo, J.A. Richardson, G.C. Wood, *Corros. Sci.* 18 (1978) 117
- [19] R.C. Furneaux, G.E. Thompson, G.C. Wood, *Corros. Sci.* 19 (1979) 63
- [20] G. Goeminne, PhD thesis, Vrije Universiteit Brussel, Belgium (1999)
- [21] G. Goeminne, A. Hubin, H. Terry, J. Vereecken, *Proceedings of the 1<sup>st</sup> International Symposium on Aluminium Surface Science and Technology*, Antwerp, Belgium (1997) 157
- [22] H.A. Katzman, G.M. Malouf, *Appl. Surf. Sci.* 2 (1979) 416
- [23] G.M. Brown, K. Shimizu, K. Kobayashi, G.E. Thompson, G.C. Wood, *Corros. Sci.* 33 (1992) 1371

- [24] G.M Brown, K. Shimizu, K. Kobayashi, G.E. Thompson, G.C. Wood, *Corros. Sci.* 34 (1993) 1045
- [25] K. Shimizu, G.M. Brown, K. Kobayashi, G.E. Thompson, G.C. Wood, *Corros. Sci.* 34 (1993) 1853
- [26] J.A. Treverton, N.C. Davies, *Surf. Interface Anal.* 3 (1981) 194
- [27] N.J. Newhard, *Met. Finish.* 76 (1972) 49
- [28] F.W. Lytle, R.B. Greeger, G.L. Bibbins, K.Y. Blohowiak, R.E. Smith, G.D. Tuss, *Corros. Sci.* 37 (1995) 349
- [29] A.E. Hughes, R.J. Taylor, B.W.H.R. Hinton, *Surf. Interface Anal.* 25 (1997) 223
- [30] C. Mirikkannu, P. Bala Srinivasan, S. Sathiyarayanan, K. Balakrishnan, *Trans. Inst. Met. Finish.* 73 (1995) 34
- [31] L. Xia, L. McCreery, *J. Electrochem. Soc.* 146 (1999) 3696
- [32] E. Cuynen, P. Van Espen, G. Goeminne, H. Terryn, *J. Anal. Atomic Spectr.* 14 (1999) 483
- [33] J.H. Osborne, *Prog. Org. Coat.* 41 (2001) 280
- [34] J.A. Treverton, M.P. Amor, *J. Mater. Sci.* 23 (1998) 3706
- [35] Z. Yu, H. Ni, G. Zhang, Y. Wang, S. Dong, G. Zhao, *Appl. Surf. Sci.* 62 (1992) 217
- [36] K. Nakamoto, *Infrared and Raman Spectra of Inorganic and Coordination Compounds*, Part B, 5<sup>th</sup> ed., John Wiley & Sons, New York (1997)
- [37] D.B. Brown, D.F. Shriver, L.H. Schawartz, *Inorg. Chem.* 7 (1968) 77.
- [38] T. Drozda, E. Maleczki, *J. Radioanal. Nucl. Chem. Letters* 95 (1985) 339
- [39] M. Koudelkova, J. Augustynski, H. Berthou, *J. Electrochem. Soc.* 124 (1977) 1165
- [40] G.P. Halada, C.R. Clayton, D.H. Lindsley, *Mater. Sci. Eng. A103* (1988) L5
- [41] S.V. Kagwade, C.R. Clayton, G.P. Halada, *Interface Anal.* 31 (2001) 442
- [42] D. Chidambaram, G.P. Halada, C.R. Clayton, *Appl. Surf. Sci.* 181 (2001) 283
- [43] M.W. Kendig, A.J. Davenport, H.S. Isaacs, *Corros. Sci.* 34 (1993) 41
- [44] J. Wan, G.E. Thompson, K. Lu, C.J.E. Smith, *Physica B* 208&209 (1995) 511
- [45] L. Xia, R. McCreery, *J. Electrochem. Soc.* 145 (1998) 3083
- [46] L. Xia, E. Akiyama, G. Frankel, R. McCreery, *J. Electrochem. Soc.* 147 (2000) 2556
- [47] E. Akiyama, L. Xia, R. McCreery, *Proceedings of the Electrochemical Society Meeting: Passivity and Localized Corrosion: International Symposium in Honor of Professor Norio Sato* Honolulu, Hawai 27 (1999) 300
- [48] J. Zhao, G. Frankel, R. McCreery, *J. Electrochem. Soc.* 145 (1998) 2258
- [49] J.D. Ramsey, R. McCreery, *J. Electrochem. Soc.* 146 (1999) 4076
- [50] J.D.B. Sharman, *Proceedings of the 1<sup>st</sup> International Symposium on Aluminium Surface Science and Technology*, Antwerp, Belgium (1997) 118
- [51] E. McCaffery, *Corros. Sci.* 371 (1995) 481
- [52] M. Kendig, R. Addison, S. Jeanjaquet, *J. Electrochem. Soc.* 146 (1999) 4419
- [53] G.O. Ilevbare, J.R. Scully, J. Yuan, R.G. Kelly, *Corrosion* 56 (2000) 227
- [54] H.J.W. Lenderink, J.H.W. de Wit, *Proceedings of the Electrochemical Society Meeting: Modification of Passive Films*, Paris, France (1993) 214
- [55] C.R. Clayton, G.P. Halada, M.J. Vasquez, J.R. Kearns, D. Chidambaram, *Proceedings of the Electrochemical Society Meeting: Passivity and Localized Corrosion: International Symposium in Honor of Professor Norio Sato* Honolulu, Hawai 27 (1999) 290
- [56] G.O. Ilevbare, J.R. Scully, *J. Electrochem. Soc.* 148 (2001) B196
- [57] M. Kendig, S. Jeanjaquet, accepted for publication in *J. Electrochem. Soc.*
- [58] A. Kolics, A.S. Besing, A. Wieckowski, *J. Electrochem. Soc.* 148 (2001) B322

- [59] G.M. Brown, K. Kobayashi, J. Electrochem. Soc. 148 (2001) B457
- [60] Y. Liu, G.E. Thompson, P. Skeldon, C.J.E. Smith, K. Shimizu, Y. Kihn, *Proceedings of the 2<sup>nd</sup> International Symposium on Aluminium Surface Science and Technology*, Manchester, England, UK (2000) 473
- [61] J.R. Waldrop, M.W. Kendig, J. Electrochem. Soc. 145 (1998) L11
- [62] P.L. Hagans, C.M. Haas, Surf. Interface Anal. 21 (1994) 65
- [63] W.R. McGovern, P. Schmutz, R.G. Buchheit, R.L. McCreery J. Electrochem. Soc. A47 (2000) 4494
- [64] G.P. Halada, C.R. Clayton, M.J. Vasquez, J.R. Kearns, M.W. Kendig, S.L. Jeanjaquet, G.G. Peterson, G.S. McCarthy, G.L. Carr, *Proceedings of the Electrochemical Society Meeting: Passivity and Localized Corrosion: International Symposium in Honor of Professor Norio Sato* Honolulu, Hawai 27 (1999) 313
- [65] L. Juffs, A.E. Hughes, S. Furman, P.J.K. Paterson, *Proceedings of the NACE Meeting: Corrosion2000*, Orlando, US (2000)
- [66] M.J. Vasquez, G.P. Halada, C.R. Clayton, J.P. Longtin, *Proceedings of the Electrochemical Society Meeting: Corrosion and Corrosion Prevention of Low Density Metals and Alloys*, Phoenix, Arizona, US (2000) 57
- [67] G.M. Treacy, G.D. Wilcox, Appl. Surf. Sci. 157 (2000) 7
- [68] T.J. Haley, J. Pharm. Sci. 54 (1965) 633
- [69] G.K. Muecke, P. Moller, Sci. Amer. 258 (1988) 72
- [70] B.R.W. Hinton, D.R. Arnott, N.E. Ryan, Mater. Forum 9 (1986) 162
- [71] D.R. Arnott, B.R.W. Hinton, N.E. Ryan, Mater. Performance (1987) 42
- [72] D.R. Arnott, N.E. Ryan, B.R.W. Hinton, B.A. Sexton, A.E. Hughes, Appl. Surf. Sci. 22/23 (1985) 236
- [73] F. Mansfeld, S. Lin, S. Kim, H. Shih, Corros. Sci. 27 (1987) 997
- [74] B.R.W. Hinton, J. Alloy & Compounds 180 (1992) 15
- [75] M.A. Arenas, M. Bathencourt, F.J. Botana, J. de Damborenea, M. Marcos, Corros. Sci. 43 (2001)157
- [76] A.J. Davenport, H.S. Isaacs, M.W. Kendig, Corros. Sci. 32 (1991) 653
- [77] S. Böhm, R. Greef, H.N. McMurray, S.M. Powell, D.A. Worsley, J. Electrochem. Soc. 147 (2000) 3286
- [78] A.J. Aldykiewicz Jr., A.J. Davenport, H.S. Isaacs, J. Electrochem. Soc. 143 (1996) 147
- [79] J.A. Kargol, D.L. Jordan, Corrosion 38 (1982) 201
- [80] F.-B. Li, G.E. Thompson, J. Electrochem. Soc. 146 (1999) 1809
- [81] B.R.W. Hinton, N.E. Ryan and D.R. Arnott, Materials Australiasia 19 (1987) 18
- [82] J. Stoffer, T.J. O'Keefe, H. Anderson, X.Lin, E. Morris, P. Yu, M. Pittman, *Proceedings of the 26<sup>th</sup> International Waterborne, High-Solids, and Organic Coatings Symposium*, New Orleans, Louisiana, US (1999) 20
- [83] M. Dabalà, L. Armelao, A. Buchberger, I. Calliari, Appl. Surf. Sci. 172 (2001) 312
- [84] F. Mansfeld, Y. Wang, H. Shih, Electrochim. Acta 37 (1992) 2277
- [85] F. Mansfeld, Y. Wang, Mater. Sci. Eng. A198 (1995) 51
- [86] A.E. Hughes, J. D. Gorman, P.J.K. Paterson, Corros. Sci. 38 (1996) 1957
- [87] L. Wilson, B.R.W. Hinton, *A Method of Forming a Corrosion Resistant Coating*, Patent WO 88/06639 (1988)
- [88] A. E. Hughes, R.J. Taylor, B.R.W. Hinton, L. Wilson, Surf. Interface Anal. (UK) 23 (1995) 540

- [89] A.E. Hughes, S.G. Hardin, K.W. Wittel, P.R. Miller, *Proceedings of the NACE meeting: Corrosion/2000, Research topical Symposium: Surface Conversion of Aluminum and Aluminum alloys for Corrosion Protection*, Orlando, US (2000)
- [90] B. Hinton, A.Hughes, R. Taylor, M. Henderson, K. Nelson, L. Wilson, *Proceedings of the 13<sup>th</sup> International Corrosion Congress (ICC)*, Paper 337.
- [91] A.E. Hughes, K.J. Nelson, R.J. Taylor, B.R.W. Hinton, M.J. Henderson, L. Wilson, S.A. Nugent, International Patent Application No. PCT/AU94/00539, International Patent No. WO95/08008
- [92] A.E. Hughes, K.J.H. Nelson, T.W. Turney, Australian Patent AU 684,238
- [93] A.J. Aldykewicz Jr., H.W.S. Isaacs, A.J. Davenport, *J. Electrochem. Soc.* 142 (1995) 3342
- [94] C.J.E. Smith, K.R. Baldwin, M.A.H. Hewins, *Proceedings of the European Corrosion Congress: Progress in the Understanding and Prevention of Corrosion*, Barcelona, Spain (1993) 1652
- [95] B.R.W. Hinton, A. Hughes, R. Taylor, M. Henderson, K. Nelson, L. Wilson, *Proceedings of the 1<sup>st</sup> Symposium on Aluminium Surface Science and Technology*, Andwerp, Belgium (1997) 165
- [96] Y. Xingwen, C. Chunan, Y. Zhiming, Z. Derui, Y. Zhongda, *Mater. Sci. Eng. A284* (2000) 56
- [97] A. Aballe, M. Bethencourt, F.J. Botana, M. Marcos, J. Perez, M.A. Rodriguez-Chacon, *Mater. Sci. Forum* 289-292 (1998) 557
- [98] A.E. Hughes, K.J.H. Nelson, P.R. Miller, *Mater. Sci. Technol.* 15 (1999) 1124



# Microstructure and corrosion - Use of the SKPFM technique

### 4.1 Introduction

As discussed in section 2.3.1 of chapter 2, the process of alloying to improve the strength properties of AA2024 heavily compromises the corrosion properties of the metal. In particular, the susceptibility to localized corrosion is dramatically increased by the precipitation of all types of intermetallic particles due to the formation of local galvanic cells and the resulting heterogeneities of the natural oxide film. At the moment, corrosion presents a major threat to the structural integrity of aircraft components and may reduce their life significantly. As time in service increases, there is a growing probability that corrosion will be associated with other forms of damage, as fatigue cracking and embrittlement. For instance, pitting corrosion is considered one of the principal degradation mechanisms for AA2024, and pits have been identified as the major nuclei for onset of corrosion fatigue cracks [1, 2]. In addition, the literature review reported in chapter 2 has also highlighted the important role played by the heat treatment parameters, in particular cooling rate during quenching and aging procedures, on the microstructure and as a consequence on the susceptibility to localized corrosion of AA2024. According to [3], the corrosion behaviour of this alloy can be drastically affected not only by significant modifications in the heat treatment procedure, intentionally introduced to obtain specific mechanical properties, but also by very small changes, which can easily occur during industrial practice.

A better understanding of the effects of variations of the heat treatment parameters on the microstructure and as a consequence on the corrosion susceptibility of AA2024 is, therefore, of both scientific interest and technological importance. Indeed, being aware of the influence of the different heat treatment variables on the microstructure of the aluminium alloys may reduce the risk of sudden product failures resulting from unexpected severe localized corrosion. To this aim the influence of the time spent in air before water quench, referred to as quench delay time, on the microstructure and the corrosion behaviour of AA2024 has been investigated and is discussed in this chapter. In comparison with the variations expected in the industrial process some of the phenomena are deliberately over-exaggerated by the heat treatment procedure used; however, this was necessary to enable the investigation.

A second, but very important, purpose of this part of the study consisted of investigating the suitability of the Atomic Force Microscope (AFM), present in our laboratory,

to simultaneously map the topography and the potential distribution across the sample surface with sub-micrometer resolution. AFM is a relatively new surface technique that enables the acquisition of high resolution surface images of conducting and insulating materials in gas and liquid environments [4, 5]. During the first few years of application, the use of AFM in corrosion studies has been focused on the *in-situ* characterization of the electrode surface, while electrochemical processes are occurring [6-9]. However, more recently much effort has been directed toward the modification of the AFM in order to map other surface properties in addition to the topography, such as adhesion, friction, conductivity, work function, optical absorption and emission [10]. In particular, the Scanning Kelvin Probe Force Microscope (SKPFM) is a combination of the well-known Kelvin probe technique and the AFM and was developed and first used to study the surface potential of photoresist-covered Si wafers [11] and semiconductor dopant profiles [12]. This was followed by several investigations in the field of semiconductors, which reported measurements of the surface potential between different materials using this technique with high lateral ( $< 50$  nm) and surface potential (better than 0.1 mV) resolution [13, 14].

The classical Kelvin probe technique based on capacitor plates [15] has been used for some time to measure the potentials of various metal surfaces by nulling the current flowing between the sample and a closely positioned vibrating probe [16]. In 1988, Baumgärtner and Liess [17] developed a miniaturized Kelvin probe that enabled microscopic imaging of the potential difference between the probe and the sample with a lateral resolution of 40  $\mu\text{m}$ . Stratmann *et al.* [18, 19] have demonstrated the applicability of the Kelvin probe technique to the investigation of atmospheric corrosion affecting metallic surfaces. They measured the Volta potential difference of samples covered with a thin layer of electrolyte using a probe that did not touch the electrolyte and showed that this potential difference varies linearly with the corrosion potential of the sample/solution interface determined with a standard reference electrode positioned in the electrolyte layer. Scanning the probe over the sample enabled the mapping of the Volta potential with a lateral resolution of about 100  $\mu\text{m}$ . The combination of the Kelvin probe technique with the AFM, i.e. the SKPFM instrument, enables the mapping of the Volta potential with a much higher lateral resolution due to the fact that the probe is much smaller and operates at a much closer distance from the surface. The ability to map the potential on a sub-micron scale has been shown to be extremely useful in investigating the local electrochemical behaviour of aluminium alloys, since they contain heterogeneities, such as intermetallic particles, on that scale or larger [20-22].

Since the AFM present in our lab is provided with the Extender<sup>TM</sup> Electronics Module, which enables the instrument to operate as a SKPFM, the potential of the intermetallic particles with respect to the aluminium matrix has been studied as function of the quench delay time. Based on the results of the SKPFM investigation it was possible to correlate changes in localized corrosion resistance with changes in the microstructure of AA2024 induced by the variation of the heat treatment procedure. This is described and discussed in the remainder of this chapter. However, since the SKPFM technique uses a different approach for measuring the surface potential than that of the standard Kelvin probe a section dealing with the theoretical background of the SKPFM technique is given first.

## 4.2 Principles of the SKPFM technique

In general, the Volta potential of a phase is defined as the work required in vacuum for moving an electrically charged probe from infinity to a point close to the surface of the phase, where the image charges or dipole begin to be important [16]. When two metal plates are connected electrically in vacuum or inert gas a Volta potential difference,  $\Delta\Psi$ , arises between them, which is the work to bring a charge from one point close to the surface of one of the two plates to a point close to the surface of the other plate. The charge may be an electron and then the definition of the Volta potential is given as follows [23]:

$$\Delta\Psi = -\frac{\Delta\mu_e}{F} - \Delta\chi = \Delta\varphi - \Delta\chi \quad (4.a)$$

where  $\mu_e$  is the chemical potential of the electron,  $F$  the Faraday's constant,  $\chi$  the so-called surface potential corresponding to the electrostatic potential step resulting from the inhomogeneous charge distribution on the surface, i.e. surface dipole layer, and  $\varphi$  the Galvani potential arising at the equilibrium from the different chemical potentials of the electrons in the two metals.

Another approach to the description of an interface between two metals in vacuum can be found in physics, where the electronic work function ( $\phi$ ) of a metal is defined as the energy required for removing an electron from the metal, which is the difference between the Fermi level energy of the metal and the energy of free electron in vacuum [24]. The work function is determined not only by the chemical potential of the electron in the metal but also by the surface potential  $\chi$ , since the electron has to pass across the surface dipole layer [23]:

$$\phi = -\frac{\mu_e}{N_A} - e_0\chi \quad (4.b)$$

where  $N_A$  and  $e_0$  are the Avogadro's number and the electron charge, respectively. When two metal plates are connected electrically, the thermodynamic equilibrium is achieved when the Fermi energy levels of the two metals are equal, which is obtained by the flow of electrons from the plate with the lower work function, i.e. weak electron binding energy, to the plate with the higher work function, i.e. strong binding. The difference in potentials of the two plates arising from the flow of electrons is known as contact potential difference (CPD) and is the difference between the work functions ( $\Delta\phi$ ) of the two metals divided by the charge of one electron [24]:

$$CPD = -\frac{\Delta\mu_e}{N_A e_0} - \Delta\chi = -\frac{\Delta\mu_e}{F} - \Delta\chi = \Delta\Psi \quad (4.c)$$

Equation 4.c shows that contact potential difference and Volta potential difference in vacuum are equivalent. In the rest of this thesis the Volta potential formalism will be used.

If the Volta potential of one of the two metal plates is kept constant (reference surface) the changes in the Volta potential of the other plate can be measured. This is done in the standard Kelvin probe technique, where the tip of the probe electrode, which is the reference, and the surface of the metal sample under study constitute the two plates of a parallel capacitor [25]. The Volta potential difference between the vibrating tip and the

sample ( $\Delta\Psi$ ) is obtained by adjusting the value of an externally applied DC bias voltage,  $E$ , such that the alternating current generated by the sinusoidal probe vibration,  $z_0 + z_1 \sin(\omega t)$ , becomes zero:

$$i = (\Delta\Psi + E) \frac{\partial C}{\partial t} = -\varepsilon \varepsilon_0 A (\Delta\Psi + E) \frac{z_1 \omega \cos(\omega t)}{[z_0 + z_1 \sin(\omega t)]^2} = 0 \quad (4.d)$$

where  $C$  is the capacitance of the parallel capacitor,  $t$  the time,  $A$  is the tip area,  $\varepsilon_0$  the permittivity of vacuum,  $\varepsilon$  the dielectric constant of the capacitor dielectric,  $z_0$  the mean tip/sample separation, and  $z_1$  the amplitude of vibration. Under the conditions of zero current the potential applied is obviously equal to the Volta potential difference between the tip and the sample. The exact meaning of the Volta potential difference as determined by the Kelvin probe depends on the conditions under which the measurement is performed. Indeed, from the definition given above,  $\Delta\Psi$  is related to both free charges and dipole layers on the surface. Therefore, in an environment other than vacuum or inert gas, it is dependent upon the presence of oxide films and adsorbed species on the surface. The presence of surface oxide films causes  $\Delta\Psi$  measured in air to deviate from the values expected by the metallic work functions in vacuum [19]. When an electrolyte film overlays the metal surface the interpretation of the measured Volta potential difference is more complex. For example, polar molecules in an electrolyte can adopt a preferential orientation due to the interaction with the metal surface and form a dipole layer at the interface [23], and potential gradients in the solution can occur due to ionic currents between localized corrosion sites [19]. Both phenomena influence the value of  $\Delta\Psi$  measured with the Kelvin probe, which in this case is that existing between the tip and the outer surface of the electrolyte and not that between the tip and the metal surface. However, Stratmann and co-workers [18, 19] showed that the Volta potential difference measured by the Kelvin probe in presence of an electrolyte film, which is thicker than the electrical double layer and in which no ionic current is flowing, is directly related to the corrosion potential ( $E_{\text{corr}}$ ) of the metal/electrolyte interface measured with a reference electrode immersed in the electrolyte:

$$\Delta\Psi = E_{\text{corr}} + (\chi_{\text{el}} - \frac{\phi_{\text{ref}}}{F}) \quad (4.e)$$

where,  $\chi_{\text{el}}$  is the surface potential of the electrolyte and  $\phi_{\text{ref}}$  is the work function of the reference electrode, both of which are constant in many circumstances.

SKPFM measures the Volta potential difference between a conducting AFM tip and the sample under study using a different approach. The tip and the sample are still the plates of a capacitor, since they are electrically connected and have different Volta potential. Therefore, between them an electrostatic force is generated [14, 26]:

$$F = \frac{1}{2} (\Delta\Psi)^2 \frac{\partial C}{\partial z} \quad (4.f)$$

where  $\Delta\Psi$  is the Volta potential difference between tip and sample,  $z$  the tip-sample distance, and  $C$  the capacitance. If an AC voltage,  $V_{\text{ac}} \sin(\omega t)$ , with an adjustable DC offset,  $V_{\text{dc}}$ , is applied to the conducting AFM tip, the electrostatic force interaction between the tip and the sample becomes:

$$F = \frac{1}{2} \frac{\partial C}{\partial z} \{ \Delta\Psi + [V_{dc} + V_{ac} \sin(\omega t)] \}^2 \quad (4.g)$$

with spectral components at DC:

$$F_{dc} = \frac{1}{2} \frac{\partial C}{\partial z} \left\{ (\Delta\Psi + V_{dc})^2 + \frac{V_{ac}^2}{2} \right\} \quad (4.h)$$

and at frequencies  $\omega$  and  $2\omega$ :

$$F_{\omega} = \frac{\partial C}{\partial z} (\Delta\Psi + V_{dc}) V_{ac} \sin(\omega t) \quad (4.i)$$

$$F_{2\omega} = -\frac{1}{4} \frac{\partial C}{\partial z} V_{ac}^2 \cos(2\omega t) \quad (4.j)$$

As a result of  $F_{\omega}$  and  $F_{2\omega}$  the tip starts to vibrate. If the frequency of the applied AC voltage equals the resonant frequency of the cantilever of the tip the vibration amplitude at frequency  $\omega$  is directly proportional to  $F_{\omega}$  [27]. The principle of operation of SKPFM is based on nullifying the tip vibration amplitude at the resonant frequency, which is used as the feedback signal, by adjusting the external DC voltage. Indeed, when the tip vibration amplitude at the resonant frequency becomes zero the spectral component at frequency  $\omega$  is also nullified, consequently the DC offset,  $V_{dc}$ , is equal in magnitude and opposite in sign to the Volta potential difference ( $\Delta\Psi$ ) between tip and sample.

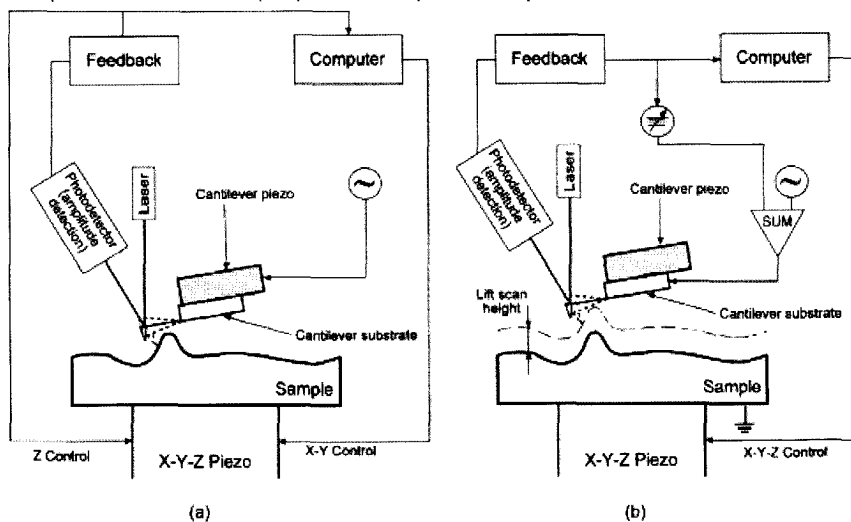


**Figure 4.1:** Schematic illustrations of the topography measurement in tapping mode (a) and Volta potential measurement in lift mode (b) [Ref. 26].

The mapping of the surface Volta potential of the sample is usually made in the so-called "lift mode", which is a two-pass technique, i.e. each line of the image is scanned twice [28]. In the first step of each scan, no external voltage is applied to the tip and the topography of the sample is determined and recorded using the tapping mode of operation (Figure 4.1-a). When operating in this mode, the AFM measures the topography by "tapping" the surface with the tip, which is oscillated near its resonant frequency (60-100 kHz) by a

piezo-element. The vertical position of the scanner at each point necessary to keep the oscillation amplitude constant is recorded to form the topographic image of the line. This is made using a feedback system based on a laser deflection detector, where the top side of the cantilever serves as a reflector (Figure 4.2).

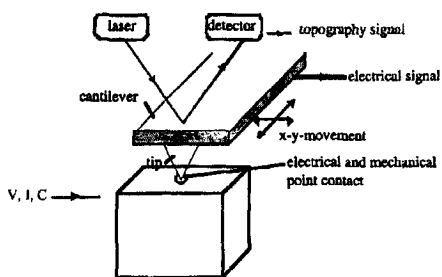


**Figure 4.2:** Basic scheme for AFM measurements [Ref. 29].

The application of an AC voltage is necessary to enhance the electrostatic force interaction between tip and sample, which is otherwise weak and only due to their Volta potential difference (equation 4.f). A second electronic feedback loop, which is provided by the Extender™ Electronics Module and based on the same laser deflection detector used for the topographic image, adjusts the DC bias on the tip in order to nullify the vibration amplitude of the cantilever and hence the spectral component of the electrostatic force at frequency  $\omega$  ( $F_{\omega}$ , equation 4.i). The required bias voltage is recorded and by reversing the sign, the Volta potential map of the sample with respect to the tip is obtained. Repeating this procedure for each line along the slow-scan axis creates the topographic and Volta potential images.

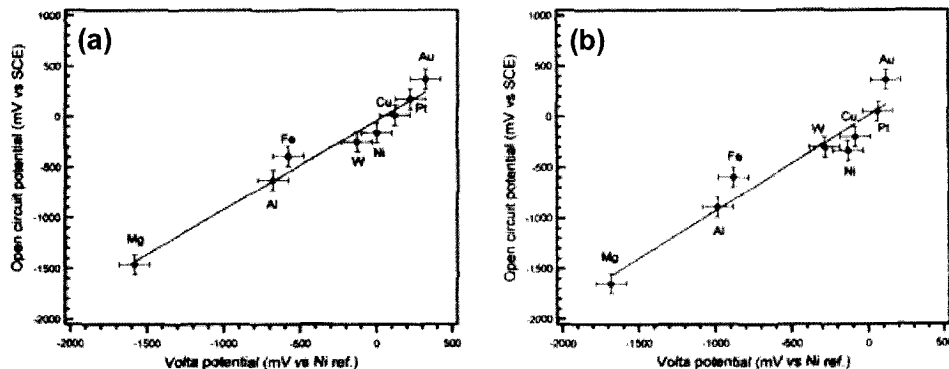


**Figure 4.3:** Comparison of the potential measured in air by the SKPFM with the open circuit potential measured in solution for different metals in: deionised water (a), 0.5M NaCl (b) [Ref. 20].

The potential measurements with SKPFM are not possible in an aqueous solution because the large voltage applied to the tip would cause faradic reactions. However, Schmutz and Frankel [20] showed that the potential measured in air with the SKPFM on a number of pure metal samples after exposure to deionised (DI) water or 0.5M NaCl is linearly related to the open circuit potential (OCP) that was measured in the bulk solution

before the samples were removed (Figure 4.3). The values of the potential measured with the SKPFM are given as a function of the potential measured on a pure Ni surface after immersion in DI water in order to avoid errors associated with variations in the tips or instabilities in the instrument electronics. Despite this correlation, questions still exist regarding both the nature of the potential measured by SKPFM and the limitations of the measurements made in air for understanding phenomena occurring in solution.

Similarly to the standard Kelvin probe, when the measurements are made in air the value of the Volta potential difference is affected by contamination, oxide layers, or trapped surface charges [30]. Guillaumin et al. [22] found that changes in adsorption of species have a strong influence on the potential measured when the tip/sample separation is lower than 100 nm and that a constant contribution related to dipole charge is also present on the Volta potential value measured at distances equal or higher than 100 nm. Ultrahigh vacuum conditions are required to obtain quantitative results on electronic properties of semiconductor surfaces on a nanometer scale [31].

According to the mode of operation of SKPFM, the measured Volta potential of the sample is relative to that of the tip. Therefore, changes in the properties of the tip can influence the measurements. An ideal tip should be hard, sharp, electrically conductive, wear resistant and have stable long-term characteristics. Metal-coated Si tips are commonly used due to ready availability and ease of fabrication. However, they are frequently affected by wear and the coating thickness, chemical composition and tip shape, which all influence the measured Volta potential, can vary from one probe to another due to inconsistencies in the coating deposition technique [26, 29]. It was found that the variation in the Volta potential using different CoCr-coated Si tips is in the order of few tens of millivolts [20]. In addition, the shape of the tip influences also the lateral resolution of the SKPFM measurements due to long-range electrostatic interactions between the probe and the sample [14]. Considering  $N$  areas with different Volta potential  $\Psi_i$ , the DC voltage to nullify  $F_{\omega}$  (equation 4.1) is given by:

$$V_{dc} = \frac{\sum_i C'_{it} \Psi_i}{\sum_i C'_{it}} \quad (4.k)$$

where  $C'_{it}$  represent the derivatives of the capacitance that depend on the lateral tip location, i.e. shape (Figure 4.4). This relation states that the measured potential is a weighted average over all potential  $\Psi_i$  on the surface, the derivatives of the capacitances being the weighting factors. Therefore, the resolution and accuracy of the measurements are defined by the capacitances between the tip and the respective surface regions. This leads to several consequences: an ideal potential step on a surface will be measured as a smoothed step potential, the measured potential of an area will approach the value of the surrounding region as the area decreases in size, true potential information can only be gained from surface areas with dimensions

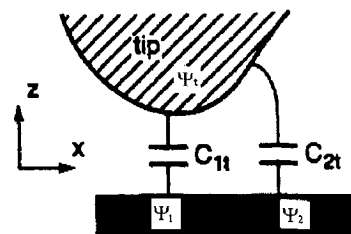


Figure 4.4: Scheme of the tip/sample interaction (Ref. 14).

very large compared to the tip. Contrast and detection limit are then improved using longer and narrower tips.

Furthermore, some parameters, which need to be set before the starting of the measurement, have been found to affect the measured potential value to different extents. The chosen lift scan height, i.e. the distance between the tip and the sample, has quite a strong effect on the Volta potential measured with SKPFM. Indeed, while for distances from 100 nm to a few micrometers the value of the measured potential remains constant [22], for distances lower than 100 nm it decreases with decreasing separation, due to the effects of image or dipole charges close to the surface [26], in accordance with textbook descriptions of Volta potential [32]. Another important parameter is the phase difference between the reference signal (used in the lock-in amplifier of the second feedback loop) and the deflection signal of the cantilever, which has to be set to an optimum value to achieve the highest sensitivity [33]. On the other hand, the effect of the amplitude of the AC voltage applied to the tip is found to be negligible [26].

Finally, the topographic features of the sample surface can also affect the Volta potential measurements, especially for samples characterized by an irregular and rough topography, i.e. large variations in height. In theory, from equation 4.1 the Volta potential difference ( $\Delta\Psi$ ) should be equal to the bias DC potential applied to nullify  $F_{\omega}$ , independently on the value of the derivative of the capacitance and consequently on any geometrical parameters. In reality, the amplitude of the tip oscillation and therefore  $F_{\omega}$  can not be suppressed completely to zero but only to some minimal detectable value ( $F_{min}$ ), which depends on the thermal excitation of the cantilever oscillations, and instrumental noise [34]. Therefore, the measured potential is given by the sum between the real Volta potential difference and a geometrical contribution, related to the derivatives of the capacitance ( $\Delta\Psi_{geom}$ ):

$$V_{dc} = - \left[ \Delta\Psi - \frac{F_{min}}{V_{ac}} \frac{\partial C}{\partial z} \right] = - [\Delta\Psi + \Delta\Psi_{geom}] \quad (4.1)$$

The geometrical contribution to the measured potential, which results in artefacts on the Volta potential image, becomes significant when the topography of the sample is very rough and the real surface potential is rather homogeneous, whereas for very flat samples, it can be considered negligible.

In conclusion, the SKPFM Volta potential measurements should be carried out and interpreted keeping in mind the various limitations previously discussed. Nevertheless, SKPFM is considered a valid method for the investigation of the corrosion behaviour of aluminium alloys, since the potential maps obtained with this technique are a reliable indication of the nobility of the intermetallic particles relative to the Al matrix [20, 21]. This is very important in determining the role of such intermetallics in the local electrochemical behaviour of the alloy and as a consequence in better understanding its corrosion susceptibility.



## 4.3 Experimental procedure

### 4.3.1 Materials

All samples were cut from a single 4 mm thick commercial AA2024 (Al-4.4%Cu-1.5%Mg-0.6%Mn-0.5%Si-<0.5%Fe) rolled sheet, which was received in the T3 temper, i.e. solution heat treated, cold worked, and naturally aged. Each sample was then solution heat treated at 495°C for 55 minutes in an air furnace. Subsequently a water quench, consisting of immersion in water at room temperature, was carried out after different periods of time spent in air, i.e. different values of quench delay time ( $t_{qd}$ ), namely 3 seconds (sample 1), 9 seconds (sample 2), 18 seconds (sample 3), 27 seconds (sample 4), 54 seconds (sample 5), 81 seconds (sample 6), and 243 seconds (sample 7). In addition, one sample (sample 8) was directly cooled in air.

### 4.3.2 Microstructural investigation

The effect of the quench delay time on the size, shape, distribution, chemical composition, and electrochemical nature of the coarse intermetallic particles present in AA2024 was investigated using different microscopic techniques:

- ✓ Optical microscopy study was carried out within the MCM group at the Faculty of Materials Science of TUDelft (Delft, NL) to obtain information concerning the distribution of the intermetallics in the bulk of the samples, which were ground and then polished with diamond paste up to  $\frac{1}{4}$   $\mu\text{m}$  using ethanol as lubricant to avoid any surface degradation. Additionally, a light microscopy investigation was also carried out on the cross section of the samples after the corrosion tests to characterize the type of attack, which had occurred.
- ✓ SEM (Scanning Electron Microscopy, Jeol JSM-6400F) and EDS (Energy Dispersive Spectroscopy) measurements were performed within the FCM group at the Faculty of Materials Science of TUDelft (Delft, NL) to characterize the size, shape, distribution and chemical composition of the intermetallics. All micrographs were obtained using a low energy electron beam of 5 keV, whereas energy of 12 keV was used for the EDS analyses. Prior to investigation the samples were polished up to  $\frac{1}{4}$   $\mu\text{m}$  and immersed for few seconds in Keller's reagent to highlight the microstructural features. The EDS technique was used in order to achieve information concerning the chemical composition of the coarse intermetallics present in the aluminium alloy. However, it is important to keep in mind that the EDS analyses can give only qualitative results due to the depth of the electron beam penetration, which for aluminium and using electron energy of 12 keV is in the order of magnitude of a few microns. This is comparable to the size of the intermetallics and therefore a background signal from the surrounding aluminium matrix is always abundantly present. Since this background signal can vary between different measurements, the spectra were normalized with respect to the maximum count for aluminium.
- ✓ AFM (Atomic Force Microscopy, Digital Instrument Nanoscope III Multimode) was used to investigate the electrochemical nature of the intermetallics, in particular their Volta

potential with respect to the aluminium matrix. The Volta potential maps were acquired using the standard feedback loop provided by the Extender™ Electronics Module. All the measurements were carried out in air at ambient temperature, pressure and humidity, with a lift scan height of 100 nm and a phase difference between the reference signal and the deflection signal of the cantilever set to  $-90^\circ$ , which was found in this case to be the optimum value to enhance the sensitivity of the potential measurement. The potential was sampled with the same pixel density as the topography, i.e. 256 x 256 pixels per image, and at a scan frequency of 0.5 Hz. The AC voltage applied to the tip had amplitude of 5 V and was tuned to the first resonant frequency of the cantilever (60-100 Hz). For all measurements commercially available  $n^+$ -silicon tips coated with  $\text{PtIr}_5$  were used, characterized by a resistivity of 0.1-0.2  $\Omega$  cm, height of  $3 \pm 0.5$   $\mu\text{m}$  and supported on a cantilever  $225 \pm 5$   $\mu\text{m}$  long,  $28 \pm 5$   $\mu\text{m}$  wide and 10-15  $\mu\text{m}$  thick. Prior to each experiment the tip was checked by performing a potential measurement on a reference sample, consisting of aluminium partially covered with a 2 nm thick gold layer. The samples were ultrasonically cleaned in ethanol and air dried to limit any effect of adsorbed species to the Volta potential value. The representation of the topographic and potential images is such that brightness is proportional to height and to potential, respectively.

### 4.3.3 Electrochemical investigation

The electrochemical measurements were carried out in a de-aerated 3.5% NaCl solution using a PAR 273A potentiostat. The pH was adjusted to a value of 4 by means of proper mixture of HCl and NaOH without buffering. During the experiments the solution was stirred and purged with  $\text{N}_2$ , in order to de-oxygenate it and to keep it homogeneous. A saturated calomel electrode (SCE) was used as reference electrode, which was immersed in a separated container with the same solution and connected to the "Green cell" through a salt bridge, filled with the solution. Hereafter, all the potential values will be given versus the SCE reference electrode, unless differently stated. The area of the working electrode was 2.25  $\text{cm}^2$  and was used to calculate the current density as the ratio between the measured current and the

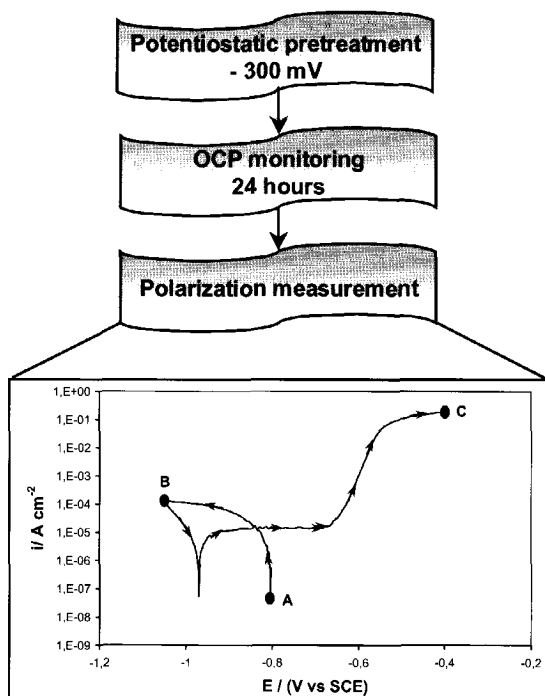


**Figure 4.5:** Scheme of experiment 1 carried out in 3.5% NaCl pH=4 solution.

measured current and the

geometrical sample area. Before each measurement the samples were mechanically polished up to 1  $\mu\text{m}$  and cleaned with ethanol. This set-up was used to carry out two different electrochemical experiments:

- ✓ **Experiment 1** (Figure 4.5) consisted of monitoring the open circuit potential (OCP) for 24 hours, preceded by the application of an anodic potential ( $-300\text{ mV}$ ) for a suitable time, in the order of tens of seconds, to maintain a constant value of charge ( $9\text{ C}$ ) that was flowing through the sample. The aim of this pretreatment was to arrive, as quickly as possible, at a steady-state situation by deliberately inducing the breakdown of the natural aluminium oxide film. The OCP monitoring was immediately followed by a potentiodynamic measurement at a scanning rate of  $0.2\text{ mV/s}$ . The polarization was carried out from the OCP value (point A in the graph given in Figure 4.5), about  $-800\text{ mV}$  for all the samples, to a cathodic potential of  $-250\text{ mV}$  vs. OCP (point B in the graph given in Figure 4.5) and back to an anodic potential of  $-400\text{ mV}$  (point C in the graph given in Figure 4.5). The final value of potential ( $-400\text{ mV}$ ) was chosen based on the knowledge that pitting occurs at this potential and consequently the whole passive range is covered during the measurement.
- ✓ **Experiment 2** (Figure 4.6) consisted of a polarization measurement, performed in order to study the repassivation behaviour of the different samples, through the evaluation of the repassivation potential ( $E_{\text{rep}}$ ) and the repassivation range ( $\Delta E_{\text{rep}}$ ). This potentiodynamic measurement was preceded by a potentiostatic pretreatment, which consisted of the application of a cathodic potential ( $-1050\text{ mV}$ ) for two days.

The aim of this pretreatment was to drive the surface potential of the samples to a value of  $-1050\text{ mV}$  (point A in the graph given in Figure 4.6). This value, given by the sum OCP+ ( $-250\text{ mV}$ ), was chosen in order to start the experiment in the cathodic area and therefore to cover the passivation and repassivation ranges with the measurement. After this pretreatment, the polarization was carried out from a cathodic potential of  $-30\text{ mV}$  vs. this previous applied potential of  $-1050\text{ mV}$  (point B in the graph given in Figure 4.6), to an anodic potential of  $-400\text{ mV}$  (point C in the graph given in Figure 4.6), and back to a potential of  $-1050\text{ mV}$  (point D in the graph given in Figure 4.6).

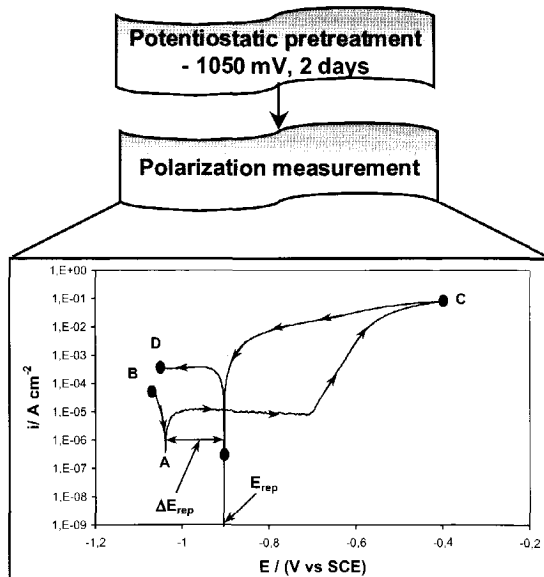


**Figure 4.6:** Scheme of experiment 2 carried out in 3.5% NaCl pH=4 solution.

## 4.4 Results and discussion

In this section the effect of the quench delay time on the microstructure of AA2024 is first discussed. Then in the second part of the section the microstructural changes are related to the corrosion behaviour of the different samples. The discussion and the conclusions, which are drawn from it, are illustrated by few examples of the surface analyses and the electrochemical investigation results, which are representative of the several measurements carried out for each sample.

### 4.4.1 Microstructural investigation

The optical micrograph in Figure 4.7, obtained with sample 6 (quench delay time=81 seconds), clearly shows the presence of a band structure of large intermetallics (IMCs). This lined up distribution of intermetallic particles, in the direction indicated by the arrow in Figure

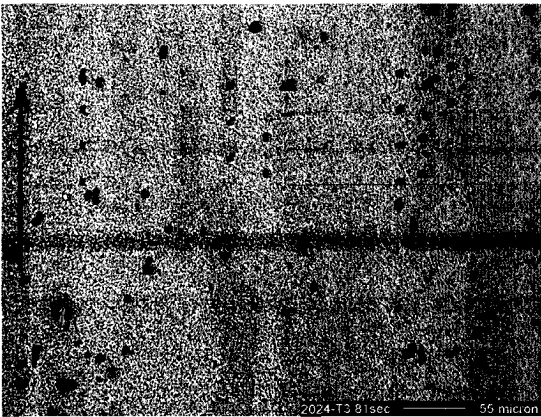


**Figure 4.7:** Optical micrograph of sample 6 (quench delay time = 81 seconds).

4.7, is not influenced by the variation of the quench delay time, as it is already formed during the dendritic solidification process in the ingot and developed further during the rolling treatment.

According to the literature, during the dendritic solidification the last liquid that solidifies, which has a high content of alloying elements, is located between the arms of the dendrites, due to the under-cooling phenomenon [35]. This leads to a high concentration of intermetallics between the arms of the dendrites

and therefore to a band structure. The alignment of large intermetallics is of course enhanced by the cold rolling process and is not modified during the solution treatment at 495°C, since these intermetallic particles are too large to redissolve.

SEM and EDS investigation distinguished two main types of intermetallics in all the samples (named IMC<sub>1</sub> and IMC<sub>2</sub> in the secondary electron image of Figure 4.8-a), which is in accordance with the results reported by many authors and discussed in the section 2.3.1 of chapter 2 [36-38]. The round-shaped Al-Cu-Mg containing intermetallics (IMC<sub>1</sub>), 1-5 μm in diameter, are probably S phases (Al<sub>2</sub>CuMg). However, the EDS analyses cannot provide a definitive confirmation due to the high penetration depth of the electron beam, which causes a strong background signal from the surrounding matrix. Other types of precipitates containing copper and magnesium, such as AlCuMg, Al<sub>5</sub>Cu<sub>6</sub>Mg<sub>2</sub> and Al<sub>6</sub>CuMg<sub>4</sub>, could also be present. Nevertheless, Mondolfo [39] has shown that the precipitation of these phases in the 2024 aluminium alloy is quite improbable. The irregularly shaped Al-Cu-Mn-Fe-Si containing intermetallics (intermetallic IMC<sub>2</sub> in Figure 4.8-a) have been found to be in general bigger than the Al-Cu-Mg particles (10 μm or more) and tend to be clustered. The

EDS spectra, an example is given in Figure 4.8-c, do not enable a quantitative identification of their chemical composition, but it has been noted that many intermetallics of this type are rich in copper and very poor in silicon, contain similar amounts of manganese and iron, and are depleted in magnesium. On the basis of these observations, the composition of these intermetallics could be given as  $(\text{Fe,Mn,Cu})_x\text{Si}(\text{Cu,Al})_y$ , whose crystal structure was identified by Gao *et al.* [40] to be rhombohedral. Many of them contain cracks (intermetallic  $\text{IMC}_2$  in Figure 4.8-a), probably resulting from the rolling process. This confirms that these large intermetallics precipitate during solidification and that they are insoluble during the solution heat treatment at  $495^\circ\text{C}$ . However, the formation of cracks can also be a result of the sample preparation procedure, i.e. grinding and polishing.

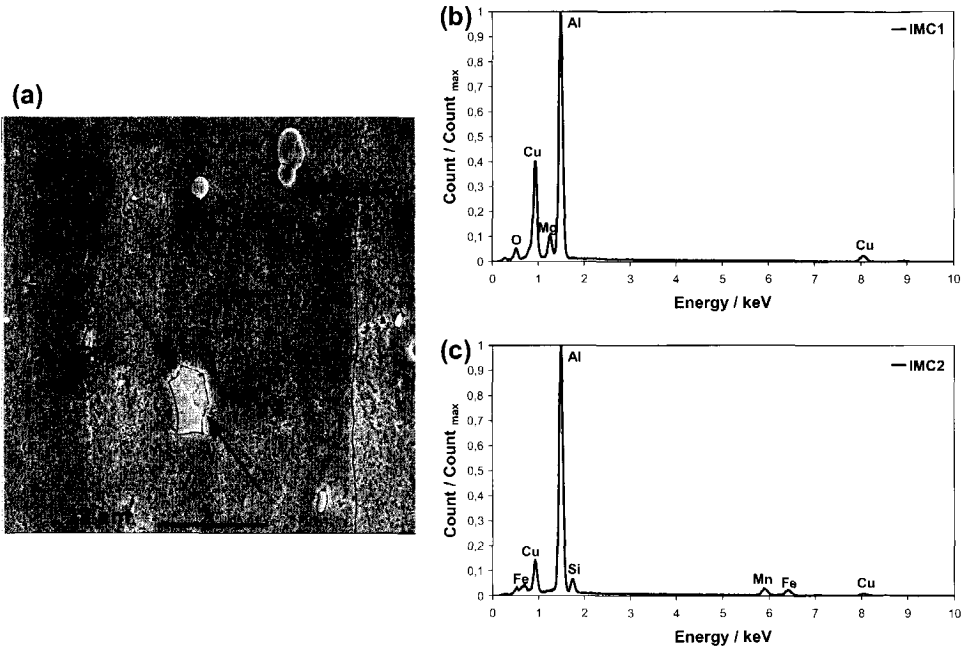


**Figure 4.8:** SEM micrograph (a) of sample 2 (quench delay time = 9 seconds) and EDS spectra of the intermetallics  $\text{IMC}_1$  (b) and  $\text{IMC}_2$  (c).

While the Al-Cu-Mn-Fe-Si large intermetallics are completely unaffected by the solution heat treatment, a coarsening of the Al-Cu-Mg ones takes place during the 55 minutes of heating at  $495^\circ\text{C}$  (intermetallic  $\text{IMC}_{1-A}$  in Figure 4.8-a). This effect of the solution treatment can be explained by the well known energetically favourable process of disappearance of the small particles in favour of the large ones [41]. This phenomenon is a diffusion-controlled process and becomes kinetically possible when the time spent at relative high temperature is long enough, as in the case of solution heat treatment. It was observed that increasing the quench delay time, especially from 3 to 27 seconds, results in a slight enhancement of the coarsening phenomenon. In addition to this, when the quench delay time is sufficiently long another inhomogeneous phase forms in the 2024 aluminium alloy.

Indeed, in samples 5 to 8 the SEM and EDS study shows the presence of “shell-like” particles, which are irregular in shape and present differences in contrast between the bulk and the surface, as can be clearly seen in the SEM micrograph of Figure 4.9-a relative to sample 6, as an example (intermetallic named  $\text{IMC}_3$ ).

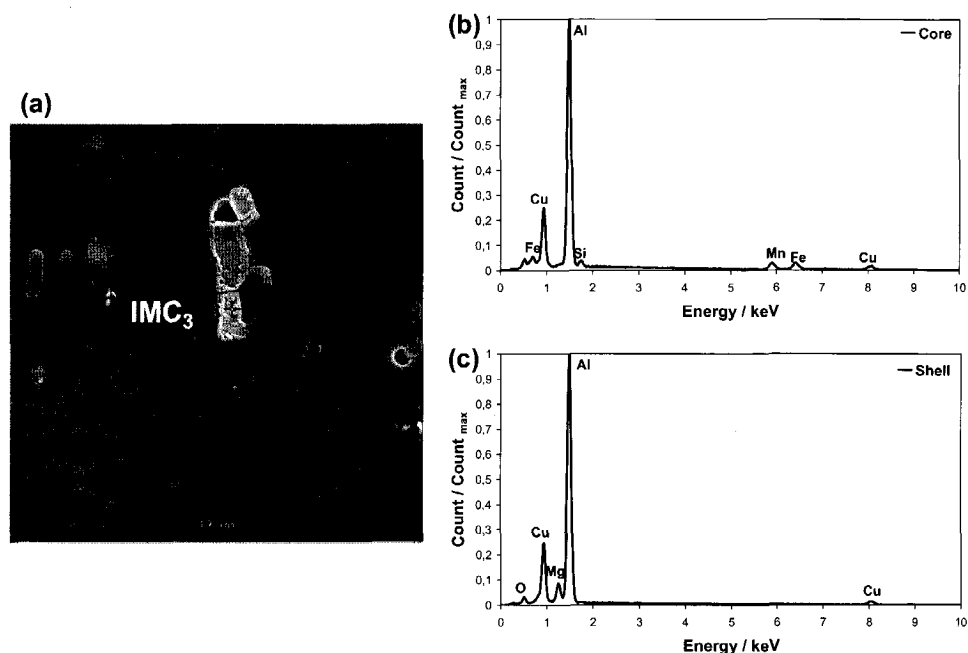


**Figure 4.9:** SEM micrograph (a) of sample 6 (quench delay time = 81 seconds) and EDS spectra of the core (b) and the shell (c) of intermetallic  $\text{IMC}_3$ .

The EDS spectra (Figures 4.9-b and -c) prove that the core and the shell of these intermetallic particles are characterized by a different chemical composition that most likely causes a different reactivity towards the Keller's etching. The EDS analyses show that the core of the shell-shaped intermetallics contains the same elements as the Al-Cu-Mn-Fe-Si large intermetallics, whereas the shell contains mainly Cu, Mg, and Al.

Going from sample 5 to 8, i.e. increasing the quench delay time, an increase in the number of the shell-shaped particles has been noted in parallel with a decreasing amount of the Al-Cu-Mn-Fe-Si intermetallics ( $\text{IMC}_2$ ). The two phenomena are related. It is believed that the original  $\text{IMC}_2$  intermetallics constitute the core of the shell-shaped particles, since they are both irregular in shape and have the same chemical composition, and that magnesium and copper, supplied by the dissolution of small Al-Cu-Mg particles during the solution treatment, segregate and/or precipitate on the surface of these intermetallics leading to the formation of the Cu-Mg-rich shell during the cooling from the solution temperature ( $495^\circ\text{C}$ ). To understand the reason why Mg and Cu segregation occurs only at quench delay times longer than 50 seconds and increases with increasing  $t_{\text{qd}}$ , it is necessary to consider the relation between this parameter and the cooling rate. Figure 4.10 shows the cooling curves

from the solution treatment to room temperature (495°C and 25°C, respectively) in the two extreme cases of water quench and air cooling. These temperature profiles are calculated using the lumped parameter model, which considers a block of material initially at a uniform temperature  $T_0$  placed in an environment of temperature  $T_\infty$  where it is cooling with a convection heat transfer  $h$  [42]. In addition, the simplified model assumes that the temperature variation in the block is negligible in comparison with the temperature difference between the block and the environment, which is reasonable in the case of high thermal conductive materials as aluminium. This leads to the following temperature/time relation:

$$T(t) = T_\infty + (T_0 - T_\infty) \exp\left[-(hA/\rho C_p V)t\right] \quad (4.m)$$

where  $A$ ,  $V$ ,  $\rho$ ,  $C_p$  are the surface area, volume, density, and thermal capacity, respectively, of the block.

The much higher convection heat transfer for water in comparison with air results in an extremely higher cooling rate in the former medium (Figure 4.10). Thus, the increase of the quench delay time decreases the cooling rate (Figure 4.11), which in turn strongly affects any segregation and precipitation process. Indeed, the rate of either segregation or precipitation depends on

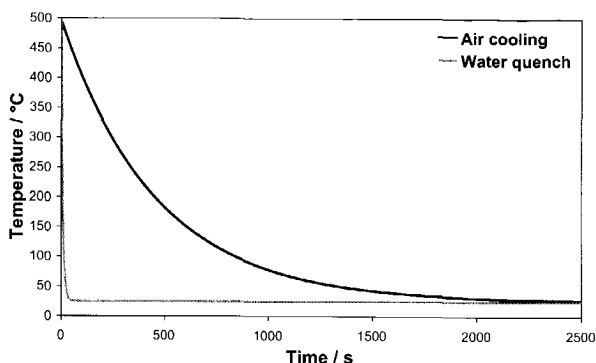


**Figure 4.10:** Cooling curves in air and water calculated using the simplified lumped parameter model.

one hand on the diffusion rate of the elements in the aluminium matrix, which is directly proportional to the temperature, and on the other hand on the driving force for segregation or

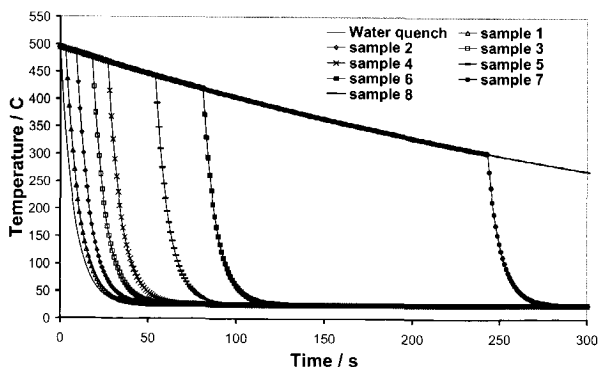


**Figure 4.11:** Cooling curves for all the samples calculated using the simplified lumped parameter model.

precipitation, which increases with increasing undercooling from the solvus temperature and then is inversely proportional to the temperature [35].

Based on this, it can be concluded that for short quench delay times the segregation or precipitation of Cu and Mg does not occur due to the limited undercooling reached during the hold in air

(25°C for  $t_{qd} = 27$  seconds, as can be calculated from equation 4.m). This results in a negligible segregation and

precipitation rate (Figure 4.12). Whereas, when the quench delay time is increased the temperature of the sample during the air cooling falls in a range where the rate of diffusion is still appreciable and the undercooling is high enough ( $52^{\circ}\text{C}$  and  $193^{\circ}\text{C}$  for  $t_{\text{qd}} = 54$  and  $243$  seconds, respectively) to enable a quite fast segregation and precipitation, especially at high energy defects that are preferential nucleation sites. The interface between the aluminium matrix and incoherent intermetallics, such as the large Al-Cu-Mn-Fe-Si particles, is one of the most favourable nucleation sites, since its energy is lower only than that of free surfaces. This explains the fact that when segregation and/or precipitation of Cu and Mg can occur, they occur on the surface of the Al-Cu-Mn-Fe-Si intermetallics leading to the formation of the shell-shaped particles (Figure 4.12).

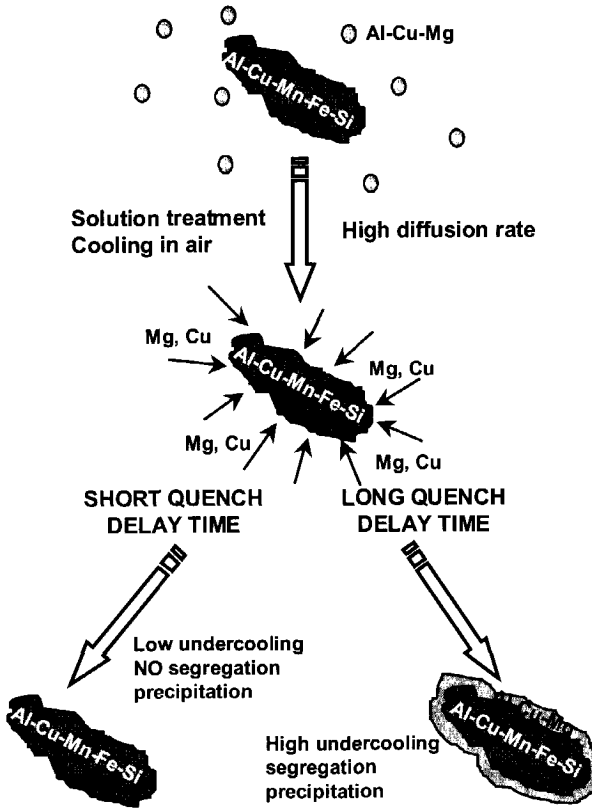


**Figure 4.12:** Scheme of the diffusion/segregation/precipitation processes during air cooling.

This is most probably related to the faster diffusion in aluminium of Mg in comparison with Cu [44]. Indeed, intermediate quench delay times (between 54 and 81 seconds) already enable the complete segregation and/or precipitation of magnesium upon the Al-Cu-Mn-Fe-Si intermetallics but only a partial segregation and/or precipitation of copper, whose extent increases with the length of the quench delay time.

This is consistent with the results obtained by other authors [43], who found that the Al-Fe-Cu-Mn phases in 7075 aluminium alloy act as heterogeneous nucleation sites for the  $\text{Al}_7\text{Cu}_2\text{Fe}$  phase. Obviously, the diffusion and preferential segregation or precipitation of Cu and Mg on the  $\text{IMC}_2$  intermetallics are enhanced by the further increase of quench delay time and reach a maximum in the air cooled sample (sample 8).

It was observed that increasing  $t_{\text{qd}}$  from 54 seconds to more than 800 seconds (air cooling) results not only in a larger number of shell-shaped intermetallics but also in a higher amount of copper in the shell. In contrast, the amount of magnesium in the shell is not affected by the time spent in air before water quench.



The electrochemical nature of both the Al-Cu-Mg and Al-Cu-Mn-Fe-Si intermetallics, which are present in all the samples, and the shell-shaped particles, which are formed only in the samples treated with a long quench delay time, has been investigated with the AFM in the Kelvin probe mode (SKPFM). Figure 4.13 shows the topographic image (a) together with the Volta potential map (b) obtained simultaneously on the surface of sample 1, as an example. From the topographic image it can be noted that even after ultrasonic cleaning with ethanol some contamination is still left on the surface. However, these particles are not visible on the potential map and therefore their effect on the measured potential is negligible. In addition, some areas, named IMC<sub>1</sub> and IMC<sub>2</sub>, can be observed to protrude slightly from the surface. These areas are associated with large intermetallic particles, which are harder than the Al matrix and therefore have a lower rate of polishing, and are clearly distinguished also in the potential map as bright areas, i.e. regions with a more noble Volta potential.

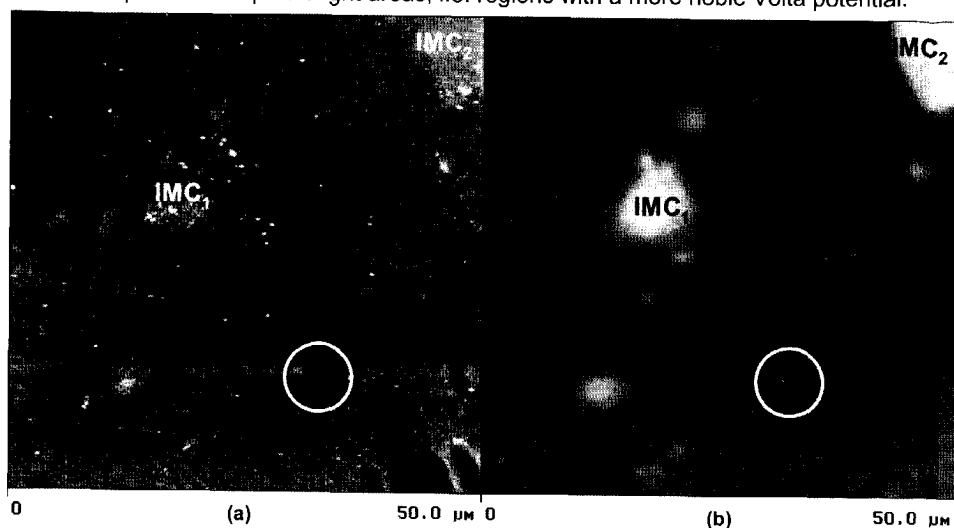


**Figure 4.13:** Topographic image with a height range of  $0.3 \mu\text{m}$  (a) and Volta potential map with a potential range of  $0.8 \text{ V}$  (b) of sample 1 (quench delay time = 3 seconds)

Besides, some smaller intermetallic particles can be identified on the surface only by the contrast in the potential image. This shows that the potential distribution measured with the SKPFM enables a clear characterization of the location of the intermetallics on a polished surface and of their electrochemical nature, i.e. anodic or cathodic, with respect to the surrounding Al matrix. From the images of Figure 4.13 two remarks concerning the limitations of the SKPFM technique discussed in section 4.2 can be made. One is the lower contrast, i.e. lower nobility, shown by the smaller intermetallic particles. Although this could be a real variation in the Volta potential value of different IMCs due to changes in their chemical composition, it is more probable that this "size effect" is related to the averaging of the Volta potential value associated with long-range tip/sample interactions (equation 4.k), which is negligible only for regions much larger than the tip size and therefore becomes important in the case of small intermetallics. The second remark concerns the influence of the topographic features on the potential map. Indeed, it can be noted that the deep hole

present on the polished surface (the area inside the circle on Figure 4.13-a) corresponds to an anodic area in the Volta potential map (circle in Figure 4.13-b). It is likely that this anodic region is an artefact introduced by the large change in height on the surface at its location rather than a real potential gradient. Therefore, in order to correctly interpret the Volta potential map obtained with the SKPFM technique it is always necessary to compare it with the topographic image. Nevertheless, Figure 4.13 shows also that once these limitations are kept in mind, the SKPFM is a very useful technique for the investigation of the local electrochemistry at the surface of aluminium alloys.

The potential profile along the black line on the potential surface scan (Figure 4.14-a), named "section analysis" (Figure 4.14-b), shows that both types of intermetallic typical of AA2024, i.e. Al-Cu-Mg (named IMC<sub>1</sub>) and Al-Cu-Mn-Fe-Si (named IMC<sub>2</sub>), are about 200 mV more noble with respect to the aluminium matrix, indicated with the letter M. The cathodic nature shown by these intermetallic particles is in agreement with the results reported by Schumtz and Frankel [20, 21].

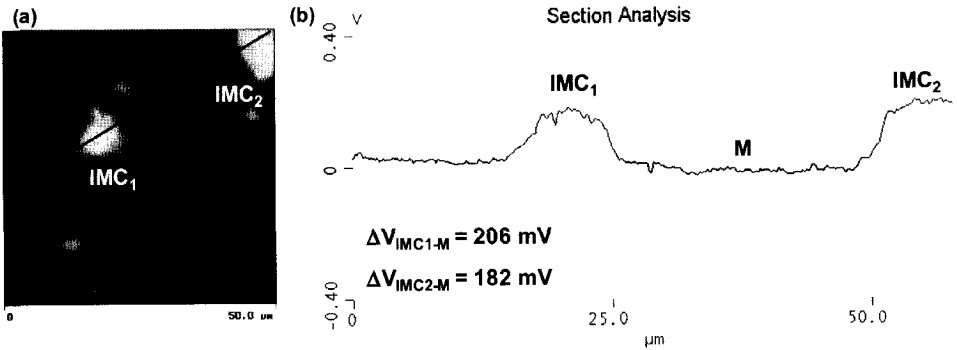


**Figure 4.14:** Volta potential map with a potential range of 0.8 V (a) and section analysis along the black line in the potential map (b) of sample 1 (quench delay time = 3 seconds).

In fact, several intermetallics have been characterized in this way and it was found that in all cases the Al-Cu-Mg and the Al-Cu-Mn-Fe-Si intermetallics show Volta potential values, which vary from 150 mV up to 300 mV more noble in comparison with the Al matrix. It should be noted that changes in the properties of the tip couldn't be the cause of this variation in the measured galvanic coupling, since it is not an absolute potential value but a relative difference between areas of the same sample. The range of galvanic coupling values can be attributed to small variations in chemical composition, below the limit of resolution of the EDS technique, among the intermetallics of the same group. However, it cannot be excluded that other parameters, such as thickness and composition of the oxide film, or the "size effect" described above, are partially responsible for this range in the Volta potential of the intermetallics of the same type. On the other hand, the length of the quench delay time does not have any effect on the Volta potential range for both types of intermetallic particles, in accordance with the absence of an evident modification of their chemical composition during the heat treatment.

As discussed in section 2.3.1 of chapter 2, while the cathodic nature of the Al-Cu-Mn-Fe-Si intermetallics is in good agreement with the corrosion potential value measured for a bulk precipitate in chloride solution, the more noble Volta potential shown by the Al-Cu-Mg intermetallics with respect to the surrounding matrix is rather surprising, since the corrosion potential of a bulk Al-Cu-Mg sample in solution has been found to be 300-400 mV lower than that of AA2024 [45]. It is believed that the cathodic Volta potential measured by the SKPFM in air for these intermetallics results from the formation of a compact surface layer enriched in copper, which is most probably a result of the polishing process (refer to section 2.3.1 of chapter 2 for a detailed explanation).

The main effect of the quench delay time on the Volta potential of the AA2024 surface is related to the formation of the shell-shaped particles. Indeed, the differences in chemical composition between the core and the shell of these intermetallics may also be expected to give rise to differences in the surface potential. This is confirmed by the SKPFM investigation carried out on the samples with quench delay time longer than 50 seconds (samples 5 to 8). Figure 4.15-a shows a Volta potential map of AA2024 treated with a quench delay time of 81 seconds, as an example, where very large intermetallic particles, up to 30  $\mu\text{m}$  (particle  $\text{IMC}_3^*$ ), can be observed. A gradient in Volta potential is present not only between the intermetallics and the Al matrix, but even between different areas of the same intermetallic. An enlargement of a topographic image (Figure 4.16) of these large intermetallics characterized by a very inhomogeneous surface potential shows that they consist of the shell-shaped particles observed with the scanning electron microscope.

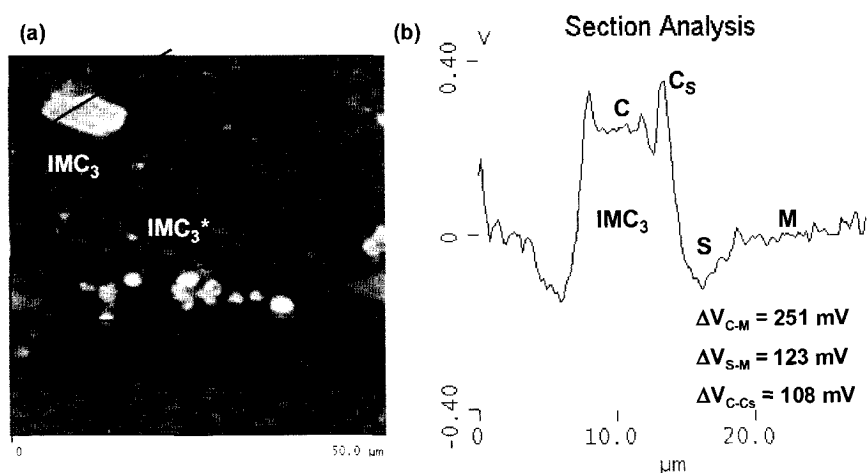


**Figure 4.15:** Volta potential map with a potential range of 0.8 V (a) and section analysis along the black line in the potential map (b) of sample 6 (quench delay time = 81 seconds).

The inhomogeneity of the Volta potential of these intermetallics becomes clearer when a section analysis is performed (Figure 4.15-b). The potential profile of the intermetallic labelled  $\text{IMC}_3$  in the potential map (Figure 4.15-a) shows the presence of two distinct regions: a central area (C) being cathodic with respect to the Al matrix (M) and an external

area (S) being anodic with respect to both the central area and the matrix. The more noble central region represents the core of the shell-shaped intermetallic, whose Volta potential difference with the matrix is found to range between 200 and 300 mV. The similarity of this Volta potential with that measured for the Al-Cu-Mn-Fe-Si intermetallics is a further confirmation that they form the core of the shell-shaped intermetallics. By extension of this argument the anodic external region could be associated with the copper and magnesium-rich shell of the shell-shaped IMCs.

This seems to be in contradiction with the cathodic nature observed for the Al-Cu-Mg intermetallics. However, it is necessary to keep in mind the extremely complex electrochemical behaviour of such phases, which can change from cathodic to anodic and back to cathodic depending on the stability of the copper-rich surface film (see section 2.3.1 of chapter 2). Therefore, it can be expected that the Al-Cu-Mg phase formed on the surface of the Al-Cu-Mn-Fe-Si intermetallics during the cooling from the solution temperature behaves differently than the Al-Cu-Mg intermetallics formed during solidification.

On the other hand, the anodic region could also be a result of the depletion in copper in solid solution in the matrix in proximity of the shell-shaped intermetallics occurring during the segregation and/or precipitation process on the Al-Cu-Mn-Fe-Si IMCs. In this case, the most noble region named  $C_s$  in the section analysis is likely to be the shell of the shell-shaped intermetallics.

However, even if the results do not give a definitive answer on the cause of the anodic external region observed around the cathodic intermetallics of the samples treated with a long quench delay time, they do show that on the surface of these samples the shell-shaped intermetallics lead to extremely severe and localized galvanic couples. Indeed, the difference in Volta potential between the core and the external region of these intermetallics varies from 400 to 500 mV, which is higher than that observed between the Al matrix and either the Al-Cu-Mn-Fe-Si or Al-Cu-Mg intermetallics (150-300 mV).

In conclusion, the SEM, EDS, and SKPFM investigation have shown that the main effect of the increase of the quench delay time, i.e. decrease in cooling rate after solution treatment, on the microstructure of AA2024 consists of the formation of shell-shaped intermetallics characterized by an inhomogeneous chemical composition and Volta potential. The role played by these intermetallics on the corrosion behaviour of AA2024 is discussed in the next section.

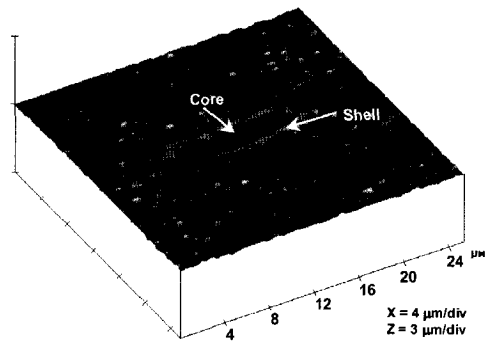


**Figure 4.16:** 3D topographic image of a shell-shaped intermetallic on the surface of sample 6 (quench delay time = 81 seconds).

#### 4.4.2 Electrochemical investigation

After anodic pretreatment, the evolution of the open circuit potential (OCP) during immersion in NaCl solution is characterized by an initial decrease from approximately  $-0.75$  V to  $-0.85$  V followed by a slower increase up to a value of  $-0.8$  V, which is reached after 4-5 hours and which subsequently remains constant until the end of the monitoring (Figure 4.17). This behaviour is independent on the length of the quench delay time. Since the measurement is carried out in de-aerated electrolyte, it is expected that the OCP value will be mainly determined by variation of the anodic current ( $I_a$ ).

This is valid only if the total real anodic and cathodic areas do not substantially change during the measurement. Although this cannot be proven it is a reasonable assumption and therefore, the initial drop in OCP is most probably due to the dissolution of the natural aluminium oxide film, which results in an initial increase of  $I_a$ . During exposure to the chloride solution the oxide film partially reforms and leads to a decrease of  $I_a$  and consequent increase in OCP. The dissolution of the natural oxide film starts already during the first few seconds of application of the anodic potential, which explains the initial relatively low value of OCP for AA2024 ( $-0.75$  V) that in general shows OCP around  $-0.6$  V.

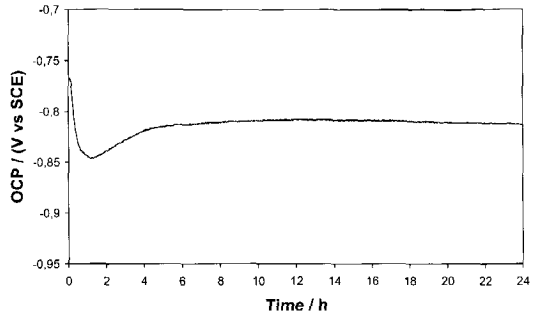


**Figure 4.17:** OCP monitoring in 3.5% NaCl pH=4 electrolyte, after the anodic pretreatment, for sample 2 (quench delay time = 9 seconds).

In addition, the quench delay time has no effect on the behaviour of the alloy during the polarization measurement of experiment 1. Indeed, all the samples show an activation of the OCP from about  $-0.8$  V to about  $-0.95$  V during the initial polarization in the cathodic branch together with a relatively large passivation range in the anodic branch of the polarization curve characterized by a current density ranging between 10 and 20  $\mu\text{A}/\text{cm}^2$  (polarization curves of Figure 4.18). It should be noted that these values are relative to the current density calculated using the geometric area of the sample and not the real area of the surface involved in the corrosion process, which is unknown. The breakdown or pitting potential, i.e. the potential at which a sudden

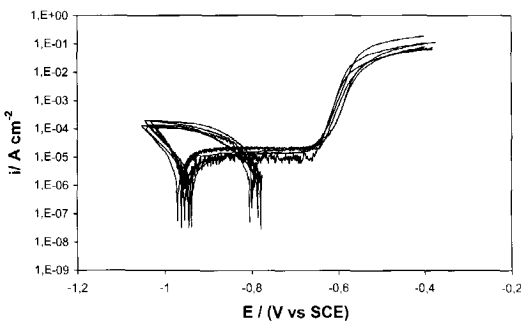


**Figure 4.18:** Potentiodynamic measurements of experiment 1 for all the samples.

which is unknown. The breakdown or pitting potential, i.e. the potential at which a sudden

increase of the current density occurs, varies for the different samples in a quite narrow range without a systematic dependency on the length of the quench delay time. However, this is apparently in contradiction with the results of the optical microscopy investigation, which was conducted on the sample surfaces at the end of the potentiodynamic measurement of experiment 1. Indeed, the micrographs of the cross sections of exposed surfaces show a change in the type of corrosion with increasing quench delay time. After anodic pretreatment, 24 hours of OCP monitoring, and cathodic and anodic polarizations (experiment 1), while samples 1 to 4 show mainly general corrosion with a few isolated small pits (Figure 4.19-a and -b), samples 5 and 6 are characterized by pitting corrosion over the entire exposed surface. This becomes more severe increasing the quench delay time from 54 to 81 seconds, i.e. going from sample 5 to 6 (Figure 4.19-c). Finally, samples 7 and 8 show the presence of some pitting but mainly exfoliation corrosion, which is typical for rolled aluminium alloys that have undergone an unsuitable heat treatment (Figure 4.19-d).

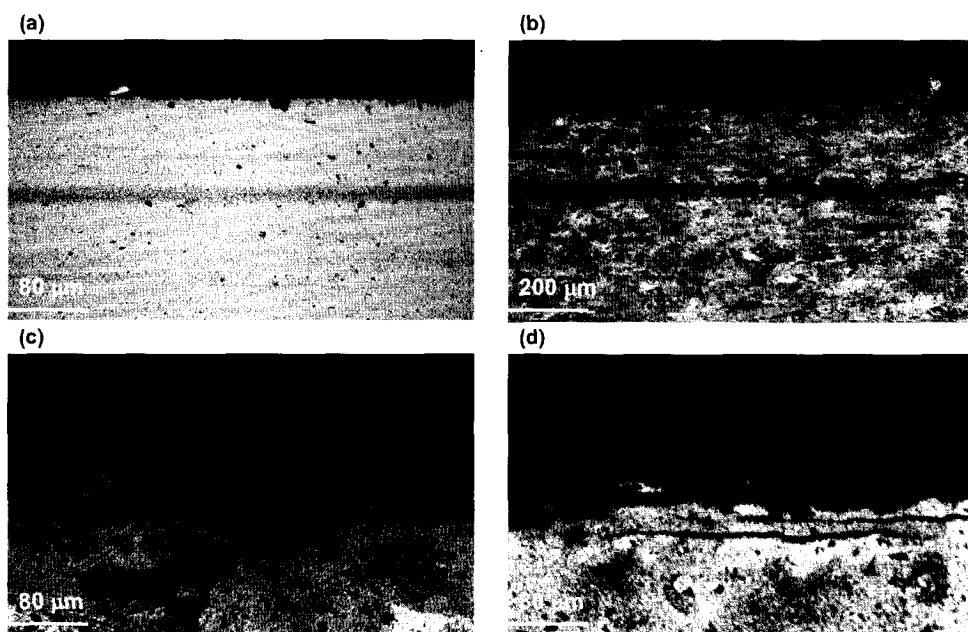


**Figure 4.19:** Optical micrographs of the cross section of the surface at the end of experiment 1: (a) sample 2 (quench delay time = 9 seconds); (b) sample 4 (quench delay time = 27 seconds); (c) sample 6 (quench delay time = 81 seconds); (d) sample 7 (quench delay time = 243 seconds).

In order to clarify this apparent contradiction between the similar electrochemical measurement results and the different aspects of the corroded surfaces, another type of potentiodynamic measurement (experiment 2) was carried out to investigate the capability of the alloy to repair its natural oxide layer once attacked, i.e. to repassivate. An indication of this capability may be obtained by the estimation of the repassivation range ( $\Delta E_{rep}$ ), which can be measured when a backward anodic scan is performed during the polarization curve (polarization curve of Figure 4.6). The increase of the quench delay time results in a

decrease of the value of the parameter  $\Delta E_{\text{rep}}$ , which indicates a worsening of the repassivation behaviour of AA2024 (Figure 4.20). This is in agreement with the more severe and localized type of attack occurring in the samples treated with a long quench delay time. All types of intermetallics, either the shell-shaped present only in the samples 5 to 8 or the Al-Cu-Mg and Al-Cu-Mn-Fe-Si present in all the samples, act as preferential nucleation sites for pitting. It is well known that the presence of intermetallic particles on the surface of aluminium alloys causes differences in the electrical resistivity, chemical composition, thickness, and porosity of the aluminium oxide film, either natural [46] or anodically grown [47].

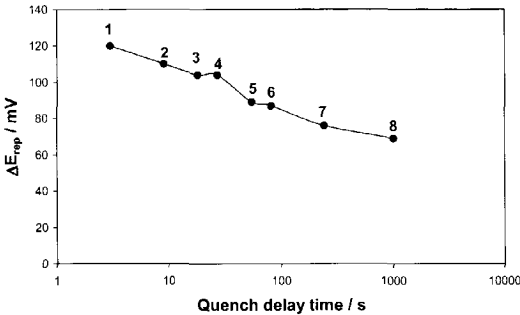


**Figure 4.20:** Repassivation range ( $\Delta E_{\text{rep}}$ ) as function of the quench delay time (numbers are relative to the samples).

4.21-a, -b, -d, -e), however differences in intermetallic type may lead to different results. In the samples treated with long quench delay time, when a pit nucleates in correspondence of a shell-shaped particle, the driving force for corrosion to continue is very high due to the presence of a severe galvanic coupling between the core and the shell or the periphery of the intermetallic, 400-500 mV as shown by the SKPFM investigation. Therefore, the pit grows rapidly leading to the drop out of the intermetallic itself and the alloy is not able to repair its oxide layer (Figure 4.21-f). Then, during the growth of the pit other shell-shaped particles may come into contact with the solution resulting in a further acceleration of the pitting attack. This may explain the worsening of the repassivation behaviour and the presence of deep pits in the samples that contain the shell-shaped particles. In contrast, in samples 1 to 4 when a pit nucleates in the proximity of the Al-Cu-Mn-Fe-Si or of the Al-Cu-Mg intermetallics the galvanic coupling is less severe, 150-300 mV, this means that a lower driving force for the localized corrosion attack exists. As a consequence, the alloy is more likely able to repair the oxide layer before the growth of the pit proceeds (Figure 4.21-c) and as a result other locations on the surface become sites for the nucleation of pits, which are unlikely to grow. This results in a more general type of attack with few isolated pits.

The similarity in behaviour shown by all the samples during the polarization of experiment 1 is not necessarily in contradiction with the different repassivation behaviour and type of attack. In fact, the absence of differences in the polarization curves may be a

Generally, the natural oxide film above the intermetallic particles has a higher conductivity, a higher amount of flaws and therefore a higher permeability to aggressive ions, such as chloride, than that formed above the Al matrix. Therefore, the aluminium oxide film preferentially breaks down in proximity of the intermetallics and pits nucleate at these locations.

This occurs in all the samples under investigation regardless of the type of intermetallics present (Figures

result of the fact that a considerable extent of the corrosion attack has already taken place during the potentiostatic anodic pretreatment and OCP monitoring. It is probable that if the polarization measurement had been carried out immediately after immersion in the aggressive solution the samples characterized by different microstructure would have shown some differences. Although this is likely to be the case, it is important to note that the current density reported in the polarization curves is obtained by dividing the measured current by the geometrical area of the working electrode. This gives a correct value only in the case of general corrosion, since when the attack is localized the area involved in the corrosion process is much smaller and unknown.

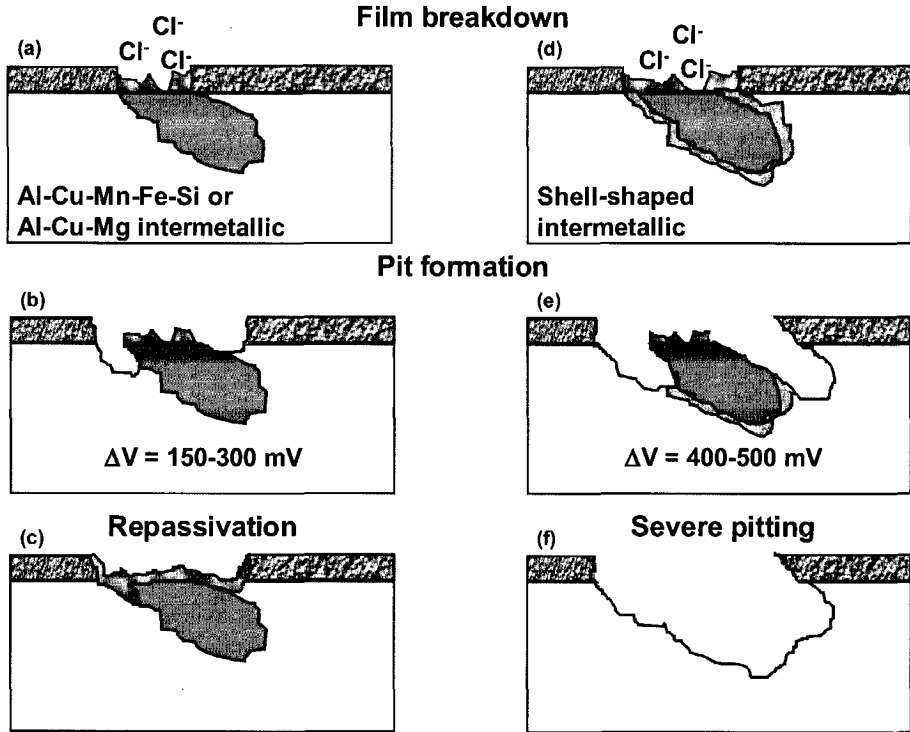


**Figure 4.21:** Schematic illustration of the pitting initiation in proximity of the intermetallic particles on the surface of AA2024 that results in different corrosion attack depending on the galvanic coupling generated by the intermetallic with the aluminium matrix.

Therefore, the comparison of the current densities of samples that undergo different types of attack can lead to misleading results and wrong conclusions. In addition, it is believed that the pitting or breakdown potential is inadequate for describing the pitting susceptibility of aluminium alloys with complex microstructure, such as that of AA2024. Indeed, the breakdown of the natural oxide layer occurs similarly in all the samples, since they all contain intermetallic particles that are weak spots in the oxide film, but the corrosion attack continues in different ways and gives rise to different results depending on the electrochemical nature of the intermetallics, as discussed previously. Therefore, it seems that the extent of the galvanic coupling between IMCs and matrix is a determining factor in



the propagation of the localized attack but not in its initiation, which is primarily influenced by the oxide film properties. Based on these considerations, the adequacy of using macroscopic electrochemical techniques, involving areas in the order of a few square centimetres, to study local corrosion events at the intermetallics, involving areas in the order of a few micrometers, can be doubted. Recently, the development of capillary-based droplet cell [48] has enabled electrochemical measurements, as OCP monitoring and polarization curves, to be carried out at the micrometer range. The micro-electrochemical cell has been shown to be particularly useful in studying the mechanism of localized corrosion at single intermetallic particles on the Al surface [49]. It is believed that this technique would provide in the context of the current investigation, an additional insight into the role played by the extent of the galvanic coupling between the matrix and the different intermetallics on the pitting corrosion susceptibility of AA2024.

In summary, it can be stated that the formation of the shell-shaped intermetallics during cooling from the solution temperature at long quench delay times is responsible for the change of the corrosion attack from general to pitting, due to a more severe and localized galvanic coupling. However, the appearance of exfoliation corrosion in the sample treated with the longest quench delay time (sample 7) or cooled in air (sample 8) can not be associated with the shell-shaped particles, since a modification of their distribution, in particular a more pronounced clustering in bands parallel to the external surface, is not observed in these samples in comparison with samples 5 and 6, in which only severe pitting corrosion takes place. The exfoliation corrosion caused by a very low cooling rate, i.e. long quench delay time, is likely to arise as a consequence of very severe intergranular corrosion, which occurs mainly parallel to the external surface due to the elongated grain structure in rolled aluminium sheets and leads to the formation of large amount of corrosion products that in turn causes the separation of layers of material (Figure 4.19-d).

It is generally recognized that intergranular corrosion in AA2024 occurs as a consequence of the formation of a copper depleted zone adjacent to the grain boundaries due to the precipitation of small  $\theta$  ( $\text{Al}_2\text{Cu}$ ) and S phases ( $\text{Al}_2\text{CuMg}$ ) along the grain boundaries [50]. This Cu-depleted zone anodically dissolves during exposure to aggressive environments resulting in an intergranular attack. As explained in the previous section, when the quench delay time is relatively long segregation and precipitation processes are favoured because the temperature is still high enough to enable appreciable diffusion of the alloying elements, and simultaneously the undercooling is sufficient to create the driving force for the nucleation of new phases. The precipitation and /or segregation take place preferentially on high energy defects, as in order of increasing energy and nucleation rate, vacancies, dislocations, stacking faults, grain boundaries, interphase boundaries, and free surfaces [35]. Therefore, it may be expected that for intermediate quench delay times copper and magnesium precipitate and/or segregate mainly on the surface of the incoherent Al-Cu-Mn-Fe-Si intermetallics, resulting in the formation of the shell-shaped particles, and partially on the grain boundaries as  $\theta$  or S-phases. When the quench delay time is further increased additional heterogeneous precipitation occurs at the grain boundaries and the extent of the

copper depleted zone along the grain boundaries increases and gives rise to severe intergranular attack and consequent exfoliation.

Although experimental evidence of the increased grain boundary precipitation with the decrease of the cooling rate is not provided in this work, this suggestion is reasonable and supported by other works that showed both the necessity to use rapid quenches after solution treatment to prevent the formation of grain boundary precipitates and copper depleted zones in AA2024 [51] and that changes in grain boundary precipitates and precipitate free zones occurs as function of the quench rate for AA7075 [52]. In conclusion, while for samples 5 and 6 the corrosion behaviour is dominated by the formation of shell-shaped intermetallics, which cause severe pitting, for samples 7 and 8 the type of attack is likely determined by the formation of a copper depleted zone along the grain boundaries, which results in severe intergranular corrosion.

## 4.5 Conclusions

It was found that important changes take place in the microstructure of AA2024 when the time spent in air before water quench, i.e. quench delay time, exceeds a threshold value, in the order of a few tens of seconds, as can occur incidentally in industrial practice. Specifically, shell-shaped intermetallics, which are characterized by inhomogeneous chemical composition and Volta potential, form as a result of copper and magnesium segregation and/or precipitation on the surface of the original Al-Cu-Mn-Fe-Si IMCs. The main characteristic of this new intermetallic is a high difference in surface potential existing between its core, which is cathodic with respect to the aluminium matrix, and its periphery, which is in turn anodic in comparison with both the core of the particle and the Al matrix. This galvanic coupling associated with the shell-shaped intermetallics results to be more severe and localized than that caused by the Al-Cu-Mg and Al-Cu-Mn-Fe-Si intermetallic particles typical of AA2024, 400-500 mV and 150-300 mV, respectively. This plays a dominant role in the propagation of the local corrosion attack in the proximity of the intermetallics rather than in its nucleation, which is believed to be mainly affected by the properties of the natural aluminium oxide film. Indeed, samples treated with long quench delay times, which contain shell-shaped intermetallics, undergo severe and deep pitting attack, whereas samples treated with short quench delay times, which contain only Al-Cu-Mg and Al-Cu-Mn-Fe-Si intermetallics, show a general attack with a few small isolated pits. A further increase in quench delay time, to values in the order of 5-10 minutes, leads to a further evolution of the corrosion attack from pitting to exfoliation. This change is not associated with modifications in the distribution of the shell-shaped intermetallic particles, and is thought to be a result of extensive grain boundary precipitation with consequent formation of a copper depleted zone along the grain boundaries.

The results of this investigation have shown once more the importance of a careful control of the heat treatment procedure, in particular the cooling rate after the solution treatment, in order to avoid sudden and unexpected failure of aluminium products due to a severe localized attack. In addition, doubts arose concerning the use of macroscopic

electrochemical measurements to investigate localized type of corrosion associated with intermetallic particles, the area of which is of micrometer scale.

Finally, it has been shown that the AFM operating in the Kelvin probe mode (SKPFM) is a very useful and powerful technique in the study of the local electrochemical properties of aluminium surfaces. Indeed, the Volta potential map obtained with this technique in air provides information regarding the anodic or cathodic nature of intermetallic particles, some micrometers in size, which in turn plays a fundamental role in determining the local electrochemical behaviour of the Al alloy. It has been shown that the lateral resolution of SKPFM, which is of the order of tens of nanometers, enables the accurate measurement of the Volta potential not only of the intermetallic particles but also of different areas within the same particle. In this chapter such information has been used to correlate different types of corrosion attack with different extents of galvanic coupling between the intermetallics and the aluminium matrix. In the following chapters the same technique will be used to better understand the nucleation and growth mechanisms of conversion coatings on aluminium surfaces.

## 4.6 References

- [1] G.S. Chen, M. Gao, D.G. Harlow, R.P. Wei, *Proceedings of the FAA/NASA Int. Symp. Advanced Structural Integrity Methods for Airframe Durability and Damage Tolerance*, NASA Conf. Pub. 3,274, Hampton, VA (1994) 157
- [2] G.S. Chen, K.-C. Wan, M. Gao, R.P. Wei, T.H. Flournoy, *Mater. Sci. Eng.* A219 (1996) 126
- [3] Internal Fokker Aircraft report
- [4] G. Bennis, C.F. Quate, C. Gerber, *Phys. Rev. Lett.* 56 (1986) 930
- [5] R. Sonnenfeld, P.K. Hansma, *Science* 232 (1986) 211
- [6] R.M. Rynders, R.C. Alkire, *J. Electrochem. Soc.* 141 (1994) 1166
- [7] K. Kowal, L. Xie, R. Huq, G.C. Farrington, *J. Electrochem. Soc.* 141 (1994) 121
- [8] J. Josefowicz, J. DeLuccia, V. Agarwala, G.C. Farrington, *Mater. Charact.* 34 (1995) 73
- [9] J.H.W. de Wit, D.H. van der Weijde, A.J. de Jong, F. Blekkenhorst, S.D. Meijers, *Mater. Sci. Forum* 289-292 (1998) 69
- [10] M. Böhmisch, F. Burmeister, A. Rettenberger, J. Zimmermann, J. Boneberg, P. Leiderer, *J. Phys. Chem. B* 101 (1997) 10162
- [11] Y. Martin, D. Abraham, H. Wickramasinghe, *Appl. Phys. Lett.* 52 (1988) 1103
- [12] C. C. Williams, J. Slinkman, W.P. Hough, H. Wickramasinghe, *Appl. Phys. Lett.* 53 (1989) 1662
- [13] M. Nonnenmacher, M.P. O'Boyle, H. Wickramasinghe, *Appl. Phys. Lett.* 58 (1991) 2921
- [14] H.O. Jacobs, H.F. Knapp, S. Müller, A. Stemmer, *Ultramicroscopy*, 69 (1997) 39
- [15] L. Kelvin, G.F. Fitzgerald, L. Lassebatere, *Philos. Mag.* 46 (1898) 80
- [16] R. Aveyard, D.A. Haydon, *An introduction of Surface Chemistry*, Cambridge University Press, Cambridge, UK (1973)
- [17] H. Baumgärtner, H.D. Liess, *Rev. Sci. Instrum.* 59 (1988) 802
- [18] M. Stratmann, H. Streckel, *Corros. Sci.* 30 (1990) 681
- [19] S. Yee, R.A. Oriani, and M. Stratmann, *J. Electrochem. Soc.* 138 (1991) 55
- [20] P. Schmutz, G.S. Frankel, *J. Electrochem. Soc.* 145 (1998) 2285
- [21] P. Schmutz, G.S. Frankel, *J. Electrochem. Soc.* 145 (1998) 2295
- [22] V. Guillaumin, P. Schmutz, G.S. Frankel, *J. Electrochem. Soc.* 148 (2001) B163

- [23] *The CRC Handbook of Solid State Electrochemistry*, P.J. Gellings, H.J.M. Bouwmeester (eds.), CRC Press, Boca Raton (1997)
- [24] E.U. Condon, H. Odishaw, *Handbook of Physics*, 2<sup>nd</sup> Edition, McGraw-Hill, New York (1968)
- [25] H.N. McMurray, D.A. Worsley, *Research in Chemical Kinetics*, Vol. 4, R.G. Compton, G. Hancock (eds.), Blackwell Science, Oxford, UK (1997)
- [26] B. Bhushan, A.V. Golbade, *Wear* 244 (2000) 104
- [27] D. Sarid, *Scanning Force Microscopy with Application to Electric, Magnetic and Atomic Forces*, Oxford University Press, New York, USA (1994)
- [28] *Digital Instrument Support Note No. 201, Rev. C, User Manual version 1.5*, published by Digital Instrument (1993) 19
- [29] T. Trenkler *et al.*, *J. Vac. Sci. Technol. B* 18 (2000) 418
- [30] M. Nonnenmacher, M.P. O'Boyle, H.K. Wickramasinghe, *Appl. Phys. Lett.* 58 (1991) 2921
- [31] Ch. Sommerhalter, S. Sadewasser, Th. Glatzel, Th.W. Matthes, A. Jäger-Waldau, M.Ch. Lux-Steiner, *Surf. Sci.* 482-485 (2001) 1362
- [32] J.O.M. Bockris, A.K.N. Reddy, *Surface Electrochemistry-A Molecular Level Approach*, Plenum Press, New York, USA (1993)
- [33] H.O. Jacobs, H.F. Knapp, A. Stemmer, *Rev. Sci. Instrum.* 70 (1999) 1756
- [34] A. Efimov, S.R. Cohen, received from the authors
- [35] D.A. Porter, K.E. Easterling, *Phase Transformations in Metals and Alloys*, 2<sup>nd</sup> edition, Chapman & Hall, London, UK (1992)
- [36] R.G. Buchheit, R.P. Grant, P.F. Hlava, B. McKenzie, G.L. Zender, *J. Electrochem. Soc.* 144 (1997) 2621
- [37] V. Guillaumin, G. Mankowski, *Corros. Sci.* 41 (1999) 421
- [38] O. Schneider, G.O. Ilevbare, R.G. Kelly, J.R. Scully, *Proceedings of the Electrochemical Society Meeting: Corrosion and Corrosion Prevention of Low Density Metals and Alloys*, Phoenix, Arizona, US (2000) 87
- [39] L.F. Mondolfo, *Aluminium Alloys: Structure and Properties*, Butterworths, London, UK (1976)
- [40] M.Gao, C.R. Feng, R.P. Wei, *Metall. Mater. Trans. A* 29A (1998) 1145
- [41] R.E. Reed-Hill, *Physical Metallurgy Principles*, 2<sup>nd</sup> edition, Van Nostrand, New York (1973)
- [42] M. Becker, *Heat Transfer: A modern approach*, Plenum Press, New York (1986)
- [43] A.K. Mukhopadhyay, *Metall. Mater. Trans. A* 29A (1998) 979
- [44] *Smithells Metals Reference Book*, 7<sup>th</sup> edition, E.A. Brandes, G.B. Brook (eds.), Butterworth-Heinemann, Oxford (1992)
- [45] R.G. Buchheit, *J. Electrochem. Soc.* 142 (1995) 3994
- [46] J.R. Scully, T.O. Knight, R.G. Buchheit, D.E. Peebles, *Corros. Sci.* 35 (1993) 185
- [47] J. Sykes, G.E. Thompson, D. Mayo, P. Skeldon, *J. Mater. Sci.* 32 (1997) 4909
- [48] M.M Lohrengel, A. Moehring, M. Pilaski, *Electrochim. Acta* 47 (2001) 137
- [49] T. Suter, R.C. Alkire, *J. Electrochem. Soc.* 148 (2001) B36
- [50] H.P. Godard, W.B. Jepson, M.R Bothwell, R.L. Kane, *The Corrosion of Light Metals*, J. Wiley and Sons Inc., New York (1967)
- [51] B.W. Lifka, D.D. Sprowls, *Localized Corrosion-Cause of Metal Failure*, in: ASTM STP 516, ASTM, Philadelphia, PA, USA (1972) 120
- [52] W.G.J. 't Hart, H.J. Kolkman, L. Schra, *The Jominy end-quench Test for Investigation of Corrosion Properties and Microstructure of High Strength Aluminium Alloys*, NLR Technical Publication, TR 80102 U (1980)

# Microstructure and chromate conversion coating-Alclad 2024

## I. Characterization

### 5.1 Introduction

As discussed in chapter 3, since its introduction the chromate conversion coating (CCC) had provoked a strong scientific interest and had been extensively investigated. More recently, a renewed interest on the mechanisms of formation and corrosion protection of the chromate films has resulted from the necessity to find a replacement for these conversion processes, due to the health and environmental risk posed by the use of chromate solutions [1]. Indeed, a better understanding of the chromate corrosion inhibition is a prerequisite for the development and improvement of alternative chromium-free systems, as highlighted by a recent view of the aircraft coating technology [2]. In particular, in the last few years the investigation of the CCC on aluminium alloys has been focused on the influence of the substrate microstructure on the formation and final properties of the film. Controversial theories have been proposed concerning the role played by the intermetallic particles on the nucleation and growth of the chromate layer and their effect on the corrosion protection provided by the conversion film has not been considered in detail.

In this PhD project the effect of the substrate microstructure on the properties of the CCC has been studied following two different approaches. The first consisted of using different aluminium alloys, specifically Alclad 2024 and bare 2024. The former is discussed in this and the next chapter, whereas the latter in chapter 7. The other approach consisted of deliberately modifying the microstructure of the alloy by using different surface preparation procedures. In particular, the length of an acid pickling treatment and the immersion in a desmutting bath were considered. This approach was chosen also because of the lack in literature concerning the influence of the surface preparation routes before the immersion in the chromate bath on the formation and final properties of the CCC on aluminium alloys. Indeed, as far as we know, until now most of the published papers dealt with the formation and growth of the chromate film on samples without any pretreatment. However, it is believed that taking into account the effect of the surface preparation procedure is fundamental for a better understanding of the chromate coating system on aluminium surfaces of practical importance, which are usually pickled and/or desmutted before the immersion in the chromate bath.

In addition to the surface preparation procedure also the parameters of the chromate bath, i.e. temperature, pH, fluoride concentration, etc., play obviously a role in determining the thickness, morphology, composition and as a consequence the corrosion resistance of the converted aluminium surface. Goeminne [3] studied in detail the effect of the free fluoride activity in the chromate bath and showed that a layer grows only within a narrow range of  $[\text{NaF}]/[\text{HF}]$  ratio in the chromate based solution. The present work investigates the variations in the structure and chemical composition of the CCC formed on Alclad 2024 resulting from the change of the pH of the chromate bath. This additional variable was considered in order to further study the relation between the morphological properties of the chromate film and the corrosion protection provided to the aluminium substrate, which was suggested during the investigation of the effect of the alloy microstructure on the morphology and the corrosion resistance of the chromate layer.

This and the next chapter focus on the formation and the corrosion protection mechanisms, respectively, of the chromate film deposited on Alclad 2024 aluminium alloy. The choice of this alloy is based on the fact that it is often used in the aircraft industry due to its high strength and good corrosion resistance, which however in most cases needs to be improved by a chromate conversion coating process. Indeed, as discussed in chapters 2 and 4 based on the literature and our own results, respectively, the process of alloying for improving the strength properties of aluminium heavily compromises the corrosion properties of the metal, due to the formation of intermetallic particles that generate galvanic couples with the Al matrix. In order to obtain the best combination of strength and corrosion performance Alclad aluminium alloys are often used. These alloys are a duplex system, in which a thin surface layer (5-10% of the total thickness) of aluminium is metallurgically bonded to the main core alloy on either one or both sides [4]. The cladding layer is selected to be at least 100 mV anodic to the core providing in this way a built-in cathodic protection. A typical Alclad system consists of an alloy of the 1xxx family as surface layer coupled with an alloy of the 2xxx series as core. Amongst them Alclad 2024 aluminium alloy is the most used, especially for aircraft applications.

In order to correlate both the microstructure and the process parameters with the morphology and the chemical composition of the chromate film various surface analysis techniques have been used and are presented in the following section. In section 5.3, the description and discussion of the results is divided into four main parts. The first deals with the changes of the alloy microstructure caused by the surface preparation procedure, while the second correlates these changes with the nucleation and growth mechanisms of the CCC on the Al surface. The third and fourth parts focus on the changes in the chromate film morphology and composition caused by the modifications in the substrate microstructure and by the variations of the solution pH, respectively.

## 5.2 Experimental procedure

This section describes the materials, surface treatments, and surface analysis techniques used in this part of the work.

### 5.2.1 Materials and treatments

An Alclad 2024-T3 aluminium alloy in rolled sheet form, 1.2 mm thick, was used as substrate material. The clad layer present on both sides, 60-80  $\mu\text{m}$  thick, consisted of 1230 aluminium alloy, the composition of which in weight percent is as follows: Al 99.3%, Si+Fe 0.7%, Cu 0.1%, Mn 0.05%, Mg 0.05%. The substrate is referred hereafter to as Alclad 2024 alloy. The different processes investigated in the present study are summarized in Figure 5.1. The standard chromate treatment was carried out by means of dipping in a commercial Alodine 1200 solution at  $\text{pH}=1.8$  and  $25^\circ\text{C}$  for 180 seconds. The Alodine bath consisted of 3.2 g/l of a mixture reported to be [5] 50-60%  $\text{CrO}_3$ , 20-30%  $\text{KBF}_4$ , 10-15%  $\text{K}_3\text{Fe}(\text{CN})_6$ , 5-10  $\text{K}_2\text{ZrF}_6$ , 5-10%  $\text{NaF}$  by weight, which corresponds approximately to 0.023M in Cr. In addition to the standard chromate process, other treatments were used, in which some parameters were varied from their standard value. In particular, in order to investigate the nucleation and growth of the conversion film shorter times of the conversion treatment were used: 3, 15, 27, and 81 seconds. Whereas to study the effect of the acidity of the bath on the CCC morphology, the pH was adjusted to either lower, i.e. 1.2 and 1.4, or higher, i.e. 2.2 and 2.4, values than the standard one by addition of NaOH. All the chromate processes were ended with a final drying step in an oven at  $50^\circ\text{C}$  for 1 hour. The value of the open circuit potential (OCP) was monitored and recorded during the immersion in the chromate bath. The reproducibility of the evolution of this parameter with the immersion time was checked by repeating each chromate treatment on three different panels.

Prior to immersion in the chromate bath the Alclad 2024 alloy surface was activated following different routes:

- ✓ **NP:** ultrasonic cleaning in acetone for 10 minutes, acid pickling for 5 minutes at  $60^\circ\text{C}$  in a phosphoric-sulfuric acid solution:  $10 \text{ g/dm}^3 \text{ H}_2\text{SO}_4$  (95-98%) +  $20 \text{ g/dm}^3 \text{ H}_3\text{PO}_4$  (85%) +  $0.5 \text{ g/dm}^3$  Tensagex. Samples obtained from panels that underwent this procedure are named NP, and after the standard chromate treatment ( $\text{pH}=1.8$ , 180 seconds) NPCr1.8 (Figure 5.1). The NP samples were chromated also for shorter times than the standard one, in this case the duration of the immersion in the chromate bath will be stated in the text.
- ✓ **NPD:** same procedure of NP but an additional step was carried out after the immersion in the sulfuric-phosphoric acid bath. It consisted of immersion for 30 seconds at  $25^\circ\text{C}$  in a nitric hydrofluoric acid solution (1:1  $\text{HNO}_3$ (65%)/water + 10 ml/l HF), which is normally used after an alkaline cleaning process to remove the smut left on the surface [6]. Therefore, this treatment is hereafter referred to as desmutting although in the present study its function was not the removal of oxide deposits, i.e. smut, from the Alclad 2024 surface. This nomenclature was chosen also in view of the fact that in the case of bare 2024 the acid pickling step did lead to the formation on the surface of a smut, in contrast with the usual belief that only alkaline solutions cause this phenomenon. More details will be given in chapter 7 that focuses on the formation of the CCC on bare 2024. Samples obtained from panels that underwent this procedure are named NPD, and after the standard chromate treatment ( $\text{pH}=1.8$ , 180 seconds) NPDCr1.8. The NPD samples were also chromated using different pH of the bath and are named: NPDCr1.2, NPDCr1.4,

NPDCr2.2, NPDCr2.4, where the number indicates the pH used. In addition, similar to the NP samples the NPD ones were dipped in the chromate bath for shorter times than the standard one, in this case the duration of the immersion in the chromate bath will be stated in the text (Figure 5.1).

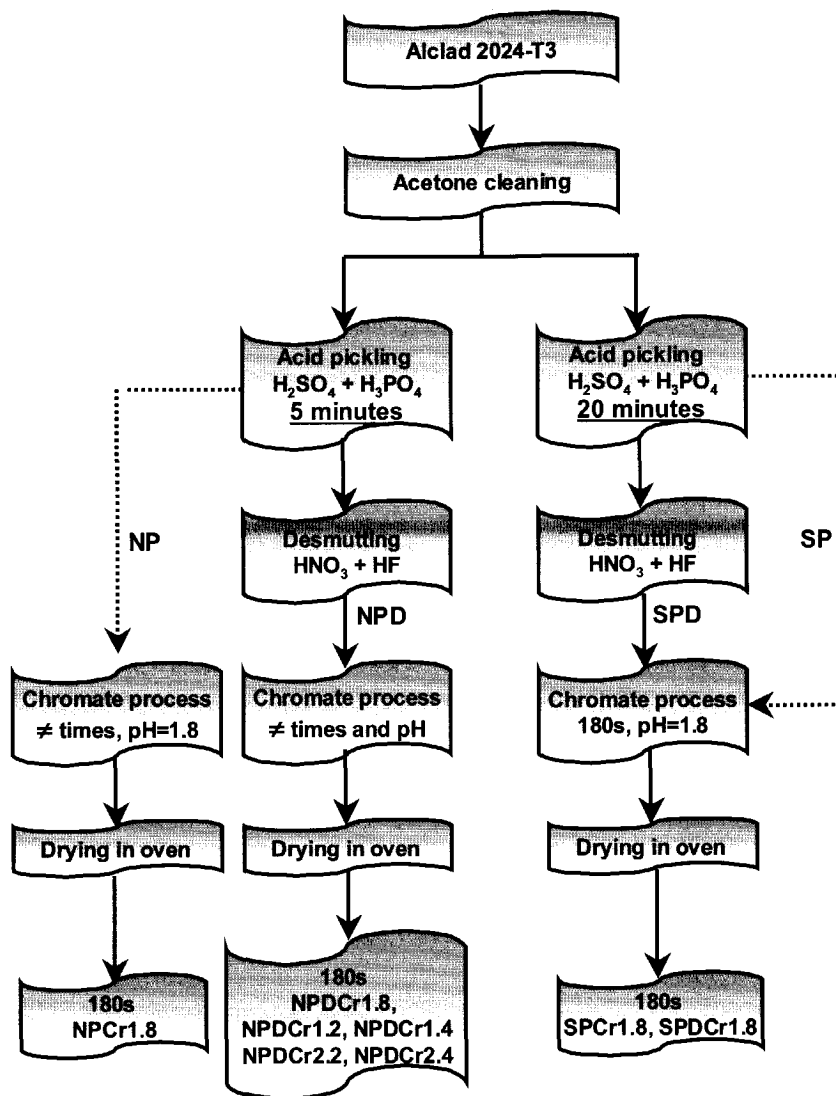


**Figure 5.1:** Schematic illustration of the different surface preparation and chromate treatment processes investigated in the case of Alclad 2024 alloy.

- ✓ **SP:** same procedure of NP but the acid pickling lasted 20 minutes. Samples obtained from panels that underwent this procedure are named SP, and after the standard chromate treatment (pH=1.8, 180 seconds) SPCr1.8. After this surface preparation procedure only the standard chromate process was carried out (Figure 5.1).



- ✓ SPD: same procedure of NPD but the acid pickling lasted 20 minutes. Samples obtained from panels that underwent this procedure are named SPD, and after the standard chromate treatment (pH=1.8, 180 seconds) SPDCr1.8. After this surface preparation procedure only the standard chromate process was carried out (Figure 5.1).

Between each step of the surface preparation procedure the panels were rinsed in deionised water for 5 minutes.

### 5.2.2 Surface analysis investigation

Various techniques were used to characterize both the morphology and the microstructure of the substrate prior to immersion in the chromate bath and the morphology, thickness, chemical composition of the chromate films:

- ✓ TEM (Transmission Electron Microscope, JEM 2000 FX II) measurements were carried out at Alcan Laboratory (Banbury, UK) to investigate the ultramicrotomed cross sections of the chromated samples, which were prepared using a Reichert-Jung ultramicrotome. The chromated samples with a surface area of 1 x 3 mm were embedded in an epoxy resin and trimmed with a glass knife. Afterwards, suitable thin sections were obtained by cutting with a diamond knife in a direction approximately parallel to the chromate film/aluminium interface and were collected on copper grids. The micrographs were obtained using a value of 200 keV as energy of the electron beam.
- ✓ SEM (Jeol JSM-6400F) an EDS investigations were performed within the FCM group at the Faculty of Materials Science of TUDelft (Delft, NL) to characterize the morphology of the Alclad 2024 surface in the as-received condition and after each step of the surface preparation and chromate processes. The samples were polished up to 1  $\mu\text{m}$  only to investigate the microstructure of the Alclad layer in the as-received condition. On the other hand, while the top surface of the samples after either the acid pickling treatment or the desmutting step was examined without further preparation, the chromated samples were observed after the deposition of either a carbon or a gold layer, 2 nm thick, necessary to reduce charging effects due to the presence of the poorly conductive chromate layer. Besides, a SEM study was carried out also on the remaining stubs left from the preparation of the ultramicrotomed cross sections in order to characterize the thickness of the chromate film.
- ✓ AFM (Digital Instrument Nanoscope III Multimode) was used in the Kelvin probe mode (SKPFM technique) to investigate simultaneously the topography and the Volta potential of the Alclad surface in the as-received condition and after each step of the surface preparation and chromate processes. The mode of operation and the settings of the AFM are described in detail in section 4.3.2 of chapter 4. Two off-line commands were applied to the topographic scans. *Roughness* command calculates several roughness parameters, such as the average of all the height ( $z$ ) values within the enclosed area, the standard deviation of the  $z$  values (RMS), the mean value of the surface relative to the centre plane ( $R_a$ ). However, the standard roughness measurements give little indication of the height distribution over the surface, whereas, this is provided by the *Bearing*

analysis that determines what percentage of the surface lies above or below a given height [7].

- ✓ SE (Spectroscopic Ellipsometry) measurements were carried out at the Department of Metallurgy, Electrochemistry, and Materials Science of the Vrije Universiteit in Brussel (Belgium). SE in the visible and infrared ranges was used to investigate the thickness and the chemical composition, respectively, of the chromate film formed on samples NP and NPD. The spectroscopic ellipsometry measurements in the UV-vis-NIR range were carried out on a J.A. Woollam Co. VASE<sup>®</sup> (variable angle spectroscopic ellipsometry) instrument, which has a spectral range between 250 nm and 1700 nm. The angle of incidence was varied from 65° to 85° by steps of 5°. The ellipsometric  $\Psi$  and  $\Delta$  spectra for all the samples were fitted by means of an optical model using the WVASE software from the J.A. Woollam Co. The IR-SE measurements were performed on a J.A. Woollam Co. IR-VASE<sup>®</sup> (infra-red variable angle spectroscopic ellipsometry) instrument, using three different angles of incidence: 75°, 80°, and 85°. The set up used contained a compensator transparent over the spectral range between 1.5  $\mu\text{m}$  and 43  $\mu\text{m}$ . In order to keep the measurement spot at the same location on the sample during all the measurements at different angles of incidence a standard two-step alignment procedure, proper of both instruments, was used. The wavelength range was scanned by steps of 5 nm for the UV-vis-NIR measurements and 15 nm in the case of IR-SE.
- ✓ GDOES (Glow Discharge Optical Emission Spectroscopy, Jobin Yvon 5000 RF) at Corus RD&T (IJmuiden, NL) was used to obtain the depth profiles of the CCC formed on samples NP and NPD, in order to calculate the film thickness and to support the data obtained by the fitting of the SE spectra. The samples were placed in a holder, which formed the cathode during operation, and argon was admitted at a pressure of 3.5 mbar. Afterwards, a glow discharge was established applying a power of 30 Watt. The positive argon ions produced in the discharge sputtered the samples surface on a circular area, 5 mm in diameter, at a rate of about 2  $\mu\text{m}/\text{min}$ . Light emissions of characteristic wavelengths, which are associated with the sputtered species excited by collisions in the discharge region, were monitored with a sampling interval of 0.1 seconds to obtain the depth profiles.
- ✓ RBS (Rutherford Backscattering Spectrometry) measurements were performed at the Debye Institute of Utrecht University (Utrecht, NL) to measure the thickness of the CCC as function of the immersion time in the Alodine 1200 solution. The experiments were carried out using a 2 MeV  $\text{He}^{2+}$  ion beam from a 3 MeV Van de Graaf accelerator. The incident beam formed an angle  $\theta_1=0^\circ$  with the sample normal and the backscattered ions were collected at an angle  $\theta_2=10^\circ$  to the sample normal. The beam spot size was 1.5x1.5 mm. A sample of  $\text{SiO}_2$  covered with a mono-atomic layer of gold was used for the calibration.
- ✓ AES (Auger Electron Spectroscopy, PHI-650 scanning Auger microprobe) measurements were carried out at the Department of Metallurgy, Electrochemistry, and Materials Science of the Vrije Universiteit in Brussel (Belgium) to obtain the depth profiles of the chromate layers formed on samples NP and NPD with the purpose to

investigate the presence of aluminium oxide at the interface between the CCC and the aluminium substrate. The Auger depth profiles were carried out using a primary electron energy and current of 5 keV and 100 nA, respectively. A CMA detector was used with a relative energy resolution of 0.6%. An area of 3x3 mm was sputtered with Ar<sup>+</sup> particles at a gun voltage of 4 keV and gun current of 15 mA. The AES depth profiles were recorded in alternating mode with an estimated sputter velocity of 10 nm/min.

### 5.3 Results and discussion

This section is divided into four main parts. The effect of the surface preparation treatment, in particular the length of the acid pickling step and the immersion in the desmutting bath, on the morphology and microstructure of the surface of Alclad 2024 alloy is discussed first. The second part focuses on the influence of the intermetallics on the nucleation and growth of the chromate film. The third and fourth parts present and explain the effects of the microstructural changes caused by the pickling and desmutting processes and of the pH of the chromate bath on the composition, thickness, and morphology of the film. In the various sections for each sample only 1 or 2 examples of SEM micrographs, EDS spectra, and AFM topographic and potential maps are given to illustrate the conclusions, which are however based on several measurements.

#### 5.3.1 Surface morphology and microstructure

- *As-received*

Figure 5.2 shows the SEM micrograph (a) and EDS analyses (b and c) of the polished surface of Alclad 2024 in the as-received condition.

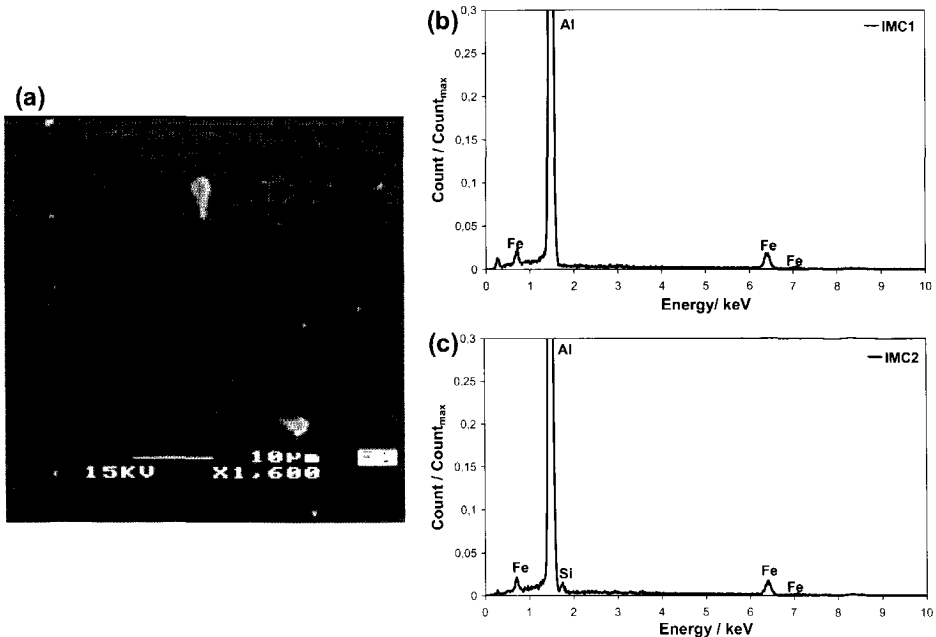


**Figure 5.2:** SEM micrograph of Alclad 2024 alloy after mechanical polishing up to 1 μm (a) and EDS spectra of the intermetallic IMC<sub>1</sub> (b) and IMC<sub>2</sub> (c).

In the secondary electron image several brighter spots can be observed, which are intermetallics (IMCs). Most of them are very small in size, less than  $1\ \mu\text{m}$ , whereas only few (named  $\text{IMC}_1$  and  $\text{IMC}_2$ ) reach the dimension of  $3\text{--}4\ \mu\text{m}$ . These large intermetallics contains always iron and in some cases silicon, as shown by the EDS analyses (Figure 5.2-b and -c), which as already stressed in the previous chapter give only qualitative information due to the strong background signal from the aluminium matrix. In the case of the intermetallics smaller than  $1\ \mu\text{m}$  this background signal is strong enough to hide any other signal and it render impossible the identification of these IMCs. Anyway, based on the composition of the clad layer it is very likely that they are also Fe or Fe, Si-rich intermetallics.

These types of intermetallic particles are formed during solidification and not by peritectic reaction and are present in virtually all commercial aluminium alloys, including the commercially pure aluminium, like AA1230 used as clad material for AA2024 [8]. The equilibrium phase diagram of the binary system Al-Fe shows the presence of an eutectic in aluminium rich alloys at  $655^\circ\text{C}$  with a probable composition within the range 1.7 to 2.2% iron [9]. Therefore, the AA1230 has a hypoeutectic composition since its content of iron and silicon is 0.7%. In this case, the equilibrium phase of the Al-Fe system is  $\text{Al}_3\text{Fe}$ , however other metastable phases ( $\text{Al}_6\text{Fe}$ ,  $\text{Al}_x\text{Fe}$ ,  $\text{Al}_9\text{Fe}_2$ ,  $\text{Al}_m\text{Fe}$ ) can precipitate during solidification, depending upon the melt composition and especially the local cooling rate [8, 10]. It was found [10] that the equilibrium phase forms when the cooling rate is lower than 1 K/s, whereas at a cooling rate of 1-4 K/s and 4-10 K/s, the majority of precipitates are the highly disordered phase  $\text{Al}_x\text{Fe}$  and the nearly stable structure  $\text{Al}_6\text{Fe}$ , respectively. Finally, at a cooling rate higher than 10 K/s the formation of  $\text{Al}_9\text{Fe}_2$  and  $\text{Al}_m\text{Fe}$  is more probable. Moreover, the presence of silicon in commercially pure aluminium, as AA 1230, causes the precipitation of silicon-rich intermetallics ( $\alpha\text{-Al-Fe-Si}$ ,  $\beta\text{-Al-Fe-Si}$ ,  $\text{Al}_3\text{FeSi}$ ,  $\text{Al}_4\text{FeSi}_2$ ) especially at high solidification rate [8].

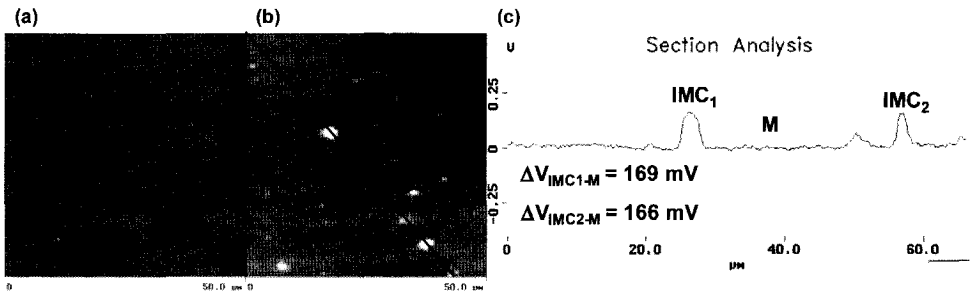


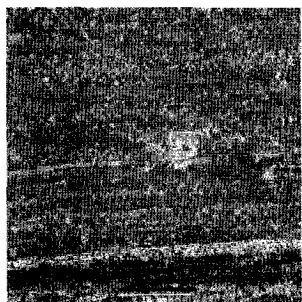
**Figure 5.3:** Topographic image with a height range of  $1\ \mu\text{m}$  (a), Volta potential map with a potential range of  $0.8\ \text{V}$  (b), and section analysis along the black line in the potential map (c) of Alclad 2024 alloy after mechanical polishing up to  $1\ \mu\text{m}$ .

The same surface area of the SEM micrograph of Figure 5.2-a has been investigated also using the SKPFM technique. The topographic image, Volta potential map and section analysis, i.e. potential profile along the black line in the potential map, are given in Figure 5.3. The two holes observed in the SEM micrograph (marked with a circle), which are likely the original locations of intermetallic particles removed during the polishing process, can be

clearly recognized also in the topographic image obtained with the AFM operating in the tapping mode (Figure 5.3-a). On the other hand, while the intermetallic particles shown by the SEM/EDS study are not visible in this topographic scan, they can be easily identified in the Volta potential map as bright areas (Figure 5.3-b). That means the Fe and Fe, Si-rich intermetallics have a more noble Volta potential in comparison with the Al matrix, i.e. they act as local cathodic sites. This is expected since both iron and silicon are more noble elements with respect to aluminium. The potential of the Fe and Fe-Si containing intermetallics is found by means of the section analyses, an example of which is reported in Figure 5.3-c, to vary between 80 and 180 mV with respect to the Al matrix (named M in all section analyses). The existence of a range of potentials can be due either to small variation in chemical composition of the intermetallics, which cannot be observed by EDS analysis, or to a "size effect" that results in a decrease of the measured potential when the size of the intermetallics is very small (see sections 4.2 and 4.4.1 for more details). Anyway, it should be noted that even the intermetallics lower than 1  $\mu\text{m}$  in size observed in the SEM micrograph and indicated by arrows show up in the potential scan. Although, the measured potential of these intermetallics could be lower than the real one, the important result of the SKPFM investigation is the existence of numerous galvanic couples on the Alclad 2024 surface associated with intermetallic particles that serve as cathode while the Al matrix behaves as anode. This determines the behaviour of the aluminium surface during the immersion in the acid pickling and desmutting solutions.

- *Acid pickling*

The SEM investigation carried out on the Alclad 2024 alloy surface after immersion for 5 minutes in the phosphoric-sulfuric acid bath (sample NP) shows the presence of a large



amount of small pits (Figure 5.4-a) together with the occurrence of local attack in proximity of the intermetallic particles (Figure 5.4-b). The fact that the formation of a large number of pits being very limited in size is a consequence of the pickling

**Figure 5.4:** SEM micrographs of Alclad 2024 alloy after 5 minutes of immersion in the  $\text{H}_3\text{PO}_4\text{-H}_2\text{SO}_4$  solution (sample NP).

treatment is confirmed by the comparison of the AFM topographic images of Figures 5.3-a and 5.5-a, relative to the

as-received and pickled conditions, respectively. On the other hand, the markings of the rolling process are still visible in both the SEM micrograph and the topographic map of sample NP. This suggests that the Alclad surface is not strongly etched by the 5 minutes contact with the  $\text{H}_3\text{PO}_4\text{-H}_2\text{SO}_4$  solution. When the aluminium is exposed to an acid environment a chemical attack of its natural oxide layer takes place, followed by an electrochemical attack of the aluminium [11, 12]. The strength of both attacks depends on

the level of acidity, i.e. the pH, and on the nature of the anion of the acid, in particular its tendency to form soluble compounds with Al. In the bath used for the pickling process the corrosive attack is essentially due only to the low pH, below 4 that is the low limit of stability for the aluminium oxide, since the sulfuric and phosphoric anions do not give rise to compounds with aluminium that are soluble in aqueous solution.

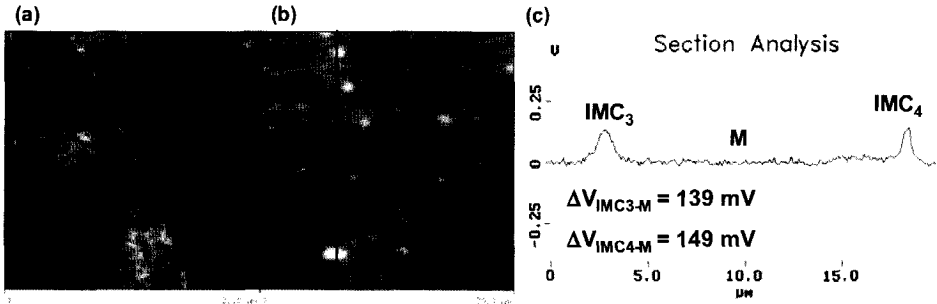


**Figure 5.5:** Topographic image with a height range of 1  $\mu\text{m}$  (a), Volta potential map with a potential range of 0.8 V (b), and section analysis along the black line in the potential map (c) of sample NP.

Therefore, the immersion for only few minutes in the pickling bath results in a moderate etching of the Alclad 2024 alloy that leads to the appearance of small pits uniformly distributed on the whole surface. These pits are likely located at areas where the natural aluminium oxide film is thinner and/or contains more flaws and therefore undergoes a faster chemical dissolution. This thins the oxide film allowing electron tunnelling and electrochemical dissolution of Al to occur and leading to a dynamic equilibrium between dissolution and formation of alumina. As discussed in chapter 2, one of the weak spots of the aluminium oxide is the location of the intermetallic particles, where once the Al oxide is dissolved the attack of aluminium is enhanced and accelerated by the galvanic coupling existing between the intermetallics, which act as cathode, and the aluminium matrix, which acts as anode and dissolves leading to the local attack in proximity of the IMCs observed by SEM. The SKPFM study of sample NP shows that after the immersion for 5 minutes in the pickling bath the intermetallic particles continue to be more noble than the aluminium matrix (bright spots in the potential map of Figure 5.5-b). In addition, the range of the Volta potential

of the Fe and Fe, Si-rich intermetallics is not affected by the contact with the pickling solution, which suggests that their chemical composition is not changed by the surface treatment.

When the time of immersion in the phosphoric/sulfuric acid bath is increased to 20 minutes

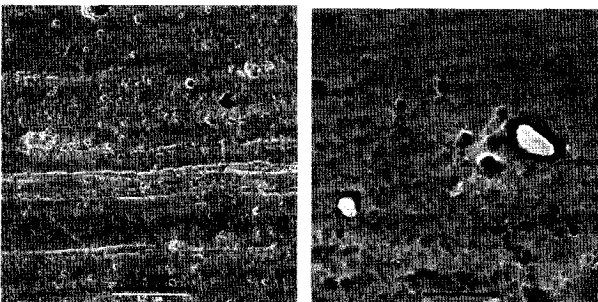


**Figure 5.6:** SEM micrographs of Alclad 2024 alloy after 20 minutes of immersion in the  $\text{H}_3\text{PO}_4\text{-H}_2\text{SO}_4$  solution (sample SP).

(sample SP) a stronger etching of the surface of Alclad 2024 occurs, which is characterized by the presence of some scalloping, i.e. shallow hemispherical pits, as can be observed in the SEM micrograph of Figure 5.6-a. The longer exposure to the pickling bath affects not only the morphology of the Alclad surface but also its microstructure. Indeed, the SEM investigation of the surface of sample SP shows that the intermetallics become fewer in number and that the local dissolution of the Al matrix in their proximity is enhanced (Figure 5.6-b). These two phenomena are correlated, since the stronger attack of the matrix at the periphery of the IMCs can lead to the loss of the intermetallics themselves. The more severe etching undergone by sample SP and the partial removal of the intermetallic particles from its surface are confirmed by the results of the AFM investigation.

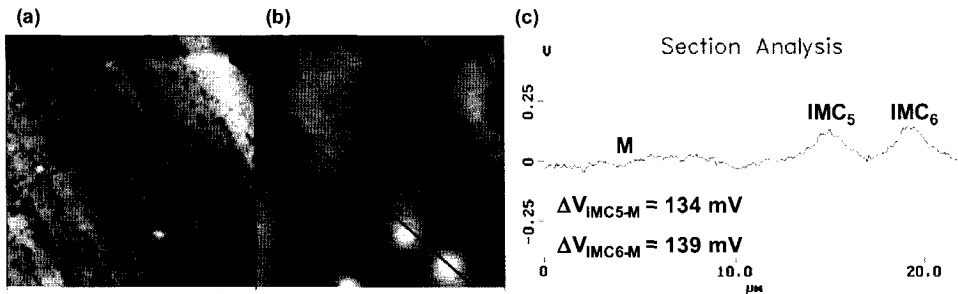


**Figure 5.7:** Topographic image with a height range of 1 μm (a), Volta potential map with a potential range of 0.8 V (b), and section analysis along the black line in the potential map (c) of sample SP.

Indeed, the topographic image of Figure 5.7-a of the Alclad 2024 surface after immersion in the  $\text{H}_3\text{PO}_4\text{-H}_2\text{SO}_4$  bath for 20 minutes shows the presence of pits together with larger and deeper trenches aligned along the rolling direction. In the top right corner of this image a large hole can be observed, which is likely the location of an intermetallic removed during the long immersion in the pickling bath. In general, the Volta potential of the surface of sample SP is characterized by less cathodic areas, related to intermetallic particles, in comparison with sample NP that is in agreement with the partial removal of IMCs observed with the SEM investigation. Figure 5.7 shows an example of Volta potential map for sample SP (b) together with the section analysis (c) through two intermetallics (named IMC<sub>5</sub> and IMC<sub>6</sub>), which shows a galvanic coupling between the IMCs and the Al matrix of about 140 mV. Several intermetallic particles were analysed and similarly to the as-received condition and sample NP their Volta potential is found to range from 80 up to 180 mV. Therefore, even a longer acid pickling treatment seems to not influence the extent of the galvanic coupling between the Al matrix and the IMCs, which continue to serve as cathodic sites on the Alclad 2024 alloy surface.

- *Desmutting*

Further changes in the morphology and microstructure of the aluminium surface occur during the immersion in the desmutting bath (samples NPD and SPD). The SEM micrographs of the desmutted surfaces (Figure 5.8) show the presence of a severe scalloping as a result of a stronger acid etching of the desmutting solution in comparison

with the pickling one. The similarity of the two micrographs of Figure 5.8 clearly indicates that the effect of the desmutting step is independent on the length of the previous acid pickling procedure. Indeed, the strong attack of the desmutting bath overrules the effect of the first treatment, i.e. pickling, on the morphology and microstructure of the Alclad surface.

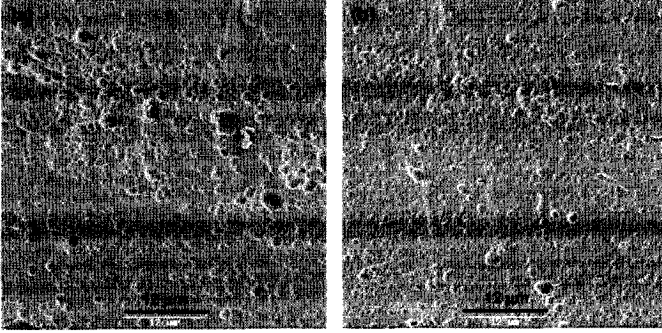


**Figure 5.8:** SEM micrographs of Alclad 2024 alloy after 5 minutes of immersion in the  $H_3PO_4$ - $H_2SO_4$  solution followed by 30 seconds of immersion in the  $HNO_3$ -HF solution, sample NPD (a), and after 20 minutes of immersion in the  $H_3PO_4$ - $H_2SO_4$  solution followed by 30 seconds of immersion in the  $HNO_3$ -HF solution, sample SPD (b).

The more severe etching of the surface of samples NPD and SPD is a consequence of the presence of the strongly aggressive hydrofluoric acid in the desmutting bath. Indeed, as mentioned before, the extent of attack of an acid environment towards aluminium depends not only on its acidity but also on the type of anions present. In

particular, halogen anions, like as  $Cl^-$ ,  $Br^-$  and  $F^-$ , give rise to the formation of soluble compounds with aluminium and as a consequence to a severe corrosion, which is localized when the pH falls inside the range of stability of the aluminium oxide (about 4 - 8.5) and is more general when the pH is outside such a range, as in the case of the desmutting solution. In section 2.2.1 of chapter 2 it was reported the stepwise chlorination process that is the most common theory explaining the interaction between chloride ions and aluminium oxide, which results in the dissolution of aluminium and its oxide with the formation of soluble  $AlCl_3$ . The effect of the fluoride ions on the corrosion of Al is similar, although  $F^-$  ions are markedly more aggressive than chloride. The overall dissolution process of aluminium oxide in contact with  $F^-$  has been proposed to be [13]:



Besides, the unique accelerating effect of  $F^-$  on the dissolution of aluminium and its oxide is also partly attributed to its ability to replace some of the  $O^{2-}$  in the oxide layer because of the similar ionic radii ( $r(F^-) = 0.136$  nm and  $r(O^{2-}) = 0.14$  nm). This results in the change of the charge distribution and as a consequence increases both the ionic and electronic conductivity of the oxide film [14], which in turn enhances the rate of the electrochemical reactions, as the anodic dissolution of aluminium. In addition, the formation of soluble compounds with the fluoride ions further increases the aluminium attack [15, 16]:







It can be noted that the presence of  $H^{+}$ , i.e. low pH, has a synergetic effect both for the chemical attack of the aluminium oxide and for the electrochemical attack of aluminium by means of fluoride ions. This explains the extremely strong etching undergone by the Alclad 2024 alloy surface during only 30 seconds of contact with the desmutting bath. The SEM investigation shows that this strong etching results not only in severe scalloping of the surface but also in a almost complete removal of the intermetallic particles. Indeed, as already discussed above the Al matrix dissolves more rapidly in proximity of the cathodic IMCs and leads to the drop out of the intermetallics. This phenomenon is obviously enhanced by the presence of fluoride ions and therefore the loss of intermetallics is higher during the immersion in the desmutting bath (samples NPD and SPD) than during the pickling step, even if it lasts 20 minutes.

The removal of the IMCs is observed also on the AFM topographic images of samples NPD and SPD (Figure 5.9-a and -c), which show the presence of deep trenches together with large holes, indicated by arrows, that are likely the position of the removed intermetallic particles. The absence of IMCs on the surface of these samples is reflected also in the Volta potential maps given in Figure 5.9-b and -d. Indeed, bright areas associated with the cathodic intermetallics are not detected anymore. On the other hand, some regions characterized by a lower potential, which appear

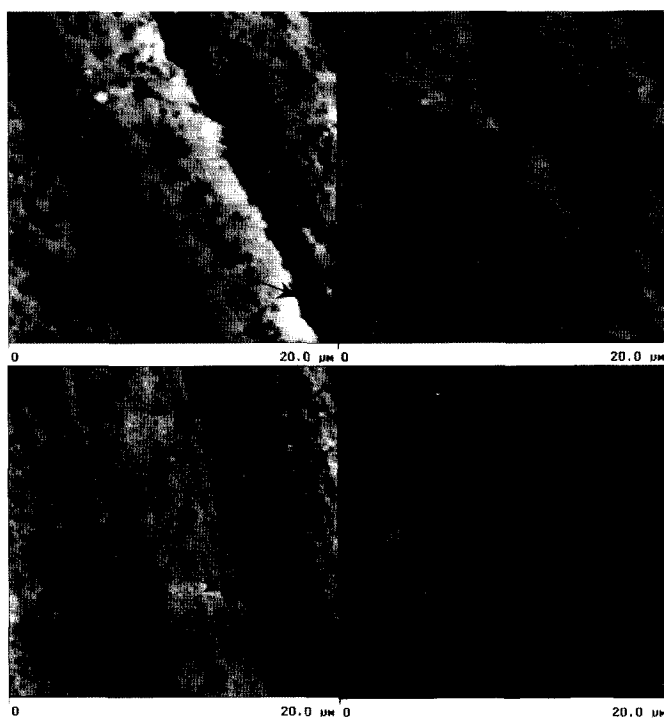


**Figure 5.9:** Topographic image with a height range of  $1 \mu\text{m}$  of samples NPD (a) and SPD (c) and Volta potential map with a potential range of  $0.8 \text{ V}$  of samples NPD (b) and SPD (d).

darker in the map and are indicated by the arrows, are present. However, comparing the potential map with the topographic image it can be noted that these features are artefacts resulting from the contribution of the topography during the surface potential measurements that was discussed in section 4.2 of chapter 4. Indeed, while the surface of samples NPD and SPD is very rough with sudden height variations at the location of the trenches and

holes, which seem to be reproduced also on the potential map (see arrows in the topographic images and potential maps of Figure 5.9), its real potential is quite homogeneous due to the almost complete absence of IMCs. This is obviously the case when the contribution of the topographic features on the potential map is more evident. Figure 5.9 shows the difficulties in using the SKPFM technique for measurements on very rough surfaces.

In conclusion, the dipping in the nitric-hydrofluoric acid bath gives rise, independently on the earlier treatment, to a more etched surface, but with a lower content of intermetallics, i.e. cathodic sites. As the formation of the chromate conversion coating on the aluminium involves electrochemical reactions (see chapter 3, section 3.2.1), the removal of cathodic intermetallics from the external surface is expected to have a large influence on the nucleation, growth, and as a consequence on the performance of the chromate films. Since the largest changes of the properties of the Alclad 2024 alloy surface are caused by the immersion in the  $\text{HNO}_3$ -HF bath after 5 minutes of immersion in the  $\text{H}_2\text{SO}_4$ - $\text{H}_3\text{PO}_4$  solution, it was decided to investigate the relation between the surface microstructure and the nucleation and growth mechanisms of the CCC for samples NP and NPD. The results of this investigation are reported and discussed in the next section.

### 5.3.2 Nucleation and growth of the CCC: effect of the surface preparation

#### • Nucleation

The SEM micrograph of Figure 5.10-a shows that the immersion for 3 seconds in the chromate bath leads to a smoothening of the surface of sample NP together with formation of local deposits, which appear as bright spots in the SEM image.

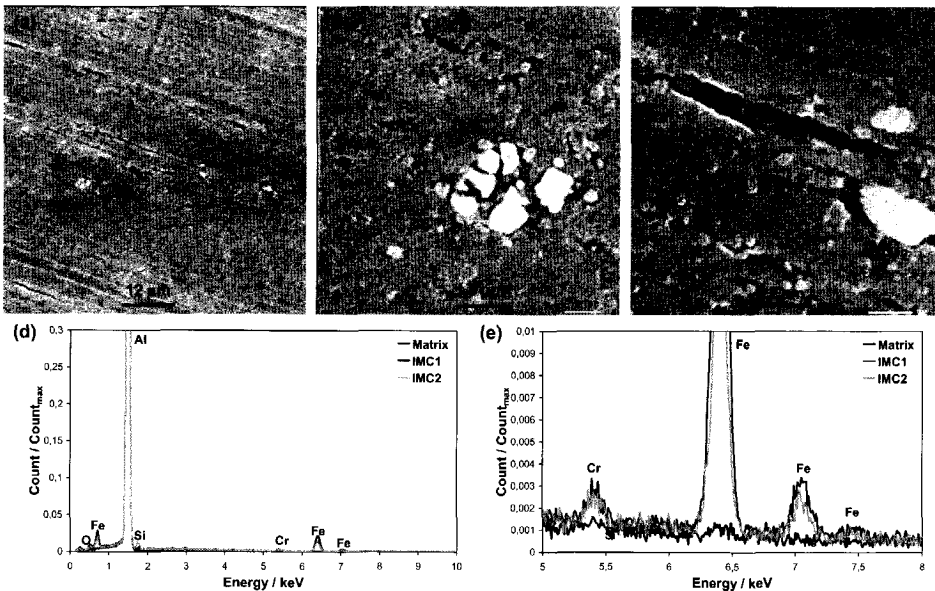


**Figure 5.10:** SEM micrographs (a, b, c) and EDS spectra (d, e) of sample NP after 3 seconds of immersion in the chromate bath.

A zoom into two of these bright areas (named  $IMC_1$  and  $IMC_2$ ) are shown in the higher magnification SEM micrographs given in Figure 5.10-b and -c. The EDS analyses identify these areas as Fe or Fe-Si containing intermetallics on top of which a chromium oxide deposit is formed (Figure 5.10-d and -e). On the other hand, in the EDS spectra carried out on the Al matrix the peak relative to oxygen and that relative to chromium are absent, indicating that during the 3 seconds of contact with the Alodine bath chromium oxide has not precipitated above the Al matrix or in such low extent to be below the detection limit of EDS.

The preferential deposition of the chromate film at the location of the intermetallic

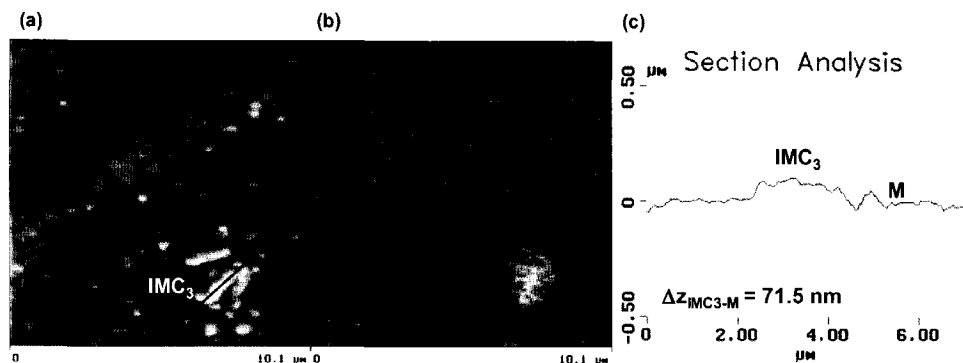


**Figure 5.11:** Topographic image with a height range of 1 μm (a), Volta potential map with a potential range of 0.8 V (b), and section analysis along the black line in the topographic image (c) of sample NP after 3 seconds of immersion in the chromate bath.

particles is confirmed by the AFM investigation of the surface of sample NP after 3 seconds of dipping in the chromate bath, given in Figure 5.11. It can be noted the presence of discrete areas (named  $IMC_3$ ) that are characterized by a higher height together with a higher Volta potential in comparison with the rest of the surface. This suggests that they are the intermetallic particles observed by the SEM study and that are covered with a thin chromate film. The section analyses carried out on the topographic image shows that the deposit on top of the IMCs has a thickness in the order of a few tens of nanometers. From the SEM and AFM results it can be stated that the presence of intermetallic particles on the surface of sample NP plays a dominant role in the early stage of nucleation of the CCC. Indeed, the nucleation of the chromate layer preferentially occurs above the intermetallics and it is extremely fast giving rise to a film of some tens of nanometers in few seconds.

Referring to section 3.2.3 it can be noted that our findings are in agreement with those of some authors [17-20] and apparently in contradiction with the theories proposed by some other groups [21-24]. However, since the studies reported in literature all concern the Cu-containing intermetallics of bare 2024 aluminium alloy, it was preferred to give a comparative discussion of our results and those of the literature in chapter 7, where the nucleation and growth of the chromate film is investigated for this alloy.

On sample NPD the very short (3 seconds) immersion in the chromate bath results in a decrease of the scalloping of the surface, as can be observed by both the SEM micrograph

of Figure 5.12-a and the AFM topographic image given in Figure 5.13. The change of the morphology of the pickled and desmutted Alclad 2024 surface can be likely attributed to the formation of a thin film over the whole surface.

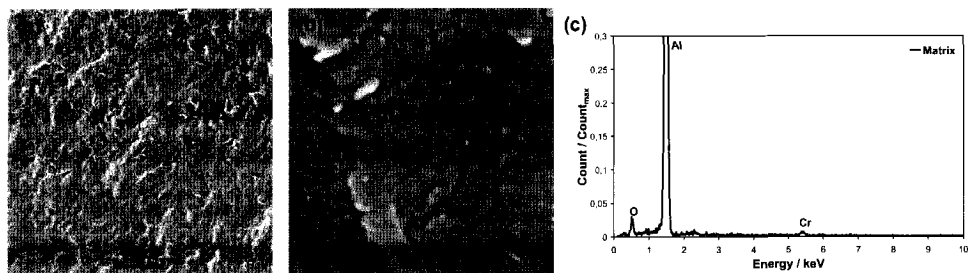


**Figure 5.12:** SEM micrographs (a, b) and EDS spectrum (c) of sample NPD after 3 seconds of immersion in the chromate bath.

This is confirmed by the small cracks observed on the high magnification SEM micrograph (Figure 5.12-b). Indeed, they are indicative of the presence of a film and are a consequence of the thermal stresses built up in the layer during the final drying step. The presence of the peaks of oxygen and chromium in the EDS spectra (Figure 5.12-c) shows that this film is actually a thin CCC formed during the 3 seconds of contact with the chromate solution. These results suggest that the nucleation mechanism of the chromate layer on samples NPD and NP is completely different: homogeneous for the former, heterogeneous for the latter.

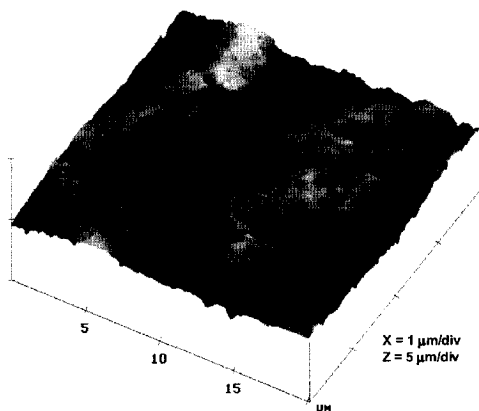


**Figure 5.13:** 3D topographic image of sample NPD after 3 seconds of immersion in the chromate bath.

by the different surface preparation procedure used: less etched surface still containing cathodic particles when only a pickling step is carried out (sample NP), more etched surface, from which almost all the intermetallics are removed, when the pickling treatment is followed by a desmutting one (sample NPD).

As described in section 3.2.1 of chapter 3, the formation of the CCC on the aluminium surface is a result of electrochemical reactions that involve the oxidation of aluminium and the reduction of chromate species:



The increase in pH caused by the cathodic reduction of the chromate species (reactions 5.7 and 5.8) and partially also by the  $H_2$  evolution, as secondary cathodic reaction, enables the precipitation of a gel of chromium hydroxide,  $Cr(OH)_3$ , which can transform into chromium oxide,  $Cr_2O_3$ , during the final drying step of the chromate process. Besides, the literature survey reported in chapter 3 highlighted also that a surface activation, i.e. thinning or complete dissolution of the natural aluminium oxide film, by the fluoride species present in the chromate bath is necessary for the deposition of the chromate layer. Indeed, the aluminium oxide should at least be thin enough to enable the tunnelling of the electrons, which are one of the reagents in the chromate reduction reactions. Both these characteristics of the chromate film formation, i.e. electrochemical nature and request of a surface activation, are important to understand the different nucleation observed for samples NP and NPD. On sample NP the intermetallic particles favours the reduction of the chromate species to occur in their proximity because of two main reasons: they have a more noble potential with respect to the Al matrix, i.e. they serve as cathodic sites, and the Al film at their location is thinner and contains more defects since during the pickling step a localized attack has taken place at their periphery. Therefore, the surface in proximity of the IMCs is immediately activated by the fluoride species of the chromate bath and during the first few seconds of immersion  $HCrO_4^-$  and  $Cr_2O_7^{2-}$  species reduce very rapidly at their location resulting in an increase of pH and consequent precipitation of a thin film of chromium hydroxide, as observed by SEM and AFM studies. On the other hand, the surface of sample NPD does not contain discrete areas being cathodic and locally active but it is homogeneously activated by the desmutting treatment, which partially dissolves and thins the natural Al oxide film. As a consequence, on this sample the conversion process takes rapidly place over a broad front and does not involve preferential nucleation sites. The positions of the active areas most likely change continuously depending on both the local concentration of fluoride and the thickness of the natural aluminium oxide. This leads to the fast formation of a layer covering the whole surface already after 3 seconds of dipping in the bath.

The differences in the nucleation mechanism of the chromate conversion coating on the two samples of Alclad 2024 alloy are reflected also in the evolution of the open circuit potential (OCP) during the immersion in the Alodine 1200 solution, reported in Figure 5.14. For both samples, the general trend of the OCP consists of a decrease during the first seconds and afterwards a constant value (about  $-650$  mV) is found until the end of the chromate treatment. The major changes occur during the first seconds of immersion, as can be observed by the enlargement of the diagram of OCP vs. time during the first 15 seconds of dipping in the chromate bath (Figure 5.14-b).

The OCP is the potential at which the total rates of oxidation and reduction are equal, and then considering the anodic and cathodic current densities ( $i_a$  and  $i_c$ ):

$$i_a = \frac{I_a}{A_a} = i_c = \frac{I_c}{A_c} \quad (5.a)$$

where  $I_a$  and  $I_c$  are the anodic and cathodic current, respectively, and  $A_a$  and  $A_c$  the anodic and cathodic areas. Therefore the variation of OCP with time is complicated by its dependency on many variables, namely the electrochemical reactions taking place during the formation of the CCC and the extension of the real cathodic and anodic areas. However, some considerations can be made and some indicative information on the chromate process can be obtained by the OCP monitoring. In accordance with the literature [25] the initial fast decrease of OCP (region I of the graph of Figure 5.14-b) is related to the activation of the surface caused by the presence of fluoride compounds in the Alodine bath, which give rise to an increase of the anodic dissolution of aluminium with consequent decrease of the OCP. However, after few tenths of a second, the increase in the cathodic current density due to

the reduction of the chromate species partially balances the decrease in OCP caused by the anodic dissolution of Al, leading to a slower decrease in OCP (region II of the graph of Figure 5.14-b). Finally, when the sample surface is completely covered by a relatively thick chromate layer, which contains pores and defects anyhow, a steady-state situation is reached that is reflected in the constant value of OCP (region III of Figure 5.14-b). This is a consequence of the thickening of the conversion layer that lowers the possibility of both the electrons tunnelling through the coating itself and access of the solution to the aluminium surface and therefore reduces the coating growth rate, i.e. both the anodic and cathodic current densities. The decrease in anodic current density would cause an increase of the OCP, whereas the decrease in cathodic current density would cause a decrease of the OCP, then the anodic and cathodic current densities vary in such a way that the two effects likely compensate each other and the OCP remains constant until the end of the chromate treatment.

Although, samples NP and NPD show a similar general trend of the OCP some differences during the first seconds of immersion, before the achievement of a constant value, are observed (Figure 5.14-b), which can be related to the different nucleation mechanisms. The main difference is that the sample characterized by a heterogeneous

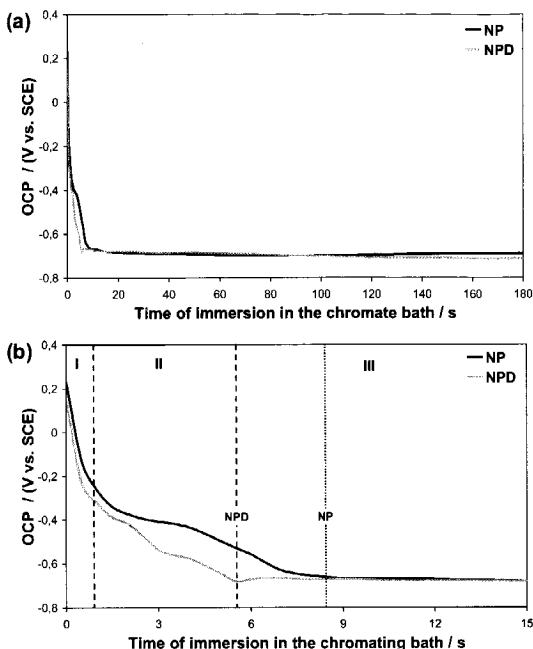


**Figure 5.14:** OCP evolution during the immersion in the chromate bath for samples NP and NPD (a). Enlargement of the first 15 seconds of immersion in the chromate bath (b).

nucleation (sample NP) reaches a constant value of OCP after a longer time of immersion with respect to sample NPD, on which a homogeneous nucleation takes place. According to the interpretation of the trend of OCP given above, this means that on sample NP the complete coverage of the surface also occurs but with a certain delay compared to sample NPD. Indeed, this is found by the SEM investigation that shows the presence of a CCC on the whole surface of samples NPD and NP after 3 and 15 seconds of immersion, respectively (Figures 5.12 and 5.15-a). The presence of a thin chromate film on the surface of sample NP is indicated by the appearance of the typical cracks of the CCC in the SEM micrograph of Figure 5.15-a and by the O and Cr peaks in the EDS spectra, not shown here. The starting of the deposition of the CCC also on the Al matrix of sample NP can be explained by the fact that once the chromate film has covered the intermetallic particles they become less active, and therefore the reduction of the chromate species and the deposition of the chromium hydroxide continue in the other areas of the surface resulting in a thin layer covering the whole surface of the sample.

Another difference, which was found to be reproducible, in the trend of the OCP during the initial decrease consists of a higher value of OCP shown by sample NP in comparison with sample NPD. A possible reason for this behaviour can be found in the different extent of the cathodic areas in the two samples, i.e. much smaller in the case of sample NP since at least in the early stages of the film formation the cathodic reduction of chromate species is taking place only on top of the IMCs and not on the whole surface. Assuming an equal cathodic current for both samples, this would imply that the cathodic current density is higher for sample NP and as a consequence its OCP is shifted towards the positive direction. Therefore, when the electrochemical reactions involved in the film deposition start to take place all over the surface of sample NP, similarly to the situation of sample NPD, the OCP of the two samples reaches similar values. Although this is likely true, the interpretation of the OCP evolution is made difficult by the several variables involved and needs to be supported by other measurements, as the SEM investigation in the present study.

- *Growth*

The heterogeneous nucleation of the CCC occurring on sample NP affects the properties of the film also at longer time of immersion in the bath.

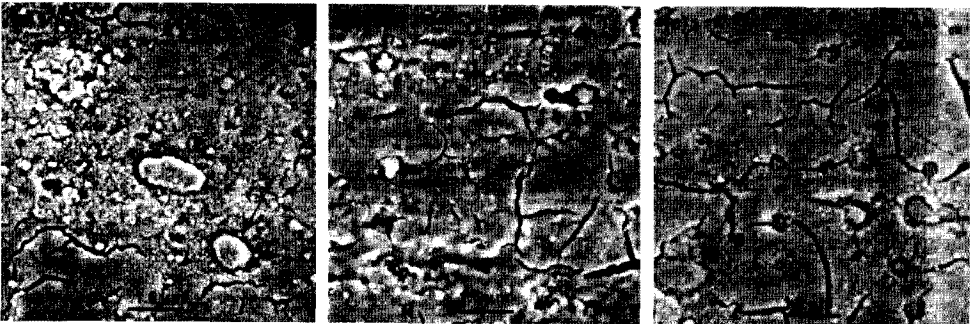


**Figure 5.15:** SEM micrographs of sample NP after 15 (a), 27 (b), and 81 (c) seconds of immersion in the chromate bath.

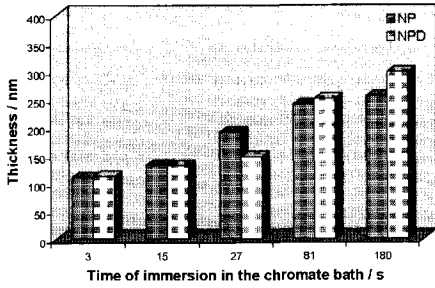


**Figure 5.16:** Layer thickness as function of the immersion time in the chromate bath calculated from the RBS spectra.

Indeed, although increasing the length of the chromate treatment the layer formed on the Al matrix becomes more uniform (Figure 5.15) and thicker (Figure 5.16), the intermetallics always represent weak spots in the chromate film formed on sample NP since at their location discontinuities and defects are present in the layer (arrows in the SEM micrographs of Figure 5.15). This is a consequence of the heterogeneous nucleation of the CCC on this sample, which leads to a lack of continuity between the layer formed on the

Al matrix and that formed on the IMCs, since they deposit at different time and rate.

The negative influence of the intermetallics on the uniformity of the chromate film is confirmed by the much more homogeneous CCC deposited, independently on the length of the chromate treatment, on the surface of sample NPD, which does not contain IMCs, in comparison with that formed on sample NP (Figures 5.15 and 5.17).

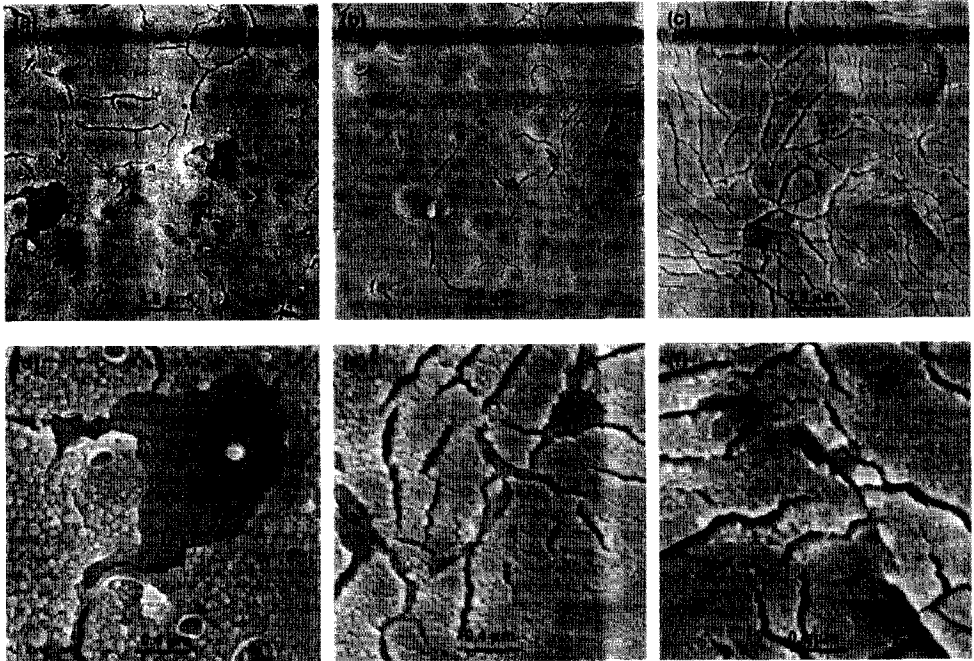


**Figure 5.17:** SEM micrographs at 8000x of sample NPD after 15 (a), 27 (b), and 81 (c) seconds of immersion in the chromate bath. SEM micrographs at 30000x of sample NPD after 15 (d), 27 (e), and 81 (f) seconds of immersion in the chromate bath.

The chromate film formed on this sample presents a layered structure. The high magnification SEM micrographs (Figure 5.17-d, -e, and -f) show the presence of a compact



barrier layer on top of which a more porous film is deposited that seems to consist of small, few nanometers in size, spherical particles. Our findings are in agreement with the results of Treverton and Amor [26] described in chapter 3. On the other hand, since this second porous layer is not observed after few seconds of immersion in the Alodine bath (Figure 5.12) it is suggested that a two stages growth of the CCC takes place on this sample: an extremely fast formation of a thin compact layer, within few seconds of immersion, followed by a slower deposition of spherical chromium hydroxide particles that coalesce and form the top porous film. Increasing the time of immersion in the Alodine bath leads to an increase of the extent of coalescence of these particles, which indeed become less clearly distinguished during the SEM investigation (Figure 5.17-f). Goeminne [3] proposed a similar mechanism of growth for the chromium-phosphate conversion coating on Al alloys.

The duplex structure of the chromate film is further discussed in the next section that deals with the morphology and chemical composition of the layer formed after a standard time of immersion in the Alodine bath, i.e. 3 minutes.

### 5.3.3 Morphology and composition of the CCC: effect of the surface preparation.

The results of the spectroscopic ellipsometry measurements are discussed first followed by the microscopic investigation, i.e. TEM, SEM and AFM, results. However, since SE is not a widely used technique, especially in the field of conversion films on rolled metals, a short description of the principles of this surface analysis method is given.

- SE technique

Recently at the Vrije Universiteit in Brussel the applicability of spectroscopic ellipsometry (SE) as a non-destructive alternative method in the study of both thin conversion coatings [27-29] and anodic oxide films [30, 31] on aluminium has been established. SE measures the variation in polarization of the radiation due to interaction with the system under study (Figure 5.18). The measured values are expressed as the two ellipsometric angles ( $\Psi$  and  $\Lambda$ ) as function of the wavelength ( $\lambda$ ), which are related to the ratio of the Fresnel reflection coefficients ( $\tilde{R}$ ) of radiations polarized parallel (p) and perpendicular (s) to the plane of incidence [32]:

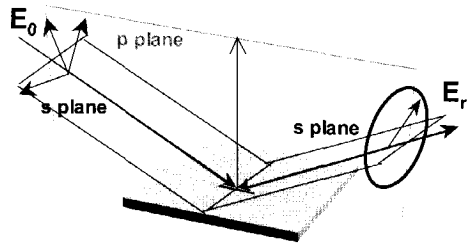


**Figure 5.18:** Schematic illustration of the interaction between the radiation and the system under study during the SE measurements [Ref. 29].

$$\tan \Psi e^{j\Lambda} = \frac{\tilde{R}_p}{\tilde{R}_s} = \frac{|\tilde{R}_p|}{|\tilde{R}_s|} e^{j(\delta_p - \delta_s)} \quad (5.b)$$

$$\tilde{R}_i = \frac{\tilde{E}_{r,i}}{\tilde{E}_{0,i}} = \frac{|\tilde{E}_{r,i}|}{|\tilde{E}_{0,i}|} e^{j\delta_i} \quad i = p, s \quad (5.c)$$

where  $\delta_i$  is the phase shift of the component  $i$  of the reflected radiation.

Fitting the spectra of these two parameters in the visible range using a proper optical model enables to determine the thickness and the optical constants of the film. Besides, the  $\Psi$  spectra in the infrared region provide information concerning the chemical composition of the film, since absorption peaks occur in these spectra similar to those detected with other types of infrared techniques, like reflection-absorption infrared spectroscopy (RAIRS). In contrast with RAIRS, IR-SE does not require a background spectrum of the substrate since IR-SE measures the ratio between reflections of p and s polarized radiations and not the absolute reflected intensity. This eliminates the problems of different size between the reference and the studied surface, and especially of the presence of a film on the reference that causes apparent change of reflection of the measured surface. This is a great advantage especially for aluminium, which is always covered by a thin natural oxide layer.

- *Spectroscopic ellipsometry in the IR region*

Figure 5.19 shows the IR-SE spectra of the ellipsometric angle  $\Psi$  for the CCC formed on samples NP and NPD using standard time (3 minutes) and pH (1.8), i.e. samples NPCr1.8 and NPDCr1.8, respectively. Five major peaks can be observed in the spectra of both samples.

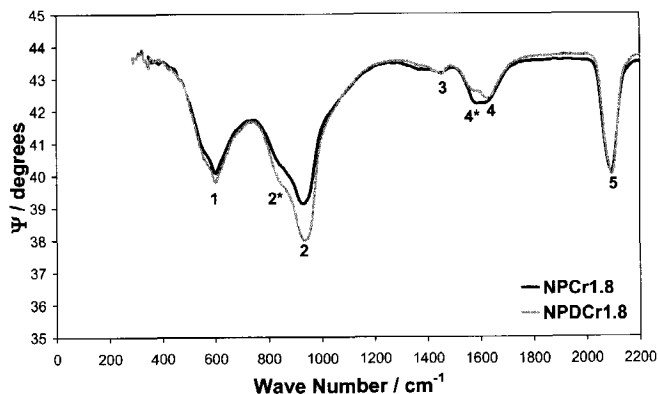


**Figure 5.19:** The  $\Psi$  IR-SE spectra, using  $75^\circ$  as angle of incidence, of the chromate conversion coating formed on samples NP and NPD using standard conditions (pH = 1.8, t = 3 minutes).

The assignment of the different peaks has been based on both the literature data and the analysis of the changes caused in the spectra by the variation of the pH of the chromate bath, which is discussed in detail in the next section. The peaks at  $594\text{ cm}^{-1}$  and at  $925\text{ cm}^{-1}$ , named 1 and 2 in Figure 5.19, can be assigned to  $\text{Cr}_2\text{O}_3 \cdot 2\text{H}_2\text{O}$  modes [29, 33-35].

Moreover, a contribution to the peak at  $594\text{ cm}^{-1}$  can also be due to Fe-CN vibration [34, 35]. The strong peak at  $925\text{ cm}^{-1}$  present a shoulder at  $840\text{ cm}^{-1}$  (peak 2\*), which can be related to Cr(VI)-O vibration, since this mode has been associated [35] to peaks at  $816\text{ cm}^{-1}$  and  $903\text{ cm}^{-1}$ . Besides, Xia *et al.* [34] assigned the peaks at 817, 919, and  $960\text{ cm}^{-1}$  to the Cr(VI)-O vibration, and other authors [36] considered the absorption at 860, 945, and  $990\text{ cm}^{-1}$  caused by Cr(III) chromates, like as  $\text{Cr}_2(\text{Cr}_2\text{O}_7)_3$  into  $\text{Cr}_2\text{O}_3$ . The absorption at  $1620\text{ cm}^{-1}$  (peak 4) is attributed to H-O-H bending of physically adsorbed water [29, 34], whereas the peak at  $1427\text{ cm}^{-1}$ , named 3, can be caused either by the bending vibration of water co-ordinated to chains of

tetrahedrally and octahedrally co-ordinated aluminium ions [37, 38] or by the  $\text{Cr}_2\text{O}_3 \cdot 2\text{H}_2\text{O}$  modes [39]. In addition, it can be noted that the peak at  $1620\text{ cm}^{-1}$  is very broad and present a shoulder, named  $4^*$ , that is extended until  $1573\text{ cm}^{-1}$  and is stronger in the case of sample NPCr1.8. This absorption can be due to the presence of organic material on the conversion coated surface in accordance with Ahern *et al.* [38] or to the presence of aluminium oxide in accordance with Dodiuk *et al.* [40]. Indeed, Ahern assigned a peak at  $1584\text{ cm}^{-1}$  to graphitic carbon, whereas Dodiuk related a shoulder located at  $1580\text{ cm}^{-1}$  to  $\text{Al}=\text{O} \cdot \text{H}_2\text{O}$  stretch. The presence of aluminium oxide is the most probable cause of this peak, since the AES investigation has shown in both samples the existence of an aluminium oxide layer at the interface between the substrate and the conversion film. Finally, a clear and strong peak is present at  $2090\text{ cm}^{-1}$  (peak 5) that is certainly related to the stretching of  $\text{C}\equiv\text{N}$  groups, presumably derived from the ferricyanide compounds used as accelerators in the chromate bath Alodine 1200 [34]. More specifically, based on the literature, discussed in the section 3.2.1 of chapter 3, this peak can be attributed to four different compounds: physisorbed  $\text{Fe}(\text{CN})_6^{3-}$  on  $\text{Cr}(\text{OH})_3$ , Berlin Green, chromium iron mixed cyanides, and  $\text{Cu}_2\text{Fe}(\text{CN})_6$ . However, the formation of copper cyanide complexes is quite improbable on a CCC deposited on Alclad 2024 alloy, since the clad layer contains only 0.1% of copper. Whereas, the presence of chromium iron mixed cyanides would be in agreement with Drozda and Maleczki [41], who studied the chemical composition of a chromate film deposited on pure Al (99.5% wt.) by means of radioactive tracer technique and proposed the presence of  $\text{Cr}_4(\text{Fe}(\text{CN})_6)_3$  species.

Although the spectra of samples NPCr1.8 and NPDCr1.8 show the same absorption peaks, few differences can be noted. First of all, the peak at  $925\text{ cm}^{-1}$  and the shoulder at  $840\text{ cm}^{-1}$  are clearly more intense for the chromate film formed on sample NPD than that deposited on sample NP. This can be partially due to the higher thickness of the CCC of sample NPDCr1.8, as observed by RBS measurements (Figure 5.16). However, since this higher thickness does not affect so strongly also the other peaks of the spectra, a real difference in chemical composition should be co-responsible for the variation in absorption intensity relative to peak 2 and shoulder  $2^*$ . One possibility could be a higher amount of Cr(VI) species adsorbed in the chromate layer in the case of sample NPDCr1.8. This would be in agreement with the findings of Halada and co-workers [23], who found that the chromate film formed in proximity of the intermetallic particles results depleted in Cr(VI) species. Therefore, the complete removal of IMCs from the surface of sample NPD likely favours not only the formation of a homogeneous film, as discussed in the previous section, but also the adsorption of hexavalent chromium compounds inside the layer. A further difference in the IR-SE spectra of the two samples consists in the stronger absorption at  $1573\text{ cm}^{-1}$  (peak  $4^*$ ) shown by sample NPCr1.8, which indicates the presence of a larger amount of aluminium oxide in the CCC of this sample, probably at the interface with the aluminium substrate. Although, this could be true since the acid etching used as surface preparation for sample NP is less aggressive than the desmutting process used in the case of sample NPD, the AES depth profiles do not show for the two samples a clear difference in the amount of aluminium oxide at the CCC/Al interface.

Summarizing, the chromate conversion coating formed on the two samples under investigation consists mainly of chromium oxide/hydroxide, into which chromate and cyano compounds are adsorbed. From a qualitative evaluation of the spectra it seems that the film formed after the acid pickling and desmutting steps, i.e. sample NPDCr1.8, contains a larger amount of Cr(VI) species and a lower amount of aluminium oxide.

- *Spectroscopic ellipsometry in the UV-vis-NIR region*

While the absorption peaks of the ellipsometric spectra in the infra-red region provide information regarding the chemical composition of the film, the value of the thickness of the film cannot be quantitatively determined by their height or area, since although these two quantities, i.e. thickness and peak intensity, are somehow interdependent their correlation is not linear especially at high angle of incidence [42]. On the other hand, the number of maxima and minima in the  $\Psi$  and  $\Delta$  spectra in the UV-vis-NIR range is associated with the layer thickness, which can be quantitatively calculated by means of a fitting procedure. In the present study this is made using a two-layer optical model that was developed by the research group at the Vrije Universiteit of Brussel for the chromium-phosphate coating on aluminium [27, 28] and is shown in Figure 5.20.

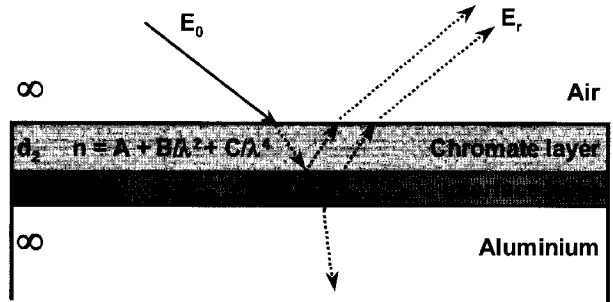


**Figure 5.20:** Optical model describing the chromate conversion coating on aluminium and used to fit the SE spectra.

The two layers, which are delimited on top by air and on bottom by the aluminium substrate, represent the bulk of the chromate conversion coating and an interface layer between the chromate film and the aluminium substrate. The air and the substrate are considered semi-infinite layers with known optical constants; refractive index, 1 for air and a dispersion relation taken from literature for aluminium [43]. The refractive index  $n$  of the bulk chromate film is not known and is modelled as a function of the wavelength ( $\lambda$ ) using a Cauchy dispersion relation whose terms are fitted during the regression procedure:

$$n = A + \frac{B}{\lambda^2} + \frac{C}{\lambda^4} \quad (5.d)$$

This dispersion relation is often used to represent the refractive index of transparent dielectrics. However, since the chromate coating has a light yellowish colour, absorption of radiation also occurs at wavelengths in the visible range. Nonetheless, it was observed in agreement with previous results [27], that the inclusion of the absorption parameters in the fit does not lead neither to a relevant improvement of the fitting or to significant changes in the thickness of the two layers in the optical model and in the trend of the index of refraction as function of the wavelength. Based on this, the approximation of regarding the porous chromate layer as a transparent dielectric can be considered acceptable.

A thickness non-uniformity option for the bulk chromate layer is included in the model, since the SEM study, that has been previously discussed for short immersion times and will be given later in this section for standard conversion time, shows that the chromate films are far from uniform.

**Table 5.1:** Results of the fit of the SE spectra with the two-layer optical model given in Figure 5.20 for samples NPCr1.8 and NPDCr1.8.

	<b>NPCr1.8</b>	<b>NPDCr1.8</b>
<b>d<sub>1</sub> (nm)</b>	170.1±2.74	197.3±0.77
<b>d<sub>2</sub> (nm)</b>	35.7±0.72	34.6±0.19
<b>d<sub>tot</sub> = d<sub>1</sub>+ d<sub>2</sub></b>	<u>205.8</u>	<u>231.9</u>
<b>% non-uni</b>	18.88±0.54	17.1±0.14
<b>%-EMA</b>	72.19±0.52	71.9±0.21
<b>A</b>	1.51	1.68
<b>B</b>	0.0527	0.0027607
<b>C</b>	0.000254	0.0051855
<b>MSE</b>	13.74	22.15

The interface layer accounts for either the microscopic substrate roughness or the presence of a very thin and dense barrier layer at the interface chromate film/aluminium. However, the Bruggeman [44] effective medium approximation (EMA) is used in modelling this interface layer. Doing so, the interlayer is assumed to consist of a homogeneous mixture of aluminium and chromium oxide:

$$f_{Al} \frac{\tilde{\epsilon}_{Al} - \tilde{\epsilon}}{\tilde{\epsilon}_{Al} + 2\tilde{\epsilon}} + f_{CrOx} \frac{\tilde{\epsilon}_{CrOx} - \tilde{\epsilon}}{\tilde{\epsilon}_{CrOx} + 2\tilde{\epsilon}} = 0 \quad (5.e)$$

where  $f_{Al}$  and  $f_{CrOx}$  are the volume fraction of aluminium and chromium oxide, respectively,  $\tilde{\epsilon}_{Al}$  and  $\tilde{\epsilon}_{CrOx}$  the dielectric constants of the two phases and  $\tilde{\epsilon}$  the effective dielectric constant of the mixture.

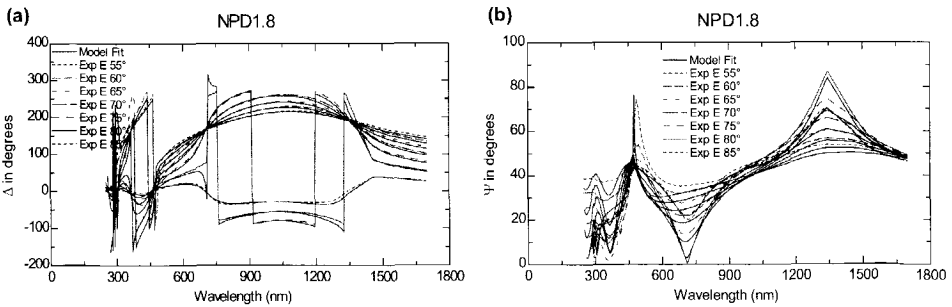


**Figure 5.21:** Experimental and fitted ellipsometric data for sample NPDCr1.8:  $\Delta$  spectra (a) and  $\Psi$  spectra (b).

Summarizing, the parameters to be fitted are the thickness ( $d_1$ ), and the thickness non-uniformity (% non-uni) of the chromate film, the coefficients of the Cauchy dispersion relation

(A, B, and C), the thickness ( $d_2$ ) and the percentage of chromium oxide (%-EMA) of the interface layer. The fit results together with the MSE value (mean square error fit, whose value is equal to 1 for a perfect fit [45]) for both samples are presented in Table 5.1 and the experimental and fitted spectra for sample NPDCr1.8, as an example, are given in Figure 5.21. Keeping in mind the complex nature of the chromate film and the relatively pronounced roughness of the rolled aluminium surface that serves as substrate, the fit of the ellipsometric data can be considered acceptable for an indicative evaluation of the CCC thickness. Figure 5.22 shows the index of refraction ( $n$ ) for the two samples as a function of the wavelength. These are physically meaningful index of refraction spectra, since when no absorption is considered  $n$  should not exhibit strong dispersion and should decrease monotonically with increasing wavelength [46].

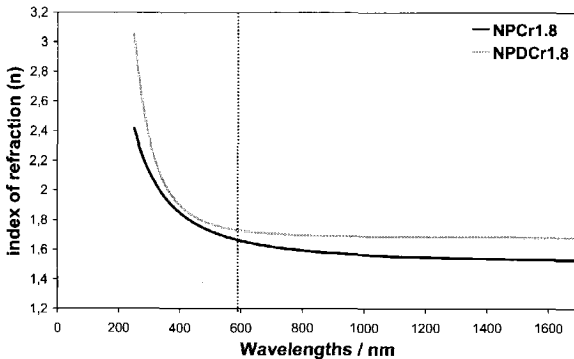


**Figure 5.22:** Refractive indices as a function of the wavelength, obtained using the Cauchy dispersion relation, for samples NPCr1.8 and NPDCr1.8.

In addition, the value of  $n$  at  $\lambda = 600\text{nm}$ , which is the wavelength used in all the references reported below, are 1.66 and 1.72 for samples NPCr1.8 and NPDCr1.8, respectively. These values are in agreement with the interpretation of the IR-SE spectra, reported previously, which considers the chromate films consisting mainly of chromium oxide/hydroxide with certain enrichment in aluminium oxide. Indeed, in

literature values of 2.54, 2 and 1.62 are reported for the refractive indices of  $\text{Cr}_2\text{O}_3$ ,  $\text{CrOOH}$  and  $\text{Cr}(\text{OH})_3$ , respectively [47-49] and that of aluminium oxide and hydroxide was found to be in the range of 1.583 and 1.77 depending on its structure [50]. Besides, the presence of voids in the porous chromate coating is likely the cause of the lower value of  $n$  compared with that of  $\text{Cr}_2\text{O}_3$  found in literature, which is relative to dense and pure chromium oxide [27, 51]. According to this, sample NPDCr1.8 shows a higher refractive index with respect to sample NPCr1.8 as a consequence of the higher density of the CCC formed on the desmuted Al surface, as shown by the SEM study previously described.

In conclusion, the consistency of the values of the refractive indices with the chemical composition of the chromate films is a further proof of the validity of the optical model used to fit the ellipsometric spectra. This is also confirmed by the comparison of the thicknesses of the film obtained by the fitting of the SE spectra (row 3 of Table 5.1) with the values measured using other techniques, specifically RBS and GDOES depth profiles, SEM and TEM study of the ultramicrotomed cross sections (Figure 5.23).

Taking into account that inherent to each method some errors can be present in the thickness estimation, the values relative to each sample obtained by these different techniques show a good accordance. It can be noted that while all the different methods show a higher thickness of the chromate film deposited on the desmutted surface (sample NPDCr1.8) with respect to that deposited on the pickled surface (sample NPCr1.8), such difference is quite limited, about 25-50 nm. Since this range is very close to the limit of reproducibility of the different techniques, an absolute statement of the formation of a thicker chromate film when a desmutting step is carried out during the surface preparation procedure cannot be made.

- *TEM and SEM investigation*

The TEM investigation (Figure 5.24) confirms the duplex structure of the chromate film formed on aluminium alloys. Indeed, it is evident the presence of a thin (10-20 nm) and dense layer, called barrier layer (BL), at the interface between the aluminium substrate and a more porous and thicker film, named porous layer (PL), on top of it. The porous film is characterized by a columnar structure and by the presence, through its whole thickness, of trenches, which are likely the cracks formed during the drying step.

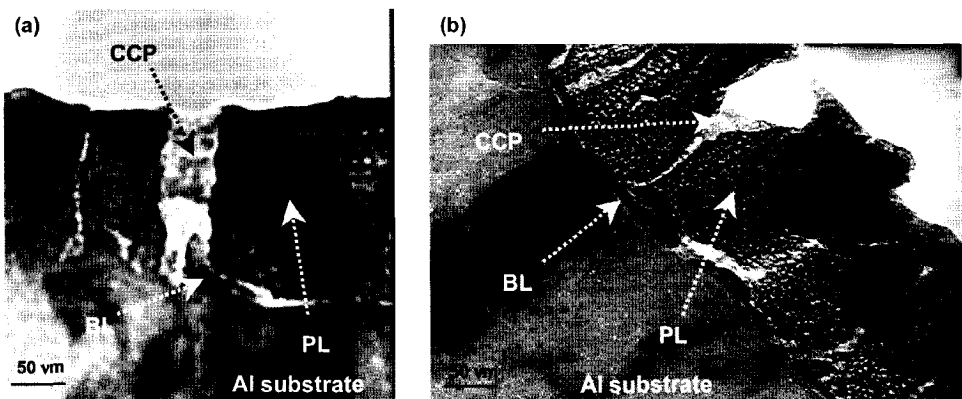


**Figure 5.24:** TEM micrographs of the ultramicrotomed cross section of samples NPCr1.8 (a) and NPDCr1.8 (b). BL = barrier layer, CCP = chromate corrosion products, PL= porous layer.

In addition to these large defects, which are in some cases partially filled by chromate corrosion products (CCP), the porous layer contains also small pores of size in the order of nanometers or tenths of nanometers. These pores are a consequence of the growth of the layer through the deposition and coalescence of small spherical particles, as described in the previous section. The corrosion products are likely formed during the sample preparation, which involves the floating of the thin slides in water prior to be collected on the copper grid. These products are defined chromate corrosion products based on the results reported in literature and discussed in section 3.2.2 of chapter 3.

It is important to note that the barrier layer is present not only at the bottom of the large defects of the porous layer but along the whole interface Al substrate/porous chromate film. According to the literature (see section 3.2.1 of chapter 3) the barrier layer could consist of either aluminium oxy-fluorides or a mixed aluminium/chromium oxide. Therefore, the origin of this thin and dense film is not completely clear, since in the first case (aluminium oxy-fluorides) it would be a consequence of the incomplete removal of the natural aluminium oxide by the fluoride species present in the chromate bath, whereas in the second case (mixed aluminium/chromium oxide) it would be formed during the early stages of the chromate film deposition. In view both of the EDS analyses that detected chromium also at the bottom of the large defects and of the thickness of the barrier layer, higher than expected for the natural oxide on an etched surface, it is more probable that under the treatment conditions used in the present study the barrier layer derives from the initial fast precipitation of chromium hydroxide. This was already suggested in section 5.3.2 according to the morphology of the chromate film as function of the duration of the chromate treatment.

The TEM study shows that the CCC deposited on the Al surface after the pickling treatment (sample NPCr1.8) has a thinner and less continuous barrier film and larger and more numerous defects are present in the porous layer in comparison with the CCC deposited after the pickling+desmutting procedure (sample NPDCr1.8). Although part of those large defects could be a consequence of the ultramicrotomed cross section preparation, the larger amount observed for sample NPCr1.8 is likely related to the presence of intermetallic particles on the substrate surface of this sample. This appears clearly during the SEM investigation, which shows that even after the immersion in the Alodine bath for 3 minutes the location of the IMCs is easily identified on the surface of sample NPCr1.8 (Figure 5.25).

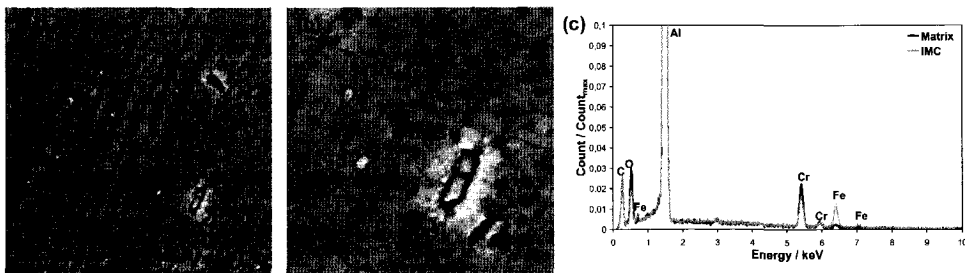
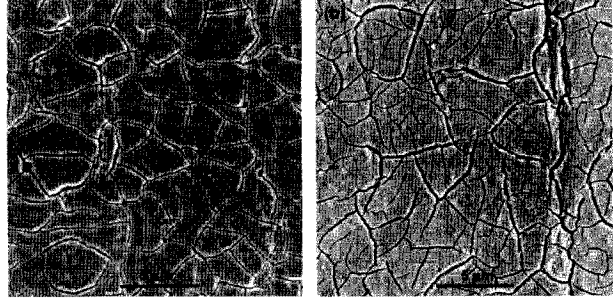


Figure 5.25: SEM micrographs (a, b) and EDS spectrum (c) of sample NPCr1.8.



As already discussed in the previous section, this is a consequence of the heterogeneous nucleation of the chromate film caused by the intermetallics that act as cathodic sites. Indeed, even if the chromate film covers the IMCs (EDS spectra of Figure 5.25-c), a lack of continuity in the layer is present at their periphery, which gives rise to large defects (Figure 5.25-a and -b).

Whereas, the homogeneous nucleation occurring on the desmuted surface, where the IMCs are almost completely removed, leads to the formation of a more homogeneous CCC (sample NPDCr1.8), in which the main defects are related to the cracks caused by the stresses induced in the film during the drying step (Figure 5.26-a).



**Figure 5.26:** SEM micrograph of samples NPDCr1.8 (a) and SPDCr1.8 (b).

The negative effect of the intermetallic particles on the homogeneity of the chromate layer is confirmed by the SEM study of the chromate film formed in standard condition ( $t = 3$  minutes and  $\text{pH} = 1.8$ ) on the Alclad 2024 alloy after either a long pickling treatment (sample SPCr1.8, Figure 5.27) or a long pickling process followed by a desmutting step (sample SPDCr1.8, Figure 5.26-b). Indeed, in section 5.3.1 it has been shown that when the time of immersion in the pickling treatment is increased from 5 to 20 minutes the IMCs are only partially removed. This results in the formation of a chromate film containing deep and large defects, less in number with respect to sample NPCr1.8, in proximity of the intermetallics (Figure 5.27-a and -b). On the other hand, when a desmutting process is carried out after the acid pickling step, the Al surface becomes free of IMCs and a CCC being very homogeneous is deposited on the surface (Figure 5.26-b).

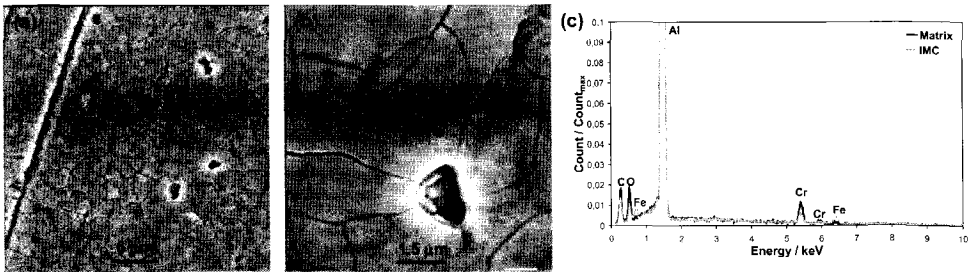


**Figure 5.27:** SEM micrographs (a, b) and EDS spectrum (c) of sample SPCr1.8.

The chromium and oxygen peaks of the EDS spectra given in Figures 5.25-c and 5.27-c show that although the CCC starts to form first above the IMCs, after a relatively long immersion in the chromate bath it is thinner at these sites in comparison with that deposited on the aluminium matrix. This is likely due to a modification of the electrochemical nature of the intermetallics after being covered by the CCC, which renders them less active. A more

detailed discussion of this topic will be given in chapter 7, which deals with the formation of the chromate film in the case of bare 2024 alloy.

- *AFM investigation*

The average values of the roughness, which were calculated for each sample using various AFM topographic images and are expressed as the standard deviation of the height

**Table 5.2:** RMS values of the CCC formed after different surface preparation procedure.

	NPCr1.8	NPDCr1.8	SPCr1.8	SPDCr1.8
<b>RMS<sub>10</sub> (nm)</b> <b>A = 10 x 10 μm</b>	58.1	30.4	46.7	34.5
<b>RMS<sub>1</sub> (nm)</b> <b>A = 1 x 1 μm</b>	16.2	9.8	12.1	10.4

values (RMS), are given in Table 5.2. The first row (RMS<sub>10</sub>) is relative to the values obtained on the total AFM image with a size of 10x10 μm, whereas the second row (RMS<sub>1</sub>) gives the values obtained on a smaller area, 1x1 μm in

size, that does not contain large defects, as shown in Figure 5.28 for sample NPCr1.8.

The CCC formed after the acid pickling treatment, especially when a short time of immersion is used (sample NPCr1.8), is characterized by a higher roughness, both on the large and small areas, with respect to the chromate film formed on the desmutted surfaces (samples NPDCr1.8 and SPDCr1.8). The higher RMS<sub>10</sub> for the samples NPCr1.8 and SPCr1.8 is

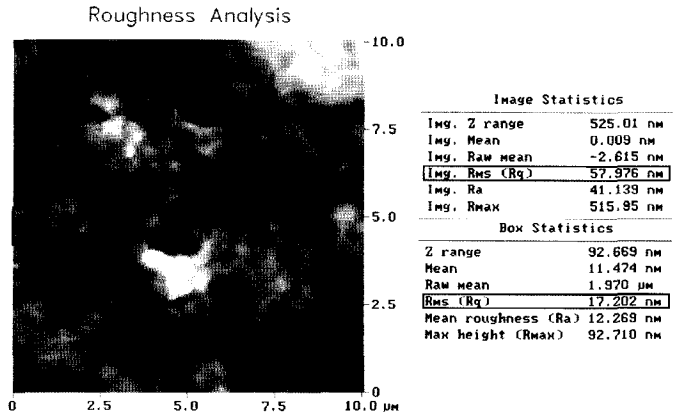


**Figure 5.28:** Roughness calculation based on the AFM topographic image, on the whole area (10x10 μm) and on the small square (1x1 μm).

caused by the presence of large and deep defects associated with the intermetallic particles. This explains also the difference between these two samples, since the substrate of sample SPCr1.8 contains a lower amount of IMCs due to the longer pickling treatment.

On the other hand, the different extent of large defects cannot be responsible also for the different values of RMS<sub>1</sub> shown by the samples, since large discontinuities are not present in the small area. The porosity of the chromate layer, highlighted by the SEM and TEM studies, is more likely to be the cause of the roughness of the chromate films at the nanometer scale. Indeed, when the bearing command is applied on the small area of the AFM image a Gaussian distribution of depth is obtained, which is in accordance with the fact that the porous chromate layer consists of small spherical particles that in turn lead to nanoporosity. Therefore, according to the values of RMS<sub>1</sub> it seems that the CCC of sample

SPCr1.8 and especially of sample NPCr1.8 is more porous than that of samples NPDCr1.8 and SPDCr1.8. The reason for this is not completely understood. One possibility could be a higher solubility in the chromate bath due to a lower homogeneity and stability of the chromate film itself.

Summing up, it has been shown, in accordance with the literature reported in chapter 3, that independently on the surface preparation the CCC formed on Alclad 2024 alloy consists of chromium oxide/hydroxide with chromate and cyanide species adsorbed, contains a certain amount of aluminium oxide at the interface with the substrate, and has a layered structure. A thin and dense barrier layer is in contact with the substrate and on top of it a porous layer containing large defects is formed by precipitation and coalescence of nano-particles spherical in shape. While the surface preparation procedure has only a slight effect on the chemical composition and the thickness of the CCC, it has a strong influence on the morphology of the film. Indeed, more intermetallics are removed by the surface preparation treatment more the nucleation of the chromate layer becomes homogeneous, since the amount of preferential nucleation sites decreases, and more the deposited film becomes uniform and free of large and deep defects. These results highlight the inadequacy of the current standard industrial method used to rank the chromate conversion coating, which is based on an indirect thickness measurement by means of the weight change of the panel during the chromate treatment. Indeed, it has been shown that chromate films with a similar thickness can simultaneously have a completely different density and amount of defects, which is expected to strongly affect the corrosion protection provided by the film, as will be described in the next chapter.

#### 5.3.4 Morphology and composition of the CCC: effect of the chromate bath pH.

The influence of the pH of the conversion bath has been investigated using desmutted Alclad 2024 (sample NPD) as substrate, in order to eliminate any effect related with the presence of the intermetallic particles and therefore to simplify the study by considering only the parameter of interest in this part of the research.

- *OCP monitoring*

Figure 5.29 shows the OCP curves during the immersion in the Alodine bath, the pH of which is varied from 1.2 to 2.4. As discussed in section 5.3.2 the evolution of the OCP during the chromate film formation is characterized by an initial fast decrease, which is related to the activation of the Al surface by the fluoride species, followed by a slower decrease, when the chromate reduction and chromium hydroxide deposition become important, and finally a constant value is reached, which is indicative of a steady-state situation related with a complete coverage of the surface. Until the end of the immersion, the OCP maintains this value, which decreases and is reached after a longer time when the pH of the chromate bath is increased from 1.2 to 2.4 (see arrows in Figure 5.29). These effects of the pH, i.e.  $H^+$  ions concentration, on the OCP evolution are due to the fact that the chemical reactions, which occur both during the activation of the aluminium surface (reactions 5.1-5.5) and during the formation of the CCC (reactions 5.7 and 5.8) involve  $H^+$  ions.

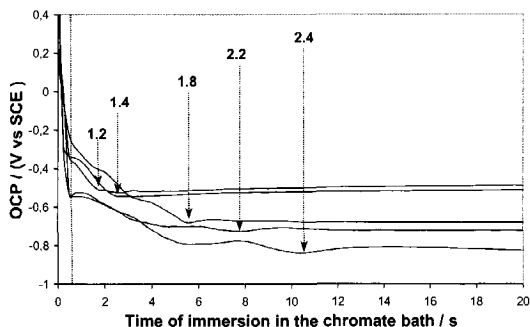


**Figure 5.29:** OCP evolution during the immersion in the chromate bath at different pH.

Indeed, a decrease of pH accelerates the activation of the aluminium surface due to the synergetic effect between  $F^-$  and  $H^+$  ions both in the chemical dissolution of the Al oxide and the electrochemical attack of Al. Besides, a higher amount of  $H^+$  ions favours the occurrence of the cathodic reactions, either the reduction of the chromate species (reactions 5.7 and 5.8), which predominates during the film formation, or the hydrogen evolution, which predominates during the initial surface activation. Assuming that the extent of the anodic and cathodic areas is not affected by the pH of the bath, a lower pH, i.e. higher  $H^+$  concentration, results in a higher value of the nearly constant OCP, as a consequence of a higher cathodic current, and a more rapid achievement of this value due to a faster activation of the surface and reduction of chromate species that lead to a faster coverage of the surface.

However, the higher OCP at the end of the initial surface activation (interceptions with the dashed line in Figure 5.29) shown by the samples treated at low pH seems to be in contradiction with the stronger attack of the fluoride species when the pH is decreased. Indeed, Goeminne *et al.* [25] have shown that the increase of HF concentration, i.e. increase of  $F^-$  attack, lowers the value of OCP at the end of the surface activation. Nevertheless, from the thermodynamic of the conversion solution, these authors found that  $[HF]$  does not affect the pH and the Cr(VI) concentration and then the cathodic reactions are not significantly changed by the change in HF concentration. Whereas, when the strength of the fluoride attack is enhanced by a decrease in pH, as in the present work, the increase in cathodic current caused by the increased concentration of  $H^+$ , which leads to an increase of the OCP, is likely preponderant to the increase of the anodic current caused by the stronger fluoride attack, which leads to a decrease of the OCP. As consequence, the decrease in pH has as net result an increase of the value of OCP at the end of the surface activation.

- *Spectroscopic ellipsometry in the IR region*

The stronger attack of the aluminium oxide and the faster reduction of Cr(VI) species caused by the decrease in pH of the chromate bath influence the chemical composition and the morphology of the chromate film deposited on the Al surface. The IR-SE spectra of the ellipsometric angle  $\Psi$  for the CCCs formed using different pH of the bath are given in Figure 5.30. All the spectra show the absorption peaks already observed for samples NPCr1.8 and NPDCr1.8, the assignment of which has been discussed in section 5.3.3.

The chromate film formed at pH 1.2 or 1.4 are characterized by an additional peak at  $555\text{ cm}^{-1}$ , named 1\*, that can be attributed, similarly to peaks 1 and 2, to  $Cr_2O_3 \cdot 2H_2O$  modes

[29, 33-35]. A further difference between the samples is the shoulder at  $840\text{ cm}^{-1}$  (named  $2^*$ ), assigned to Cr(VI)-O vibration, which is more evident for the samples treated using a low pH in the chromate bath.

It is important to note that this feature is observed also in the measurements taken at high angle of incidence ( $85^\circ$ ), at which the influence of the film thickness on the intensity of the peaks is less pronounced. Thus, the presence of this shoulder in the spectra of the samples chromated at pH 1.2, 1.4, and 1.8, is not due to the higher

thickness of the CCC on these samples, which will be discussed later in the section, but likely to a real higher quantity of Cr(VI) species adsorbed in the film. The increase of adsorbed Cr(VI) with the decrease of the pH of the chromate bath is in agreement with the results of other researchers [52] and the dynamic equilibrium between Cr(III)/Cr(VI) mixed oxide and soluble Cr(VI) proposed by Xia *et al.* [34], which was discussed in section 3.2.1 of chapter 3:

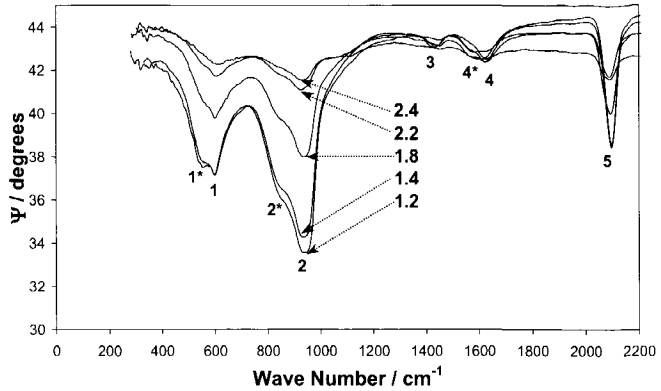
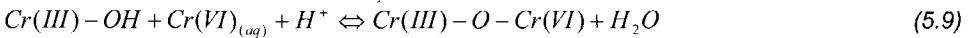


Figure 5.30: The  $\Psi$  IR-SE spectra, using  $75^\circ$  as angle of incidence, of the CCC formed at different pH of the chromate bath.

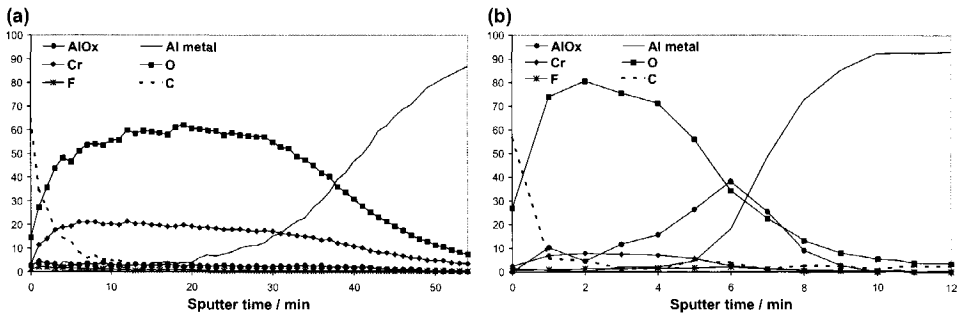


Figure 5.31: AES depth profiles of samples NPDCr1.2 (a) and NPDCr2.4 (b).

Some other differences between the samples can be observed in the spectral range between  $1200$  and  $2000\text{ cm}^{-1}$ . When the pH used in the chromate bath is increased, especially above 1.8, the intensity of the peak at  $1427\text{ cm}^{-1}$  (peak 3) decreases and the peak at  $1620\text{ cm}^{-1}$  (peak 4) becomes very broad and has a shoulder that is extended until  $1573\text{ cm}^{-1}$  (named  $4^*$ ). In the previous section the peak  $4^*$  has been attributed to  $\text{Al}=\text{O}\cdot\text{H}_2\text{O}$

stretch. This assignment is supported by the AES depth profiles, which show the presence of aluminium oxide at the interface chromate film/aluminium substrate only for the samples chromated using a bath with pH higher than 1.8, i.e. samples showing the shoulder at  $1573\text{ cm}^{-1}$ . This can be observed in Figure 5.31, where the AES measurements are given for samples NPDCr1.2 and NPDCr2.4. The absence of aluminium oxide in the CCC formed at low pH (1.2 and 1.4) suggests also that the peak at  $1427\text{ cm}^{-1}$  (peak 3) is caused by  $\text{Cr}_2\text{O}_3 \cdot 2\text{H}_2\text{O}$  modes rather than by the bending vibration of water co-ordinated to aluminium oxide.

The AES and IR-SE results bring to the conclusion that when the pH of the Alodine solution is adjusted at values equals or above 1.8, the synergetic effect between  $\text{F}^-$  and  $\text{H}^+$  ions is not strong enough to completely remove the natural aluminium oxide film prior to the start of the deposition of the chromium oxide/hydroxide, leading to the presence of a thin layer of Al oxide at the interface between the substrate and the CCC.

- *Spectroscopic ellipsometry in the UV-vis-NIR region*

The thickness of the chromate films formed at different pH was calculated fitting the ellipsometric spectra in the UV-vis-NIR range using the optical model given in Figure 5.20 and previously described. The accuracy of the fit decreases for samples chromated at lower pH, as can be noted from the MSE values reported in Table 5.3 together with the values of all the other parameters used in the fit.

**Table 5.3:** Results of the fit of the SE spectra with the two-layer optical model given in Figure 5.20 for the CCC formed at different pH of the chromate bath.

	<b>NPD1.2</b>	<b>NPD1.4</b>	<b>NPD1.8</b>	<b>NPD2.2</b>	<b>NPD2.4</b>
<b>d<sub>1</sub> (nm)</b>	471.4±2.76	477.6±3.61	197.3±0.77	97.4±0.73	66.9±0.32
<b>d<sub>2</sub> (nm)</b>	43.9±0.41	37.9±0.33	34.6±0.19	19.4±0.12	15.2±0.13
<b>d<sub>tot</sub> = d<sub>1</sub> + d<sub>2</sub></b>	<u>515.3</u>	<u>515.4</u>	<u>231.9</u>	<u>116.8</u>	<u>82.1</u>
<b>% non-uni</b>	16.7±0.24	16.9±0.03	17.1±0.14	15.7±0.74	10.3±0.1
<b>%EMA</b>	73.8±0.19	74.2±0.21	71.9±0.21	80.2±0.36	69.9±0.98
<b>A</b>	1.516	1.532	1.68	1.668	1.63
<b>B</b>	0.031467	0.037339	0.0027607	0.014568	0.015511
<b>C</b>	0.0067877	0.0024346	0.0051855	0.00014085	0.00019268
<b>MSE</b>	38.97	44.03	22.15	3.746	4.642

The increase of the MSE value especially for samples NPDCr1.2 and NPDCr1.4 is likely due to an increase of the roughness of the CCC when the pH of the bath is decreased, which will be shown later in the section. However, another reason for the worsening of the fit for these samples is the larger number of maxima in their  $\Psi$  spectra and larger number of minima in their  $\Delta$  spectra that cannot be modelled perfectly. Nonetheless, the thicknesses obtained can still be considered as a good estimation.

The validity of the fit is confirmed by the values of the indices of refraction ( $n$ ) for the different samples (Figure 5.32), which are all consistent with the chemical composition of the chromate film. The value of  $n$  at 600 nm varies from 1.66 (samples NPDCr1.2, NPDCr1.4, and NPDCr2.4) to 1.72 (samples NPDCr1.8 and NPDCr2.2), which is in accordance with the

values reported in literature for Cr and Al oxides/hydroxides. The lower value of  $n$  obtained for samples chromated at pH 2.4, 1.2, and 1.4 is believed to be due to different reasons.

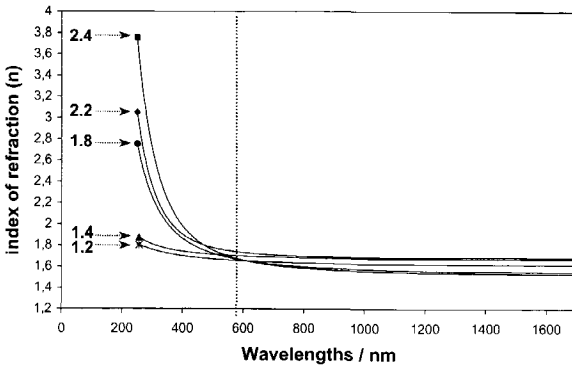


**Figure 5.32:** Refractive indices as function of the wavelength, obtained using the Cauchy dispersion relation, for the CCC formed at different pH of the chromate bath.

and NPDCr1.4, the thickness of which is much higher than 100 nm, the lower value of  $n$  can have several physical causes: a larger amount of fluoride species, since the index of refraction for  $\text{AlF}_3 \cdot \text{H}_2\text{O}$  ranges between 1.473 and 1.511 [49]; a larger amount of chromate species adsorbed in the film [27], the lower density of the film of these samples [27, 51], as will be shown later. The former explanation is quite improbable because the AES measurements do not show evident differences in the fluoride content amongst the films formed at different pH of the Alodine solution.

The fitting of the SE spectra, in agreement with the SEM investigation of the ultramicrotomed cross sections and the GDOES depth profiles, show that the decrease of the pH of the chromate bath results in an increase of the thickness of the CCC deposited on the Alclad 2024 alloy surface. In addition, while the changes of pH from 2.2 to 1.8 and from 1.8 to 1.4 cause a very strong increase in thickness, when the pH is varied from 2.4 to 2.2 or from 1.4 to 1.2 the thickness is only slightly affected (Figure 5.33). The observed increase of the thickness with the decrease of the pH of the Alodine solution can be explained considering

In the case of sample NPDCr2.4 the decrease in the value of  $n$  is likely an artefact introduced by the small thickness of this film (row 3 of Table 5.3). Indeed, it has been found that the index of refraction and the layer thickness become correlated for coatings thinner than 100 nm [53], which means that a decrease in the thickness causes a decrease of  $n$  in the fitting procedure. Whereas, in the case of samples NPDCr1.2

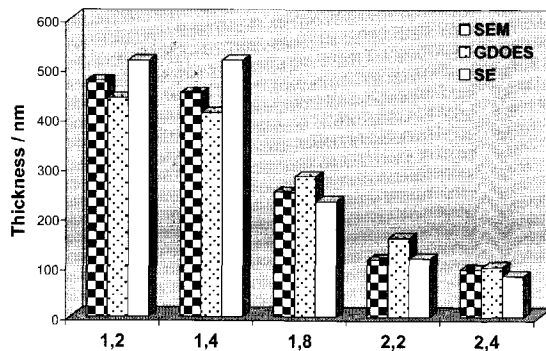
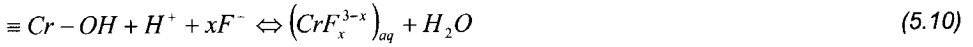


**Figure 5.33:** Thickness of the CCC formed at different pH of the chromate bath, obtained using different techniques: SEM study of the cross sections, GDOES depth profiles, and fitting of SE spectra.

The observed increase of the thickness with the decrease of the pH of the Alodine solution can be explained considering

that the growth of the chromate film reaches a steady state situation when the rate of chromium hydroxide deposition (reactions 5.7 and 5.8) equals the rate of dissolution of this oxide:



Theoretically, an increase of  $H^+$  concentration, i.e. decrease of pH, would result in an acceleration of the chromate film deposition, due mainly to a faster and stronger surface activation and to a speed up of reactions 5.7 and 5.8, but also in a higher rate of film dissolution, since it favours reaction 5.10. However, since chromium hydroxide is much more resistant to fluoride attack than aluminium oxide/hydroxide [54], it is expected that the change of the pH from 2.4 to 1.2 does not increase significantly the dissolution of  $Cr_2O_3 \cdot 2H_2O$ , as on the contrary happens in the case of  $Al_2O_3 \cdot 3H_2O$ . As a consequence, the effect of the decrease in pH on the surface activation and on the rate of reactions 5.7 and 5.8 overrules that on the rate of reaction 5.10 and thus the net result of the change in pH of the Alodine bath from 2.4 to 1.2 consists of the increase of the rate of chromate film formation, i.e. thickening of the film.

- *SEM and AFM investigation*

The SEM micrographs of Figure 5.34 and the AFM topographic images of Figure 5.35 show that when the pH of the Alodine solution is decreased the chromate film obtained is not only thicker but contains also more numerous and larger cracks.

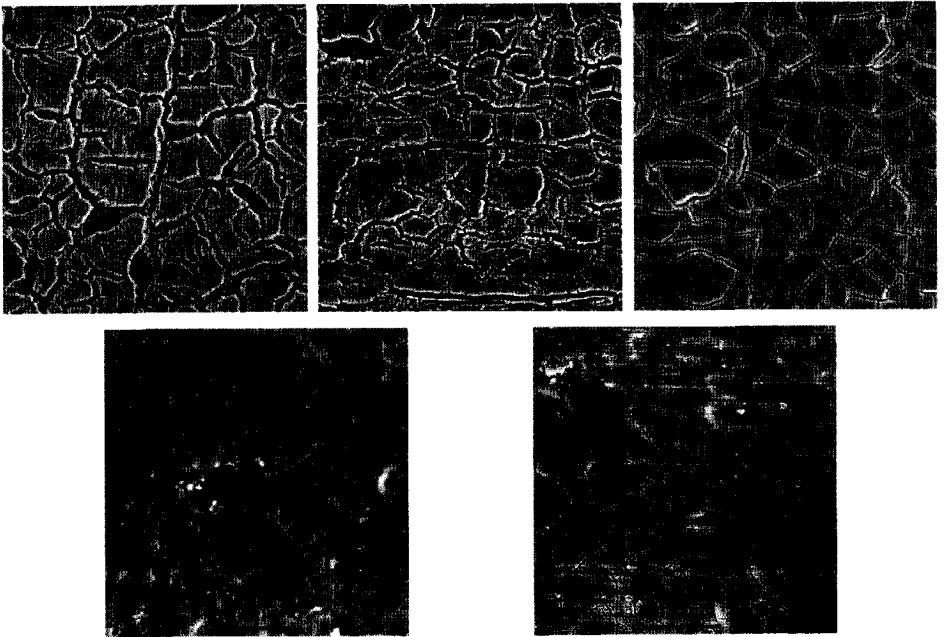


**Figure 5.34:** SEM micrographs of the CCCs formed at different pH of the chromate bath: 1.2 (a), 1.4 (b), 1.8 (c), 2.2 (d), and 2.4 (e).



The two phenomena, i.e. higher thickness and cracks density, are likely related. Indeed, the stresses induced during the final drying step of the chromate treatment become stronger in thicker films and therefore lead to cracks being wider and higher in number.

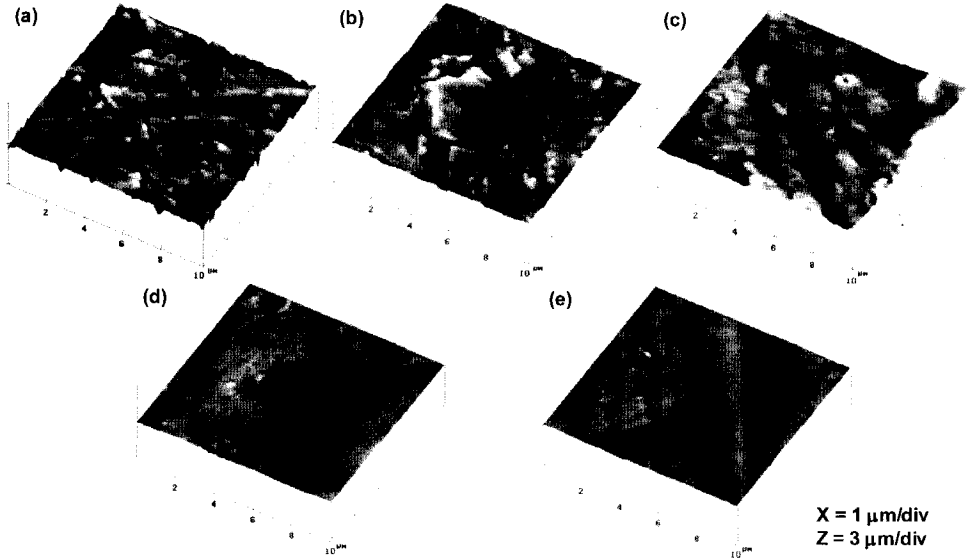


**Figure 5.35:** Topographic images of the CCC formed at different pH of the chromate bath: 1.2 (a), 1.4 (b), 1.8 (c), 2.2 (d), and 2.4 (e).

This is reflected in the roughness of the chromate layer at a micrometer scale, which increases going from sample NPDCr1.2 to sample NPDCr2.4, as can be seen by the  $RMS_{10}$  values given in Table 5.4. In addition, also the nano-porosity of the film seems to be affected by the variation of the chromate solution pH. In particular, the  $RMS_1$  parameter is found to be inversely proportional to the pH of the Alodine bath (second row of Table 5.4).

**Table 5.4:** RMS values for the CCC formed at different pH of the chromate bath.

	NPDCr1.2	NPDCr1.4	NPDCr1.8	NPDCr2.2	NPDCr2.4
$RMS_{10}$ (nm) A = 10 x 10 μm	97	50	30.4	20.7	17
$RMS_1$ (nm) A = 1 x 1 μm	28	14.5	9.8	7.8	5.4

As already observed in the previous section, according to the calculation method used the value of  $RMS_1$  does not depend on the large cracks present in the CCC, whereas it does depend on the nano-porosity of the film. Therefore, a decrease in pH of the chromate bath results in a chromate layer being more porous at a nanometre scale.

Summarizing, varying the pH of the Alodine solution from 2.4 to 1.2 leads to changes in the chemical composition and morphology of the CCC deposited on Alclad 2024 alloy: higher amount of Cr(VI) species adsorbed, lower amount of aluminium oxide at the interface

film/substrate, higher thickness, higher density of larger cracks, and more pronounced nano-porosity.

## 5.4 Conclusions

The surface preparation procedure before immersion in the chromate bath has been shown to play an important role in determining the nucleation and growth mechanisms of the CCC formed on Alclad 2024 alloy and as a consequence it affects the final properties of the film. This is due to the large modifications in the microstructure of the surface caused by the surface preparation treatments. Specifically, the immersion in the nitric/hydrofluoric acid bath, i.e. the desmutting treatment, after the acid pickling step (dipping in a sulfuric/phosphoric acid bath) results in an almost complete removal of the intermetallic particles, which act as cathodic sites, due to the local dissolution of the matrix at their periphery that leads to the drop out of the IMCs themselves. A similar effect, but on a lower extent, is caused by the increase of the time of immersion in the pickling solution from 5 to 20 minutes. The removal of the intermetallics from the aluminium surface results in the change of the nucleation mechanism from heterogeneous to homogeneous, since local cathodes, where the reduction of chromate species and the deposition of chromium oxide preferentially occur, are not anymore present. This, in turn, leads to the formation of a chromate layer being more homogeneous, denser, and containing a lower amount of defects. Indeed, the heterogeneous nucleation above the IMCs results in a lack of continuity and in large defects in the CCC in proximity of the intermetallics, which are weak locations in the layer although they are covered by the chromate film.

It has been found that the chromate process parameters, specifically the pH of the bath, also influence the morphology of the CCC. Besides, while the chemical composition and thickness of the film is only slightly affected by the surface preparation procedure, the pH of the Alodine solution has some effects on them. Indeed, the decrease of the pH of the chromate bath from 2.4 to 1.2 results in the thickening of the chromate layer together with the formation of a higher amount of defects and a more pronounced nano-porosity in the film, which has a higher content of Cr(VI) species and a lower content of aluminium oxide at the interface with the Alclad 2024 alloy substrate.

These differences in morphology, thickness, and chemical composition of the CCC have consequences in the corrosion protection provided by the film. This is discussed in the next chapter.

## 5.5 References

- [1] L. Friberg, G.F. Nordberg, V.B. Vouk, *Handbook of Toxicology of Metals*, Vol. II, Elsevier, Amsterdam, NL (1986)
- [2] Report by the Air Force Blue Ribbon Advisory Panel on Aircraft Coatings (1995)
- [3] G. Goeminne, PhD thesis, Vrije Universiteit Brussel, Belgium (1999)
- [4] M.S. Hunter, A.M. Montgomery, G.W. Wilcox, *Aluminium: Physical Properties and Metallurgy*, 6<sup>th</sup> edition, J.E. Hatch (ed.), Metals Park, Oh (1984)
- [5] Materials Safety Data Sheet for Alodine 1200

- [6] S. Wernick, R. Pinner, *The Surface Treatment and Finishing of Aluminium and its Alloys*, 5<sup>th</sup> edition, Finishing Publication, Teddington, UK (1986)
- [7] Digital Instruments, *Atomic Force Microscopy: Command Reference Manual*, Version 4.10, published by Digital Instruments (1995)
- [8] P. Skjerpe, J. Gjonnes, *Ultramicroscopy* 22 (1987) 239
- [9] *Special Metals Handbook: Aluminium and Aluminium Alloys*, J.R. Davis (ed.), Materials Park: ASM International (1994)
- [10] R.M.K. Young, T.W. Clyne, *Scr. Metall.* 15 (1981) 1211
- [11] K.R. Trethewey, J. Chamberlain, *Corrosion for Science and Engineering*, 2<sup>nd</sup> ed., Longman, Essex, UK (1995)
- [12] *Encyclopaedia of Electrochemistry of the Elements*, A.J. Bard (ed.), Vol. 6, Marcel Dekker, New York, USA (1976)
- [13] V. Zutic, W. Stumm, *Geochim. Cosmochim. Acta* 48 (1984) 1493
- [14] T. Valand, G. Nilson, *Corros. Sci.* 17 (1977) 449
- [15] S Spring, K. Wood, *Corrosion* 45 (1989) 354
- [16] A.D. Yfantis, D.K. Yfantis, *Proceedings of the 1<sup>st</sup> International Symposium on Aluminium Surface Science and Technology*, Antwerpen, Belgium (1997) 25
- [17] A. Kolics, A.S. Besing, A. Wieckowski, *J. Electrochem. Soc.* 148 (2001) B322
- [18] G.M. Brown, K. Kobayashi, *J. Electrochem. Soc.* 148 (2001) B457
- [19] Y. Liu, G.E. Thompson, P. Skeldon, C.J.E. Smith, K. Shimizu, Y. Kihn, *Proceedings of the 2<sup>nd</sup> International Symposium on Aluminium Surface Science and Technology*, Manchester, England, UK (2000) 473
- [20] J.R. Waldrop, M.W. Kendig, *J. Electrochem. Soc.* 145 (1998) L11
- [21] P.L. Hagans, C.M. Haas, *Surf. Interface Anal.* 21 (1994) 65
- [22] W.R. McGovern, P. Schmutz, R.G. Buchheit, R.L. McCreery *J. Electrochem. Soc.* A47 (2000) 4494
- [23] G.P. Halada, C.R. Clayton, M.J. Vasquez, J.R. Kearns, M.W. Kendig, S.L. Jeanjaquet, G.G. Peterson, G.S. McCarthy, G.L. Carr, *Proceedings of the Electrochemical Society Meeting: Passivity and Localized Corrosion: International Symposium in Honor of Professor Norio Sato* Honolulu, Hawaii 27 (1999) 313
- [24] L. Juffs, A.E. Hughes, S. Furman, P.J.K. Paterson, *Proceedings of the NACE Meeting: Corrosion2000*, Orlando, US (2000)
- [25] G. Goeminne, A. Hubin, H. Terryn, J. Vereecken, *Proceedings of the 1<sup>st</sup> International Symposium on Aluminium Surface Science and Technology*, Antwerpen, Belgium (1997) 153
- [26] J.A. Treverton, M.P. Amor, *J. Mater. Sci.* 23 (1998) 3706
- [27] T. Schram, J. De Leat, H. Terryn, *Thin Solid Films* 313-314 (1998) 727
- [28] G. Goeminne, J. De Leat, H. Terryn, J. Vereecken, *Surf. Interface Anal.* 22 (1994) 445
- [29] T. Schram, PhD thesis, Vrije Universiteit Brussel, Belgium, 1998-1999
- [30] J. De Laet, J. Vanhellefont, H. Terryn, J. Vereecken, *Thin Solid Films* 233 (1993) 58
- [31] J. De Laet, J. Vanhellefont, H. Terryn, J. Vereecken, *Appl. Phys.* 54A (1992) 72
- [32] R.M.A Azzam, N.M. Bashara, *Ellipsometry and Polarized Light*, North-Holland, Amsterdam, (1977)
- [33] M. Handke, A. Stoch, S. Sulima, P.L. Bonora, G. Busca, V. Lorenzelli, *Mater. Chem.* 7 (1982) 7
- [34] L.Xia, R. McCreery, *J. Electrochem. Soc.* 145 (1998) 3083
- [35] N.E. Fouad, S.A. Halaway, M.A. Mohamed, M.I. Zaki, *Thermochim. Acta* 329 (1999) 23
- [36] F. Petit, H. Debontride, M. Lenglet, G. Juhel, D. Verchere, *Appl. Spectr.* 49 (1995) 207

- [37] L. Vlaev, D. Damyanov, M.M. Mohammed, *Colloids and Surface* 36 (1989) 427
- [38] A.M. Ahern, P.R. Schwartz, L.A. Shaffer, *Appl. Spectr.* 46 (1992) 1412
- [39] T. Vaderbergh *et al.*, *An Infrared Spectroscopy Atlas for the Coatings Industry*, Federation of Societies for Coatings Technology, Philadelphia, Pennsylvania, USA (1980)
- [40] H.Dodiuk, A.E. Yaniv, N.Fin, *Appl. Surf. Sci.* 29 (1987) 67
- [41] T. Drozda, E. Maleczki, *J. Radioanal. Nucl. Chem.* 7 (1968) 77
- [42] T. Schram, H. Terryn, *J. Electrochem Soc.* 148 (2001) F12
- [43] D. Y. Smith, E. Shiles, M. Inokuti, *Handbook of optical constants of solids*, Vol.1, E.D. Palik (ed.), Academic Press, San Diego (1998)
- [44] D.A.G. Bruggeman, *Annalen de Physik*, 5 (1935) 636
- [45] *Manual WVASE32™*, J.A. Woollam Co., INC., Lincoln, USA
- [46] L. Ward, *The optical constants of bulk materials and films*, 2<sup>nd</sup> edition, Institute of Physics publications (1994)
- [47] M.A. Grenshaw, R.S. Sirohi, *J. Electrochem. Soc.* 118 (1971) 1558
- [48] S. Haupt, H.-H. Strehblow, *J. Electroanal. Chem.* 228 (1987) 365
- [49] *Handbook of Chemistry and Physics*, 80<sup>th</sup> edition, D.R. Lide (ed.), CRC Press, Boca Raton (1999)
- [50] S. Bertling, *Identification of thin surface films on aluminium with FTIR spectroscopy*, Report NTIS 96 4 (1996)
- [51] P. Hones, M. Diserens, F. Levy, *Surf. Coat. Technol.* 120-121 (1999) 277
- [52] A.J. Bosch, T. Zuidwijk, A. Hovestad, TNO Industrie-Eindhoven, Internal report 99MI-00761/HOV/HOV (1999)
- [53] S.F. Fang, W. Chen, Y. Yamanaka, C.R. Helms, *J. Electrochem. Soc.* 144 (1997) L231
- [54] I. Barin, O. Knacke, *Thermodynamic Properties of Inorganic Substances*, Springer-Verlag, Berlin/Heidelberg and Verlag Stahleisen m.b.H., Düsseldorf, Germany (1973)

# Microstructure and chromate conversion coating-Alclad 2024

## II. Corrosion protection

### 6.1 Introduction

In chapter 5 it has been shown that both the surface preparation procedure and the chromate process conditions, specifically the pH of the Alodine bath, affect the morphology and chemical composition of the CCC formed on Alclad 2024 alloy. In particular, the amount of large defects, the extent of nano-porosity, the thickness, the content of Cr(VI) species and aluminium oxide are changed. The present chapter deals with the consequences of these variations on the corrosion resistance of the chromate film and based on this a model of the corrosion protection mechanism of the chromate conversion coating on aluminium is proposed.

The corrosion behaviour of the chromated aluminium surface has been investigated by means of electrochemical impedance spectroscopy (EIS), which is a small signal perturbation technique extensively used to study the electrochemical processes occurring at metal surfaces. The characterization of either chemical [1-5] or anodic [6, 7] surface treatments for aluminium alloys is amongst the various applications of this technique. When the measurements are carried out in aggressive electrolytes, the fit of the EIS data to a theoretical equivalent circuit enables to gain information regarding the corrosion behaviour of the conversion film. However, in order to confirm the interpretation of the fitting results complementary techniques are necessary. In the present study, the choice of a suitable equivalent circuit is based on a physical model of the chromate layer, which was derived from the SEM and TEM investigations and has been described and discussed in the previous chapter. In addition, the differences in corrosion resistance amongst the different chromate coatings derived by the interpretation of the fitting results were checked by means of a SEM study carried out after the impedance experiments and were supported by electrochemical noise measurements. This additional electrochemical technique was chosen since it has been shown to be a useful method in the investigation of the onset of localized corrosion [8-11]. Therefore, in principal, it should be a suitable technique to study the corrosion behaviour of the chromate conversion coating on aluminium alloys, since the corrosion phenomena taking place at these surfaces are certainly not uniform all over the exposed area but localized at the defects always present in the chromate film.

The next section describes the principles and the experimental procedure of both the impedance and the electrochemical noise methods. Whereas the results of these investigations are given and discussed in section 6.3, after the description and explanation of the equivalent circuit used to fit the impedance data. Similarly to the morphology and chemical composition of the chromate film, discussed in the previous chapter, the results concerning the corrosion protection provided by the layer are divided into two parts. While the first deals with the effect of the surface preparation procedure, the second focuses on the influence of the pH of the chromate bath.

## 6.2 Experimental procedure

The materials and the surface treatments are described in section 5.2.1 of the previous chapter, while the SEM operation conditions are given in section 5.2.2. In the following of this section the electrochemical techniques used for the study of the corrosion behaviour of the chromate film are described.

### 6.2.1 Electrochemical Impedance Spectroscopy (EIS).

Impedance is the equivalent of resistance in AC conditions and is generally measured under potentiostatic controls, that means a perturbing voltage, which is usually sinusoidal, is applied to the system under study:

$$E = E_0 \sin(\omega t) \quad (6.a)$$

which can be expressed as a complex function:

$$E = E_0 \exp(j\omega t) \quad (6.b)$$

where  $E_0$  is the amplitude of the perturbation,  $\omega$  the frequency expressed in radian per second, and  $t$  the time. If the system is linear, i.e. the potential and current are linearly correlated, the current response will be:

$$I = I_0 \sin(\omega t + \phi) \quad (6.c)$$

which can be expressed as a complex function:

$$I = I_0 \exp(j\omega t - j\phi) \quad (6.d)$$

where  $I_0$  is the current amplitude and  $\phi$  the phase shift between the perturbing potential and the current response. In electrochemical systems a non-linear behaviour is often observed, however if the amplitude of the perturbation is very small (5-15 mV) the system can be considered quasi linear, and equation 6.c is a good approximation of the current response. In this case the impedance, defined as the ratio between potential and current, is given as:

$$Z(\omega) = \frac{E_0}{I_0} \exp(j\phi) = |Z|(\cos \phi + j \sin \phi) \quad (6.e)$$

The impedance can be displayed graphically using either the Nyquist plot, which is the representation in the complex plane, or the Bode plots, in which the logarithm of the modulus of the impedance  $|Z|$ , and the phase angle  $\phi$ , are given as function of the logarithm of the frequency.

The impedance measurements were performed on the chromated samples in an Avesta cell containing ca. 0.3 dm<sup>3</sup> of solution, which was kept at room temperature and purged with nitrogen. The experiments were carried out in 3% NaCl solution with the pH adjusted to a value of 4 by means of proper mixture of HCl and NaOH. A three electrode configuration was employed: chromated Alclad 2024 alloy panel as working electrode, with a surface area of 0.84 cm<sup>2</sup>, a platinum gauze as counter electrode and a silver/silver chloride electrode (Ag/AgCl) as reference electrode. A platinum wire was connected in parallel to the reference electrode wire by means of a 10 nF capacitor in order to avoid high frequency distortions [12]. An electrochemical interface (Solartron 1286 ECI) in combination with a frequency response analyser (Solartron 1255 FRA) was used to apply a small periodic perturbation to the system. The amplitude of the perturbation was 10 mV and the open circuit potential (OCP) was chosen as bias potential. Since the amplitude of the perturbation is very small, several measures were undertaken in order to reduce noise problems as much as possible: Faraday-cage, connection of the ECI/FRA to a clean earth, connection of the computer to the ECI/FRA through optical fibre. The examined frequency range (650 kHz - 10 mHz) was split up in eight parts that differed in the value of integration time, delay time and frequencies per decade. The integration time and the frequencies per decade were decreased going from high to low frequencies. When the frequency of the perturbation exceeded 10 kHz, a delay time was imposed to allow the system to follow the applied perturbation. The measurements started after 30 minutes of OCP monitoring and were carried out during a period of about 60 hours. Each measurement was repeated at least three times and a good reproducibility was obtained. The simulation of the impedance spectra was performed using the Boukamp "Equivcrt" program [13]. The choice of a suitable equivalent circuit to model the physical system under study is discussed later in the chapter. The denotation of the elements in the equivalent circuits defined by Boukamp [13] is used hereafter in the thesis.

### 6.2.2 Electrochemical Noise (EN)

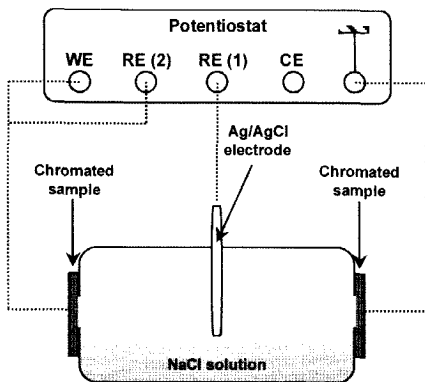


**Figure 6.1:** Scheme of the ZRA set-up. WE=Working Electrode, RE=Reference Electrode, CE=Counter Electrode.

The Zero Resistance Ammetry (ZRA) technique was used to investigate the corrosion behaviour of the chromate conversion coating by means of electrochemical noise measurements. This technique measures the fluctuations of the current flowing between two nominally identical working electrodes connected to the terminals of the ZRA set-up. The existence of current flowing through the system is due to the fact that in real life the two electrodes will be slightly different and the ZRA keeps them at the same potential, measuring at the same time their voltage fluctuations with respect to a reference electrode. Figure 6.1

shows the ZRA set-up used in the present work. The electrochemical noise measurements were carried out on the chromated samples using a Solartron 1286 potentiostat working as a zero resistance ammeter by short-circuiting the working electrode and the second reference electrode outputs, connecting the second working electrode to the chassis ground provided by the instrument, and letting the counter electrode output unused [14]. The experiments were performed using a flat cell, in which the two working electrodes with exposed area of  $1 \text{ cm}^2$  are positioned vertically facing each other at a distance of 10 cm (Figure 6.1). A Ag/AgCl electrode served as reference electrode and the electrolyte consisted in 3.5% NaCl solution, the pH of which was adjusted to a value of 4 by mixing HCl and NaOH. No stirring and de-aeration were undertaken during the experiments, which were repeated at least three times for each sample, and potential and current readings were made every half seconds for a period of 22 hours.

Generally, the analysis of the noise data is made either in the time domain or in the frequency domain. In the first case the noise resistance ( $R_n$ ) is calculated as the ratio of a second-order statistics, often the standard deviation over a fixed period of time, of the voltage fluctuations divided by the same quantity relative to the current fluctuations. If  $R_n$  is calculated over a period of time shorter than the total recording time, it becomes a function of time and its evolution is used to follow the electrochemical behaviour of the system under study. Although, attempts have been made to correlate  $R_n$  with the polarization resistance (zero-frequency limit of the impedance) [15, 16], doubts still exist on the validity of this parameter in describing the corrosion behaviour of the investigated system [17]. Indeed, it should be noted that based on the definition of  $R_n$  two completely different series of current and potential records, e.g. large standard deviation for both current and potential and small standard deviation for both current and potential, can lead to the same value of this parameter, which is then not able to make a clear distinction between different corrosion behaviours.

The analysis in the frequency domain is based on the calculation of the power spectral density (PSD) of the noise using either the fast Fourier transform (FFT) or the maximum entropy method (MEM). In practice, the PSD is measured in a limited frequency bandwidth, where the low frequency limit,  $f_{\min}$ , is the inverse of the measurement time, usually 1 mHz, and the high frequency limit,  $f_{\max}$ , is one-half of the sampling frequency, usually around 1 Hz. Bertocci *et al.* [18, 19] have introduced the parameter called spectral noise impedance ( $R_{sn}$ ) and defined as follows:

$$R_{sn} = \left( \frac{\Psi_V(f)}{\Psi_I(f)} \right)^{1/2} \quad (6.f)$$

where  $\Psi_V$  and  $\Psi_I$  are the PSD of the voltage and the current noise, respectively. The authors found the following correlation between  $R_n$  and  $R_{sn}$ :

$$R_n = \left( \frac{\int_{f_{\min}}^{f_{\max}} \Psi_I(f) R_{sn}^2(f) df}{\int_{f_{\min}}^{f_{\max}} \Psi_I(f) df} \right)^{1/2} \quad (6.g)$$



that shows that  $R_n$  is equal to  $R_{sn}$  only when  $R_{sn}$  does not depend on the frequency in the range  $f_{min} - f_{max}$ . In addition, they have theoretically and experimentally shown that if the two working electrodes have identical impedance much higher than the solution resistance,  $R_{sn}$  is equal to the impedance modulus of the system under study. Therefore, it was stated that the frequency domain analysis can give more information than the time domain one. On the other hand, Motard and co-workers [20] claimed that the signal features of the PSD curves depend on the analysis procedure (FFT or MEM) and are not reliable.

In the present study, the current and potential time records were analysed using both the usual approaches and a more direct evaluation. In some cases the data showed a DC trend in addition to the dynamic noise. Therefore, before each of these analyses any drift of the potential and/or current fluctuations was removed using a linear detrending method, which consists in fitting a linear function to the time record and then subtracting the computed curve so as to keep the residuals.

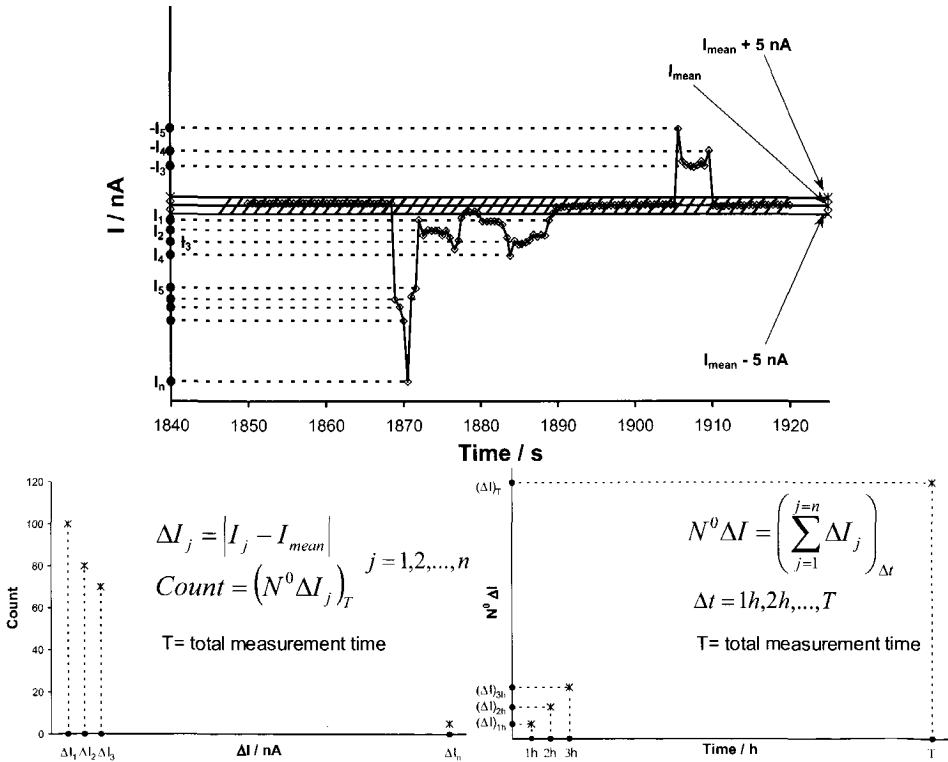


Figure 6.2: Direct evaluation of the raw data of the electrochemical noise measurements.

The usual approaches consisted in processing the data by calculating either  $R_n$ , over a fixed period of time of 3600 seconds, or  $R_{sn}$ , using the PSD curves obtained with the FFT method, in the frequency range:

$$f_{min} = \frac{1}{T} = \frac{1}{3600s} = 0.28mHz \tag{6.h}$$

$$f_{\max} = \frac{1}{2 * T} = \frac{1}{2 * 0.5s} = 1Hz \quad (6.i)$$

where T and t are the measurement and sampling time, respectively.

On the other hand, the direct evaluation of the raw data was carried out by considering the modulus of the deviation of the current from the mean value at each reading (Figure 6.2):

$$\Delta I = |I - I_{\text{mean}}| \quad (6.j)$$

Only deviations higher than 5 nA were taken into account, since for lower values the deviations can be a result of the instrumental noise. Afterwards, the cumulative number of  $\Delta I$  having a certain value was plotted as function of that value and the total number of  $\Delta I$ , independently from the value, was calculated over a period of 60 minutes and given as function of the exposure time (Figure 6.2). These two plots are believed to give information concerning the corrosion susceptibility of the system under investigation. Indeed, the first plot is correlated with the frequency, width, and amplitude of the current transients, which in turn are corrosion events occurring on one of the two working electrodes, and the second one is in relation with the evolution of the corrosion attack with the time of exposure to the aggressive environment. In addition, it was observed that systems, whose different corrosion susceptibility appeared clear from the raw current and potential time records, were better distinguished using this direct evaluation rather than the data processing either in the time or frequency domain. Therefore, in view also of the controversial results found in literature on the validity of  $R_n$  and  $R_{sn}$  in analysing the noise data, in this thesis the direct approach described above is used. However, we are aware that this way of visualizing the results from the ZRA measurements enables only a ranking of the corrosion susceptibility of the samples and does not provide information relative to the mechanism of the corrosion attack. This information can be obtained only from a more detailed analysis of the shape of the current and potential fluctuations that is anyway behind the scope of this PhD project.

### 6.3 Results and discussion

The choice of a suitable equivalent circuit able to model the impedance response of the chromate layer and of the reactions taking place at the samples surface is explained first. Afterwards, the results of the fitting of the impedance spectra and of the direct evaluation of the electrochemical noise measurements are discussed separately for the chromate films formed after different surface preparation procedures and for those formed at different pH of the chromate bath.

In the discussion of the impedance data only the results relative to one set of measurements are shown. However, the conclusions are drawn based on the evolution with the exposure time of the equivalent circuit parameters, whose trend and differences amongst the samples were found to be reproducible. Similarly, a good reproducibility of the variations amongst the different samples of the noise data was found to exist and therefore the discussion is illustrated using only few examples, which are representative for the several measurements that were performed.

### 6.3.1 Choice of a suitable equivalent circuit

Examples of the impedance diagrams (Bode plots) obtained at the beginning and the end of the exposure to the chloride-containing electrolyte are given in Figure 6.3. From the visual analysis of the spectra, especially those relative to short immersion time, two time constants, i.e. relaxations, can be observed and are indicated by arrows.

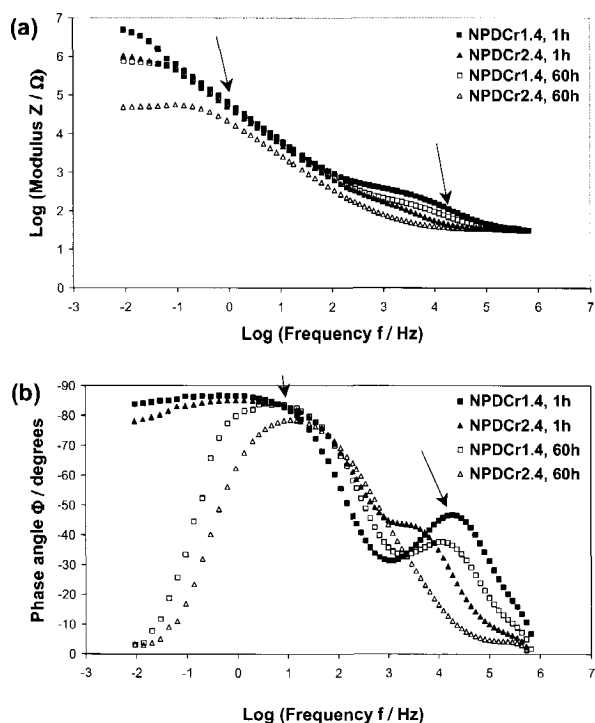


**Figure 6.3:** Bode plots, logarithm of the modulus of the impedance (a) and phase angle (b) vs. the logarithm of the frequency, for samples NPDCr1.4 and NPDCr2.4 at different times of immersion in 3% NaCl pH=4 solution.

The different parameters were interpreted as follows:  $R_1$  models the resistance of the electrolyte, the resistance  $R_2$  and the constant phase element (CPE)  $Q_1$  represent the resistive and capacitive responses of the pores and defects of the layer, whereas the resistance  $R_3$  and the CPE  $Q_2$  are ascribed to the remaining intact conversion layer. The constant phase elements are used instead of capacitors to account for the non-ideal capacitive behaviour of the conversion film, which is often suggested to be related to surface roughness [21-23]. The impedance of a CPE when, as in this case, is considered to be a non-ideal parallel plates capacitor depends on the area ( $A$ ) and the thickness ( $d$ ) of the layer [24]:

$$Z_{CPE} = \frac{1}{Y_0(j\omega)^n} \quad (6.k)$$

$$Y_0 = \frac{\epsilon\epsilon_0}{d} A \quad (6.l)$$

where  $Y_0$  and  $n$  are the admittance constant and the power, respectively, of the CPE,  $\epsilon_0$  the permittivity or dielectric constant of vacuum ( $8.8542 \times 10^{-12}$  F/m), and  $\epsilon$  the relative dielectric constant of the medium, 13.3 and 9.8 for  $\text{Cr}_2\text{O}_3$  and  $\text{Al}_2\text{O}_3$ , respectively. The fitting of our impedance data with the Boukamp program [13] using this equivalent circuit led to values and time evolution of the circuit parameters without any physical meaning.

Another two-time constants equivalent network to model conversion coated Al surfaces was proposed by Goeminne *et al.* [1] and is given in Figure 6.4-b. The authors claimed that  $R_2$  is due to a conductive path in the layer,  $Q_1$  describes a network of electrolyte resistances and double layer capacitors in the pores of the conversion film, whereas  $R_3$  and the ideal capacitor  $C_2$  represents the layer resistance and capacity. Using this equivalent circuit, in which the ideal capacitor is substituted with a CPE, a good fit of our impedance spectra is obtained only for the data relative to a long time of immersion in the aggressive electrolyte. The time after which the data

can be fitted with this model varies from sample to sample. Thus, it is thought that the system, at least during the first hours of immersion, is more complex. Indeed, although the visual evaluation of the impedance diagrams relative to the beginning of the exposure would yield to two time constants, the analysis with the "EQUIVCRT" program leads to the derivation of at least three relaxations. The number of time constants was determined using the "frequency-error" option in the Boukamp program that calculates the difference between the fitted and the experimental data as function of the frequency. When this difference shows a periodicity it means that not all the time constants have been taken into account. Other authors have previously described this method in several publications [25-28].

The transmission electron microscope investigation, which has been discussed in section 5.3.3 of the previous chapter, was then used to build a physical model of the chromate conversion coating/aluminium substrate system in order to figure out a more appropriate equivalent circuit to represent its impedance response. The TEM study shows that the chromate layer consists of a thin and dense layer (barrier layer) covering the whole surface and of a thick layer (porous layer) on top of it that contains small pores and large defects partially filled with corrosion products, which are likely formed during the preparation of the samples with the ultramicrotome technique. Other authors have shown that the corrosion products formed when a chromate film is in contact with an aqueous environment are a mixture of aluminium and chromium oxide and are formed due to leaching and diffusion of Cr(VI) species to the weak locations of the layer, where they can reduce and precipitate as  $\text{Cr}(\text{OH})_3$  and/or adsorb on the aluminium oxide [29]. As concern the barrier layer, it is not clear whether it is the original aluminium oxide film or a mixture of aluminium

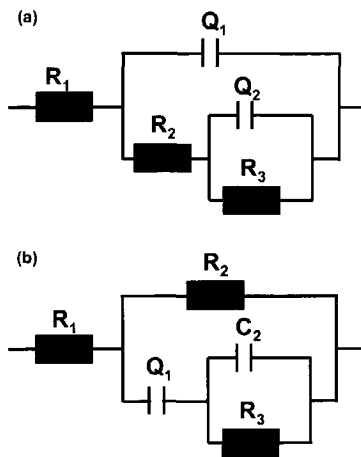


**Figure 6.4:** Equivalent circuits used to model the impedance behaviour of the CCC on aluminium alloys.

oxy-fluoride and chromium oxide. Although our results and those found in literature [30-34] do not unequivocally clarify the nature of this thin and dense film present at the interface substrate/chromate layer, they do show the existence of a layered structure in the CCC formed on aluminium.

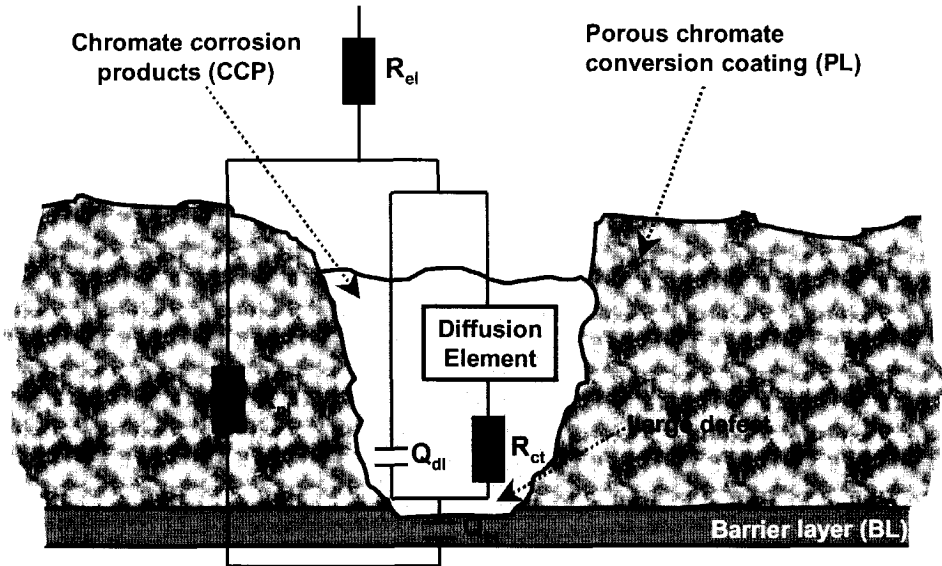


**Figure 6.5:** Schematic illustration of the chromate conversion coating before deterioration together with the equivalent circuit used to model it.

According to our TEM investigation and to the literature discussed in chapter 3 the chromate film on aluminium can be schematically represented as in Figure 6.5 and therefore the more appropriate equivalent circuit to fit the impedance of such complex system should account for several phenomena: the (RQ) responses of the porous chromate layer, of the barrier layer below it, of the barrier layer at the bottom of the defects, the impedance response of the flaws and defects, and the electrochemical reactions occurring during the exposure that can modify the system. However, the impedance measurements cannot reflect all these phenomena, since not all the parameters can be isolated and especially because the measured frequency range is not infinite. This means that very fast or very slow responses are not included in the recorded impedance spectra and as a consequence should not be considered in the equivalent circuit, likewise the parameters that cannot be separated.

Based on these considerations, the equivalent circuit given in Figure 6.5 is proposed to model the impedance behaviour of the chromate conversion coating formed on aluminium. This network is partially derived from the circuit of Figure 6.4-b, the interpretation of which is slightly changed, and is not considered as an absolute model of the CCC/Al system but it well represents its impedance response under the conditions used in the present study and within the frequency range investigated, i.e. from 0.1 Hz up to 650 kHz. It consists of the uncompensated resistance of the electrolyte between the working and counter electrodes

( $R_{el}$ ), a resistor ( $R_{pl}$ ), which models the conductive paths determined by the nano-pores in the porous layer and is placed in parallel with a constant phase element ( $Q_{bl}$ ), which represents the non-ideal capacitive behaviour of the barrier layer at the bottom of the large defects and cracks. Moreover,  $Q_{bl}$  is in series with a (RQ) element describing the electrochemical reactions taking place in the defects of the chromate film. In particular, the charge transfer resistance ( $R_{ct}$ ) is inversely related to the rate constant for the electrochemical reactions [24], whereas the double layer capacitance ( $Q_{dl}$ ) that is also modelled using a constant phase element is related to the amount of surface involved in the corrosion process (equation 6.1).

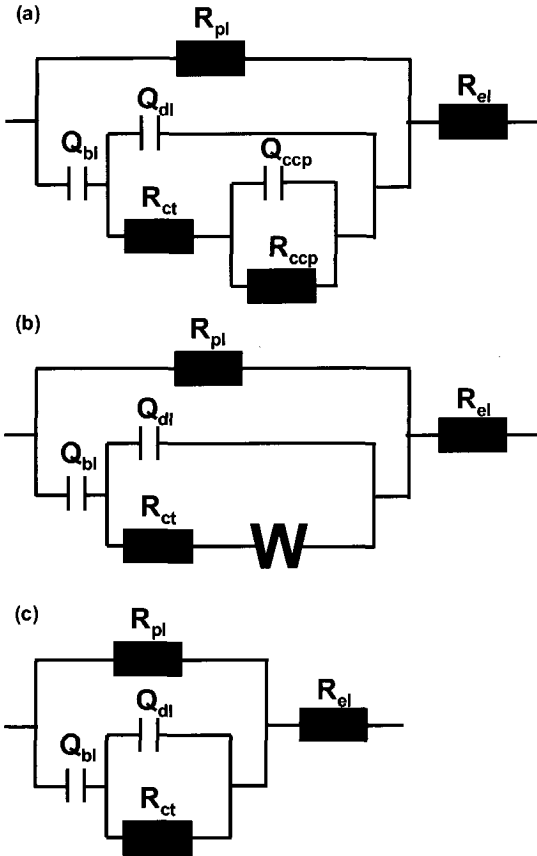


**Figure 6.6:** Equivalent circuits used to model the impedance spectra depending on the type of chromate film and on the time of immersion in 3% NaCl pH=4 solution.

situations are thought to occur during the immersion in the electrolyte:

- ✓ A small amount of CCP is produced inside the defects forming a thin, dense and protective layer that gives rise to a finite length of the diffusion path. This situation is

The main difference between this interpretation of the various circuit elements and that given in [1] is the inversion of the assignment of the two (RQ) elements. Indeed, in this study  $R_2$  and  $Q_1$ , corresponding to  $R_{pl}$  and  $Q_{bl}$ , are ascribed to the chromate layer rather than to the large pores of the film, whereas  $R_3$  and  $C_2$ , corresponding to  $R_{ct}$  and  $Q_{dl}$ , represent the electrochemical processes inside the defects rather than the CCC itself. This was also based on the values obtained for the power  $n$  of the two CPEs: close to 1 for  $Q_{bl}$ , which is typical for films that behave almost as perfect capacitors, ranging between 0.7 and 0.85 for  $Q_{dl}$  that is more usual for the double layer capacitive behaviour.

A further difference between the equivalent circuit of Figure 6.4-b and that of Figure 6.5 consists in the addition of a diffusion element in series with  $Q_{bl}$ , which models the diffusion process through the chromate corrosion products (CCP) formed inside the large defects and then it strongly depends on the nature of CCP. Three different

more probable to take place during the immersion in non- or middle aggressive electrolytes and during the beginning of exposure to aggressive solutions, before the occurrence of strong corrosive attack. In this case the equivalent circuit assumes the form of the circuit in Figure 6.6-a, where the diffusion element consists of a CPE ( $Q_{ccp}$ ) with  $n$  power close to 5 in parallel with a resistor ( $R_{ccp}$ ). Indeed, it was found that in practical situations the finite length diffusion can be reasonably modelled by a (RQ) element instead of an O-element (Open Boundary Finite Length Diffusion OBLFD) [28]. The finiteness of the length of the diffusion path is represented by the resistance, which is inversely proportional to the diffusion rate and directly proportional to the thickness of the diffusion layer [24]. A large increase of the resistance related to the diffusion process indicates that the diffusion path becomes infinite. This can be due both to a thickening of the diffusion layer and/or to a decrease of the diffusion coefficient ( $D$ ) of the charge carriers due to a denser diffusion layer. The impedance response of the diffusion process is represented by the CPE element, whose admittance is proportional to the charge carrier concentrations and to the square root of the diffusion coefficients [24]. The correctness of the interpretation of this additional (RQ) element in comparison with the circuit proposed by Goeminne *et al.* (Figure 6.4-b) is supported by the fact that the  $n$  power of  $Q_{ccp}$  for all the samples was found to range from 0.4 up to 0.6

- ✓ A large amount of CCP is produced resulting in the formation of a thick, porous and less protective layer in the defects of the chromate film that leads to an infinite length of the diffusion path with consequent strong increase of the  $R_{ccp}$  parameter. In this case the RQ parallel circuit becomes equivalent to a simple Q element with the power  $n$  value of 0.5, i.e. a Warburg element (W), in the ideal situation (equivalent circuit in Figure 6.6-b). The admittance  $Y_0$  of a Warburg element depends on the charge carrier concentrations ( $C_{red}$  and  $C_{ox}$ ) and on the diffusion coefficients ( $D_{red}$  and  $D_{ox}$ ), similarly to the CPE element representing the finite length diffusion process [24]:

$$W = \sigma \omega^{-1/2} - j \sigma \omega^{-1/2} = \frac{\sqrt{2} \sigma}{(j \omega)^{1/2}} = \frac{1}{Y_0 (j \omega)^{1/2}} \quad (6.m)$$

$$Y_0 = \frac{1}{\sqrt{2} \sigma} \quad (6.n)$$

$$\sigma = \frac{RT}{n^2 F^2 \sqrt{2}} \left[ \frac{1}{C_{ox} (D_{ox})^{1/2}} + \frac{1}{C_{red} (D_{red})^{1/2}} \right] \quad (6.o)$$

This situation is more probable to occur after a long time of immersion in middle aggressive electrolytes and after a relatively short time of exposure to highly aggressive solutions.

- ✓ A very large amount of CCP is produced that is strongly attacked and results in a very spongy and poorly adherent layer that does not hinder anymore the diffusion of the charge carriers inside the defects. Therefore, the CCP do not provide any protection and the contribution of the diffusion process to the impedance spectra becomes negligible, leading to an equivalent circuit without diffusion element (Figure 6.6-c). This situation is likely to take place after long time of exposure to aggressive electrolytes.

The three equivalent networks of Figure 6.6 have been used to fit the impedance data from 0.1 Hz up to 650 kHz of all the chromated samples at different times of immersion in the chloride-containing electrolyte. In particular, the spectra of some of the samples are best simulated using the circuit of Figure 6.6-a during the first hours of exposure, the circuit of Figure 6.6-b during the middle part of the exposure, and the circuit of Figure 6.6-c during the rest of the immersion. On the other hand, the impedance behaviour of other chromated samples is best described by the circuit of Figure 6.6-b during the first half of the immersion and by the circuit of Figure 6.6-c during the second one. More details concerning each sample will be given in the next two sections prior to the discussion of the fitting results. It is important to note that the comparison between the fitted parameters obtained with the three different circuits is possible, since these circuits differ only in the diffusion related part, whereas the physical interpretation of the other elements remains identical. Besides, the trend of the other parameters is not affected by the change of the diffusion related part of the equivalent circuit; this is also due to the fact that the contribution of the diffusion process to the impedance response takes place at different frequencies than the other phenomena involved.

It should be mentioned that the impedance measurements have been carried out also in a less aggressive electrolyte, namely 0.5M  $K_2SO_4$  pH=4 solution, in order to be able to compare our own results with those reported in literature [1]. Also these impedance spectra could be fitted using one of the equivalent networks given in Figure 6.6. Specifically, during the 60 hours of exposure in the sulfate solution the circuit of Figure 6.6-a best modelled the impedance behaviour of the chromated samples that had the best corrosion resistance in the chloride solution, whereas the impedance data of the other samples was best fitted using the circuit of Figure 6.6-a and the circuit of Figure 6.6-b during the first and the last part of the exposure, respectively. These findings are in accordance with the interpretation of the equivalent circuits discussed above, especially as regards the diffusion element. Indeed, it is reasonable that the degradation of the CCP, which causes the changes of the diffusion path and as a consequence the necessity to use different equivalent networks to obtain the best fit, occurs much more slowly in the sulfate solution than in the more aggressive chloride one. In addition, also the comparison of the evolution of the different circuit elements with the immersion in the two electrolytes is physically meaningful. However, for sake of simplicity and since the main purpose of the impedance investigation is to characterize the corrosion resistance of the chromate film rather than its morphology, only the fitting results of the impedance measurements made in the NaCl solution will be presented and discussed in this thesis.

In conclusion, although the equivalent circuit given in Figure 6.5 is not the only possible model of the impedance response of chromated aluminium, it has been found to well represent the impedance behaviour of the CCC/Al system under the experimental conditions used and the frequency range studied in this work and to enable the comparison of the corrosion protection provided by chromate films having different morphology, as it will be discussed in the following two sections.

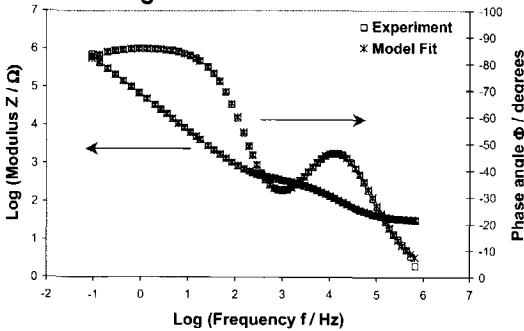


### 6.3.2 Corrosion protection provided by the CCC: effect of the surface preparation

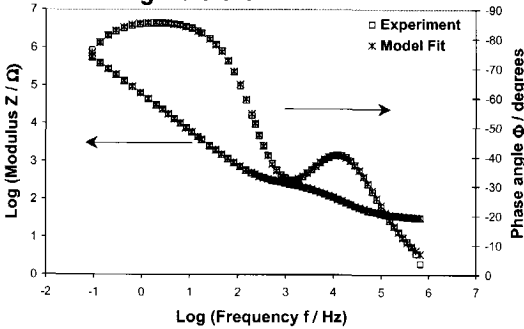
In this section the corrosion protection provided by the CCC formed after different surface preparation procedures, i.e. short (5 minutes) or long (20 minutes) pickling with or without a subsequent desmutting step, is discussed based on both impedance and noise results.

- *Electrochemical Impedance Spectroscopy (EIS)*

**Circuit of Figure 6.6-a**



**Circuit of Figure 6.6-b**



**Circuit of Figure 6.6-c**

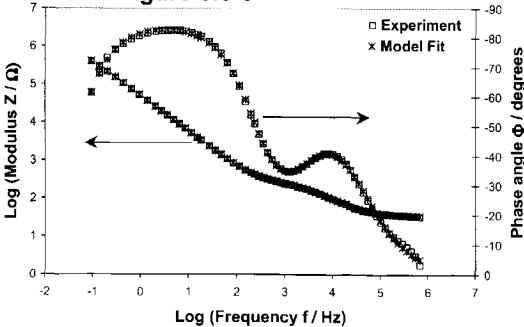


**Figure 6.7:** Examples of experimental and fitted data obtained using the equivalent circuits of Figure 6.6.

The different equivalent circuits best model the impedance response was found to be reproducible within few hours for each sample. According to the physical interpretation of the

Figure 6.7 shows some representative examples of the experimental and fitted data obtained with the equivalent circuits described in the previous section. The impedance spectra of the CCC formed on the desmuted Al surfaces, i.e. samples NPDCr1.8 and SPDCr1.8, are well described during the first 5 and 10 hours of immersion, respectively, using the equivalent circuit of Figure 6.6-a. Afterwards, the equivalent network of Figure 6.6-b gives the best fit between 5 and about 45 hours of immersion in the chloride solution in the case of sample NPDCr1.8 and between 10 and 50 hours in the case of sample SPDCr1.8. Finally, the impedance behaviour of these samples during the rest of the exposure is best modelled by the equivalent circuit of Figure 6.6-c. On the other hand, for the CCC deposited on the pickled surfaces, i.e. samples NPCr1.8 and SPCr1.8, the best fit is obtained with the equivalent circuit of Figure 6.6-b during the first 10 and 40 hours of immersion in the aggressive solution, respectively, and then with the circuit of Figure 6.6-c until the end of the exposure. It should be mentioned that the period during which the

used equivalent networks, the change from one circuit to another corresponds to changes in the diffusion process through the CCP caused by a degradation of the corrosion protection provided by the CCP themselves. Therefore, all the samples show such degradation but it becomes faster going from samples NPDCr1.8 and SPDCr1.8, to sample SPCr1.8, to sample NPCr1.8.

The following discussion of the evolution of the equivalent circuit parameters as function of the exposure to the aggressive electrolyte is illustrated using the plots relative to one set of measurements; however it is based on the results of various experiments for each sample, which showed a good reproducibility in the trend of the parameters and in the differences amongst the samples. The chart of Figure 6.8-a shows the evolution with time of exposure of the diffusion resistance ( $R_{ccp}$ ) for samples NPDCr1.8 and SPDCr1.8.

The only difference between the two samples is the time at which this parameter has a sudden increase, which is related to the change of the diffusion path from finite to infinite, i.e. the formation of a thicker but more porous and less protective layer of CCP.

On the other hand, the admittance  $Y_0$  of  $Q_{ccp}$  or  $W$  (Figure 6.8-b) stays first relatively constant and after a certain period of exposure, depending on the sample, starts to increase. This is believed to be related to the formation of a spongier layer of CCP, as well, that results in an increase of the diffusion coefficients of the charge carriers and as a consequence of  $Y_0$  of  $Q_{ccp}$  or  $W$  (equations 6.m-6.o). The time at which the increase of this parameter

occurs is shorter in the case of the chromate films formed on the Alclad 2024 surface after the pickling step, especially in the case of a short pickling treatment (sample NPCr1.8). This is in line with the faster deterioration of the CCP for these samples suggested by the different equivalent circuits required to obtain the best fit at different times of immersion in the NaCl solution. The lower stability of the corrosion products in the defects of the CCC formed after the pickling treatment can be partially due to the lower amount of Cr(VI) species

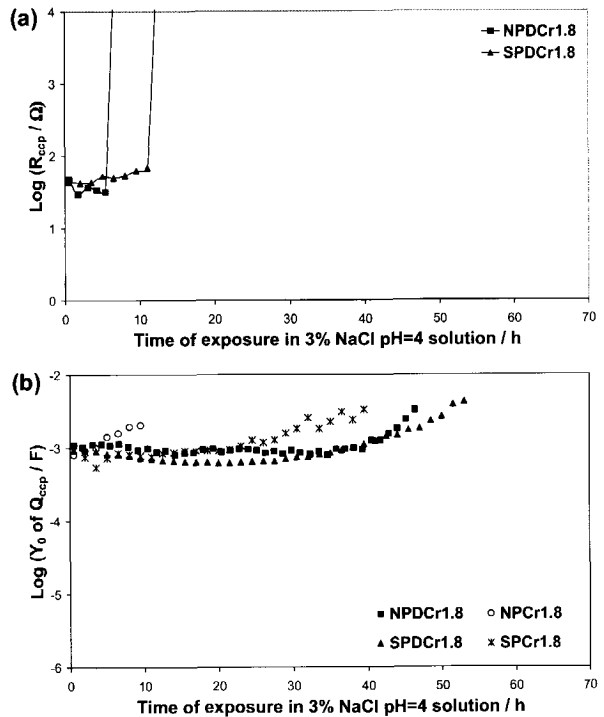


**Figure 6.8:** Diffusion resistance  $R_{ccp}$  (a) and diffusion impedance  $Q_{ccp}$  (b) as function of the exposure time in 3% NaCl pH=4 solution.

adsorbed in the film when intermetallics are left on the substrate surface, which was hypothesised in the previous chapter based on IR-SE results and on the literature.

As regards the resistance of the porous chromate layer ( $R_{pi}$ ), a gradual decrease during the exposure to the electrolyte is observed for all the samples (Figure 6.9). This is likely a result of the formation of a larger amount of pores in the chromate film, which serve as conducting paths through the layer, and/or to a thinning of the layer itself.

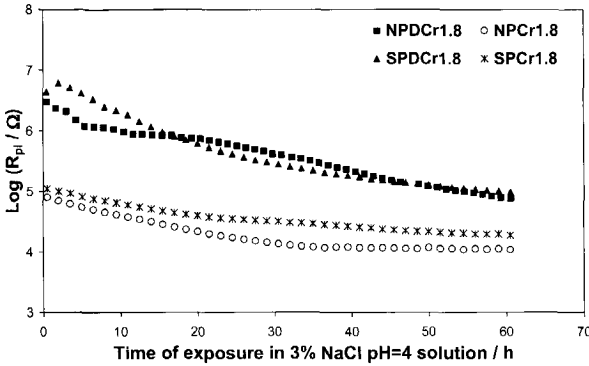


**Figure 6.9:** Resistance of the porous chromate layer  $R_{pi}$  as function of the exposure time in 3% NaCl pH=4 solution.

and especially of sample NPCr1.8. These differences can be explained by the variations in morphology of the CCC caused by the surface preparation procedure and discussed in the previous chapter: more pronounced nano-porosity for the pickled surfaces, especially when a short pickling time is used, than for the desmutted ones. The immersion in the chloride solution leads also to an increase of the admittance  $Y_0$  of the CPE representing the capacitive behaviour of the barrier layer, i.e.  $Q_{bl}$ . This can be due to a thinning of the barrier layer itself and/or to an increase of the area of the barrier layer in contact with the electrolyte (equation 6.1). Amongst the samples some differences in the value of this parameter are observed, however they are limited and fall inside the limit of reproducibility of the measurements. Nonetheless, its rate of increase appears always to be higher for samples NPCr1.8 and SPCr1.8, in comparison with samples NPDCr1.8 and SPDCr1.8.

The deterioration of the corrosion protection provided by the CCC during the immersion in the chloride solution is confirmed by the decrease of the charge transfer resistance (chart of Figure 6.10-a) and by the increase of the admittance of the CPE modelling the non-ideal capacitive behaviour of the double layer at the bottom of the defects, i.e.  $Y_0$  of  $Q_{dl}$  (chart of Figure 6.10-b). While the trend of the former indicates that an increase of the corrosion rate occurs during exposure, the trend of the latter is a consequence of the increase of the area involved in the corrosion attack (equation 6.1). Also for these parameters, while the trend is similar for all the samples the values and the rate of change (decrease or increase) are clearly different from sample to sample. Specifically, the value of  $R_{ct}$  becomes lower and that of  $Y_0$  of  $Q_{dl}$  higher and the decrease of the former and the increase of the latter is more pronounced going from sample SPDCr1.8 to NPDCr1.8 to

Although, all the porous chromate films deteriorate during the exposure, a clear distinction exists between those formed after a pickling + desmutting treatment and those deposited after the solely pickling step. The former, i.e. samples NPDCr1.8 and SPDCr1.8, show a similar value of  $R_{pi}$  that is higher during the whole exposure period in comparison with that of sample SPCr1.8 and

SPCr1.8 to NPCr1.8. This means that the rate and the extent of the corrosion attack in the chloride solution is more limited for the chromate films formed after the desmutting treatment than for those formed after the pickling process, especially if it is carried out for a short time.

Similarly to the deterioration of the porous chromate layer, also these findings can be related to the differences in morphology shown by the different chromate films. Indeed, it was observed that the prolongation of the pickling step from 5 to 20 minutes and especially the realization of the desmutting step result in the removal of the intermetallic particles from the aluminium surface, which in turn leads to the formation of a CCC containing a lower amount of large defects. According to the interpretation of the equivalent circuits, given in the previous section, during exposure most of the electrochemical reactions are taking place inside these large defects. As a consequence, the area involved in the corrosion attack is the lowest for samples SPDCr1.8 and NPDCr1.8, intermediate for sample

SPCr1.8, and the highest for sample NPCr1.8 that explains the corresponding differences in the value of  $Y_0$  of  $Q_{dl}$  since the beginning of the exposure. In addition, it was found that in the case of samples NPCr1.8 and SPCr1.8 many of these large defects are located in proximity of the IMCs. Therefore, for these samples once the corrosion attack starts at the bottom of the defects it is enhanced by the galvanic coupling existing between the intermetallic and the Al matrix, leading to a higher corrosion rate, i.e. lower  $R_{ct}$ , and higher extent of attack, i.e. higher increase of  $Y_0$  of  $Q_{dl}$ . Obviously, higher is the amount of IMCs left on the surface, i.e. sample NPCr1.8, more pronounced is this phenomenon.

It should be noted that the differences in  $R_{ct}$  of samples NPDCr1.8 and SPDCr1.8 cannot be explained based on the morphology of the CCC, since these two samples show a very similar chromate films. Another feature that is not completely understood is the evident variation in  $Y_0$  of  $Q_{dl}$  and the absence of a specific trend in  $Y_0$  of  $Q_{dl}$  amongst the samples, since both these parameters are supposed to depend upon the extent of the large defects in

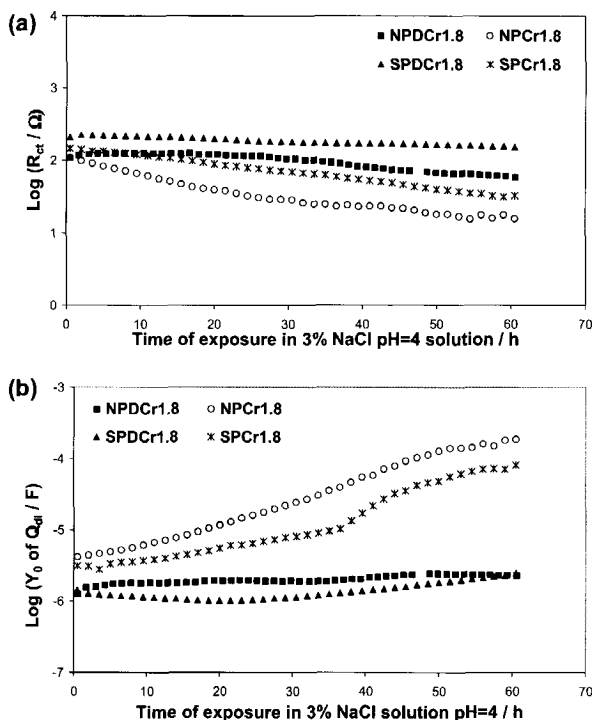
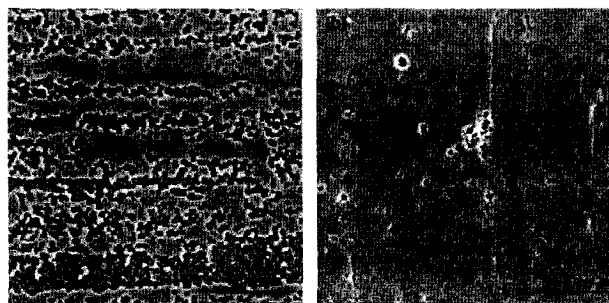


Figure 6.10: Charge transfer resistance  $R_{ct}$  (a) and non-ideal double layer capacitance  $Q_{dl}$  (b) as function of the exposure time in 3% NaCl pH=4 solution.

the layer. One possible reason is that the thickness and the dielectric constant of the barrier layer are two additional variables in determining the value of  $Y_0$  of  $Q_{bl}$  (equation 6.1). Although these unclear points, it can be concluded, that the fitting of the EIS spectra with the equivalent circuits given in Figure 6.6 leads to an evolution of the various circuit parameters with the time of immersion in the chloride solution that is physically meaningful and enables to distinguish between chromate films having different morphology.

- *SEM/EDS investigation*

The better corrosion protection provided by the CCC formed after the desmutting step (samples NPDCr1.8 and SPDCr1.8) with respect to that formed after the pickling step (samples NPCr1.8 and SPCr1.8) due to a lower deterioration of both the porous chromate layer and the CCP together with a less pronounced corrosion attack at the bottom of the defects is confirmed by the SEM/EDS investigation carried out after the impedance measurements.



**Figure 6.11:** SEM micrographs of samples NPCr1.8 (a) and NPDCr1.8 (b) after 60 hours of exposure in 3% NaCl pH=4 solution.

The SEM study shows that while sample NPCr1.8 is strongly attacked (Figure 6.11-a), on the surface of sample NPDCr1.8 only few areas appear to be affected by the immersion in the chloride solution (Figure 6.11-b). A more detailed SEM investigation of the corrosion attack undergone during the impedance measurements by the chromate film formed after

a short pickling treatment is given in Figure 6.12 and enables several observations. First of all, the micrograph of Figure 6.12-a shows the presence of a large and deep pit, at the bottom of which a white particle is present that is identified by EDS analysis as a Fe, Si-rich intermetallic (Figure 6.12-d). This confirms the negative effect of the presence of IMCs on the corrosion performance of Al surfaces even when covered by a CCC, as previously suggested. In the other two micrographs (Figure 6.12-a and -b) the formation of a large amount of extremely spongy corrosion products inside the defects of the CCC can be observed. These are actually the chromate corrosion products mentioned above, since in the EDS analyses carried out at their location an evident peak relative to chromium and an extremely strong peak relative to oxygen are always present (Figure 6.12-e). In addition, in all the EDS spectra of the CCP a chloride peak is detected and in some cases also a strong copper peak (Figure 6.12-e). While, the presence of Cl<sup>-</sup> is expected since a chloride containing solution is used for the EIS study, the enrichment in copper is quite surprising since the clad layer of the alloy used as substrate contains only 0.1% of Cu. This highlights the high tendency of copper to become enriched on the aluminium surface during exposure to aggressive media. Obviously, this phenomenon is more pronounced and has important

consequences on the electrochemical behaviour of copper-rich alloys, as will be discussed in the next two chapters for bare 2024 aluminium alloy.

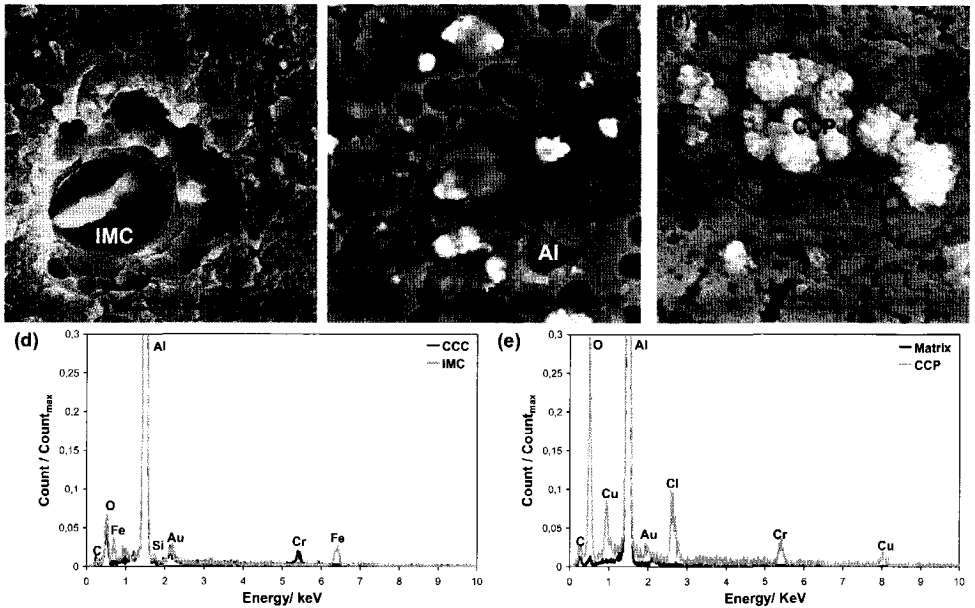


**Figure 6.12:** SEM micrographs (a, b, c) and EDS spectra (d, e) of sample NPCr1.8 after 60 hours of exposure in 3% NaCl pH=4 solution.

The micrograph of Figure 6.12-b shows that the large volumes of spongy CCP inside the defects of the film are not only poorly protective but induce also stresses in the chromate film, which in turn result in circular cracks, indicated by arrows, at their periphery. This is likely responsible for the detachment of the chromate film in the surrounding areas (named Al in the micrograph) leaving the bare substrate exposed to the chloride solution; indeed at these locations chromium is not anymore detected by EDS analysis (Figure 6.12-e).

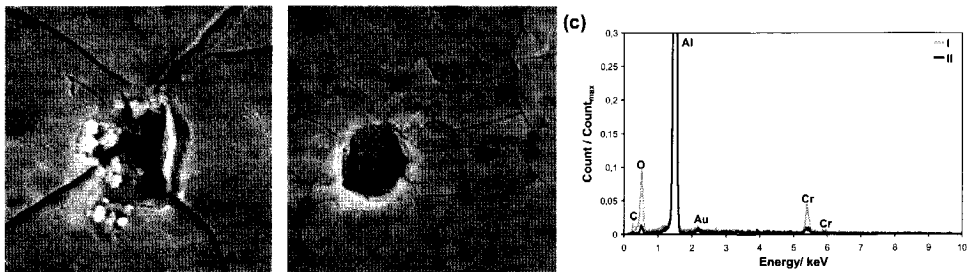


**Figure 6.13:** SEM micrographs (a, b) and EDS spectra (c) of sample NPDCr1.8 after 60 hours of exposure in 3% NaCl pH=4 solution.

The removal of large parts of the CCC from the surface of sample NPCr1.8 occurring via detachment rather than via dissolution explains the stronger increase of  $Y_0$  of  $Q_{dl}$ , i.e. area involved in the corrosion attack, in comparison with the decrease of  $R_{ct}$ , i.e. acceleration of the corrosion attack. More details about this are given in the next section

when the influence of the pH of the chromate bath on the corrosion protection provided by the CCC is discussed.

In agreement with the evolution of the circuit parameters during exposure, when sample NPDCr1.8 is concerned the extent of the corrosive attack is more limited (SEM micrograph of Figure 6.11-b) and corrosion products being lower in quantity and more dense are formed inside the defects of the film (SEM micrographs of Figure 6.13-a and -b). The EDS spectra of Figure 6.13-c show that, although less strong than in the rest of the surface, the chromium and oxygen signals are detected also inside the defects, which indicates the presence of a thin chromium oxide film that is only rarely enriched in chloride.

- *Electrochemical Noise (EN)*

A further confirmation of the better corrosion protection provided by the CCC formed on desmutted surfaces with respect to that formed on pickled surfaces is given by the noise measurements.

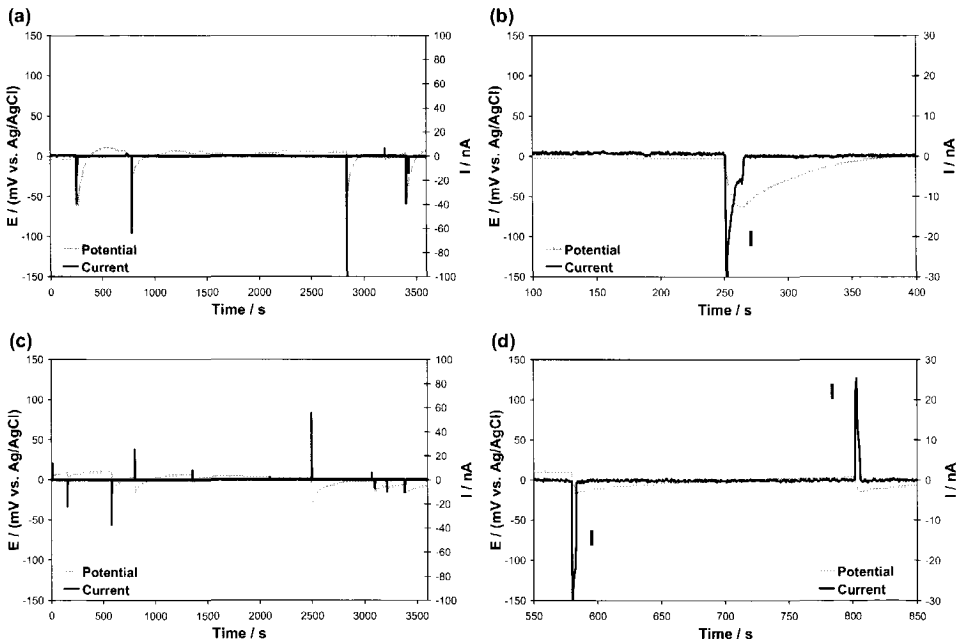


**Figure 6.14:** Current and potential time records during the 4<sup>th</sup> hour of exposure to 3.5% NaCl pH=4 solution for samples NPDCr1.8 (a) and SPDCr1.8 (c). Enlargement of 300 seconds of the same measurements: sample NPDCr1.8 (b) and sample SPDCr1.8 (d). Zero of scales arbitrary.

Some typical examples of current and potential transients are given in Figures 6.14 to 6.17. At the beginning of the immersion in the chloride solution the time records show for all the samples fairly sharp transients for both the potential and the current (Figures 6.14 and 6.16). In the case of samples NPDCr1.8 and SPDCr1.8 during the first hours of immersion the current spikes assume a shape characterized by a sudden increase of the current followed by a gradual decrease to an intermediate value and finally a sudden drop to the

initial value occurs (spikes named I in the charts of Figure 6.14-b and -d). These current transients of samples NPDCr1.8 and SPDCr1.8 are either positive or negative depending on which of the two working electrodes is involved in the corrosion event and are characterized by a maximum value, i.e. amplitude, varying between 10 and 100 nA and a width in the range of 5-15 seconds.

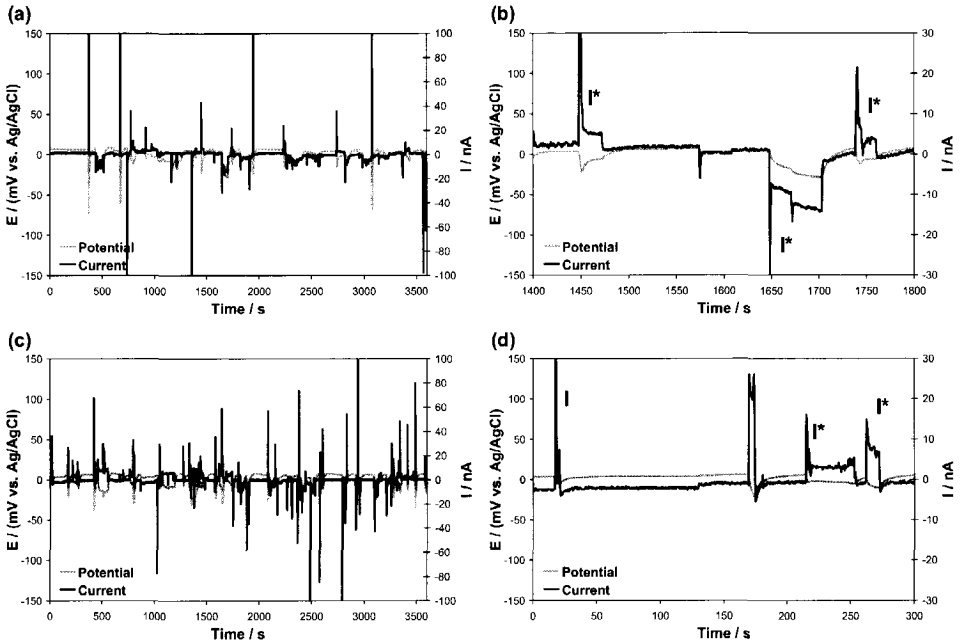


**Figure 6.15:** Current and potential time records during the 20<sup>th</sup> hour of exposure to 3.5% NaCl pH=4 solution for samples NPDCr1.8 (a) and SPDCr1.8 (c). Enlargement of 300 seconds of the same measurements: sample NPDCr1.8 (b) and sample SPDCr1.8 (d). Zero of scales arbitrary.

It can be noted that while the changes in current take place in few seconds the variations of the potential are more gradual, both during the initial drop associated with the increase in the current and during the subsequent increase back to the initial value associated with the decrease in current, i.e. conclusion of the corrosion attack event. The shape of the current spikes suggests that they are caused by a sudden breakdown of the barrier layer at the bottom of the defects of the CCC, responsible for the initial rapid increase in current, followed by the formation of corrosion products (CCP), responsible for the intermediate gradual decrease in current, that repair and plug the flaw leading to the final sudden drop of the current.

The increase of the time of exposure to the aggressive electrolyte results in more frequent and longer corrosion events occurring at the location of the defects of the chromate film of samples NPDCr1.8 and SPDCr1.8. Indeed, the width of the current spikes reaches value up to 50 seconds, whereas the maximum value of the current stays in the range of 10-100 nA (Figure 6.15). The shape of the current spikes (named I\* in the charts of Figure 6.15-b and -d) is still characterized by a sudden increase in current followed by a gradual



decrease to an intermediate value, however a further step, in which the current remain constant at this intermediate value, is observed before the sudden drop to the initial value occurs.

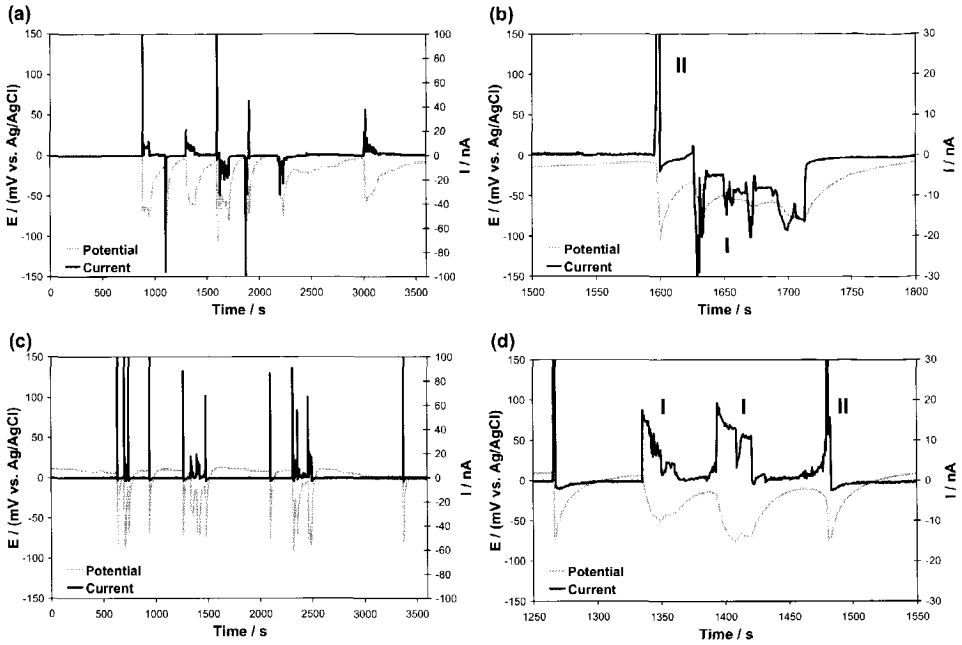


**Figure 6.16:** Current and potential time records during the 4<sup>th</sup> hour of exposure to 3.5% NaCl pH=4 solution for samples NPCr1.8 (a) and SPCr1.8 (c). Enlargement of 300 seconds of the same measurements: sample NPCr1.8 (b) and sample SPCr1.8 (d). Zero of scales arbitrary.

This modification in the shape and width of the current transients is believed to be due to a decrease of the protective properties of the corrosion products, which are produced in larger amount but are spongier and therefore need a longer time to stop the corrosion process. Indeed, after the breakdown of the barrier layer at the bottom of the defect, which causes the sudden increase in current, a porous layer of CCP is formed, which leads to a decrease of the current; however the corrosion attack can continue through the spongy CCP, resulting in the plateau in the current transient, before the defect is repaired and plugged, causing the sudden drop in current. According to this interpretation of the current spikes of samples NPDCr1.8 and SPDCr1.8, the noise measurements indicate that during exposure to the chloride solution a deterioration of the layer of CCP formed in the defects of the CCC takes place, in line with the results of the EIS investigation.

The charts given in Figure 6.16 show that since the first hours of exposure to the chloride solution on the surface of samples NPCr1.8 and SPCr1.8 more numerous corrosion events, associated with current spikes, take place with respect to samples NPDCr1.8 and SPDCr1.8 (Figure 6.14). In the time records of the CCC formed on the pickled surfaces, the current transients of type I are also observed, which are characterized by a range of maximum current value similar to that of samples NPDCr1.8 and SPDCr1.8, 10-100 nA, and

by a higher width, 10-100 seconds (charts of Figure 6.16-b and -d). Again, the potential transients are more gradual than the current ones. In addition, in some cases the current transients assume a different shape consisting in a gradual increase of the current followed by a sudden drop to the initial value (spikes named II). It is suggested that these transients are associated with corrosion events taking place at locations in the CCC where spongy corrosion products are already present, which lead to a gradual and continuous attack rather than to a sudden breakdown. These results show that the chromate films formed on the pickled surfaces provide a lower corrosion protection in comparison with those formed on the desmutted surfaces already at the beginning of the exposure due to the formation in the defects of CCP being more porous and less protective. It should be noted that this was also at the base of the choice of different equivalent circuits to fit the impedance diagram of the various samples.

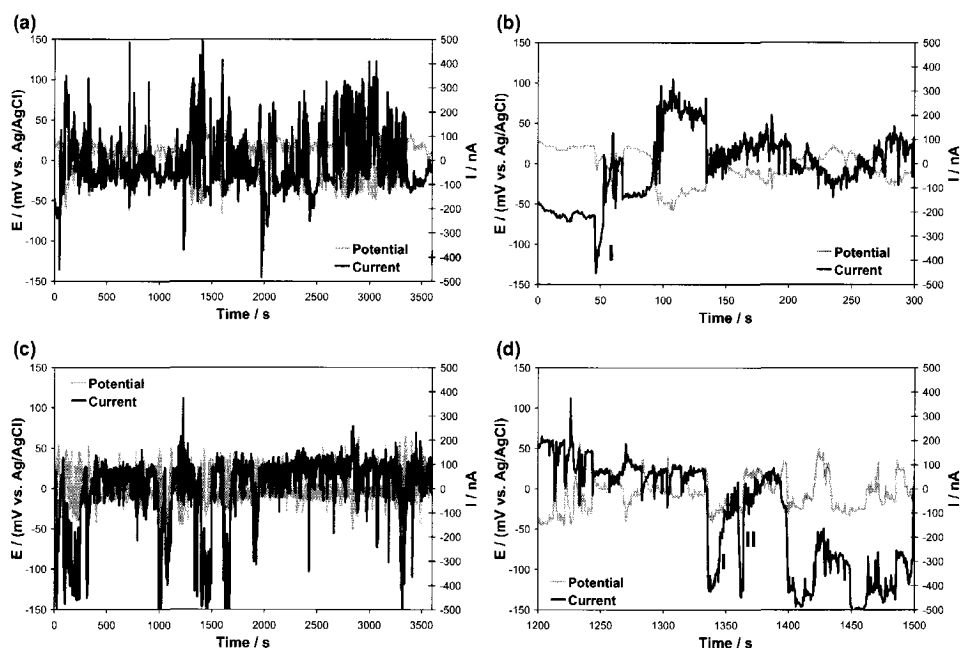


**Figure 6.17:** Current and potential time records during the 20<sup>th</sup> hour of exposure to 3.5% NaCl pH=4 solution for samples NPCr1.8 (a) and SPCr1.8 (c). Enlargement of 300 seconds of the same measurements: sample NPCr1.8 (b) and sample SPCr1.8 (d). Zero of scales arbitrary.

The difference in corrosion resistance shown by the chromate layers formed after different surface preparation treatments becomes more pronounced at longer time of immersion in the solution (Figures 6.15 and 6.17). Indeed, for samples NPCr1.8 and SPCr1.8, when the time of exposure in the aggressive electrolyte is increased the frequency, width, and amplitude (note that a larger current scale is used in the charts of Figure 6.17) of the current spikes strongly increase leading to an overlapping of several transients, the shape of which is hardly distinguished (Figure 6.17).

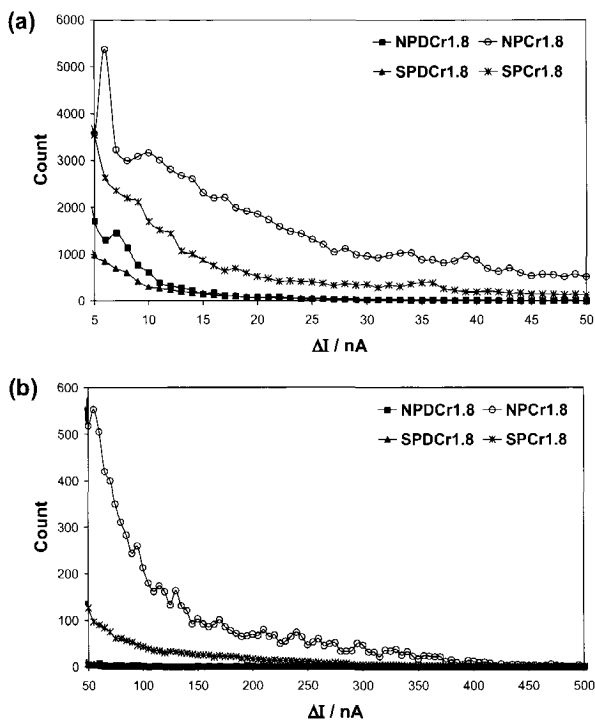


**Figure 6.18:** Number of current deviations from the mean value ( $\Delta I$ ) as function of the value of the deviation: between 5 and 50 nA (a) and between 50 and 500 nA (b).

(Figure 6.19).

The former gives information regarding the corrosion protection provided by the CCC, while the latter describes the variation of the corrosion resistance during the immersion in the chloride solution. Figure 6.18 shows that both the amount and the maximum value of the current deviations increase going from samples SPDCr1.8 and NPDCr1.8 to sample SPCr1.8, to sample NPCr1.8. Besides, from Figure 6.19 it can be

noted that this ranking is maintained and the differences between the samples are enhanced

This indicates that the extent of the corrosive attack on the surface of these samples is strongly enhanced during immersion and that a complete repair and plug of the defects of the CCC does not occur anymore. This is likely due also to the detachment of large pieces of the chromate film, as observed during the impedance experiments.

The results of the noise measurements are summarized into two charts: the number of deviations from the mean current values ( $\Delta I$ , equation 6.j), which is related to the number, width and amplitude of the current spikes, as function of the value of the deviation (Figure 6.18) and the total amount of deviations as function of the time of exposure to the solution

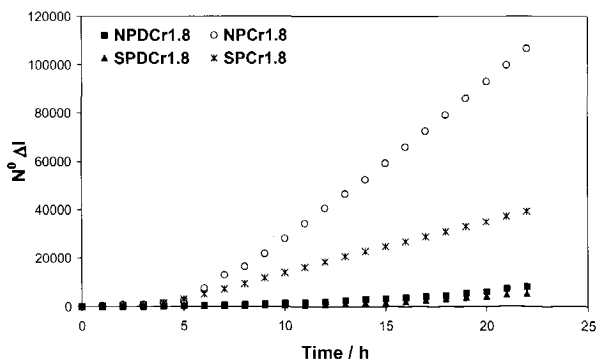


**Figure 6.19:** Total number of current deviations from the mean value ( $\Delta I$ ) as function of the immersion time in 3.5% NaCl pH=4 solution.

during the immersion in the chloride solution. This means that the chromate films formed after the desmutting step (samples NPDCr1.8 and SPDCr1.8) provide the best corrosion protection to the aluminium surface, the CCC deposited after a long pickling treatment (sample SPCr1.8) provide an intermediate protection, whereas that formed after a short pickling step (sample NPCr1.8) is the less protective, in agreement with the findings of the EIS investigation.

An apparent contradiction between the impedance and the noise results consists in the values of the charge transfer resistance, in the order of magnitude of hundred ohms, and of the current spikes, in the order of hundred nano-amperes. Indeed, a theoretical relationship between the corrosion current density ( $i_{corr}$ ) and the polarization resistance ( $R_p$ ) exists [35]:

$$R_p = \frac{\beta_a \beta_c}{2.3 i_{corr} (\beta_a + \beta_c)} \quad (6.p)$$

where  $\beta_a$  and  $\beta_c$  are the anodic and cathodic Tafel parameters given by the slope of the polarization curves. Based on this equation and considering  $R_p$  equal to the charge transfer resistance a higher  $R_{ct}$  should be expected. However, the applicability of this simple relationship relies on the presence of a single charge-transfer-controlled cathodic reaction and a single charge-transfer-controlled anodic reaction, which is likely not the case in the corrosion processes occurring at chromated aluminium surfaces. In addition, in the system under study the current and the charge transfer resistance cannot be directly correlated through equation 6.p for two main reasons. First, the charge transfer resistance is much lower than the polarization resistance for a conversion coated surface and under diffusion-controlled conditions [36], since the resistance of the layer and the diffusion resistance contribute also to the polarization resistance. Second, the area involved in the corrosion attack does not correspond to the geometrical area of the sample, is unknown, and can vary between different measurement and even during the same measurement, which last several hours. Therefore, it is believed that the analysis of local corrosion events occurring at a micro-scale using macro-electrochemical methods, as EIS and EN, does provide qualitative information regarding the corrosion behaviour of the system and does enable a ranking between different systems, but does not provide quantitative information. These can be obtained only using local electrochemical techniques, as the micro-capillary method [37], which can monitor a single corrosion event occurring at a location with a well-defined micro-area.

In conclusion, the impedance and noise investigations together with the SEM/EDS study of the corroded samples show that the presence of intermetallic particles on the aluminium surface is deleterious for the corrosion resistance of the CCC. This is related to the variations in morphology of the chromate film caused by the IMCs: film containing a higher amount of large and deep defects located in their proximity. This results in a higher extent of the corrosive attack, formation of spongy and poorly protective corrosion products, which induce stresses and consequent detachment of the film. Besides, a decrease of the protection provided by the CCP is likely associated also with a lower amount of Cr(VI) species adsorbed in the chromate film when intermetallics are present on the substrate

surface. Finally, it should be noted that the much lower corrosion protection provided by the CCC formed directly after the acid pickling treatment in comparison with that formed after the desmutting process could not be foreseen by the standard methods of coating evaluation used in the industry, which are based on thickness measurements. Indeed, in section 5.3.3 of chapter 5 it has been shown that the variations in thickness amongst the chromate films deposited after different surface preparation procedures are very limited.

### 6.3.3 Corrosion protection provided by the CCC: effect of the chromate bath pH

In the previous chapter it was shown that the morphology of the chromate film depends also on the chromate process parameters, specifically the pH of the chromate bath, which affect also the chemical composition of the film. Therefore, the CCCs formed at different pH are expected to provide different level of corrosion protection. This is discussed in the present section based on impedance and noise data.

- *Electrochemical Impedance Spectroscopy (EIS)*

The impedance spectra of the samples chromated after a pickling + desmutting treatment, as surface preparation procedure, varying the pH of the chromate bath from 1.2 up to 2.4 were fitted using the equivalent circuits given in Figure 6.6.

**Table 6.1:** Equivalent circuits used to fit the EIS data of the CCC, formed at different pH of the chromate bath, during the exposure in 3% NaCl pH=4 solution.

Equivalent circuit	Figure 6.6-a	Figure 6.6-b	Figure 6.6-c
NPDCr1.2	0-30h	30-60h	-
NPDCr1.4	0-25h	25-45h	45-60h
NPDCr1.8	0-5h	5-45h	45-60h
NPDCr2.2	-	0-40h	40-60h
NPDCr2.4	-	0-50h	50-60h

For samples chromated at pH 2.2 and 2.4 (samples NPDCr2.2 and NPDCr2.4) the best fit is obtained with the equivalent circuit of Figure 6.6-b during the first 40 h and 50 h, respectively, of immersion in the chloride solution and afterwards with the circuit of Figure 6.6-c (Table 6.1). On the other hand, the data of samples chromated at pH 1.8, 1.4, and 1.2 (samples NPDCr1.8, NPDCr1.4, and NPDCr1.2) are well

described by the equivalent network of Figure 6.6-a during the first 5, 25, and 30 h of immersion, respectively. Then, the circuit of Figure 6.6-b gives the best fit up to 45 h for the samples chromated at pH 1.8 and 1.4, and until the end of the exposure for sample NPDCr1.2. Finally, the circuit of Figure 6.6-c best fits the impedance response of samples NPDCr1.8 and NPDCr1.4 during the remaining period of immersion. These differences amongst the samples chromated at different pH of the Alodine solution were found to be reproducible.

As explained in section 6.3.1, the necessity of using the different circuits of Figure 6.6 to fit the impedance data is associated with the deterioration of the film of CCP occurring during the immersion in the chloride solution. Based on Table 6.1, it seems that the protective properties of the chromate corrosion products formed in the defects of the CCC decreases when the pH of the chromate bath is increased, especially above 1.4. A possible reason of this can be found in the variations of the chemical composition resulting from the

change of the bath pH. In section 5.3.4 of chapter 5 a decrease of the quantity of Cr(VI) species adsorbed in the CCC as a consequence of the increase of the pH of the Alodine solution is suggested based both on our own results and on the literature. The Cr(VI) species in the chromate film are believed to be responsible for the "self-healing" behaviour of the CCC, since they can leach, diffuse and precipitate in the defects (see section 3.2.2 of chapter 3 for more details). Therefore, the lowering of the Cr(VI) species in the chromate layer is expected to lead to a weakening of the CCP deposited in the flaws of the chromate film during exposure, since they will consist more of aluminium oxide that is less stable and resistant than aluminium/chromium mixed oxide.

The chart in Figure 6.20-b shows that the value of the admittance  $Y_0$  of  $Q_{ccp}$  or  $W$  decreases going from sample NPDCr1.2 to sample NPDCr1.4 to samples NPDCr1.8, NPDCr2.2, and NPDCr2.4. The trend of this parameter and its variation amongst the CCCs formed at different pH of the chromate solution showed a good reproducibility, similarly to all the other circuit parameters that are discussed later in this section. According to the interpretation of  $Y_0$  of  $Q_{ccp}$ , its increase is related to an increase of the diffusion coefficients of the charge carriers in the film of CCP, i.e. to the formation of a more porous and less protective film of corrosion products in the defects. Therefore, the

different values of  $Y_0$  of  $Q_{ccp}$  or  $W$  shown by the samples are in line with the suggestion that the protective properties of the CCP increase when the pH of the chromate bath is decreased. In the chloride solution this is evident for pH 1.4 and especially 1.2, while the results of the EIS investigation in a less aggressive solution (0.5M  $K_2SO_4$  pH=4), not given here, make a clear distinction also amongst the samples chromated at pH higher than 1.4. In particular, the presence of chloride seems to negatively affect the corrosion resistance of the CCP of sample NPDCr1.8 since the beginning of the exposure, whereas for samples

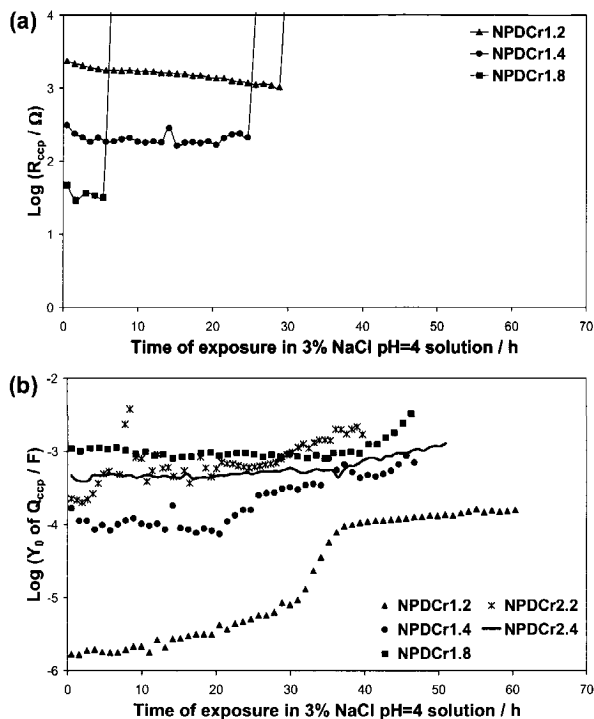


**Figure 6.20:** Diffusion resistance  $R_{ccp}$  (a) and diffusion impedance  $Q_{ccp}$  (b) as function of the exposure time in 3% NaCl pH=4 solution.

NPDCr1.4 and especially NPDCr1.2 a similar deterioration of the CCP occurs only after a certain period of immersion.

The stronger degradation of the CCP on samples chromated at pH 1.4 and 1.8 compared with sample chromated at pH 1.2 is evident also in the change of  $R_{ccp}$  with the exposure time (Figure 6.20-a). Indeed, while varying the pH of the chromate bath from 1.2 to 1.4 to 1.8 the diffusion resistance decreases and the time of its sudden increase, which is related to the change of the diffusion path from finite to infinite and therefore to the formation of a thicker but less dense and protective film of CCP, becomes shorter. Based on the choice of the equivalent circuit and on the evolution with time of immersion of both the diffusion capacitance and the diffusion resistance, it is suggested that a decrease of the pH of the chromate bath leads to the formation of a chromate conversion coating characterized by a better "self-healing" behaviour, i.e. dynamic repair of the defects.

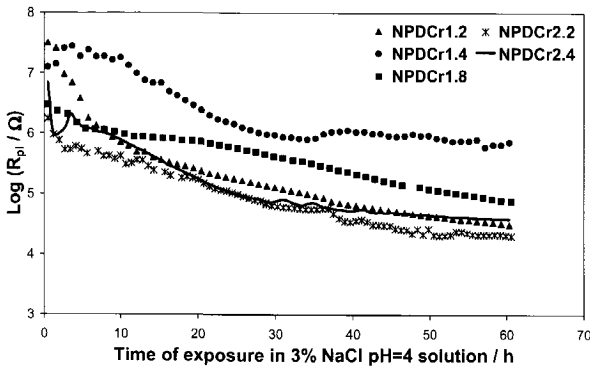


**Figure 6.21:** Resistance of the porous chromate layer  $R_{pl}$  as function of the exposure time in 3% NaCl pH=4 solution.

During immersion in the electrolyte all the samples show a decrease of the circuit parameter  $R_{pl}$  (Figure 6.21), which can be associated with a degradation of the barrier properties of the porous chromate layer, but to a different extent: a slower deterioration of the porous layer, i.e. less pronounced decrease of  $R_{pl}$ , characterizes the samples chromated at pH 1.8 and especially 1.4. This

can be explained taking into account that a decrease in pH of the chromate bath leads to a decrease of the density of the porous layer but also to an increase of its thickness, as described in section 5.3.4 of chapter 5. Therefore, a decrease of the pH of the chromate solution has two contrasting effects on the resistance of the porous layer, since a higher thickness would increase it whereas a lower density would decrease it. It seems that when the pH is changed from 2.4 to 1.4 the increase of the thickness is preponderant on the decrease of density resulting in an improvement of the resistance of the porous layer and in a slower deterioration during exposure. On the other hand, the decrease of the pH from 1.4 to 1.2 leads to an opposite situation, i.e. the decrease in density is more significant than the increase in thickness, and then the porous layer becomes less resistant.

The stronger influence of the variation of the pH from 1.4 to 1.2 on the density than on the thickness of the CCC is in accordance with the results of the surface analysis investigations, discussed in the previous chapter. Indeed, an increase of only a few tens of nanometres for the thickness (Figure 5.23) and a doubling of the roughness of the surface (second row of Table 5.4), related to the nano-porosity, were observed for the chromate film formed at pH 1.2 in comparison with that formed at pH 1.4. Based on the physical

interpretation of the circuit parameter  $R_{pi}$  and on its evolution with time of exposure for the different samples (Figure 6.21), it can be concluded that the use of a pH 1.4 in the Alodine solution gives rise to a CCC with optimised thickness and density of the porous layer.

Similarly to the surface preparation procedure, the change of the pH of the chromate bath does not systematically affect the value of the admittance ( $Y_0$ ) of the constant phase element modelling the barrier layer ( $Q_{bl}$ ), which for all the different samples slightly increases during the exposure.

Figure 6.22 shows that during the whole exposure in the chloride solution the samples chromated at pH 2.2 and 2.4 are characterized by a lower charge transfer resistance ( $R_{ct}$ ), i.e. faster corrosion, and especially by a higher admittance of the barrier layer ( $Y_0$  of  $Q_{dl}$ ), indicative of a higher area involved in the corrosion process. This is in accordance with the optimisation of the resistance of the porous layer when the pH of the chromate bath is adjusted at a value between 1.4 and 1.8 and the increase in the protective properties provided by the chromate corrosion products (CCP) when the pH is decreased from 2.4 to 1.2. Besides, the IR-SE and AES studies discussed in section 5.3.4 of chapter 5 show

that the increase of the pH of the chromate solution leads to the presence of Al oxide at the interface CCC/Al substrate. This could be an additional cause of the lower corrosion resistance shown by samples NPDCr2.2 and NPDCr2.4.

In the case of sample NPDCr1.2, the slower corrosion attack involving a smaller area with respect to samples NPDCr2.2 and NPDCr2.4 is likely due to the formation of a thinner but denser layer of CCP inside the defects that provides a better protection and induces a low level of stress limiting the detachment of the CCC. Whereas, the better corrosion performance of the chromate films formed at pH 1.8 and 1.4 is related to the better barrier properties, i.e. lower amount of defects and higher thickness, of the porous chromate layer that increase also the threshold stress for the initiation of cracks, rather than to the film of

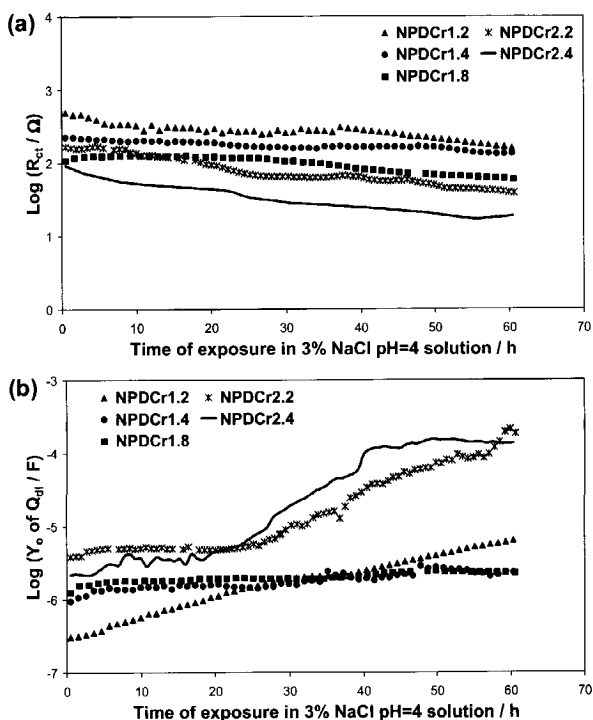


**Figure 6.22:** Charge transfer resistance  $R_{ct}$  (a) and non-ideal double layer capacitance  $Q_{dl}$  (b) as function of the exposure time in 3% NaCl pH=4 solution.



CCP, which undergoes a similar degradation as for samples NPDCr2.2 and NPDCr2.4. This explains also the better corrosion resistance at the beginning of the exposure to the chloride solution together with the heavier degradation during the immersion shown by sample NPDCr1.2 with respect to samples NPDCr1.4 and NPDCr1.8. Indeed, it is suggested that the better CCP formed in the former leads to a better behaviour at the beginning of the immersion, whereas the better properties of the porous layer, i.e. higher density and the lower amount of defects, observed in the last become preponderant after a certain exposure period and limit the deterioration of the corrosion protection provided by the film during the immersion.

- *SEM/EDS investigation*

The SEM investigation (Figure 6.23 and Figure 6.11-b) carried out at the end of the EIS measurements confirms the higher extent of the corrosive attack undergone by samples NPDCr2.2 and NPDCr2.4 in comparison with the other CCCs, especially those formed at pH 1.4 and 1.8.

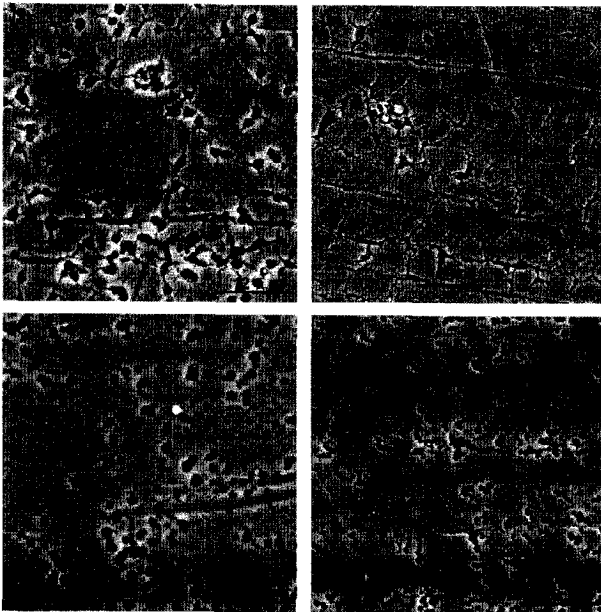


**Figure 6.23:** SEM micrographs of samples NPDCr1.2 (a), NPDCr1.4 (b), NPDCr2.2 (c), and NPDCr2.4 (d) after 60 hours of exposure in 3% NaCl pH=4 solution.

Indeed, the SEM micrographs relative to the surface of samples NPDCr2.2 and NPDCr2.4 (Figure 6.23-c and -d) show a large number of locations where corrosion has taken place leading to the formation of round pits 1-10  $\mu\text{m}$  in diameter, whereas the chromate film of samples NPDCr1.8 (Figure 6.11-b) and NPDCr1.4 (Figure 6.23-b) are affected only at few sites and that of sample NPDCr1.2 (Figure 6.23-a) has undergone an intermediate extent of attack. The charts given in Figure 6.22 show also that during exposure while the decrease of the charge transfer resistance, i.e. acceleration of the corrosion

process, is gradual for all the samples, the increase of  $Y_0$  of  $Q_{dl}$ , i.e. increase of the extent of attack, is gradual in the case of the chromate films formed at pH lower or equal than 1.8 and much more pronounced for the others. As already noted in the previous section, this lack of correspondence in the rate of variation of  $R_{ct}$  and  $Y_0$  of  $Q_{dl}$  suggests that the round pits observed on the surface of samples NPDCr2.2 and NPDCr2.4 are created mainly via

detachment of the chromate layer as a consequence of the stresses induced by the corrosion products rather than via dissolution of the film.

This is confirmed by the micrographs of Figure 6.24 that show on the surface of these

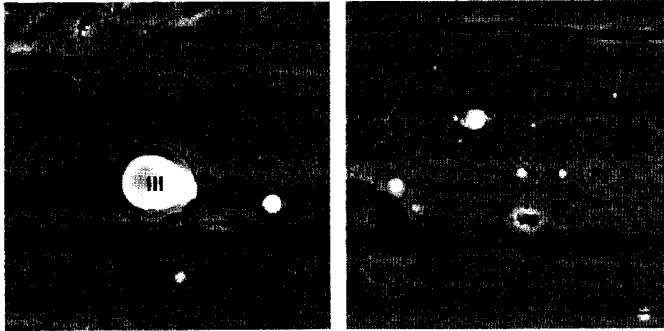


**Figure 6.24:** SEM micrographs of samples NPDCr2.2 (a) and NPDCr2.4 (b) after 60 hours of exposure in 3% NaCl pH=4 solution.

samples the presence of white deposits of corrosion products, which by means of EDS analyses are found to be enriched in Cl<sup>-</sup>.

On these micrographs four steps of the mechanism of detachment of the chromate layer caused by the corrosion products can be observed:

- I A large amount of very spongy corrosion products fills completely the defects and starts to be visible on the top surface.
- II The deposit of corrosion products grows in size and leads to a variation in volume that induces stresses in the chromate layer and gives rise to the initiation on the top surface of a circular crack around the defect.
- III The circular crack grows and radial cracks are also formed due to the increase of the stresses exerted by the corrosion products.
- IV The circular crack reaches the aluminium substrate and a large portion of the chromate film is detached giving rise to a weak location in the film that afterwards can undergo further corrosion.

- *Electrochemical Noise (EN)*

Based on the impedance results, it can be stated that when the pH of the chromate bath is adjusted at a value of 1.4 - 1.8 the CCC that is deposited on the Alclad 2024 alloy provides the best "long-term" corrosion resistance to the substrate, since an optimum compromise between the barrier properties of the porous chromate film and the self-healing ability is reached. The noise measurements are in accordance with these findings. Similarly to the current records of sample NPDCr1.8 discussed in the previous section (Figure 6.14-a), at the beginning of the exposure few type I spikes characterize also the time records of the current for samples NPDCr1.4 and NPDCr1.2. Comparing the CCC formed at pH 1.2 with those formed at 1.4 or 1.8, while the number of the current transients, related to the number of corrosion events occurring on the surface of the two working electrodes, is higher their width, related to the time necessary to repair a site of attack in the film, is smaller. These observations are in agreement with the higher amount of defects, i.e. potential sites of corrosion attack, present in the chromate film formed at pH 1.2, and the better corrosion protection provided by the CCP of this film, as suggested by the impedance investigation.

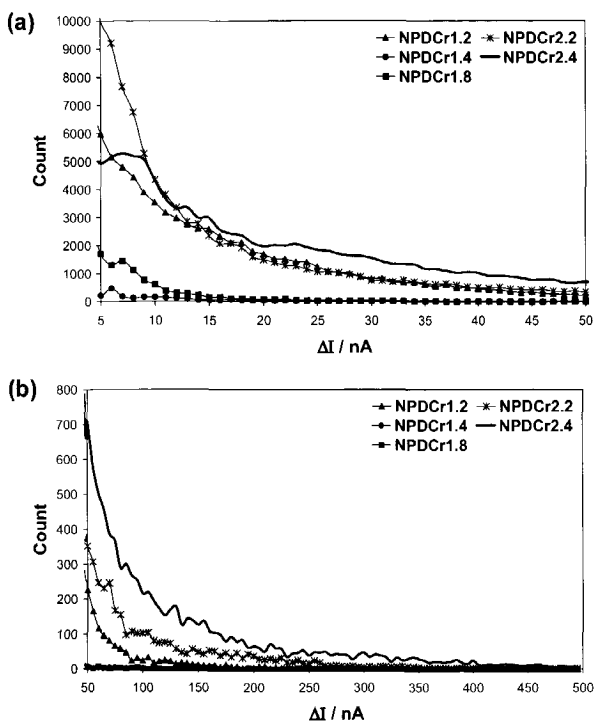


**Figure 6. 25:** Number of current deviations from the mean value ( $\Delta I$ ) as function of the value of the deviation: between 5 and 50 nA (a) and between 50 and 500 nA (b).

show the highest number of  $\Delta I$  independently upon the value of the deviation together with the highest maximum value of the deviation (Figure 6.25). On the other hand, samples NPDCr1.4 and NPDCr1.8 are characterized by the lowest value of these parameters, and sample NPDCr1.2 by intermediate values. This is indicative of a worsening of the corrosion protection provide by the CCC when the pH of the chromate bath is decreased

below 1.4 and especially when is increased above 1.8. In addition, the plot of the number of current deviations versus the time of immersion (Figure 6.26) clearly shows that the corrosion resistance of samples NPDCr2.2 and NPDCr2.4 is much lower since the beginning

When samples NPDCr2.2 and NPDCr2.4 are concerned, the frequency, width, and amplitude of the current spikes are much higher since the beginning of the exposure and are strongly enhanced during immersion.

The findings of one set of noise experiments, which are representative for all the measurements, are summarized in the plots of Figures 6.25 and 6.26 that show the number of deviations from the mean current value ( $\Delta I$ ), which are related to the frequency, width and amplitude of the current transients, as function of the value of the current deviation and the time of exposure, respectively. It can be observed that samples NPDCr2.2 and NPDCr2.4

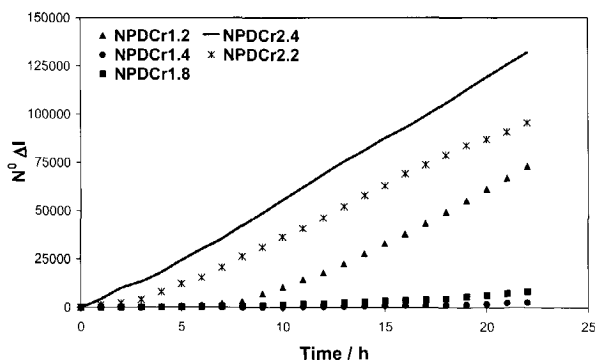


**Figure 6. 26:** Total number of current deviations from the mean value ( $\Delta I$ ) as function of the immersion time in 3.5% NaCl pH=4 solution.

of the exposure and deteriorates much faster during exposure than that of samples NPDCr1.4 and NPDCr1.8. Whereas, the chromate film formed at pH 1.2 behaves similarly to those formed at pH 1.4 or 1.8 during the first 6-8 hours of immersion and afterwards its corrosion protection decreases as fast as that of the films formed at higher pH, i.e 2.2 and 2.4. This is in line with the EIS results, which indicate a more pronounced worsening during the immersion in the chloride solution of the corrosion resistance of sample NPDCr1.2 in comparison with samples NPDCr1.4 and NPDCr1.8.

In conclusion, based on the EIS and EN investigations the effect of the pH of the chromate bath on the corrosion resistance provided by the chromate conversion coating to the aluminium substrate can be summarized as follows:

- ✓ A decrease of the pH of the chromate bath causes the formation of a chromate film being thicker, which would then have better barrier properties and better resistance to detachment.
- ✓ A decrease of the pH of the chromate bath causes the formation of a chromate film containing a higher amount of pores and defects, which would then have lower barrier properties and lower resistance to stresses.
- ✓ A decrease of the pH of the chromate bath causes the deposition during exposure of corrosion products being denser, and having lower variation in volume that leads to less pronounced stresses in the chromate film. The chromate film would then have a better self-healing behaviour and adhesion to the substrate.

Therefore, varying the pH of the chromate bath from 2.4 to 1.4 improves the corrosion behaviour of the chromate conversion coating. However, when the pH is further decreased the increase of the amount of pores and defects has a stronger effect than the increase of the thickness and of the protection provided by the CCP and as a consequence the corrosion performance of the chromate film becomes worst.

## 6.4 Conclusions

The impedance behaviour of the chromate film/aluminium substrate system has been modelled using an equivalent circuit, which was developed on the basis both of the TEM investigation and of the results reported in literature. Although the proposed network does not include all the phenomena involved in the response of such complex system during the impedance measurements, it does well represent the behaviour of the CCC on aluminium alloys in the conditions and especially within the frequency range that were used in this investigation. The validity of this equivalent circuit in representing the impedance response of the chromate conversion coating/Al substrate system is supported by both the evolution with the exposure time of the different electrical parameters, which have a well-defined physical meaning, and by the SEM study carried out on the sample surfaces after the impedance experiments.

In addition, the noise measurements have confirmed the differences in the corrosion resistance amongst the different chromate films, which were highlighted by the fitting of the impedance spectra. Specifically, the analysis of the impedance and noise data has shown

that the corrosion protection of the chromate conversion coating on Alclad 2024 alloy depends mainly on the following three factors:

- ✓ Barrier properties, i.e. capability to avoid the contact of the aluminium substrate with aggressive species, that depends on the thickness and the micro and nano-porosity of the film.
- ✓ Corrosion products deposited inside the defects that are determined by the chemical composition of the layer, in particular the amount of Cr(VI) adsorbed in the film.
- ✓ Adhesion to the aluminium substrate, i.e. capability to stand the stresses caused by the increase in volume due to the formation of extremely spongy corrosion products, that depends on the thickness and density of the layer.

These factors depend on the chromate process conditions, and also on the surface preparation procedure, since both affect the morphology and the chemical composition of the chromate conversion coating.

The decrease of the pH of the chromate bath leads to the formation of a thicker layer, which improves the barrier properties of the film, and to a higher amount of Cr(VI) adsorbed in the layer, which gives rise to the formation of corrosion products being more protective. In addition, the better protection caused by the CCP limits their own amount and the change in volume caused by them, which leads to the induction of lower stresses in the film and then a higher adhesion to the substrate. On the other hand, the decrease of the pH of the chromate bath causes also a larger amount of pores and defects, which makes worst the barrier and adhesion properties of the film. Therefore, the corrosion performance of the chromate conversion coating can be improved decreasing the pH of the chromate bath up to a value that optimises thickness, density and Cr(VI) content of the film.

The presence of intermetallic particles on the aluminium substrate negatively affects the corrosion protection provided by the CCC, since they are location of large defects in the film and as a consequence decrease the barrier and adhesion properties of the film itself. Once the corrosion attack has started inside the defects, the existence of the galvanic coupling between the IMC and the Al matrix leads to an acceleration of the attack with consequent formation of large quantity of spongy CCP. Besides, although not unequivocally proved, it seems that when IMCs are left on the surface a lower amount of Cr(VI) species is adsorbed in the CCC, which contributes to the decrease of the protection provided by the chromate corrosion products. This highlights the importance of the surface preparation procedure, which should enable the removal of most of the intermetallics from the aluminium surface in order to obtain a CCC being highly protective. In conclusion, it has been shown that the IMCs play a fundamental role in the corrosion behaviour of aluminium alloys, even when covered by a conversion film and even in the case of alloys containing a relatively small amount of intermetallics, as AA1230 used as clad layer for Alclad 2024 alloy. When alloys with a more complex microstructure, as AA2024, are considered this phenomenon is of course more pronounced, as will be described and discussed in the next chapter.

## 6.5 References

- [1] G. Goeminne, H. Terryn, J. Vereecken, *Electrochim. Acta* 40 (1995) 479

- [2] D. Ende, W. Kessler, D. Oekrug, R. Fuchs, *Electrochim. Acta* 38 (1993) 2577
- [3] H.J.W. Lenderink, J.H.W. de Wit, *Proceedings of the Electrochemical Society Meeting: Modification of Passive Films*, Paris, France (1993) 214
- [4] G.M. Tracy, G.D. Wilcox, M.O.W. Richardson, *Surf. Coat. Technol.* 114 (1999) 260
- [5] C. Marikkannu, P. Bala Srinivasan, S. Sathiyarayanan, K. Balakrishnan, *Trans. Inst. Met. Finish.* 73 (1995) 34
- [6] J. Hitzig, K. Jüttner, W.J. Lorenz, W. Paatch, *J. Electrochem. Soc.* 133 (1986) 886
- [7] J. De Leat, J. Scheers, H. Terry, J. Vereecken, *Electrochim. Acta* 38 (1993) 2103
- [8] C. Gabrielli, F. Huet, M. Keddad, R. Oltra, *Corrosion* 46 (1990) 266
- [9] J. Stewart, D.B. Wells, P.M. Scott, D.E. Williams, *Corros. Sci.* 33 (1992) 73
- [10] M. Hashimoto, S. Miyajima, T. Murata, *Corros. Sci.* 33 (1992) 885
- [11] A. Aballe, M. Bethencourt, F.J. Botana, M.J. Cano, M. Marcos, *Proceedings of Eurocorr2000*, London, UK (2000)
- [12] C.C. Hermann, Perraults, *Anal. Chem.* 40 (1968) 7
- [13] B.A. Boukamp, *Solid State Ionics* 20 (1986) 31
- [14] *Corrware for Windows, Electrochemistry / Corrosion Software, Operating Manual*, Scribner Associates Inc., Southern Pines, NC, USA (1998) 5.15
- [15] G.P. Bierwagen, *J. Electrochem. Soc.* 141 (1994) L155
- [16] D.A. Eden, A.N. Rothwell, *Proceedings of the NACE Meeting: Corrosion 92*, Nashville, TN, US (1992) Paper 292
- [17] F. Huet, *J. Electrochem. Soc.* 142 (1995) 2861
- [18] U. Bertocci, C. Gabrielli, F. Huet, M. Keddad, *J. Electrochem. Soc.* 144 (1997) 31
- [19] U. Bertocci, C. Gabrielli, F. Huet, M. Keddad, P. Rousseau, *J. Electrochem. Soc.* 144 (1997) 37
- [20] R.L. Motard, B. Joseph, X.D. Dai, *Proceedings of InterCorr/96, 1<sup>st</sup> Global Internet Corrosion Conference*, Technical Session 4,  
<http://www.corrosionsource.com/events/intercorr/techsess/papers/session4/abstracts/motard.htm>
- [21] L. Nyikos, T. Pajkossy, *Electrochim. Acta* 36 (1991) 163
- [22] U. Rammelt, G. Reinhard, *Corros. Sci.* 27 (1987) 373
- [23] M. Keddad, H. Takenouti, *Electrochim. Acta*, 33 (1988) 445
- [24] J.R. McDonald, *Impedance Spectroscopy: Emphasizing Solid Materials and Systems*, Wiley, New York, USA (1987)
- [25] D.H. van der Weijde, E.P.M. van Westing, J.H.W. de Wit, *Corros. Sci.* 36 (1994) 643
- [26] E.P.M. van Westing, D.H. van der Weijde, G. M. Ferrari, J.H.W. de Wit, *Proceedings of the 10<sup>th</sup> European Congress of Corrosion*, Barcelona, Spain (1993)
- [27] D. H. van der Weijde, Ph.D. thesis, TU-Delft, NL, (1996)
- [28] E.P.M. van Westing, Ph.D. thesis, TU-Delft, Delft, NL, (1992)
- [29] L.Xia, R. McCreery, *J. Electrochem. Soc.* 145 (1998) 3083
- [30] M.F. abd Rabbo, J.A. Richardson, G.C. Wood, *Corros. Sci.* 18 (1978) 117
- [31] G. Goeminne, PhD thesis, Vrije Universiteit Brussel, Belgium (1999)
- [32] H.A. Katzman, G.M. Malouf, *Appl. Surf. Sci.* 2 (1979) 416
- [33] A.E. Hughes, R.J. Taylor, B.W.H. Hinton, *Surf. Interface Anal.* 25 (1997) 22
- [34] E. Cuynen, P. Van Espen, G. Goeminne, H. Terry, *J. Anal. Atomic Spectr.* 14 (1999) 483
- [35] M.G. Fontana, *Corrosion Engineering*, 3<sup>rd</sup> edition, McGraw-Hill Book Company (1986)
- [36] J.R. Scully, *Corrosion* 56 (2000) 199
- [37] M.M. Lohrengel, A. Moehring, M. Pilaski, *Electrochim. Acta* 47 (2001) 137

# Microstructure and chromate conversion coating-Bare 2024

### 7.1 Introduction

In chapters 5 and 6 it has been shown that the surface preparation procedure largely affects the nucleation, growth and final properties of the CCC formed on Alclad 2024 aluminium alloy. This strong influence has been correlated to the different amount of intermetallic particles left on the surface after the surface preparation treatment. Indeed the IMCs of Alclad 2024 alloy are rich in iron and/or silicon and act as local cathodes leading to a preferential nucleation of the chromate film at their location and as a consequence to the formation of a chromate film containing a large amount of defects and providing less corrosion protection.

In this chapter the role played by the alloy microstructure on the formation and the corrosion protection mechanisms of the CCC is further investigated considering bare 2024 aluminium alloy as substrate. The choice of this alloy was based on both technological and scientific considerations. On one hand, amongst the aluminium alloys for aerospace applications, AA2024 is one of the most used and studied and on the other hand it contains a large amount of alloying elements in solid solution and of cathodic intermetallic particles. Therefore, it may be expected that the use of this alloy would enable not only to further confirm the effect of the cathodic IMCs on the nucleation, growth and final properties of the chromate film but also to highlight an eventual role played by the redeposition on the surface of small particles of some alloying elements, which are generally named smut and may occur during the activation processes preceding the chromate treatment. In particular, the surface preparation parameters studied are the same used in the case of the clad alloy, i.e. length of the acid pickling treatment and presence of a desmutting step.

In the first section of the chapter the experimental procedure, which is almost identical to that used for Alclad 2024 alloy, is shortly summarized. Afterwards, the main section concerning the description and discussion of the results is given divided into five main parts. Similarly to chapter 5, the first part deals with the influence of the surface preparation processes on the morphology and microstructure of the alloy surface, since this is the base for understanding the differences in the nucleation, growth and final properties of the CCC formed after the different surface treatments. Particular attention is given to the amount and type of intermetallic particles and to the redeposition of alloying elements, namely copper, on the surface. The effects of these two microstructural parameters on the nucleation and growth

mechanisms of the CCC are then discussed in the second and third part, respectively, of the section. Whereas, their influence on the final morphological features of the chromate film formed after a standard time of immersion in the Alodine bath is the topic of the fourth subsection. Finally, the last part discusses the influence of the morphological properties of the film on its corrosion resistance leading to a correlation between microstructure, specifically IMCs and copper deposits, of the aluminium substrate and the protection provided by the CCC.

## 7.2 Experimental procedure

### 7.2.1. Materials and treatment

A bare 2024 aluminium alloy in the T3 temper, which was rolled to a thickness of 0.8 mm, was used as substrate. The chromate conversion treatment was carried out as explained in section 5.2.1 of chapter 5 using the standard conditions, i.e. pH of 1.8 and temperature of 25°C.

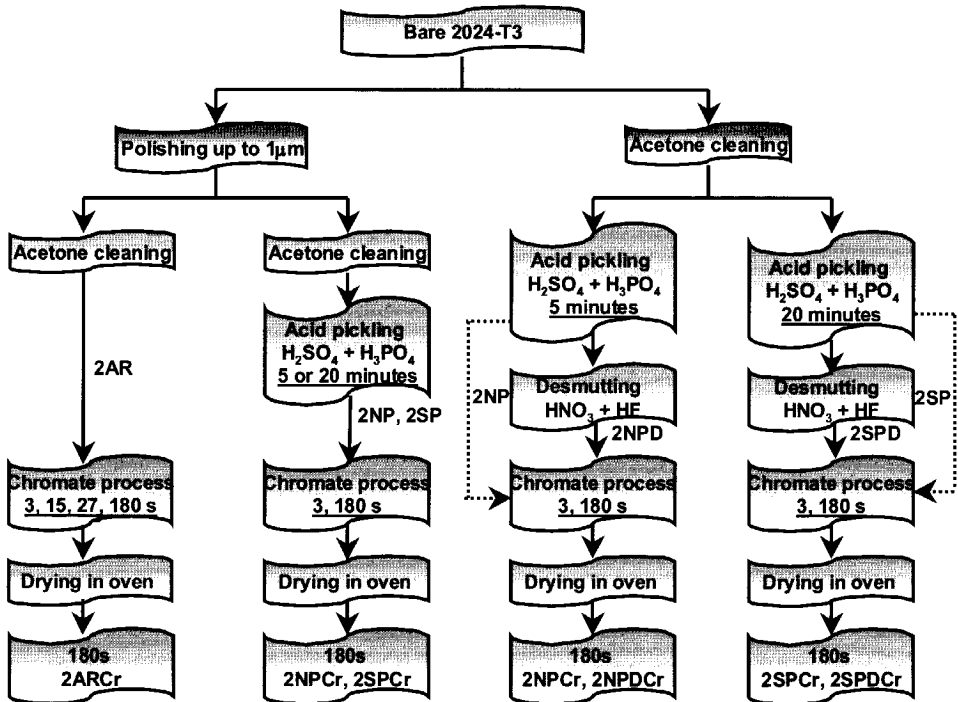


**Figure 7.1:** Schematic illustration of the different surface preparation and chromate treatment processes investigated in the case of bare 2024 alloy.

As in the case of the Alclad 2024 substrate four different surface preparation treatments were used before the immersion in the chromate bath: acetone cleaning and acid pickling for 5 or 20 minutes with or without a subsequent desmutting step (Figure 7.1).



The same code for the samples is used, except for the addition of the digit 2 in order to distinguish the bare 2024 samples from the Alclad ones: 2NP, 2SP, 2NPD, and 2SPD before chromate process and 2NPCr, 2NPDCr, 2SPCr, and 2SPDCr after the immersion in the Alodine 1200 solution for 3 minutes. In addition, a very short duration of the chromate treatment, i.e. 3 seconds, was also used in order to investigate the early stages of the CCC nucleation. This will be opportunely stated in the text.

The acid pickling treatment, i.e. procedure NP and SP, was carried out also on samples that were mechanically polished up to 1  $\mu\text{m}$  using diamond paste and ethanol as lubricant. Similarly to the unpolished samples, they were afterwards immersed in the chromate solution for 3 seconds or 3 minutes (Figure 7.1). The use of polished surface was mainly motivated by the attempt of avoiding any topographic artefacts in the SKPFM potential map.

Besides, some coupons of bare AA2024-T3 were polished up to 1 $\mu\text{m}$ , stored for 10 days in air and then directly immersed without any surface activation in the Alodine 1200 bath at room temperature and for different times: 3, 27, and 180 seconds. The samples before the chromate treatment are called 2AR and after the standard time of immersion in the chromate bath, i.e. 180 seconds, 2ARCr (Figure 7.1). The purpose of this part of the study was to enable the comparison of our own results with those reported in literature, which in most cases regard polished and untreated surfaces.

### **7.2.2. Surface analysis investigation**

The alloy surface was investigated by means of SEM, EDS, and SKPFM techniques after each step of the surface preparation and chromate processes described in the previous section. The experimental conditions used are the same of those given in the sections 4.3.2 of chapter 4 and 5.2.2 of chapter 5.

### **7.2.3. Electrochemical investigation**

The corrosion protection provided by the chromate conversion coating formed on unpolished surfaces after the different surface preparation procedures were studied using both electrochemical impedance spectroscopy (EIS) and electrochemical noise (EN). The theoretical principles and the experimental conditions of these techniques have been described in section 6.2 of chapter 6.

## **7.3 Results and discussion**

This section describes and discusses first the results of the SEM/EDS, SKPFM studies and afterwards the corrosion protection behaviour of the different CCCs extrapolated from the impedance and noise data. Both for the surface analysis measurements and for the electrochemical experiments for each sample 1 or 2 examples are given in order to illustrate the effect of the intermetallics and the copper deposits on the formation and corrosion protection mechanisms of the chromate film. On the other hand, this correlation between microstructural features and nucleation, growth, and final properties of the CCC was based on the results of several measurements.

### 7.3.1 Surface morphology and microstructure

- *As-received*

In agreement with the literature and our previous results, which have been described in chapter 2 and 4, respectively, the microstructure of bare 2024 aluminium alloy is characterized by the presence of numerous large intermetallic particles (Figure 7.2-a). The EDS spectra, some examples are given in Figure 7.2-b and -c, show that these IMCs belong to two main groups: the round shaped Al-Cu-Mg intermetallics (named hereafter IMC<sub>1</sub>), which are likely the equilibrium S-phase (Al<sub>2</sub>CuMg), and the Al-Cu-Mn-Fe-Si containing intermetallics (named hereafter IMC<sub>2</sub>), which are characterized by an irregular shape and a larger size in comparison with IMC<sub>1</sub>.

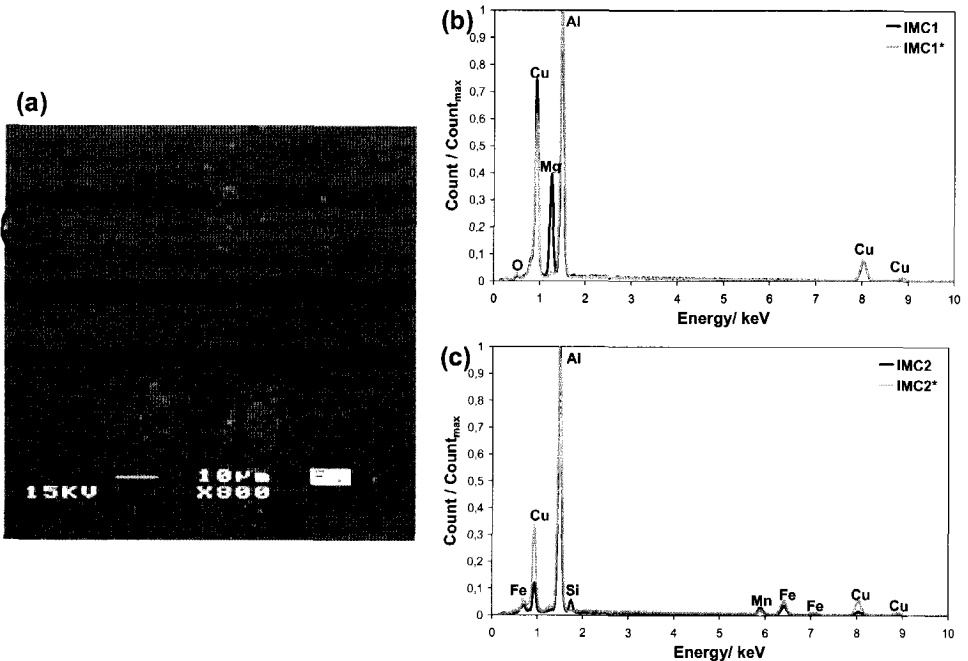


**Figure 7.2:** SEM micrograph (a) of bare 2024 alloy after mechanical polishing up to 1µm (sample 2AR) and EDS spectra of intermetallics IMC<sub>1</sub>/IMC<sub>1</sub>\* (b) and IMC<sub>2</sub>/IMC<sub>2</sub>\* (c).

In addition, amongst the round shaped intermetallics a small percentage was found to not contain magnesium (named IMC<sub>1</sub>\*) and some irregularly shaped IMCs are silicon-free (named IMC<sub>2</sub>\*). Although the EDS analyses do not enable a quantitative identification of the chemical composition of the intermetallic particles due to the strong background signal coming from the Al matrix, the Al-Cu intermetallics (IMC<sub>1</sub>\*) can be assigned, based on the equilibrium phase diagram of aluminium and copper, to the  $\Theta$ -phase, i.e. Al<sub>2</sub>Cu [1]. It should be noted that this type of intermetallics were not observed amongst the several IMCs analysed in the AA2024 coupons, which were used for the heat treatment investigation discussed in chapter 4 and which were obtained from a rolled batch of different thickness

provided by a different aluminium producer. This suggests that the amount of  $\Theta$ -phase, and more in general the percentage of the different intermetallics typical of 2024 aluminium alloy, can vary from batch to batch. This is likely related to the compositional ranges allowed for AA2024, specifically copper can vary from 3.8 up to 4.9 %, magnesium from 1.2 to 1.8%, and manganese from 0.3 to 0.9% in weight [2].

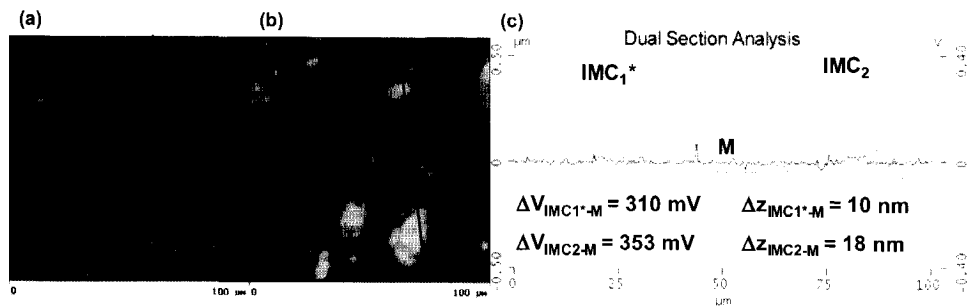


**Figure 7.3:** Topographic image with a height range of 1  $\mu\text{m}$  (a), Volta potential map with a potential range of 0.8 V (b), and dual section analysis (c) along the black lines in the topographic image (black) and in the potential map (grey) of sample 2AR.

Figure 7.3 reports the topographic image (a) and the Volta potential map (b) obtained with the SKPFM technique on the same area of the sample shown in the SEM micrograph of Figure 7.2-a. The correspondence of the AFM topographic map and the SEM micrograph can be found observing the presence of a small hole on the bottom-left corner and of a small debris on the top-left corner (enclosed in circles) of both images. Besides, they both show at the periphery of the intermetallic named  $\text{IMC}_2$  the presence of a hole, which is likely a consequence of the mechanical polishing procedure.

On the other hand, while it is almost impossible to identify the intermetallic particles in the topographic image they are clearly visible in the potential map as very bright areas. All types of IMCs are found to have a more noble Volta potential with respect to the surrounding aluminium matrix (named hereafter M in all section analyses). Figure 7.3-c shows the section analyses carried out along the same line, marked in black, of the topographic and potential scans. This operation is made using the "dual section" option of the software controlling the SKPFM instrument, which enables to obtain the height (black line) and potential (grey line) profiles along exactly the same line of the sample surface. Several section analyses lead to the conclusion that the difference in Volta potential between the matrix and the intermetallics, either those belonging to the  $\text{IMC}_1$  group, with or without Mg, or those belonging to the  $\text{IMC}_2$  group, containing or not silicon, varies from 150 up to 360 mV. In addition, the IMCs have been observed to slightly protrude from the surface, since the height at their sites is often 10-20 nm higher with respect to the rest of the surface. This is a consequence of the more pronounced hardness of the intermetallics in comparison with the Al matrix, which results in a different extent of thickness reduction at these two sites of the surface during the mechanical polishing procedure.

From our investigation it is not possible to distinguish the different intermetallic particles based on the value of their galvanic coupling with the matrix, since the ranges for

the various types of IMCs overlap. As already explained in chapters 4 and 5, the variation in the value of the Volta potential amongst intermetallics of the same group is a consequence either of small differences in chemical composition, which are below the detection limit of EDS, or of differences in size, which affect the measured potential due to the "size effect" phenomenon. While the cathodic nature of the Al-Cu and Al-Cu-Mn-Fe-(Si) intermetallics is expected, since they contains elements that are more noble than aluminium, that of Al-Cu-Mg is in contrast with the presence of a strongly anodic element as magnesium. Nonetheless, the more noble Volta potential of the Al-Cu-Mg intermetallics is in accordance with our own results given in chapter 4 and with those found in literature [3, 4]. As already mentioned in section 4.4.1 of chapter 4, the cathodic nature of these IMCs can be attributed to the presence of a modified surface layer enriched in copper.

It can be noted that the small variations in chemical composition and microstructure amongst 2024 aluminium alloys of different batches are reflected also in the surface Volta potential. Indeed, small differences in the range of the galvanic coupling of the IMCs with the Al matrix are observed between the alloy used in the heat treatment study (150-300 mV) and that used in the present investigation (150-360 mV).

The comparison of these results with those given in section 5.3.1 of chapter 5, relative to Alclad 2024 alloy, shows that AA2024 with respect to AA1230, used as clad layer, is characterized by a higher density of coarse intermetallic particles that are larger in size and cause a stronger galvanic coupling with the surrounding matrix. These differences in the microstructure of the two aluminium alloys is of course expected based on their different chemical composition.

- *Acid pickling (polished surfaces)*

The SEM study (Figure 7.4) shows that the immersion in the sulfuric/phosphoric acid bath of the polished AA2024 surface leads not only to a local attack in proximity of the intermetallic particles, which is a consequence of the cathodic nature of the IMCs themselves that cause the dissolution of the Al matrix at their periphery,

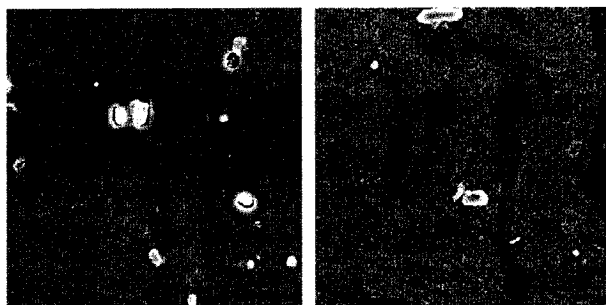


**Figure 7.4:** SEM micrographs of bare 2024 alloy after mechanical polishing and 5 minutes, sample 2NP (a), or 20 minutes, sample 2SP (b), of immersion in the  $\text{H}_3\text{PO}_4\text{-H}_2\text{SO}_4$  solution.

but also to the deposition of small particles over the whole surface, i.e. formation of a smut. Similarly to the Alclad 2024 alloy, the extent of the local attack increases with the increase of the immersion time in the pickling solution leading to the drop out of some IMCs,

which indeed were observed to be lower in number in sample 2SP than in sample 2NP.

Besides, the additional phenomenon of the smut formation that was not observed in the case of Alclad 2024 appears evident especially after relatively long time of immersion in

the pickling bath (Figure 7.4-b). However, the SEM investigation carried out at higher magnifications shows that the deposition of small particles, few nanometers in size, occurs already after five minutes of contact with the sulfuric/phosphoric acid bath (Figure 7.5-a). The comparison of the EDS spectra relative to areas of the surface free or covered by these deposits (named I and II, respectively, in the SEM micrograph of Figure 7.5-a) suggests that these small particles consist of copper, since the signals relative to this element are slightly stronger in the analyses made on the area where the deposits are present (Figure 7.5-d).

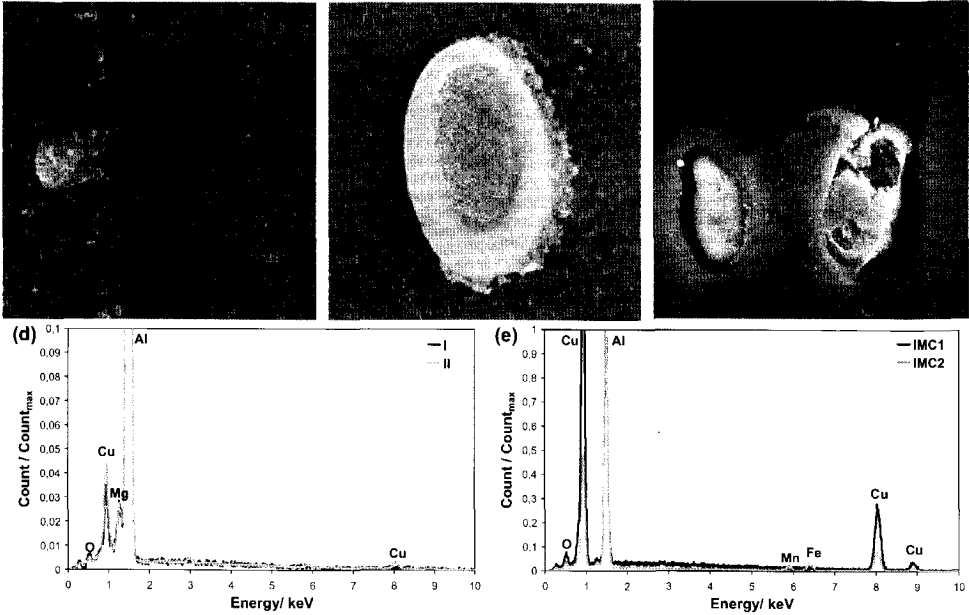


**Figure 7.5:** SEM micrographs (a, b, c) and EDS spectra (d, e) of sample 2NP. Polished sample.

Although the difference in the Cu peaks is quite limited due to the extremely small size of the particles that results in a strong background aluminium signal, the existence of such difference was found to be reproducible. The chemical composition of these particles is confirmed by the EDS analyses carried out on the surface of AA2024 after 20 minutes of immersion in the pickling bath, i.e. sample 2SP (Figure 7.6-d). Both the copper and oxygen signals are much stronger on the zones covered by the white deposits (SEM micrograph of Figure 7.6-a), which are present in larger amount than on sample 2NP and as a consequence the background signal of the matrix is limited enabling the identification of the chemical nature of these particles. According to these results, it can be stated that the immersion in the pickling bath results in the deposition of either metallic copper or copper oxide particles on the surface of AA2024. Besides, this phenomenon is strongly enhanced by the prolongation of the acid pickling treatment from 5 to 20 minutes.

The dissolution and redeposition of copper particles takes place more or less uniformly across the whole surface. This type of copper smut is a consequence of Cu release from the solid solution and is generally associated with high dissolution rate and relatively short solution-substrate contact time (few tens of minutes), as it is the case of the used acid

pickling process [5]. The formation of metallic copper and/or copper oxide deposits on aluminium surfaces is a well-known and studied phenomenon in the case of alkaline decreasing solution [6], however it can also occur in acid solution, according to our own results reported above and to the results of other researchers [7].

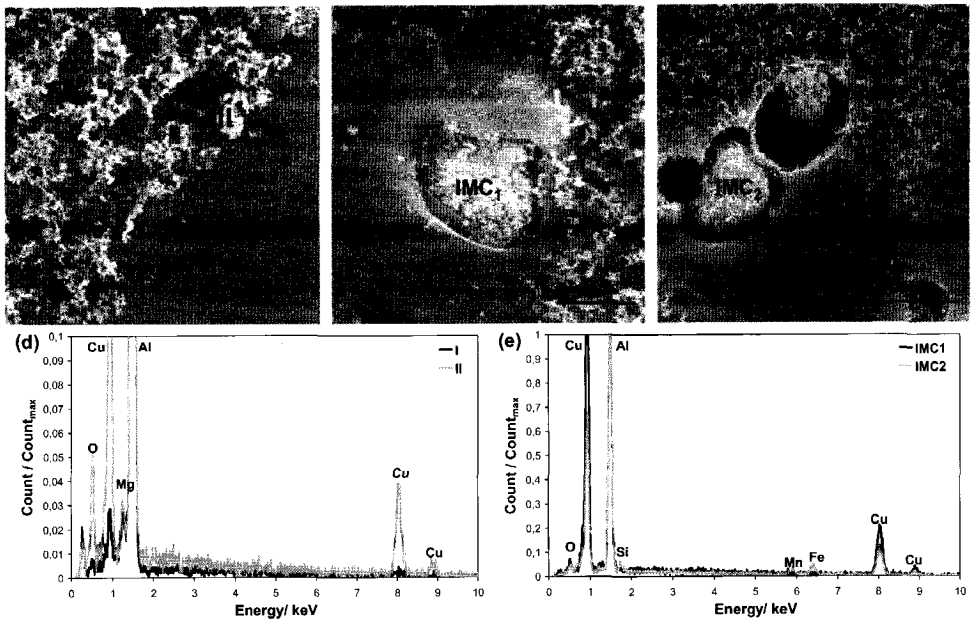


**Figure 7.6:** SEM micrographs (a, b, c) and EDS spectra (d, e) of sample 2SP. Polished sample..

As concern the intermetallic particles, the acid pickling process results not only in a local attack of the Al matrix at their periphery but it also affects their own morphology and chemical composition. The SEM investigation (Figures 7.5-b and -c and 7.6-b and -c) shows that both types of IMCs are characterized by some spongy zones, which are likely the results of a selective dissolution and the extent of which increases with the increase of the duration of the pickling process. According to the literature discussed in section 2.3.1 of chapter 2, preferential dissolution of Al, Fe, and Si from the Al-Cu-Mn-Fe-Si intermetallics and especially of Al and Mg from the S-phase occurs in aggressive environment [8-13]. This seems to take place also in the acid solution used as pickling bath, since the EDS analyses detect a much stronger Cu signal at the location of either the Al-Cu-Mn-Fe-(Si) or Al-Cu-Mg intermetallics after the immersion in the sulfuric/phosphoric acid bath (comparing Figure 7.2-b and -c with Figures 7.5-e and 7.6-e). The selective corrosion phenomenon involving the intermetallic particles may partially contribute to the formation of the Cu-rich smut observed on the whole surface. Indeed, as reported in section 2.3.1 of chapter 2, Buchheit et al. [9, 14, 15] suggested that the spongy structure of the IMCs caused by the selective dissolution of some elements favours the formation of small clusters of metallic copper, which can electrically detach from the sample surface enabling the dissolution of copper ions in the bath that in turn reduce and deposit back in other areas of the surface. Although this is likely the case, it is believed in view of the large amount of copper deposits on the surface,

especially after 20 minutes of immersion in the sulfuric/phosphoric acid bath, that the selective dissolution of the IMCs plays only a secondary role in the copper deposition phenomenon, which is mainly caused by the general and extensive release of copper from the solid solution over the whole surface.

Figure 7.7 shows the topographic images (a and d) and potential maps (b and e) of the same area of samples 2NP and 2SP of the SEM micrographs given in Figure 7.4. First of all, it should be noted that the quality of these images is lower in comparison with those obtained for the polished sample in the as-received condition (Figure 7.3). Especially in the case of sample 2SP, the signal of both the height and the potential appears to be disturbed in several horizontal scan lines (indicated by arrows in Figure 7.7). This is a consequence of both the deep pits in proximity of the IMCs and the presence of copper deposits, i.e. smut, on the surface. Indeed, the former feature constitutes sudden and large changes in the height of the sample that cannot be completely followed by the tip while scanning the surface, and on the other hand the copper deposits may remain attached to the tip during the scan leading to problems in measuring the Volta potential.

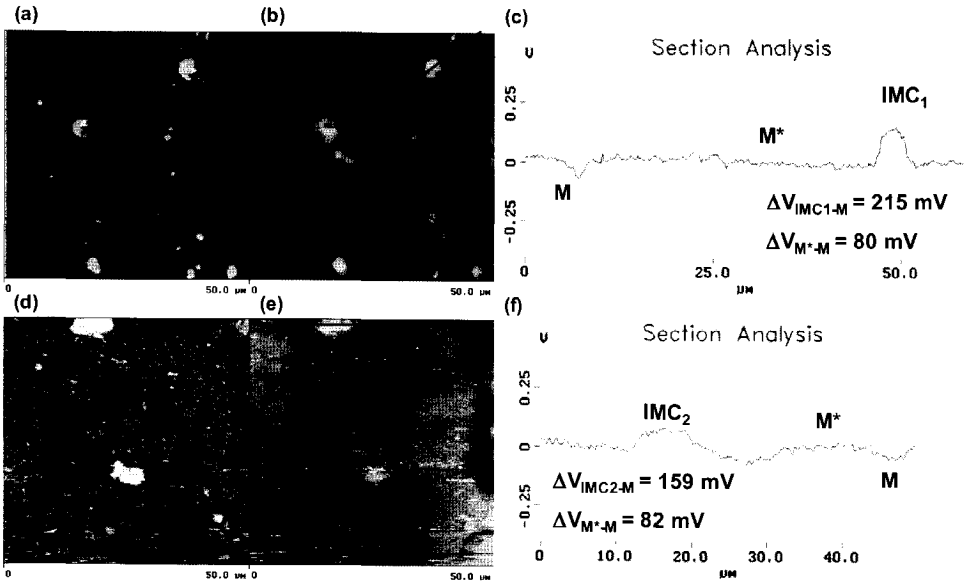


**Figure 7.7:** Topographic image with a height range of 1  $\mu\text{m}$  of samples 2NP (a) and 2SP (d), Volta potential map with a potential range of 0.8 V of samples 2NP (b) and 2SP (e), and section analysis along the black line in the potential map of samples 2NP (c) and 2SP (f). Polished samples.

Nevertheless, the SKPFM investigation confirms the conclusions drawn from the SEM study on the changes in the microstructure of AA2024 caused by the acid pickling treatment and enables also some additional considerations. The topographic images (Figure 7.7-a for sample 2NP and Figure 7.7-d for sample 2SP) show both the local attack at the periphery of the IMCs together with the presence of very small particles on the surface. On the other hand, the potential maps (Figure 7.7-b for sample 2NP and Figure 7.7-e for sample 2SP) present two main features: cathodic areas, which are clearly associated with the intermetallic

particles, and some zones characterized by a less noble Volta potential (named M) with respect to the rest of the surface (named M<sup>\*</sup>). The comparison of the potential maps with both the topographic images and the SEM micrographs (Figure 7.4) suggests, especially in the case of sample 2SP, that these anodic zones correspond to areas where the copper or copper oxide particles have been removed during the handling of the samples and the bare aluminium matrix is left, which is less noble in comparison with the copper deposits. This leads also to the conclusion that the copper or copper oxide particles are not strongly adherent to the AA2024 surface.

Finally, it is found by means of section analyses, examples are given in Figure 7.7-c and -e, that while the potential difference between the regions of the matrix enriched in copper (named M<sup>\*</sup>) and the bare Al matrix (named M) varies from 60 up to 100 mV, the galvanic coupling between the intermetallics and the bare Al matrix ranges between 150 and 350 mV. Therefore, similarly to the Alclad 2024 alloy, the immersion in the acid pickling bath seems to not affect either the electrochemical nature of the IMCs, which continue to behave as local cathodes, or the extent of their galvanic coupling with the Al matrix. On the other hand, due to the copper enrichment observed at the location of the intermetallics (EDS spectra of Figures 7.5-e and 7.6-e) an increase of the potential difference between Al matrix and intermetallics would have been expected. The reason of the lack of variation in the Volta potential of the IMCs after the pickling treatment, while their chemical composition is changed by this process, is not clear.

- *Acid pickling (unpolished surfaces)*

A SEM/EDS investigation (Figure 7.8) has been carried out also on the samples that were immersed in the pickling bath for 5 or 20 minutes without being previously polished in order to verify that the polishing procedure does not affect the reactivity of the AA2024 surface towards the sulfuric/phosphoric acid bath. It can be noted that also on the unpolished surfaces a local attack in proximity of the IMCs together with the formation of a smut, i.e. copper and/or copper oxide particles, takes place during the pickling treatment, especially when the duration of the process is increased from 5 to 20 minutes. The only difference observed between the polished (Figure 7.4) and unpolished surfaces (Figure 7.8) is that on the latter the corrosive attack is localized also along the trenches

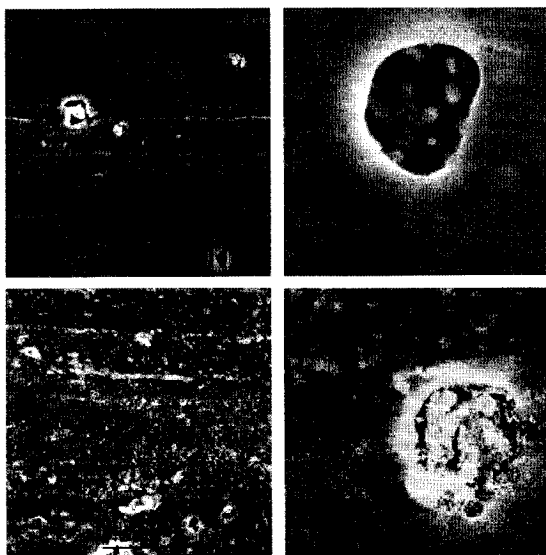


**Figure 7.8:** SEM micrographs of bare 2024 alloy after 5 minutes, sample 2NP (a, b) or 20 minutes, sample 2SP (c, d) of immersion in the H<sub>3</sub>PO<sub>4</sub>-H<sub>2</sub>SO<sub>4</sub> solution. Unpolished samples.



left by the rolling process, where the natural aluminium oxide film is likely weaker and therefore more susceptible to breakdown.

In conclusion, the immersion in the sulfuric/phosphoric acid solution causes local dissolution of the Al matrix at the periphery of the IMCs, selective attack of the IMCs themselves, and deposition of small copper or/and copper oxide particles on the AA2024 surface. The increase of the duration of the pickling treatment from 5 to 20 minutes enhances all these phenomena leading to a surface being more enriched in Cu and containing a lower amount of intermetallics as a consequence of the stronger attack of the matrix in their proximity, which in turn can result in the drop out of the IMCs themselves.

- *Desmutting (unpolished surfaces)*

Likewise observed for Alclad 2024 alloy (section 5.3.1 of chapter 5), the immersion in the nitric/hydrofluoric acid solution gives rise to a stronger attack of the AA2024 surface as a consequence of the simultaneous presence of the aggressive  $F^-$  ions and the low pH. This appears evident when the SEM micrographs of Figure 7.8-a, -b, and -c and those of Figure 7.9-a and -d are compared.

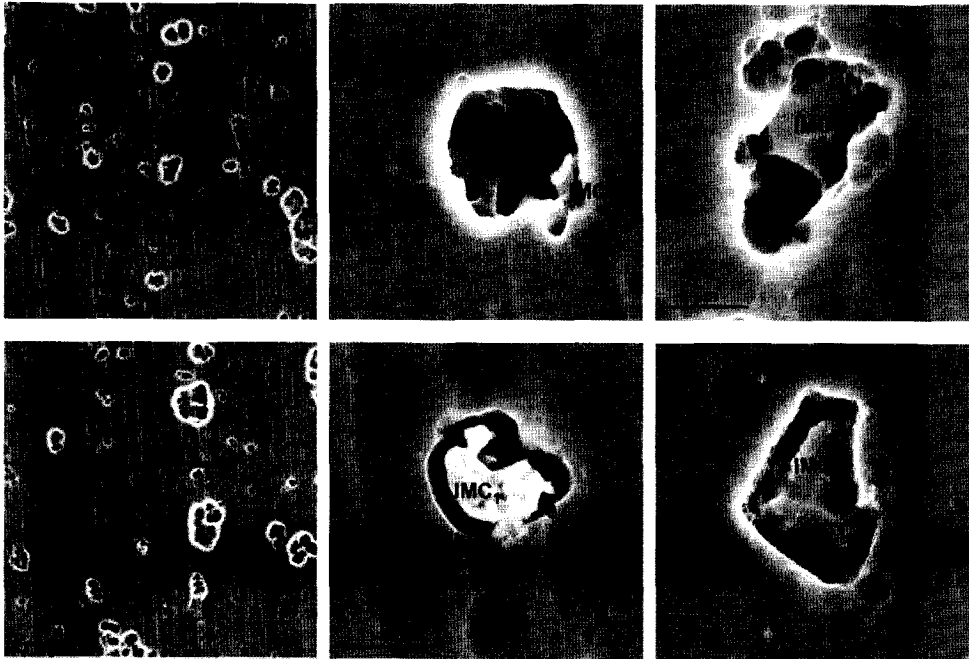


**Figure 7.9:** SEM micrographs of bare 2024 alloy after 5 minutes of immersion in the  $H_3PO_4-H_2SO_4$  solution and 30 seconds of immersion in the  $HNO_3-HF$  solution, samples 2NPD (a, b, c), and after 20 minutes of immersion in the  $H_3PO_4-H_2SO_4$  solution and 30 seconds of immersion in the  $HNO_3-HF$  solution, samples 2SPD (d, e, f). Unpolished samples.

The surface of samples 2NPD and 2SPD is characterized by the presence of numerous large pits and by a more pronounced attack at the location of the markings caused by the rolling process. The pits are developed by the preferential dissolution of the Al matrix in proximity of the intermetallics, which takes place during the pickling treatment and

even more during the desmutting step leading to the removal of the IMCs themselves. In some cases at the location of the pits part of the intermetallic is still present, as can be observed in the SEM micrographs of Figure 7.9-b and -c for sample 2NPD and of Figure 7.9-e and -f for sample 2SPD, which show also that the IMCs themselves are attacked by the contact with the nitric/hydrofluoric acid solution. The immersion in the desmutting bath removes not only a large percentage of the intermetallics but also eliminates completely the copper smut from the surface, even when present in very large quantity as a consequence of the long pickling treatment. The absence of copper and/or copper oxide deposits appears clear from the SEM investigation and from the EDS analyses, not shown here, which are characterized by copper peaks similar to those of the as-received surface. Therefore, in the case of AA2024 the nitric/hydrofluoric acid treatment fulfils really the function of a desmutting process.

The presence of large and numerous pits, inside some of which an or part of an intermetallic particle is still present, on the surface of samples 2NPD and 2SPD is confirmed by the topographic images and the potential maps given in Figure 7.10. Indeed at the

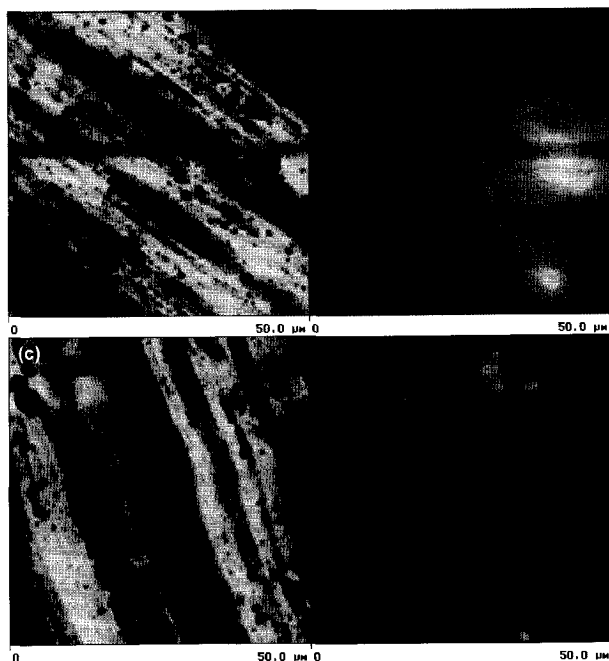


**Figure 7.10:** Topographic image with a height range of 1  $\mu\text{m}$  of samples 2NPD (a) and 2SPD (c) and Volta potential map with a potential range of 0.8 V of samples 2NPD (b) and 2SPD (d). Unpolished samples.

location of some pits, which are clearly visible in the topographic map of the surface, on the potential map bright areas are observed, i.e. areas having a more noble Volta potential in comparison with the rest of the surface. The value of these galvanic couples is found by means of section analyses to vary from 140 up to 300 mV. The similarity of this range with those observed for the IMCs either in the as-received condition or after the acid pickling step suggests that these local cathodes are associated with the intermetallics left on the surface after the desmutting treatment.

The similarity of both the SEM micrographs and the SKPFM images of samples 2NPD and 2SPD shows that the effect of the duration of the acid pickling treatment on the microstructure of AA2024 is completely overruled by the desmutting process, which results in the removal of both the smut rich in copper and of a

large part of the intermetallics independently from the previous surface treatment. This was found also to be the case for Alclad 2024 alloy.

Although the influence of the various surface preparation steps on the microstructure of bare 2024 and Alclad 2024 shows some similarities, which were mentioned during the previous discussion of the results, important differences are observed for the two types of substrate. First of all, the main effect of the acid pickling process consists of the deposition of copper and/or copper oxide particles on the surface of AA2024, whereas in the case of Alclad 2024 is the formation all over the surface of small pits that become larger and shallower with the increase of the duration of the treatment. As concern the desmutting step, while the intermetallics are completely removed from the surface of Alclad 2024, a non-negligible amount is left on the surface of the bare alloy. In addition, the corrosive attack appears to be more general and involving the whole surface, especially during the desmutting process, in the case of the clad alloy than in the case of the bare one, which shows a more localized type of attack with the formation of more isolated and deeper pits. Obviously, these differences are related to the different microstructure of the two alloys: more numerous, bigger IMCs having a stronger galvanic coupling with the matrix, together with higher amount of copper in solid solution for bare AA2024 in comparison with AA1230 that forms the clad layer of the Alclad 2024 alloy.

It is expected that the presence of both the numerous and large cathodic intermetallics and the copper deposits on the surface of AA2024 affects the nucleation and growth of the chromate conversion coating. Therefore, an attempt to separately study the role of these two microstructural features, i.e. IMCs and Cu-rich smut, on the formation of the CCC is made by investigating the nucleation and growth of the film first on untreated AA2024, where only IMCs are present, and then on the pickled and/or desmuted AA2024, where in some cases the deposition of Cu particles has occurred in large extent. The results of these two studies are described and discussed in the next two sections.

### 7.3.2 Nucleation and growth of the CCC: effect of the intermetallics

- *Nucleation*

Some examples of the SEM and EDS investigation carried out on bare 2024 after mechanical polishing up to 1  $\mu\text{m}$  (sample 2AR) and immersion for 3 seconds in the chromate bath are given in Figure 7.11. The SEM micrographs, especially those obtained at high magnification (Figure 7.11-a), show that some areas of the surface are covered by a thin layer, which is identified to consist of chromium oxide by the EDS analyses. In addition, from the EDS spectra it can be observed that chromium and oxygen are detected only at the location of the IMCs, either the Al-Cu-Mg ( $\text{IMC}_1$ ), Al-Cu ( $\text{IMC}_1^*$ ), or Al-Cu-Mn-Fe-(Si) ( $\text{IMC}_2$  and  $\text{IMC}_2^*$ ), whereas above the aluminium matrix they are found to be completely absent or present in such low amount to be below the detection limit of EDS. This appears even more clearly when the elemental maps relative to chromium, oxygen, and copper are recorded (Figure 7.12). Indeed, the detection of chromium and oxygen is always associated with the presence of copper, which in turn is an indication of the presence of an intermetallic particle.

The topography and the Volta potential of the same areas of the SEM micrographs given in Figure 7.11-a and -c are recorded using the SKPFM technique (Figure 7.13).

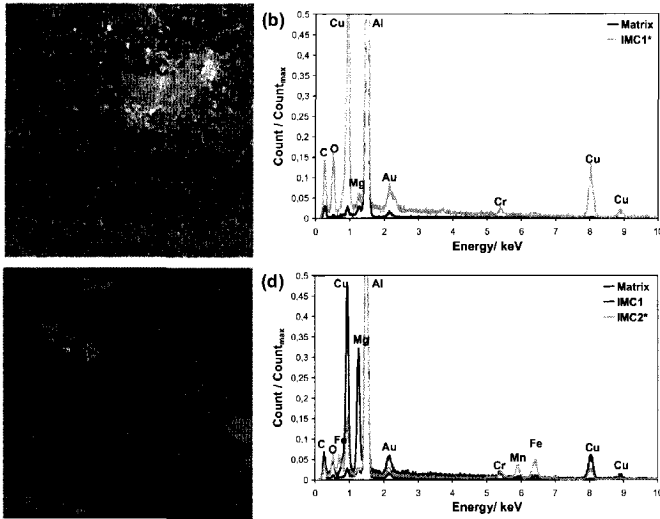


**Figure 7.11:** SEM micrographs (a, b), EDS spectra (b, d) of sample 2AR after 3 seconds of immersion in the chromate bath.

The bright areas, i.e. cathodic regions, in the potential maps correspond to the intermetallics observed in the SEM investigation and to brighter areas, i.e. zones being higher than the rest of the surface, in the topographic images. This suggests that a film is present on the AA2024 surface at discrete sites associated with the cathodic IMCs. The dual section analyses show the height (black lines in the plots of Figure 7.13-c

and -f) and the potential (grey lines in the plots of Figure 7.13-c and -f) profiles along the same line, marked in black, in the topography and potential scans. It can be clearly noted that areas having a more noble potential, i.e. the cathodic intermetallics, are also characterized by a higher height.

According to the dual section analyses across several IMCs while the increase in height at their location ranges from 40 nm up to 130 nm, their potential varies between 100 and 280 mV. It should be observed that the variation in height between the IMCs and the Al matrix cannot be a result of the solely difference in polishing rate, since this phenomenon discussed in the previous section for sample 2AR causes a very limited difference in height, in the order of 10-20 nm. Therefore the several tens of nanometers of difference measured between the location of the intermetallics and that of the matrix may be expected to be a consequence of the formation of a thin film above the IMCs. In addition, it is

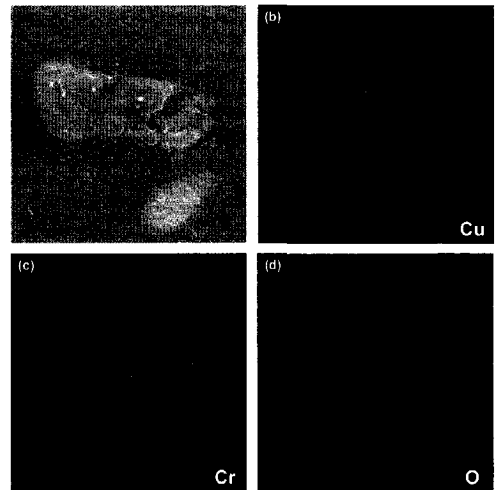


**Figure 7.12:** SEM micrograph (a) and EDS elemental maps (b, c, d) of sample 2AR after 3 seconds of immersion in the chromate bath.

important to note that the 3 seconds of exposure to the chromate bath cause also a decrease of the differences in Volta potential between the IMCs and the Al matrix from 150-360 mV to 100-280 mV.

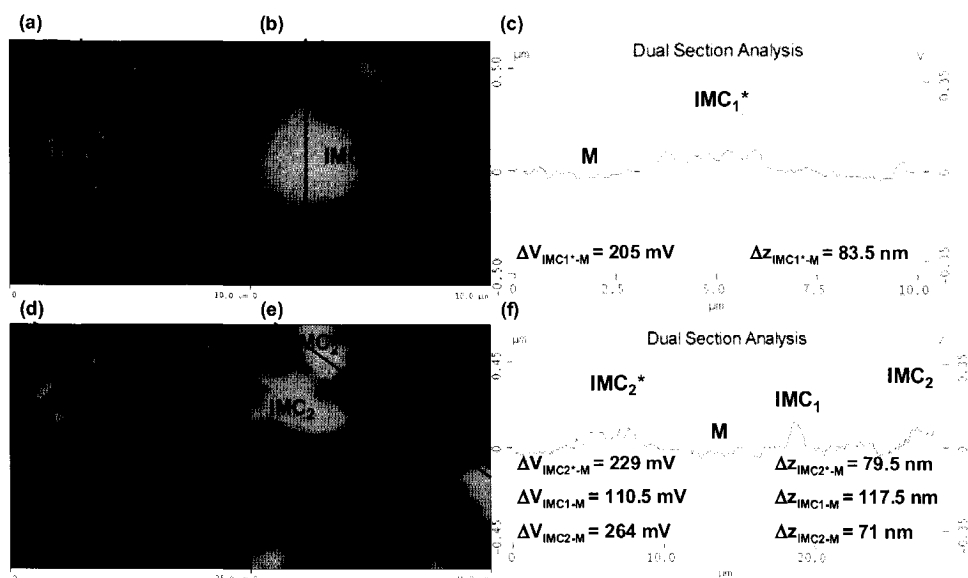


**Figure 7.13:** Topographic images with a height range of 1 μm (a, d), Volta potential maps with a potential range of 0.8 V (b, e), and dual section analysis (c, f) along the black lines in the topographic images (black) and in the potential maps (grey) of sample 2AR after 3 seconds of immersion in the chromate bath.

On the basis of the SEM/EDS and SKPFM results it can be stated that during the short immersion in the Alodine solution while at the location of the cathodic intermetallic particles a thin chromate film does form, above the aluminium matrix the precipitation of chromium oxide does not occur at all or in such a limited extent that cannot either be observed in the SEM micrographs or detected by the EDS analysis. Therefore, likewise for the Alclad 2024 alloy, the nucleation of the chromate conversion coating on bare 2024 occurs preferentially at the sites of the cathodic intermetallics, which favour the reduction of Cr(VI) species and the subsequent precipitation of chromium oxide/hydroxide (see section 5.3.2 for details). In addition, it seems that the formation of a thin CCC above the IMCs leads to a decrease of the extent of the galvanic coupling existing between the Al matrix and the intermetallic particles themselves, which in turn results in a reduction of the driving force for the deposition of chromium oxide/hydroxide at the location of the intermetallics.

It should be noted that also without any activation step, as it is the case for sample 2AR, the nucleation of the CCC above the intermetallics is extremely fast leading to the formation of a layer 40-130 nm thick above each type of IMCs after only few seconds of immersion in the chromate bath. This suggests that the cathodic nature of the intermetallics themselves overrules the necessity of removing, partially or completely, the natural aluminium oxide film from the surface to enable the precipitation of the chromate film at their location.

• Growth

When the surface of sample 2AR is investigated after 27 seconds of immersion in the Alodine solution the EDS elemental maps show that chromium and oxygen are present homogeneously on the whole surface and not anymore enriched at the site of the intermetallics (Figure 7.14). This means that after the fast nucleation of the chromate film above the IMCs the chromium hydroxide/oxide precipitates on the Al matrix resulting in a CCC of homogeneous thickness covering the whole surface. Nevertheless, the intermetallic particles can be still clearly distinguished both in the SEM micrographs and especially in the AFM topographic images (Figure 7.15-a and -d).

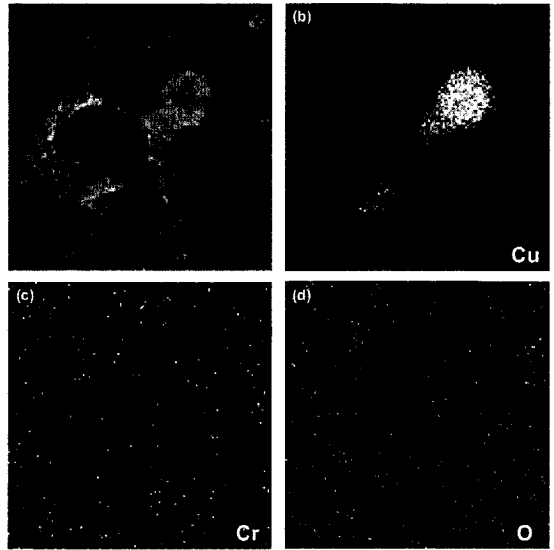


Figure 7.14: SEM micrograph (a) and EDS elemental maps (b, c, d) of sample 2AR after 27 seconds of immersion in the chromate bath.

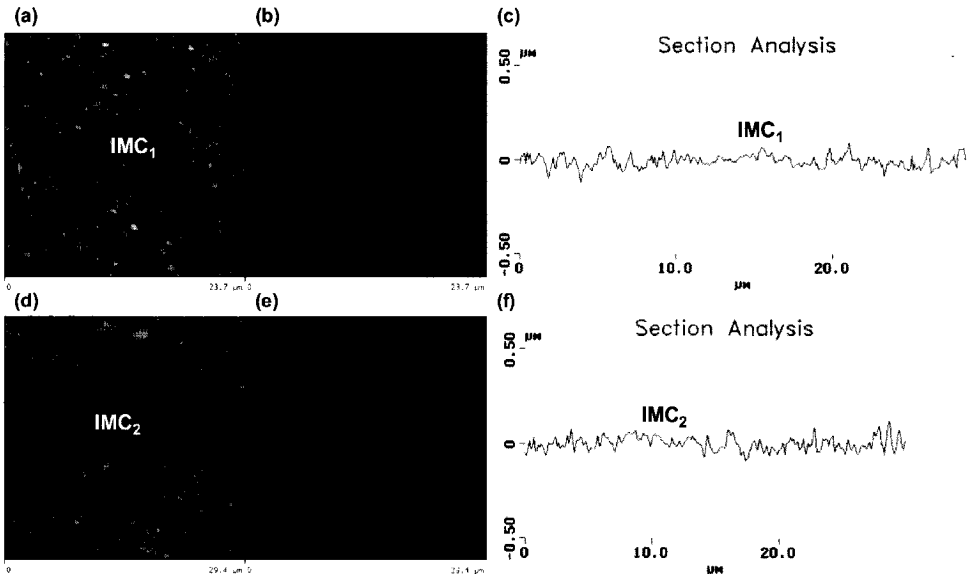
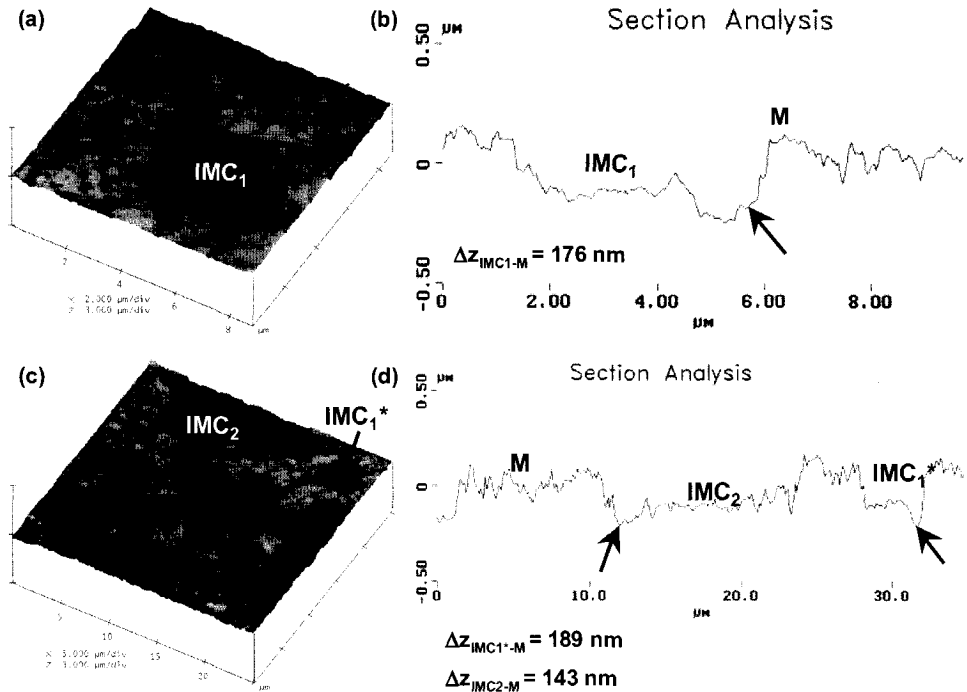


Figure 7.15: Topographic images with a height range of 1  $\mu\text{m}$  (a, b), Volta potential maps with a potential range of 0.8 V (c, d), and section analyses along the black lines in the topographic images (e, f) of sample 2AR after 27 seconds of immersion in the chromate bath.

Indeed, the chromate layer formed on the matrix has a different morphology than that formed on the IMCs, although it has a similar thickness, as can be noted in the section analyses of Figure 7.15-c and -f. The film precipitated on the matrix appears to be formed by smaller and less compact nodules and a lack in continuity of the layer at the edges of the intermetallics exists. On the other hand, the location of the IMCs is not anymore reflected in the Volta potential map, which shows the existence of an extremely homogeneous potential on the whole surface. Therefore, it seems that the immersion for 27 seconds in the chromate bath leads to the formation of a CCC above both the Al matrix and the IMCs, which hides the galvanic coupling between them.



**Figure 7.16:** 3D topographic images (a, c), and section analyses along the black lines in the topographic images (b, d) of sample 2AR after 3 minutes of immersion in the chromate bath (sample 2ARCr).

Finally, also when a conventional time of immersion in the Alodine bath, i.e. 3 minutes, is used the site of the intermetallics is easily observed in the topographic images (Figure 7.16-a and -c), whereas the Volta potential, not given here, is completely homogeneous. The section analyses of the AFM topographic scans show a large difference in height between the IMCs and the matrix, ranging from 130 up to 200 nm, that is likely due to the formation of a thicker chromate film above the matrix than on top of the intermetallics. This is in accordance with the EDS elemental maps (figure 7.17), which highlight the presence of a lower concentration of chromium and oxygen in correspondence of the areas enriched in copper, i.e. at the location of the IMCs.

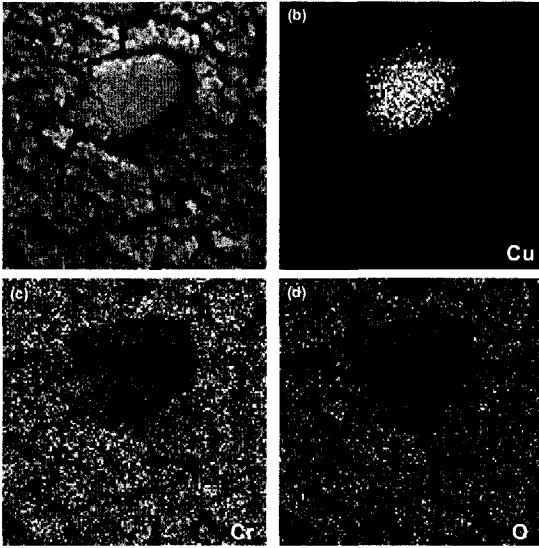


**Figure 7.17:** SEM micrograph (a) and EDS elemental maps (b, c, d) of sample 2ARCr.

In addition, likewise observed after 27 seconds of immersion, the difference in morphology of the CCC formed on top of the Al matrix and above the intermetallics is kept also after a relative long time of dipping in the Alodine solution. According to the duplex structure of the CCC, which was described in section 5.3.3 of chapter 5 in the case of Alclad 2024 alloy, it seems that in proximity of the intermetallic particles the formation of the porous film above the dense and thin barrier layer is inhibited. Besides, it is important to note that discontinuities, i.e. deep holes (indicated by arrows in the section analyses of Figure 7.16-b and -d), in the chromate film are

always present at the periphery of the intermetallics. This can be also observed in the SEM micrograph of Figure 7.17-a.

Based on the electrochemical reactions involved in the precipitation of chromium hydroxide/oxide from the chromate bath (reactions 3.2, 3.3, and 3.4 of chapter 3) and on the results previously described, the following mechanism of nucleation and growth of the CCC on aluminium alloys is proposed. The reduction of Cr(VI) to Cr(III), which leads to the formation of chromium oxide/hydroxide deposits, starts at the intermetallic particles (Figure 7.18-a and -b) due to two main reasons:

- ✓ The more noble potential of the intermetallics in comparison with the matrix favours the occurrence of the cathodic reactions at these locations. This causes an increase of pH, which in turn leads to the precipitation of chromium hydroxide.
- ✓ The natural aluminium oxide layer in proximity of the intermetallics is thinner and contains more defects and therefore is more easily attacked by the fluoride species present in the Alodine solution. The lower thickness and the higher conductivity of the aluminium oxide above the intermetallics enhance the electron tunnelling at these sites.

As a consequence, a thin and dense chromate layer is formed on top of the intermetallics after a very short time of immersion in the chromate bath. Such a film renders the intermetallics less active, since it hinders the electron transfer giving rise to a slowing down of the electrochemical reactions at their location and it also reduces the strength of the cathodic nature of the IMCs leading to a decrease of the driving force for the reduction of the chromate species at the sites of the IMCs (Figure 7.18-c). The lowering of the cathodic IMCs activity caused by the deposition of the CCC above them is in agreement with the findings of



Ilevbare *et al.* [16], who found that the rate of the oxygen reduction reaction on Al-Cu, Al-Cu-Mg, and Al-Cu-Fe-Mn analogs is reduced by the presence of the chromate film.

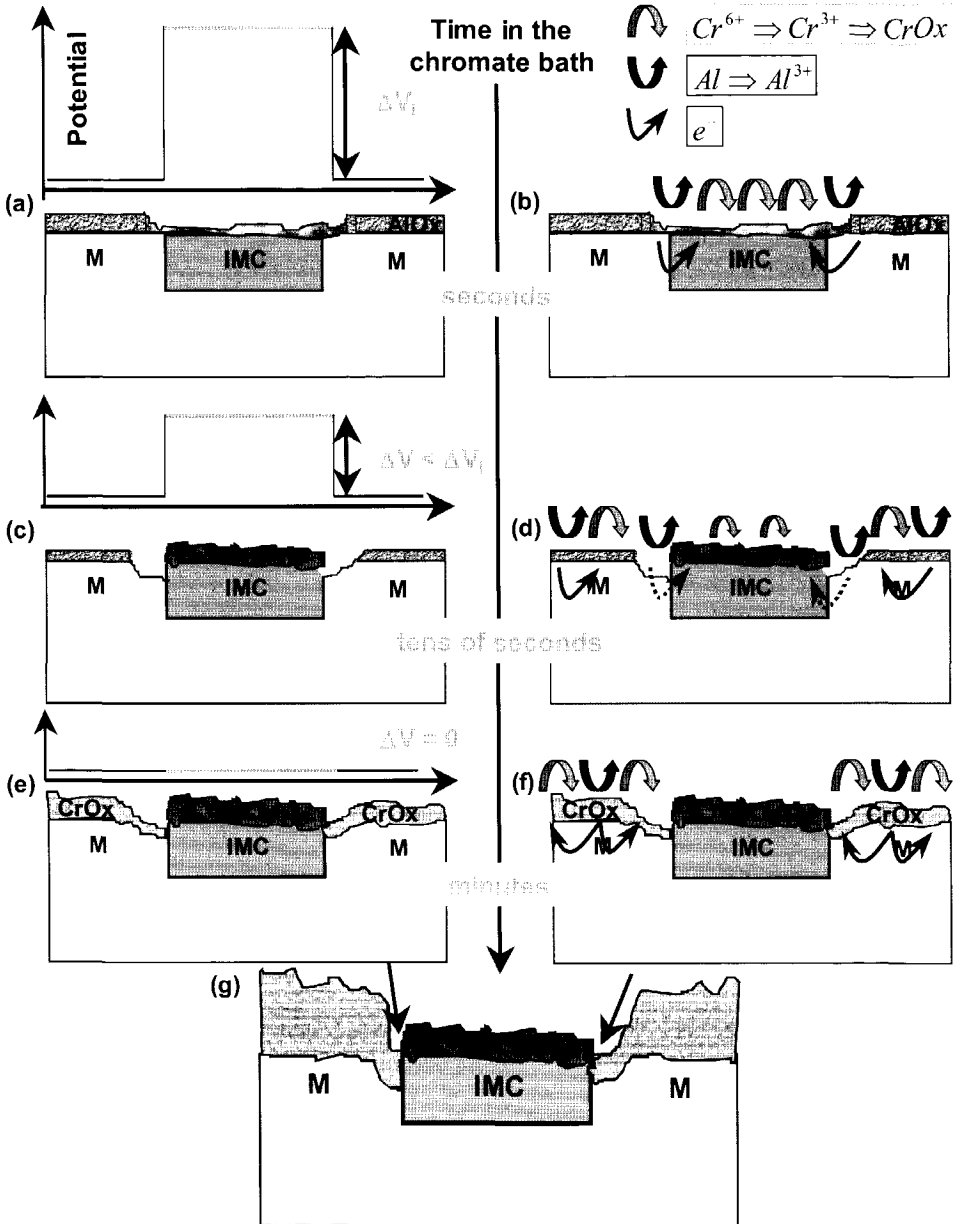


**Figure 7.18:** Schematic illustration of the influence of the intermetallic particles on the nucleation (a, b), growth (c, d, e, f), and final morphology (g) of the CCC on aluminium alloy surfaces.

Therefore, the formation of the chromate film continues afterwards on the matrix (Figure 7.18-d), resulting in the formation of a CCC above the whole surface and as a consequence to the complete elimination of the galvanic coupling between the IMCs and the

matrix (Figure 7.18-e). At this point, the driving force that causes the deposition of the layer to take place preferentially on top of the intermetallic particles does not exist anymore. The deposition of the chromate film on the intermetallics is largely faster than on the matrix and this is likely the reason of the different morphology at these two locations: compact and dense on the intermetallics, porous and consisting of small chromium oxide/hydroxide nodules on the matrix (Figure 7.15). This results in a further growth of the chromate film on the Al matrix, since the more pronounced porosity of the layer at its location enables both the electrons tunnelling through the coating itself and the solution access to the aluminium surface to be high enough for the electrochemical reactions, i.e. chromate reduction and aluminium dissolution, to continue (Figure 7.18-f). Therefore, when the time of immersion in the chromate bath is in the order of minutes, the chromate film deposited on the aluminium matrix becomes thicker in comparison with that formed above the intermetallic particles (Figure 7.18-g). It should be noted that although a thin and dense chromate film covers the IMCs, they represent always weak spots in the conversion film, since at their periphery a defect in the layer is created due to the different time and rate of the CCC formation above the matrix and above the intermetallics.

As mentioned previously in the section relative to the experimental procedure the investigation of the chromate film formation on polished and untreated 2024 aluminium alloy was carried out also to enable a comparison between our own results and those reported in literature and described in section 3.2.3 of chapter 3. The mechanism proposed above, which distinguishes between the nucleation and the growth of the chromate film, explains not only the results of our investigation but also clarify the apparent contradiction found amongst the results of different research groups. Some authors [17-19] stated that the formation of the chromate conversion coating on AA2024 takes place preferentially above the IMCs, whereas other authors [20-23] suggested that the intermetallics inhibit the deposition of the chromate film. However, while the former investigated the surface after a very short time of immersion in the chromate bath, in the order of few seconds, the latter studied the chromate film formation using a relative long treatment time, in the order of few minutes. Therefore, the former were observing the nucleation of the film, which according to the mechanism proposed is indeed occurring preferentially at the location of the intermetallics, whereas the latter were looking at the growth of the conversion coating, which based on our mechanism is indeed hindered above the intermetallics.

On the other hand, these studies reported in literature did not consider the influence of the surface preparation procedure on the formation of the CCC, which is however expected to be quite significant since the surface preparation treatments affect the microstructure of the aluminium alloys. In particular, the treatments used in this work, i.e. pickling and desmutting, have been shown to modify the density of the IMCs and to cause in some cases the deposition of a copper-rich smut on the surface. The next section deals with the effects of the various surface preparation procedures, with particular attention to the role played by the copper-rich smut, on the mechanism of the chromate film deposition.

### 7.3.3 Nucleation and growth of the CCC: effect of the Cu-rich smut

- Acid pickling (polished surfaces)

The SEM and EDS investigation carried out on the polished AA2024 immersed for 5 minutes in the sulfuric/phosphoric acid bath, sample 2NP, and afterwards for 3 seconds in the Alodine solution shows that a thin layer consisting of chromium hydroxide/oxide is formed on top of the intermetallic particles, independently on their chemical composition, but not over the aluminium matrix. Few examples of typical SEM micrographs and EDS analyses of sample 2NP treated for 3 seconds in the chromate bath are given in Figure 7.19.

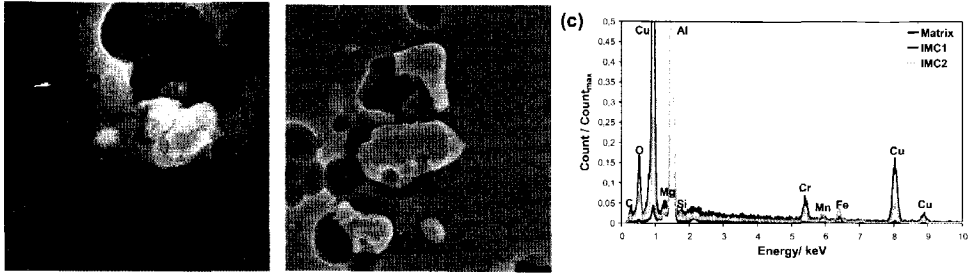


**Figure 7.19:** SEM micrographs (a, b) and EDS spectra (c) of sample 2NP after 3 seconds of immersion in the chromate bath. Polished sample.

A similar behaviour is observed also when the acid pickling treatment is prolonged up to 20 minutes, i.e. sample 2SP (Figure 7.20). On both samples it is evident a strong localized attack of the Al matrix at the periphery of the IMCs, which has taken place during the surface preparation treatment, i.e. immersion in the  $H_2SO_4/H_3PO_4$  bath, and is likely enhanced during the short chromate process due to the presence of the aggressive fluoride species in the Alodine solution. On the other hand, the short contact with the  $F^-$  ions of the chromate bath does not eliminate the copper-rich smut on the AA2024 surface. Indeed, after the 3 seconds of immersion in the chromate bath the metallic copper and/or copper oxide particles are still observed on the Al matrix, especially on sample 2SP (Figure 7.20-a and b).

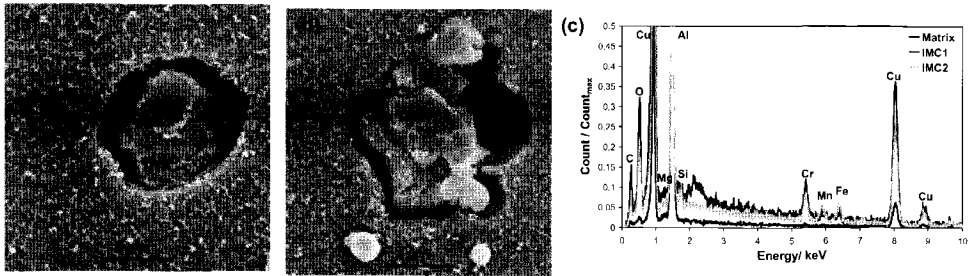


**Figure 7.20:** SEM micrographs (a, b) and EDS spectra (c) of sample 2SP after 3 seconds of immersion in the chromate bath. Polished sample.

Therefore, it can be concluded that the immersion of the polished AA2024 for either 5 or 20 minutes in the acid pickling bath prior to the chromate treatment does not modify the nucleation of the film, which occurs preferentially at the sites of the IMCs, similarly to sample

2AR (Figure 7.23-a and -b). This means that the Cu-rich smut does not play an important role in the early stages of formation of the CCC.

The topographic images of samples 2NP and 2SP after a standard time (3 minutes) of immersion in the Alodine bath, i.e. samples 2NPCr and 2SPCr, show that the chromate film deposited on the Al matrix results to be thinner and it consists of smaller and less compact nodules in comparison with that formed on the IMCs (Figures 7.21-a and 7.22-a for samples 2NPCr and 2SPCr, respectively).

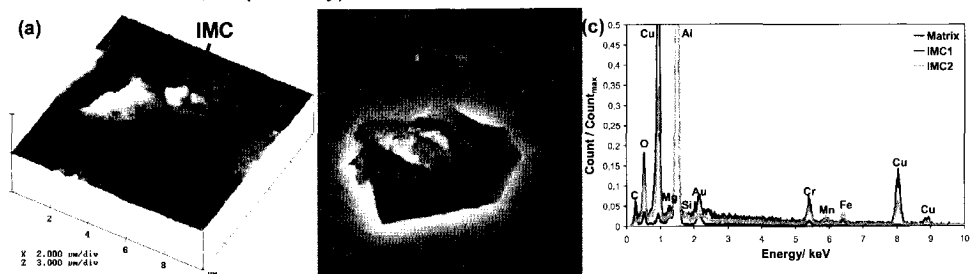


**Figure 7.21:** 3D topographic image (a), SEM micrograph (b) and EDS spectra (c) of sample 2NP after 3 minutes of immersion in the chromate solution (sample 2NPCr). Polished sample.

This is especially evident in the case of the sample undergoing the more pronounced copper redeposition during the surface preparation procedure, i.e. sample 2SPCr (Figure 7.22-a). The very limited thickness of the CCC above the Al matrix of the pickled surfaces is confirmed by the SEM study. Indeed, the presence of a chromate film is not evident from the SEM micrographs, since the typical cracks of the CCC are not visible (Figures 7.21-b and 7.22-b for samples 2NPCr and 2SPCr, respectively), and can be resolved only by means of EDS analysis, which detects chromium and oxygen all over the surface (Figures 7.21-c and 7.22-c for samples 2NPCr and 2SPCr, respectively). The absence of cracks is a consequence of the low thickness of the film, which reduces the stresses induced in the layer during the final drying step.

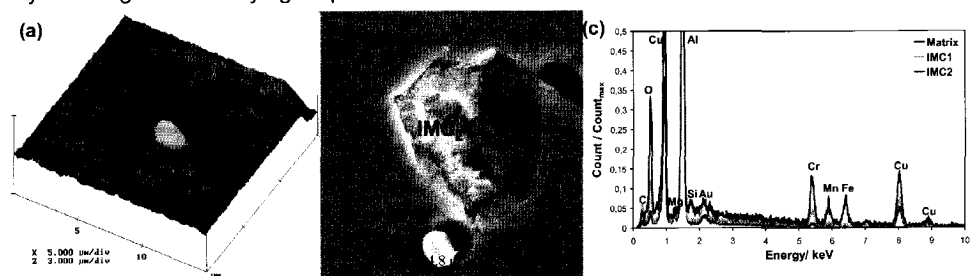


**Figure 7.22:** 3D topographic image (a), SEM micrograph (b) and EDS spectra (c) of sample 2SP after 3 minutes of immersion in the chromate solution (sample 2SPCr). Polished sample.

When comparing sample 2ARCr with samples 2NPCr and 2SPCr, a similarity can be found in the fact that the location of the intermetallics are defects in the chromate coating, whereas the main difference consists of the more pronounced growth of the CCC above the Al matrix shown by the sample chromated without any previous surface preparation

treatment. Since the only microstructural difference between the Al matrix in the as-received conditions and after the pickling treatment is the presence of a copper-rich smut, it can be stated that the Cu deposits inhibit the growth of the chromate film above the Al matrix.

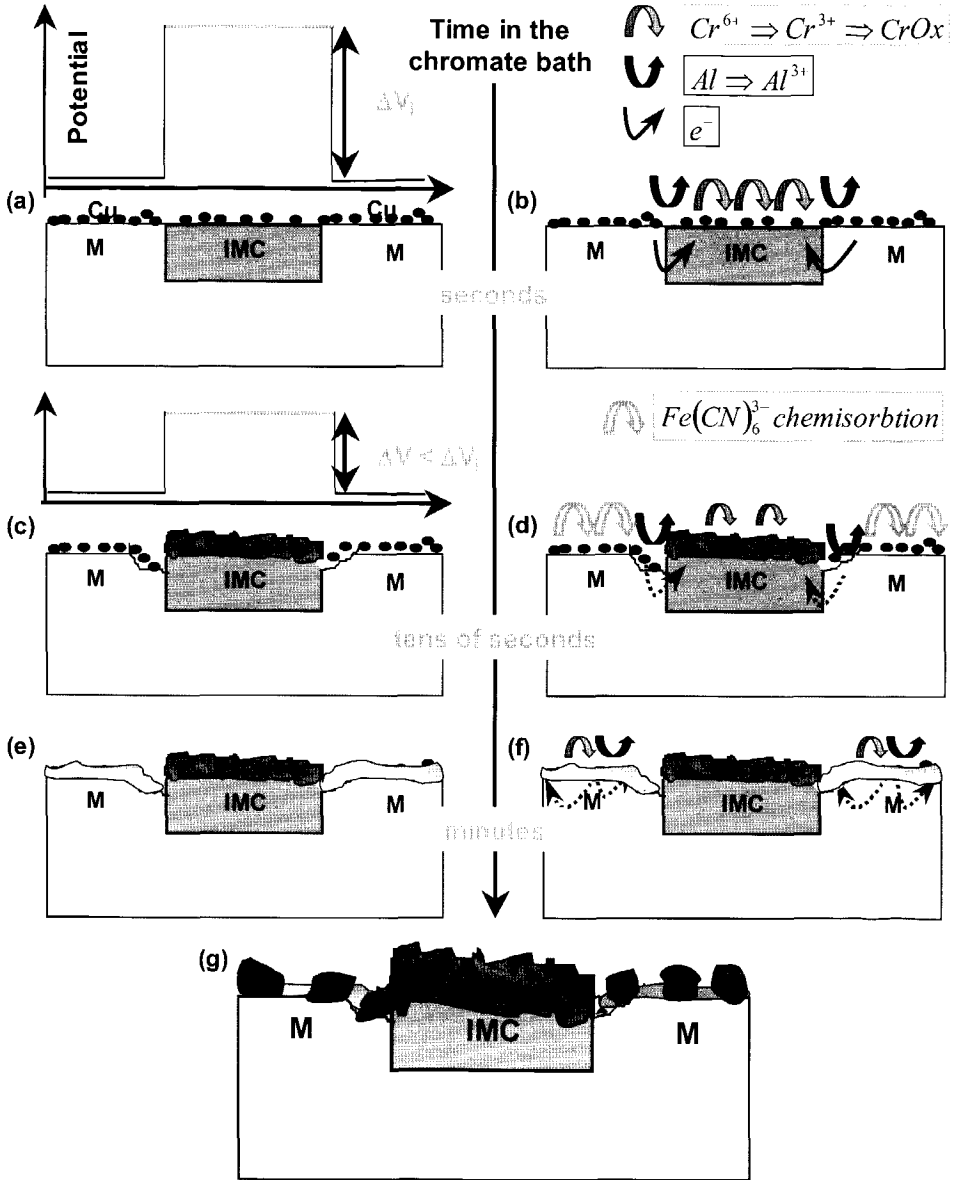


Figure 7.23: Schematic illustration of the influence of the copper-rich smut on the nucleation (a, b), growth (c, d, e, f), and final morphology (g) of the CCC on aluminium alloy surfaces.

A possible explanation to this phenomenon can be found in the interaction between copper and ferrocyanide species, which are present in the Alodine solution and are supposed to act as redox intermediate leading to an acceleration of the reduction of Cr(VI) to

Cr(III) [24] (see section 3.2.1 of chapter 3 for details). Sinha and co-workers [25] have shown that  $\text{Fe}(\text{CN})_6^{3-}$  adsorbs on pure copper and partially decomposes forming chemisorbed cyano species. Therefore, it is probable that  $\text{Fe}(\text{CN})_6^{3-}$  is adsorbed on the copper or copper oxide nodules present on the matrix of AA2024 surface after the acid pickling treatment (Figure 7.23-d) and this inhibits the electron transfer between the surface and the chromate species in solution leading to a slowing down of the chromate film formation [21] (Figure 7.23-e and -f). Therefore, even after a relatively long immersion time, in the order of a few minutes, in the Alodine bath, the chromate film deposited above the Al matrix results to be thin and inhomogeneous (Figure 7.23-g) On the other hand, our results, which show the formation of a CCC above the intermetallics already after 3 seconds of immersion in the chromate bath, and those of Halada *et al.* [22], who found that compounds of K, F and CN ions do not form on intermetallic particles, suggest that the adsorption of cyanide species does not occur at the location of the IMCs, although they are also strongly enriched in copper. This is likely a consequence of the pronounced cathodic nature of the IMCs that leads to an extremely fast reduction of Cr(VI) species and precipitation of chromium hydroxide/oxide at their sites (Figure 7.23-a, -b and -c); this in turn does not leave enough time for the adsorption of  $\text{Fe}(\text{CN})_6^{3-}$  to occur

Therefore, we do not agree with McGovern *et al.* [21], who considered the interaction between copper and ferrocyanide to be responsible for the formation after 5 minutes of immersion in the Alodine bath of a thinner chromate film at the location of the Cu-containing intermetallics of an untreated and polished AA2024 surface. In the case of an untreated surface the rate of adsorption of cyanide species above the IMCs, which contain only a certain percentage of copper, is expected to be much slower than on pure copper and therefore the cathodic nature of the intermetallics plays an even more dominant role with respect to their copper content on the formation of the chromate film. The lower thickness of the CCC formed above the IMCs during a relatively long immersion time, in the order of minutes, is actually occurring on the untreated AA2024 surface as a consequence of a deactivation of the IMCs, which is however caused by the chromate film itself, as explained in the previous section, and not by the chemisorbed cyanide species. However, in [21] it is also shown by means of Raman spectroscopy that on a polyphase  $\text{Al}_x\text{Cu}_y\text{Mg}_z$  ingot after 3 seconds of immersion in the Alodine bath the higher the content of copper was in the phase the thinner the chromate layer deposited. These results seem to contradict our theory relative to the role of the intermetallics on the nucleation of the CCC. The authors explained this behaviour considering that for a higher content of copper in the phase the adsorption of ferricyanide species is higher and therefore the formation of chromium oxide is more inhibited. However, it should be noted that although this can be the case, the polyphase ingot is not really representative for AA2024, since it does not contain the strong galvanic couples between the intermetallics and the aluminium matrix, which are the driving force for the extremely fast formation of a thin and dense chromate film at the location of the IMCs themselves.

- *Acid pickling (unpolished surfaces)*

The SEM and EDS investigation carried out on samples 2NP and 2SP, which were not polished prior to the acid pickling process, after 3 seconds or 3 minutes of immersion in the Alodine bath shows that the polishing step does not affect neither the nucleation nor the growth of the CCC. In the SEM micrographs given in Figure 7.24-a and -c the formation of a layer above the IMCs during the short chromate process (3 seconds) can be observed. This together with the presence of the oxygen and chromium peaks only in the EDS spectra, not shown here, relative to the intermetallics indicates that the nucleation of the chromate film occurs preferentially at their location. After 3 minutes of immersion in the Alodine bath the chromate film deposited on the pickled unpolished surface, i.e. samples 2NPCr and 2SPCr, is characterized by defects in proximity of the intermetallics and by a limited thickness above the Al matrix (SEM micrographs of Figure 7.24-b and -d).

These results confirm the inhibitive effect of the copper-rich smut, which was observed to form during the pickling treatment also on the unpolished surfaces, on the growth of the CCC on 2024 aluminium alloy. In the case of AA2024 treated for long time in the sulfuric/phosphoric acid solution prior to the chromate process, i.e. the sample characterized by the more pronounced deposition of Cu particles, the SEM micrograph (Figure 7.24-d) and the EDS analyses, not given here, show that even after 3 minutes of immersion in the chromate bath the film formed on the matrix is not only thinner and more porous than that deposited on the intermetallics, but it is also completely absent in some areas of the surface. Although this is likely a consequence of the hindering of the chromate film formation caused by the copper-rich smut, it may also simply result from a complete absence of adhesion between the aluminium alloy substrate and the eventually formed chromate film. This lack of adhesion is likely due to the presence of the copper or copper oxide particles at the interface between the film and the substrate, which would lead to the detachment of the chromate layer either during the rinsing step that always follows the immersion in the Alodine bath or during the handling of the sample.

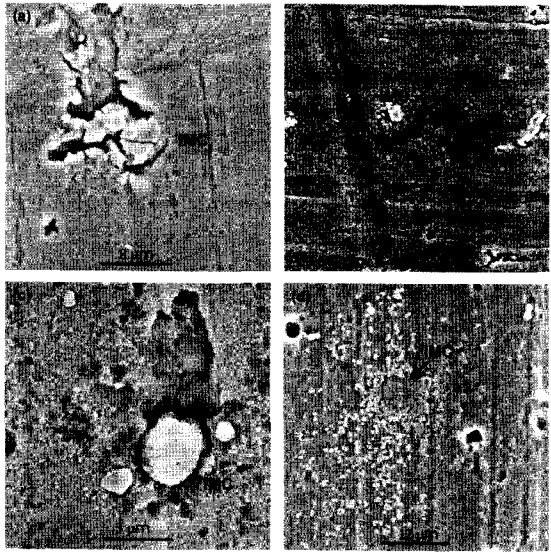


**Figure 7.24:** SEM micrographs after 3 seconds of immersion in the chromate solution of samples 2NP (a) and 2SP (c), and after 3 minutes of immersion in the chromate solution of samples 2NP (b) and 2SP (d). Unpolished samples.

- *Desmutting (unpolished surfaces)*

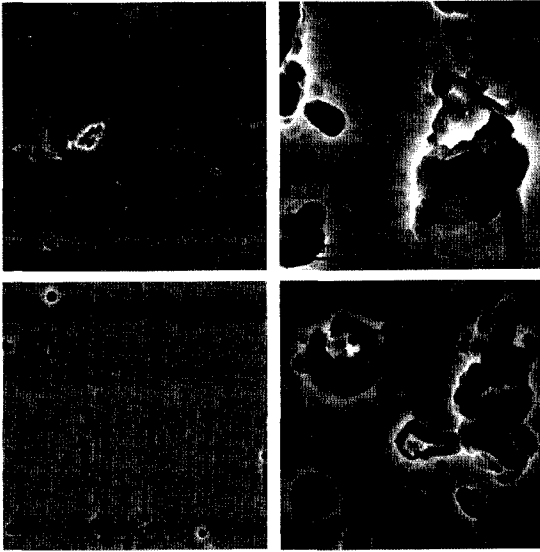


**Figure 7.25:** SEM micrographs of samples 2NPD (a, b) and 2SPD (c, d) after 3 seconds of immersion in the chromate solution. Unpolished samples.

The very important role played by the intermetallic particles and by the copper-rich smut on the nucleation and on the growth of the CCC, respectively, is confirmed by the SEM and EDS investigation carried out on the unpolished AA2024 surface, which was first immersed for 5 or 20 minutes in the pickling bath and then 30 seconds in the desmutting one, samples 2NPD and 2SPD, after both a very short chromate process (3 seconds) and a standard chromate treatment (3 minutes). In section 7.3.1 it was shown that unlike for Alclad 2024 alloy the desmutting process does not lead to a complete removal of the intermetallic particles from the surface of AA2024, however it does

completely eliminate the Cu-rich smut resulting from the pickling step.

The SEM micrographs of Figure 7.25-b and -d show that the 3 seconds of immersion in the Alodine solution lead to the formation of a deposit, which is identified by the EDS analyses, not given here, to consist of chromium oxide/hydroxide, above the few IMCs left on the surface of samples 2NPD and 2SPD. In addition, while the morphology of the Al matrix does not appear modified by the short chromate treatment (Figure 7.25-a and -c), chromium and oxygen are detected in very low amount also in some areas of the matrix. These results confirm on one hand the fact that the intermetallics act as preferential nucleation sites, and on the other hand that the desmutting treatment

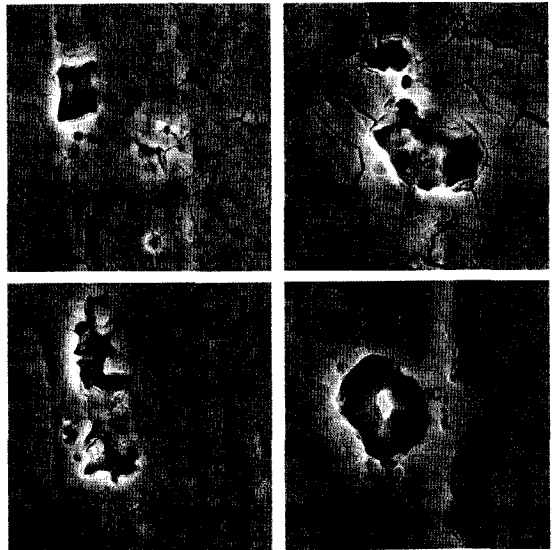


**Figure 7.26:** SEM micrographs of samples 2NPD (a, b) and 2SPD (c, d) after 3 minutes of immersion in the chromate solution (samples 2NPDcr and 2SPDcr). Unpolished samples.



renders the Al matrix more active towards the chromate film formation, as already observed and discussed in section 5.3.2 of chapter 5 in the case of the clad alloy.

The surface of samples 2NPDCr and 2SPDCr, i.e. samples 2NPD and 2SPD, respectively, treated in the Alodine bath for 3 minutes, is characterized by the presence on the Al matrix of a relatively thick film (Figure 7.26), as suggested by the cracks formed as a consequence of the thermal stresses induced during the drying step of the chromate process, which are proportional to the thickness of the film. This is a consequence of the removal of the copper-rich smut from the surface caused by the desmutting treatment, which eliminates the inhibition of the chromate growth and leads to the formation on the matrix of a CCC being similar to that deposited on the as-received surface (sample 2ARCr). In addition, likewise in all the other samples the intermetallic particles, even if covered by the chromate layer, are weak spots in the film itself, since they are sites of large and deep defects (Figure 7.26-b and -d). However, the amount of defects in the chromate layer formed on the desmuted AA2024 surface is lower in comparison with that of the film deposited on either the untreated sample or the pickled ones, since the amount of IMCs on the surface is largely decreased after the desmutting process. Finally, it should be noted that a thick CCC forms also inside the large pits present on the desmuted AA2024 surface (named I in the SEM micrographs of Figure 7.26-a and -c), which are a result of the strong attack of the nitric/hydrofluoric acid bath localized in proximity of the IMCs.

In conclusions, the heterogeneous nucleation of the chromate conversion coating above the intermetallic particles, which was found in the case of Alclad 2024, has been shown to occur also on the 2024 aluminium alloy surface. The role of the IMCs as preferential nucleation sites is even more pronounced in the bare alloy than in the clad one due to the stronger galvanic coupling created with the Al matrix by the Cu-containing intermetallics, which are present in the former, than by the Fe-containing intermetallics, present in the latter. In addition, the presence of metallic copper or copper oxide deposits on the surface of AA2024 strongly hinders the growth of the chromate film giving rise to the formation of a thin and weakly adherent CCC.

#### 7.3.4 Morphology of the CCC: effect of the surface preparation

The results of the SEM investigation, described and discussed in the previous section, show that the morphology of the chromate film deposited on unpolished surfaces during 3 minutes of immersion in the Alodine bath is strongly influenced by the surface preparation treatment carried out prior to the chromate process (Figures 7.24-b, -d and 7.26). This appears clearly also from the comparison of the AFM topographic images given in Figure 7.27. Indeed, the film formed on the Al matrix of the desmuted surfaces, i.e. samples 2NPDCr and 2SPDCr, is thicker and denser with respect to that formed on the matrix of the pickled surfaces, i.e. samples 2NPCr and 2SPCr, especially for long acid pickling time. As already explained in the previous section the growth of the CCC on the Al matrix is inhibited by the presence of the copper-rich smut, which is caused by the acid pickling process and on the other hand is removed by the desmutting treatment. Therefore, the thickness of the

chromate film decreases when the amount of copper deposits increases, i.e. going from samples 2NPDCr and 2SPDCr to sample 2NPCr to sample 2SPCr.

The higher nano-porosity of the CCC formed directly after the acid pickling process is related to the fact that the coalescence of the small spherical nodules of chromium hydroxide/oxide that form the film has not occurred in large extent as instead it is the case for the layer formed after the desmutting treatment. This is suggested by the fact that these spherical particles are still clearly distinguished in the topographic image only in the case of samples 2NPCr and especially 2SPCr and it is reflected in the value of the roughness calculated on an area of the film,  $1 \times 1 \mu\text{m}$  in size, where large and deep defects are not present, i.e. the  $\text{RMS}_1$  parameter given in the second row of Table 7.1 (see section 5.3.3 of chapter 5 for more details). These values are an average of several roughness measurements carried out on various topographic images for each sample.

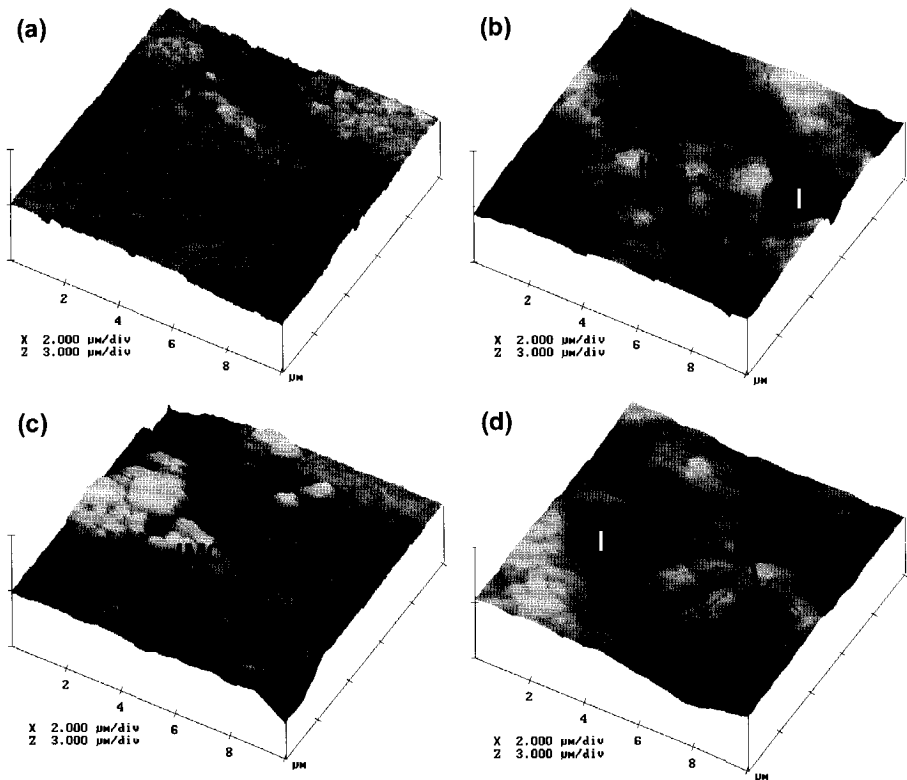


**Figure 7.27:** 3D topographic images of unpolished samples chromated for 3 minutes after different surface treatments: acid pickling for 5 minutes (sample 2NPCr, a) or 20 minutes (sample 2SPCr, c), acid pickling for 5 minutes + desmutting for 30 seconds (sample 2NPDCr, b), acid pickling for 20 minutes + desmutting for 30 seconds (sample 2SPDCr, d).

As concern the intermetallic particles, they are always location of defects in the chromate films, independently on the surface preparation procedure. Nevertheless, since the immersion in the desmutting bath largely decreases the number of IMCs on the AA2024

surface, the chromate film deposited on the desmutted surfaces results to contain a lower amount of defects. This explains the lower value shown by samples 2NPDCr and 2SPDCr for the parameter  $RMS_{10}$  (first row of Table 7.1), which is mainly determined by the large flaws of the CCC rather than by the nano-porosity of the film.

However, the  $RMS_{10}$  ranges of the chromate films deposited on bare 2024 are much higher in comparison with the values found when the clad alloy is used as substrate (first row of Table 5.2 of chapter 5), independently upon the surface preparation route followed. This difference is determined by the different microstructure of the two substrates: more numerous and larger IMCs on bare AA2024 than on Alclad 2024 alloy.

**Table 7.1:** RMS values of the CCC formed after different surface preparation procedure.

	2NPCr	2NPDCr	2SPCr	2SPDCr
$RMS_{10}$ (nm) A = 10 x 10 $\mu\text{m}$	173.5	125.2	168	120.7
$RMS_1$ (nm) A = 1 x 1 $\mu\text{m}$	46.3	18.6	45.2	20.1

Therefore, after the pickling treatment the surface of the bare alloy still contains more numerous and bigger IMCs in comparison with the clad one resulting in a larger amount of defects in the CCC. After the

desmutting treatment the removal of the IMCs leads to more numerous, larger and deeper pits on the surface of AA2024 with respect to Alclad 2024. Although these pits are covered by the chromate film (SEM micrographs of Figure 7.26-a and -c) they contribute to the roughness of the CCC itself since they determine large variations of the height of the chromated surface (areas named I in the AFM topographic images of Figure 7.27-b and -d).

Based on the SEM/EDS and SKPFM investigation it can be concluded that the increase of the length of the pickling treatment has as main consequence the decrease of the thickness and adherence of the CCC formed above the Al matrix, as a consequence of the increase in the amount of copper and/or copper oxide particles deposited on the surface. Although, the increase of the time of immersion in the pickling solution leads also to a decrease of the amount of IMCs, likewise for Alclad 2024 alloy, in the case of the bare 2024 this does not significantly affect the morphology of the chromate film, since its effect is overruled by the negative influence of the copper-rich smut. Similarly to what observed for the clad alloy, the desmutting process results in the formation of a chromate film being more homogeneous, denser and containing a lower amount of defects. However, for the bare 2024 alloy this is a result not only of the removal of a large percentage of IMCs but also of the complete elimination of the copper deposits caused by the pickling process. Nonetheless, since the amount of intermetallics is higher on bare AA2024 than on AA1230 used as clad layer, even when a desmutting treatment is carried out prior to the chromate process some IMCs are left on the surface of the bare alloy and give rise to defects in the chromate layer.

As already observed when Alclad 2024 alloy is used as substrate, the modifications in the chromate film morphology caused by the surface preparation procedure have

consequences in the corrosion protection provided by the CCC itself. This is discussed in the next section based on the results of the electrochemical impedance and noise studies.

### 7.3.5 Corrosion protection provided by the CCC: effect of the surface preparation

- *Electrochemical Impedance Spectroscopy (EIS)*

The impedance response of the chromate conversion coating formed after the long acid pickling process (sample 2SPCr) was found to be quite different with respect to the other chromate films. This appears clearly when the Bode plots, especially those relative to the phase angle, of the different chromate films are compared (Figure 7.28). While, for samples 2NPDCr, 2NPCr, and 2SPDCr the two time constants (indicated by arrows in the Bode plots) occur at two well-separated frequency ranges, for sample 2SPCr they overlap and as a consequence the fitting of the impedance data becomes more difficult. The overlapping of the two relaxations is observed for this sample in all the three set of measurements, which could be carried out only for a short period of time, about 5-10 hours, after which very high values of the current were reached leading to instability and overloading problems.

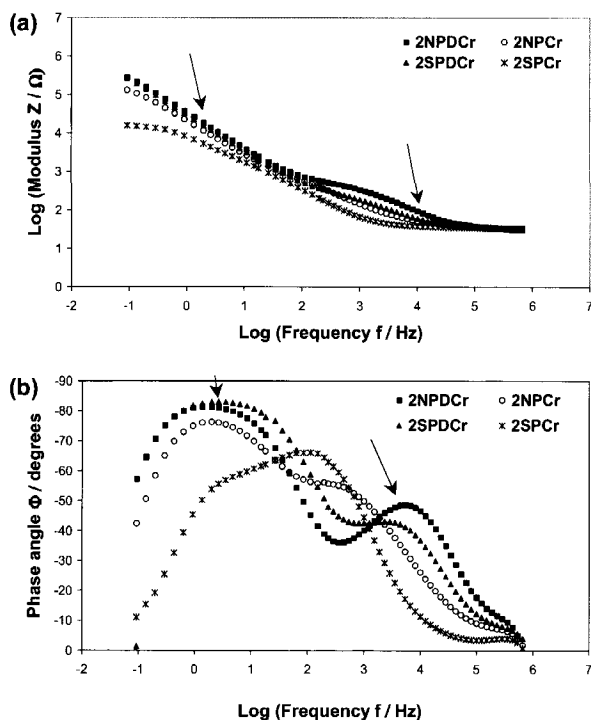


**Figure 7.28:** Bode plots, logarithm of the modulus of the impedance (a) and phase angle (b) vs. the logarithm of the frequency, for all the samples after 4 hours of immersion in 3% NaCl pH=4 solution.

This pronounced extent and strength of the corrosion attack on sample 2SPCr is a consequence of the very low corrosion protection provided by the chromate film deposited on AA2024 after the long pickling process, which can be observed in the Bode plot relative to the impedance modulus (graph of Figure 7.28-a) and which is in accordance with the morphology of the film shown by the SEM and SKPFM investigation discussed in the previous sections. In addition, the spectra obtained for sample 2SPCr could be modelled by none of the equivalent circuits proposed in chapter 6 for the representation of the impedance response of the chromate conversion coating. This is likely a consequence of the completely different

morphology of the chromate layer of this sample (Figure 7.24-d and Figure 7.27-c) in comparison with that observed for the films deposited on the Alclad 2024 alloy, independently upon the surface preparation procedure followed, and on the bare 2024 alloy, after the short pickling or the desmutting process. Indeed, sample 2SPCr shows the presence of a very thin and discontinuous chromate film, which is even completely absent in some areas, instead of a barrier layer and a porous film on top of it containing both large defects and nano-pores. Therefore, the CCC formed on AA2024 after the long pickling treatment cannot be schematically represented as in Figure 6.5 and then its impedance behaviour cannot be modelled by any of the equivalent networks described and discussed in section 6.3.1 of chapter 6.

On the other hand, these equivalent circuits well fit the impedance spectra of samples 2NPDCr, 2SPDCr, and 2NPCr. In particular, while the equivalent circuit of Figure 6.6-c best models the data of sample 2NPCr during the whole exposure, it well describes the impedance behaviour of the CCC formed on the desmuted surfaces, i.e. samples 2NPDCr and 2SPDCr, only during the last part of the immersion in the chloride solution. Indeed, the impedance spectra of samples 2NPDCr and 2SPDCr during the first 15 and 25 hours, respectively, of exposure to the aggressive electrolyte are best fitted using the equivalent circuit (b) of Figure 6.6-b. The duration of the exposure after which the equivalent circuit of Figure 6.6-b does not give anymore a good fit is reproducible within few hours for both samples.

Before to start the discussion regarding the evolution of the various circuit parameters as function of the immersion time, it is important to remark that the trends and the differences amongst the samples were found to be reproducible. The resistance of the porous chromate film (Figure 7.29) decreases during the 60 hours of exposure to the Cl<sup>-</sup>-containing electrolyte, especially when the chromate process is carried out directly

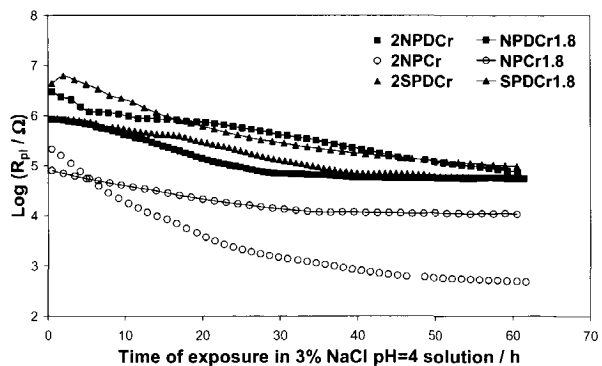


**Figure 7.29:** Resistance of the porous chromate layer  $R_{pi}$  formed on AA2024 and Alclad 2024, as function of the exposure time in 3% NaCl pH=4 solution.

after the pickling treatment (sample 2NPCr). In accordance with the lower nano-porosity of the film (second row of Table 7.1) the  $R_{pi}$  parameter is markedly higher for the chromate layer formed on the desmuted surfaces. This difference between samples 2NPDCr, 2SPDCr and sample 2NPCr can be partially due also to a different thickness of the chromate film, which is suggested by the SEM and SKPFM results even if not unequivocally demonstrated. Figure 7.29 shows that the resistance of the porous chromate layer is affected not only by the surface preparation treatments but also by the substrate used. Indeed, independently on

the surface preparation procedure the chromate film deposited on Alclad 2024 alloy, i.e. samples NPCr1.8, NPDCr1.8, and SPDCr1.8, is characterized by a higher value of  $R_{pi}$  in comparison with that formed on bare 2024 alloy. This difference is more pronounced when the chromate process is performed after the pickling step (samples NPCr1.8 and 2NPCr) and is again a consequence of the different nano-porosity of the CCC formed on the two substrates, as shown by the different values of  $RMS_1$  (second rows of Tables 5.2 and 7.1).

While the variation in density and thickness of the porous chromate film is responsible for the different value of  $R_{pi}$ , the different amount of large defects, often associated with the intermetallic particles, is the cause of the differences in the rate of corrosion process, i.e. charge transfer resistance ( $R_{ct}$ ) and especially in the extent of the corrosion attack, i.e. admittance ( $Y_0$ ) of the non-ideal double layer capacitance ( $Q_{dl}$ ), shown by the samples (Figure 7.30). The decrease of  $R_{ct}$ , associated with the acceleration of the electrochemical reactions, and even more the increase of  $Y_0$  of  $Q_{dl}$ , associated with the extension of the corroded area, is less pronounced for the CCC deposited on the desmutted AA2024 surface that contains a lower quantity of IMCs, i.e. samples 2NPDCr and 2SPDCr.

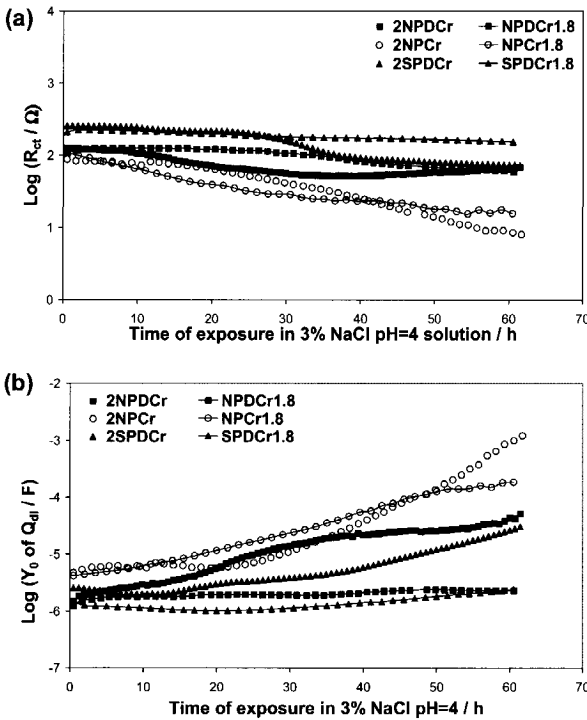


**Figure 7.30:** Charge transfer resistance  $R_{ct}$  (a) and non-ideal double layer capacitance  $Q_{dl}$  (b) of the CCC formed on AA2024 and Alclad 2024, as function of the exposure time in 3% NaCl pH=4 solution.

the corrosion attack shown by the film formed on the bare 2024 alloy may be a consequence

This is in accordance with the mechanism suggested in chapter 6, which states that the corrosion attack of the chromated aluminium surface takes mainly place at the bottom of the large defects and therefore is strongly reduced when the IMCs, which are sites of defects, are removed from the surface. For the same reason, i.e. lower amount of intermetallics associated with large defects in the chromate film, when Alclad 2024 is used as substrate instead of the bare alloy the rate and especially the extent of attack is lower independently on the surface preparation procedure used (Figure 7.30-a and -b).

As concern the CCC deposited directly after the pickling process, i.e. samples NPCr1.8 and 2NPCr, the stronger increase of the area involved in

not only of the larger quantity of intermetallics but likely also of the copper-rich smut present at the interface chromate layer/substrate, which lowers the adhesion of the film itself, as observed during the SEM investigation.

The faster and more extended attack undergone by the chromate layers formed after the desmutting process on bare 2024 (samples 2NPDCr and 2SPDCr) in comparison with those formed on the clad alloy (samples NPDCr1.8 and SPDCr1.8) is in line with the more rapid deterioration of the chromate corrosion products present inside the large defects.

This is indicated by both the faster increase of the admittance of the constant phase element related to the diffusion process ( $Y_0$  of  $Q_{ccp}$ , Figure 7.31) and by the necessity to use the equivalent circuit of Figure 6.6-c, where the diffusion element is not anymore considered, for the fitting of the data after a shorter time of exposure to the chloride solution, i.e. 15-25 hours in the case of the bare alloy and 40-45 hours in the case of the clad alloy.

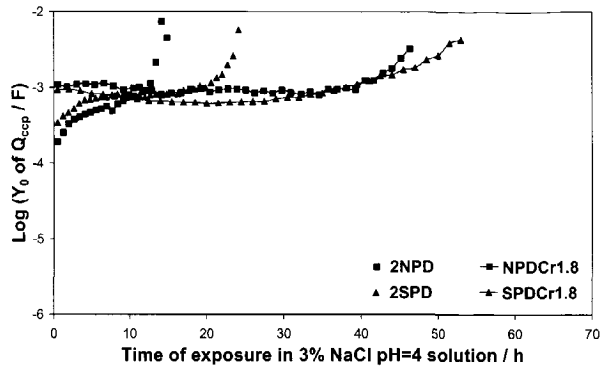


**Figure 7.31:** Diffusion impedance  $Q_{ccp}$  of the CCC formed on AA2024 and Alclad 2024 after the desmutting process, as function of the exposure time in 3% NaCl pH=4 solution.

Indeed, according to the interpretation of the equivalent circuits discussed in section 6.3.1 of chapter 6, both the increase of  $Y_0$  of  $Q_{diff}$  and the change of the equivalent circuit are associated with the formation inside the defects of the CCC of a layer of corrosion products being thicker but at the same time less dense and less protective towards corrosion.

- *Electrochemical Noise (EN)*

The completely different corrosion behaviour of sample 2SPCr and the better corrosion protection provided by the chromate films formed on the desmutted surfaces (samples 2NPDCr and 2SPDCr) are found also in the potential and current time records, not shown here, of the noise measurements. Sample 2NPCr and especially sample 2SPCr are characterized by very large and frequent current transients, which can reach value up to 500-1000 nA. More than one transient often occur simultaneously; this renders impossible to distinguish the shape of the transient itself. In addition, for sample 2SPCr the corrosion attack is found to develop more in one of the two panels and a complete repair never takes place. This is likely a consequence of the extremely high inhomogeneity shown by the chromate film deposited on AA2024 after the long pickling treatment, which leads to a high probability to have a very different level of corrosion resistance in the two panels used for the noise measurements. On the other hand, the current and potential transients observed for samples 2NPDCr and 2SPDCr are less frequent, less wide and have shapes similar to those observed for the CCCs formed on Alclad 2024 and described in section 6.3.2 of chapter 6.

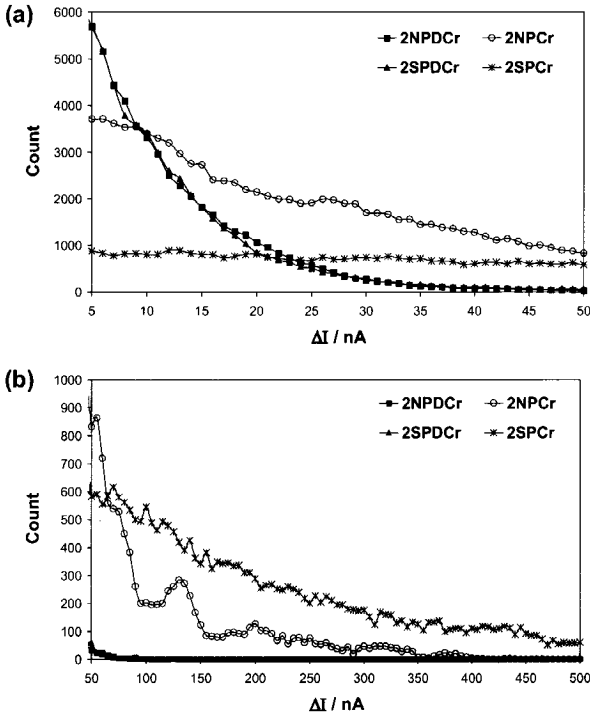


**Figure 7.32:** Number of current deviations from the mean current value ( $\Delta I$ ) as function of the value of the deviation: between 5 and 50 nA (a) and between 50 and 500 nA (b).

amount of small deviations and a higher amount of large deviations in comparison with the other samples. This means that the transients in the time records of the current for sample 2SPCr are more numerous, extremely wide and have a very pronounced amplitude. This in turn suggests that the strength and extent of the corrosive attack are higher on this sample.

The results of one set of noise measurements are given in Figure 7.32 as the number of current deviations from the mean value ( $\Delta I$ , equation 6.j), which is related to the amplitude, width, and frequency of the current transients, in function of the value of the deviation itself. The conclusions drawn from these plots are based on a certain number of experiments carried out on each sample, which were found to be reproducible at least in the general trend of  $\Delta I$  vs. the deviation value and in the differences amongst the samples. Sample 2SPCr shows a less pronounced dependency of the number of current deviations on the value of the deviation; indeed it is characterized by a lower

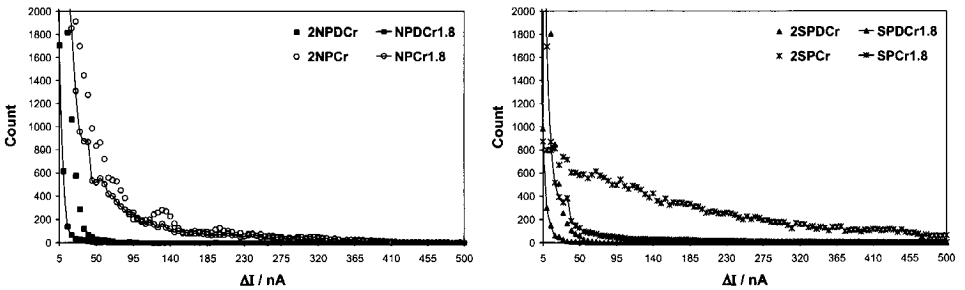


**Figure 7.33:** Number of current deviations from the mean current value ( $\Delta I$ ) as function of the value of the deviation for the CCC formed on AA2024 and Alclad 2024 after different surface preparation procedures.



On the other hand, the trend of the number of deviations vs. the value of  $\Delta I$  is similar for the chromate films formed either after a short pickling treatment or after the desmutting process. However, sample 2NPCr shows a higher amount of deviations at each value of the deviation together with a higher maximum value of the deviation with respect to samples 2NPDCr and 2SPDCr. This confirms that the corrosion protection provided by the CCC deposited on desmuted surfaces is better than that provided by the chromate film formed after the pickling process.

Figure 7.33 compares the noise results obtained for the chromated samples using Alclad 2024 (samples NPDCr1.8, NPCr1.8, SPDCr1.8, and SPCr1.8) and bare 2024 alloy (samples 2NPDCr, 2NPCr, 2SPDCr, and 2SPCr) as substrate. It can be observed that independently upon the surface preparation procedure the chromate films formed on the clad alloy are characterized both by a more limited amount of current deviations at each value and by a lower value of the maximum  $\Delta I$ . Therefore, similarly to the impedance measurements, the electrochemical noise study shows that when a clad alloy is used as substrate the CCC is more protective towards corrosion.

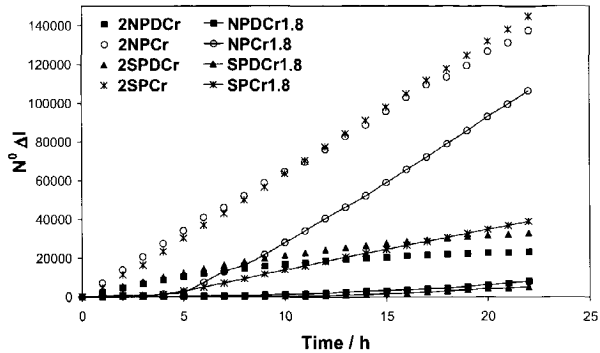


**Figure 7.34:** Total number of current deviations from the mean value ( $\Delta I$ ) as function of the immersion time in 3.5% NaCl pH=4 solution for the CCC formed on AA2024 and Alclad 2024 after different surface preparation procedures.

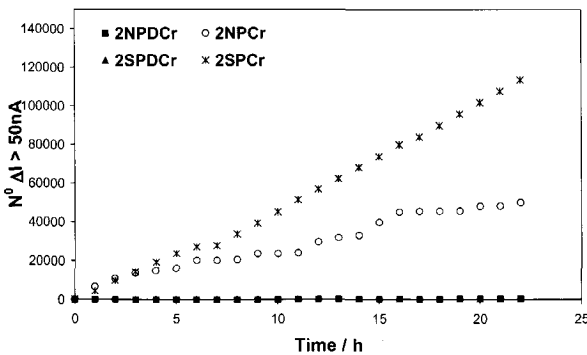


**Figure 7.35:** Total number of current deviations from the mean value ( $\Delta I$ ) higher than 50 nA as function of the immersion time in 3.5% NaCl pH=4 solution for the CCC formed on AA2024 after different surface preparation procedures.

The plot of the total number of current deviations as function of the immersion time in the chloride solution (Figure 7.34) shows that the better corrosion protection of the chromate films deposited on the desmuted AA2024 surface (samples 2NPDCr and 2SPDCr) in comparison with those formed on the pickled surfaces (sample 2NPCr and 2SPCr) is kept during the whole exposure to the aggressive electrolyte and becomes more pronounced

with the increase of the immersion time. Similarly, the higher corrosion resistance of the CCCs formed on the clad alloy with respect to those formed on bare AA2024 is not affected by the duration of the exposure to the chloride- containing solution.

In addition, the higher strength and extent of the corrosion attack occurring on sample 2SPCr than on sample 2NPCr can be observed when only deviations higher than 50 nA are considered (Figure 7.35). The plot of Figure 7.35 suggests that the negative effect of the prolongation of the pickling treatment on the corrosion protection provided by the chromate film becomes more pronounced with the increase of the exposure time to the chloride solution.

In conclusion, the impedance and noise results show that the corrosion protection provided by the CCC formed on AA2024, as already observed in the case of Alclad 2024, is improved when a desmutting treatment is carried out after the pickling and prior to the chromate process. This is due to the partial removal of the intermetallic particles, likewise for the clad alloy, and to the complete elimination from the aluminium surface of the metallic copper and/or copper oxide particles deposited during the pickling process. These effects of the desmutting treatment on the microstructure of AA2024 lead to the deposition of a thicker and more adherent chromate film containing a lower amount of flaws and defects. On the other hand, the increase of the duration of the pickling process strongly lowers the corrosion protection provided by the CCC deposited on bare 2024 alloy, in contrast with the effect that this surface preparation parameter has when a clad alloy is used as substrate. This is due to the fact that on the surface of the bare alloy the increase of the immersion time in the pickling bath results not only in the decrease of the density of the IMCs, which in turn improves the corrosion behaviour of the chromate layer, but also in a pronounced increase of the amount of copper-rich smut, which in turn results in the formation of a thinner, less homogeneous and less adherent CCC that provides a lower corrosion protection. The impedance and noise studies show that on the corrosion resistance of the chromate layer the positive effect of the prolongation of the pickling process associated with the partial removal of the intermetallics is overruled by the negative effect associated with the increase in the amount of copper and/or copper oxide particles left on the surface.

The decrease in the protection provided by the CCC caused by both the IMCs and the copper smut on the substrate surface is also responsible for the different behaviour shown by the chromate films formed on bare 2024 alloy with respect to those formed on Alclad 2024. Indeed, AA1230 used as clad layer is characterized by a lower density and size of the intermetallics together with a much lower content of copper in solid solution in comparison with AA2024. Therefore, on the surface of the clad alloy independently on the surface preparation procedure less IMCs are left and the copper deposits are not formed. As a consequence, the CCCs formed on Alclad 2024 alloy provide a better corrosion protection in comparison with those formed on bare AA2024.

## 7.4 Conclusions

A mechanism of the nucleation and growth of the CCC on 2024-T3 aluminium alloy has been proposed based on the SEM/EDS and SKPFM investigation of polished aluminium surfaces immersed for different times in the Alodine bath. The chromate film starts to form above the intermetallic particles, which act as cathodic sites and favour the reduction of Cr(VI) to Cr(III). The deposition of a thin and dense chromate film renders the intermetallics less active and as a consequence the chromate film starts to deposit on the rest of the surface eliminating the difference in potential between the matrix and the intermetallics, i.e. the driving force for the deposition of the chromate film to preferentially occur at the location of the IMCs. Therefore, the growth of the CCC continues above the matrix, where the film is more porous. As a consequence after a relatively long time of immersion, in the order of a few minutes, in the Alodine bath a thicker layer is formed above the Al matrix than above the intermetallics

In addition, it has been found that the copper-rich smut, which can eventually form during the surface preparation procedure, plays a role as important as the intermetallics in the growth of the chromate film. Indeed, the presence of copper or copper oxide particles on the surface causes a lack of adhesion of the chromate film to the aluminium substrate and inhibits the reduction of Cr(VI) to Cr(III) and the consequent deposition of the chromate film. Obviously, these effects of the IMCs and the copper smut on the formation of the CCC have important consequences on both the morphology and the corrosion resistance of the film. On one hand, at the periphery of the intermetallics large defects are present in the chromate layer due to the lack of continuity in the film at these sites deriving from the different rate and time of formation of the chromate layer above the Al matrix and above the IMCs. On the other hand, the presence of copper and/or copper oxide particles reduces both the thickness and the adherence of the chromate film. In accordance with the conclusions drawn in chapter 6 that the corrosion resistance of a chromate film depends on its barrier properties, its adhesion to the aluminium substrate, and the type of corrosion products formed inside its defects, the impedance and noise studies have shown that both the copper-rich smut and the IMCs negatively affect the corrosion protection provided by the chromate conversion coating.

These observations explain the better corrosion resistance, independently upon the surface preparation procedure, of the CCC formed on Alclad 2024 in comparison with that deposited on bare 2024 aluminium alloy, which contains a higher amount of intermetallics and especially a much higher concentration of copper in solid solution. In addition, they also explain on one hand the improvement in the corrosion protection provided by the chromate film caused by the desmutting process, which reduces the number of IMCs and completely removes the copper smut, and on the other hand the decrease caused by the prolongation of the acid pickling treatment, which strongly increases the amount of copper and/or copper oxide left on the AA2024 surface. This in turn highlights once more the extremely important role played by the surface preparation procedure on the final properties of the chromate conversion coating deposited on aluminium alloys.

## 7.5 References

- [1]. L.F. Mondolfo, *Aluminium Alloys: Structure and Properties*, Butterworths, London, UK (1976)
- [2]. M.S. Hunter, A.M. Montgomery, G.W. Wilcox, *Aluminium: Physical Properties and Metallurgy*, 6<sup>th</sup> edition, J.E. Hatch (ed.), Metals Park, OH (1984)
- [3]. P. Schmutz, G.S. Frankel, *J. Electrochem. Soc.* 145 (1998) 2285
- [4]. P. Schmutz, G.S. Frankel, *J. Electrochem. Soc.* 145 (1998) 2295
- [5]. R.G. Buchheit, R.K. Boger, *Proceedings of NACE Meeting: Corrosion/2001 Research Topical Symposium: Localized Corrosion*, Houston, TX (2001) 265
- [6]. S. Wernick, R. Pinner, *The Surface Treatment and Finishing of Aluminium and its Alloys*, 5<sup>th</sup> edition, Finishing Publication, Teddington, UK (1986)
- [7]. C.A. Drewien, R.G. Buchheit, *Proceedings of NACE Meeting: Corrosion/94*, Houston, TX (1994) Paper 622
- [8]. T. Suter, R.C. Alkire, *J. Electrochem. Soc.* 148 (2001) B36
- [9]. R.G. Buchheit, R.P. Grant, P.F. Hlava, B. McKenzie, G.L. Zender, *J. Electrochem. Soc.* 144 (1997) 2621
- [10]. V. Guillaumin, G. Mankowski, *Corros. Sci.* 41 (1999) 421
- [11]. G.S. Chen, M. Gao, R.P. Wei, *Corrosion* (1996) 8
- [12]. T. J. Warner, M.P. Schmidt, F. Sommer, D. Bellot, *Z. Metallkd.* 86 (1995) 494
- [13]. A. Kolics, A.S. Besing, T. Suter, H. Böhni, C.H. Paik, R.C. Alkire, A. Wieckowski, *Proceedings of the Electrochemical Society Meeting: Corrosion and Corrosion Prevention of Low Density Metals and Alloys*, Phoenix, Arizona, US (2000) 11
- [14]. R.G. Buchheit, *Mater. Sci. Forum* 331-337 (2000) 1641
- [15]. R.G. Buchheit, F.D. Wall, G.E. Stoner, J.P. Moran, *Corrosion* 51 (1995) 417
- [16]. G.O. Ilevbare, J.R. Scully, *J. Electrochem. Soc.* 148 (2001) B196
- [17]. Kolics, A.S. Besing, A. Wieckowski, *J. Electrochem. Soc.* 148 (2001) B322
- [18]. G.M. Brown, K. Kobayashi, *J. Electrochem. Soc.* 148 (2001) B457
- [19]. J.R. Waldrop, M.W. Kendig, *J. Electrochem. Soc.* 145 (1998) L11
- [20]. P.L. Hagans, C.M. Haas, *Surf. Interface Anal.* 21 (1994) 65
- [21]. W.R. McGovern, P. Schmutz, R.G. Buchheit, R.L. McCreery *J. Electrochem. Soc.* A47 (2000) 4494
- [22]. G.P. Halada, C.R. Clayton, M.J. Vasquez, J.R. Kearns, M.W. Kendig, S.L. Jeanjaquet, G.G. Peterson, G.S. McCarthy, G.L. Carr, *Proceedings of the Electrochemical Society Meeting: Passivity and Localized Corrosion: International Symposium in Honor of Professor Norio Sato* Honolulu, Hawaii 27 (1999) 313
- [23]. L. Juffs, A.E. Hughes, S. Furman, P.J.K. Paterson, *Proceedings of the NACE Meeting: Corrosion/2000*, Orlando, US (2000)
- [24]. L.Xia, R.L. McCreery, *J. Electrochem. Soc.*, 146, 3696 (1999)
- [25]. S. Sinha, B.D. Humphrey, A.B. Bocarsly, *Inorg. Chem.*, 23, 203 (1984)

# Microstructure and cerium-based conversion coating-Bare 2024

### 8.1 Introduction

In chapter 7 it has been shown that the nucleation, growth, and as a consequence the morphology of the chromate conversion coating formed on bare 2024 aluminium alloy is strongly affected not only by the presence of cathodic intermetallics, as already observed in the case of Alclad 2024, but also by the eventual formation of a copper-rich smut as a result of the surface preparation procedure. The presence of both IMCs and copper particles on the aluminium surface has been found to have a detrimental effect on the corrosion protection provided by the CCC, due to large defects in the film caused by the former and to inhibition of the film growth together with loss of adhesion caused by the latter.

This chapter investigates the influence of these microstructural features, i.e. intermetallics and Cu-rich smut, on the formation of a cerium-based conversion coating on bare 2024 aluminium alloy. The last part of the PhD project was focused on this alternative system on the basis of both scientific and technological reasons. On one hand, the literature survey has shown that the formation of a cerium oxide film on aluminium alloys involves electrochemical reactions, likewise the chromate process. Therefore, it may be expected that the presence of local cathodes on the surface would play an important role also in the formation and final properties of this alternative system. On the other hand, amongst the chromium-free treatments the conversion process consisting of immersion in a cerium salts bath is one of the most promising and has provoked a large interest in the last two decades.

Recently Wilson and Hinton [1] modified the cerium-based conversion treatment by adding hydrogen peroxide to the cerium chloride bath, which enabled the deposition of a relatively thick cerium oxide film in a few minutes at a relatively low temperature (about 40°C). This strongly increases the industrial applicability of the cerium-based conversion process for the corrosion protection of aluminium alloys. Unfortunately, the  $\text{CeCl}_3\text{-H}_2\text{O}_2$  bath is effective only for the Cu-rich aluminium alloys, i.e. 2xxx and 7xxx series. Although, several investigations have been carried out on the formation of the cerium oxide/hydroxide film with particular attention to the effect of the intermetallic particles, the higher reactivity towards the  $\text{CeCl}_3\text{-H}_2\text{O}_2$  solution of the Cu-containing aluminium alloys is not yet completely understood. Therefore, the aim of this part of the project is to clarify the role of different microstructural features, namely intermetallics and alloying elements, in the nucleation and growth of the cerium-based conversion coating and to explain the different behaviour shown by the

aluminium alloys of different families. A better understanding of the effect of the alloy microstructure on the formation of the conversion film is fundamental for the improvement of this alternative system, since it may be expected to strongly influence also the corrosion protection provided by the film, as it has been shown in the case of the chromate conversion coating. This knowledge may be useful in order to render the cerium-based conversion treatment a valuable replacement of the chromate one and to develop an industrially applicable process able to form a protective cerium oxide film on all families of aluminium alloys.

In the next section the experimental procedure used in this part of the research is briefly described and then section 6.3 focuses on the presentation and discussion of the results. This is divided into three main parts. In the first the influence of an additional surface preparation procedure on the microstructure of AA2024 is considered, whereas the other two parts deal with the effect of the intermetallics and the copper-rich smut, respectively, on the nucleation, growth, and morphology of the cerium-based conversion coating. Finally in the last section of the chapter some conclusions are drawn and some recommendations are given.

## 8.2 Experimental procedure

### 8.2.1 Materials and treatments

Bare 2024 aluminium alloy, coming from the same batch of rolled material used for the investigation of the chromate conversion coating, constituted the substrate. The cerium-based conversion treatment, named hereafter cerate process, consisted of immersion at room temperature in a  $\text{CeCl}_3 \cdot 7\text{H}_2\text{O}$  (13 g/l) and  $\text{H}_2\text{O}_2$  (12.3 ml/l) solution, the pH of which was adjusted to a value of 2 by means of addition of HCl, followed by a final drying step carried out in an oven for 30 minutes at 50°C. It should be noted that the cerate bath is usually heated up to 40–45 °C. In this study a lower temperature has been chosen in order to reduce the deposition rate of the cerium oxide and to enable in this way the investigation of the nucleation and growth of the conversion film. To this aim the duration of the immersion was varied from very short times, i.e. 3 and 30 seconds, to a standard time, i.e. 120 seconds, and in some cases to longer times, i.e. 6 and 15 minutes.

The panels were treated using different surface preparation procedures prior to immersion in the cerate solution (Figure 8.1). Likewise for the study of the CCC, unpolished samples were immersed in the acid pickling bath at 60°C for either 5 minutes (sample 2NP) or 20 minutes (sample 2SP), which was in some cases followed by the desmutting step (samples 2NPD and 2SPD). For details on the pickling and desmutting processes refer to section 5.2.1 of chapter 5. These samples were then immersed in the  $\text{CeCl}_3\text{-H}_2\text{O}_2$  bath for 3, 30, and 120 seconds. When the standard time is used the samples are named 2NPCe, 2SPCe, 2NPDCe, 2SPDCe, whereas when shorter times are used it is opportunely stated in the text. Some samples were mechanically polished up to 1  $\mu\text{m}$  and afterwards either directly or after the pickling process immersed in the cerate bath for both a standard time and shorter times. A code similar to that used in the case of the chromate treatment is

adopted: 2AR for the polished sample and 2NP, 2SP for the samples immersed for 5 and 20 minutes in the pickling bath, respectively. When the immersion in the  $\text{CeCl}_3\text{-H}_2\text{O}_2$  solution lasts 2 minutes the code of the sample is changed by addition of Ce, i.e. sample 2ARCe, 2NPCe, and 2SPCe (Figure 8.1). All these procedures, which were used also in the case of the chromate process, were chosen to enable a comparison between the cerate and the chromate treatments, focusing on the effect that the IMCs and the Cu-rich smut have on the formation of these conversion films.

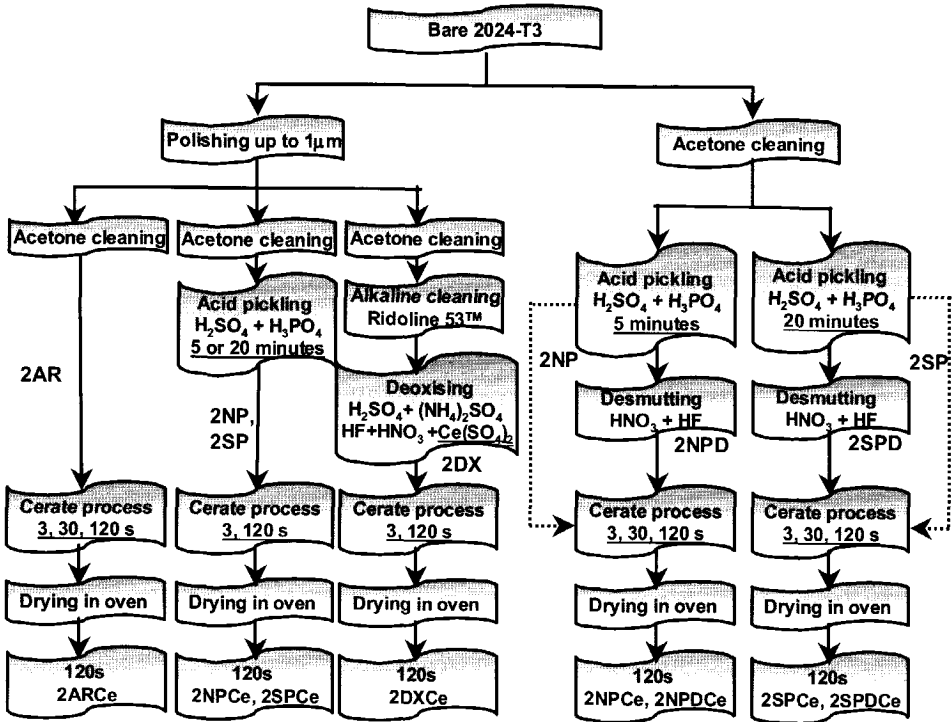


Figure 8.1: Schematic illustration of the different surface preparation and cerate treatment processes investigated in the case of bare 2024 alloy.

An additional surface preparation route for the polished samples was investigated, which consisted of ultrasonic acetone cleaning at room temperature for 10 minutes, immersion in a commercial silicate non-etching alkaline cleaner (Ridoline 53™) for 4 minutes at 65°C, followed by immersion in a Ce-based deoxidiser ( $0.5\text{M H}_2\text{SO}_4 + 1.28\text{M HNO}_3 + 0.05\text{M Ce(SO}_4)_2 + 0.04\text{MHF} + 0.1\text{M (NH}_4)_2\text{SO}_4$ ) for 10 minutes at 35°C. Between each step the panels were rinsed in deionised water for 5 minutes. Samples that underwent this surface activation process are named hereafter 2DX and after the standard cerate treatment 2DXCe (Figure 8.1). Also in this case a shorter treatment time of 3 seconds was considered in order to study the early stages of the cerium oxide film formation. This part of the research was aimed to enable a comparison between our own results and those found in literature, since this sequence of treatments is that originally developed by Wilson and Hinton [1].

Finally, the cerate conversion treatment was carried out also using Alclad 2024 alloy as substrate with the purpose of supporting the mechanism of the formation of the cerium oxide layer on aluminium alloys, which was suggested based on the results of the investigation on bare AA2024. In particular, unpolished panels of the clad alloy were immersed in the  $\text{CeCl}_3\text{-H}_2\text{O}_2$  bath after the short pickling treatment (sample NP) with eventually a subsequent desmutting step (sample NPD). Different durations of the cerate process were chosen: 3, 30 seconds, 2, 6, and 15 minutes.

### 8.2.2 Surface analysis investigation

After each step of both the additional surface preparation procedure and the cerate treatment the samples surface was investigated by means of SEM/EDS and SKPFM techniques. The experimental conditions used are the same of those given in sections 4.3.2 of chapter 4 and 5.2.2 of chapter 5.

## 8.3 Results and discussion

This section deals both with the effect of the additional surface preparation procedure, i.e. alkaline cleaning followed by a deoxidising step, on the microstructure of bare AA2024 and with the influence of the intermetallics and the copper rich-smut on the formation of the cerium-based conversion coating. While the results of the surface analysis investigation, carried out using SEM/EDS in combination with the SKPFM technique, are illustrated using 1 or 2 examples that summarize the typical behaviour shown by each sample, the conclusions are drawn on the basis of a wide series of measurements.

### 8.3.1 Surface morphology and microstructure

- *Non-etching alkaline cleaning (polished surfaces)*

The effects of the alkaline cleaning treatment on the microstructure of AA2024 are not directly related with the formation of the cerium oxide film, which is the main topic of this chapter, since a deoxidising step, which further modifies the properties of the aluminium surface, is always carried out after the alkaline cleaning itself and before the cerate process. However, the investigation of the surface morphology and microstructure after the immersion in the alkaline cleaning bath is discussed in this part of the section as it brings interesting results from the point of view of the SKPFM technique.

An example of the SKPFM measurement carried out on the surface of AA2024 after the immersion for 4 minutes in the commercial alkaline cleaner (Ridoline 53<sup>TM</sup>) at 65°C is given in Figure 8.2. While the topographic image (a) does not show many features, except for a slight protrusion of some areas, in the Volta potential map (b) several large bright, i.e. cathodic, zones can be observed together with smaller (1-2  $\mu\text{m}$ ), more numerous, and less bright areas. When the SKPFM investigation is carried out in the area enclosed in the square given in Figure 8.2-b in combination with a SEM/EDS study, the large brighter areas in the potential map are identified as either Al-Cu-(Mg) intermetallics, i.e.  $\text{IMC}_1/\text{IMC}_1^*$ , or Al-Cu-Mn-Fe-(Si) intermetallics, i.e.  $\text{IMC}_2/\text{IMC}_2^*$ , which are typical for AA2024 (Figure 8.3).



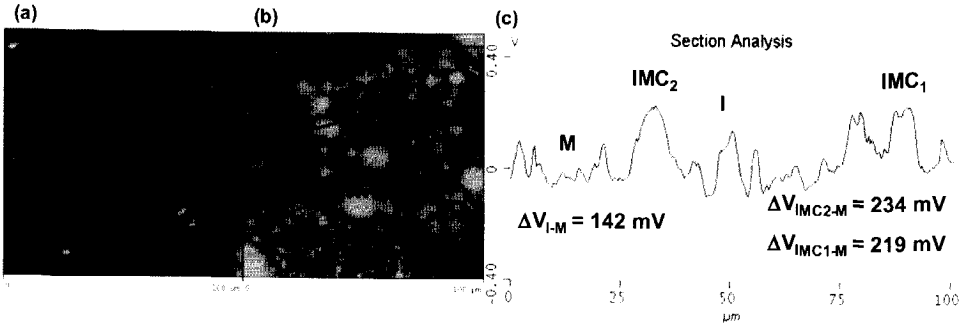


**Figure 8.2:** Topographic image with a height range of 1  $\mu\text{m}$  (a), Volta potential map with a potential range of 0.8 V (b), and section analysis along the black line in the potential map (c) of bare 2024 alloy after mechanical polishing up to 1  $\mu\text{m}$  and 4 minutes of immersion in the alkaline cleaner (Ridoline 53<sup>TM</sup>) at 65°C.

Comparing the potential image (Figure 8.3-b) with the SEM micrograph (Figure 8.3-c) and the EDS elemental maps (Figure 8.3-d to -h) it should be noted that the cathodic regions appear to laterally extend beyond the edges of the IMCs themselves. This lateral extension and the presence of the small cathodic spots, as well, seem to not correspond to any variations in the chemical composition of the surface.

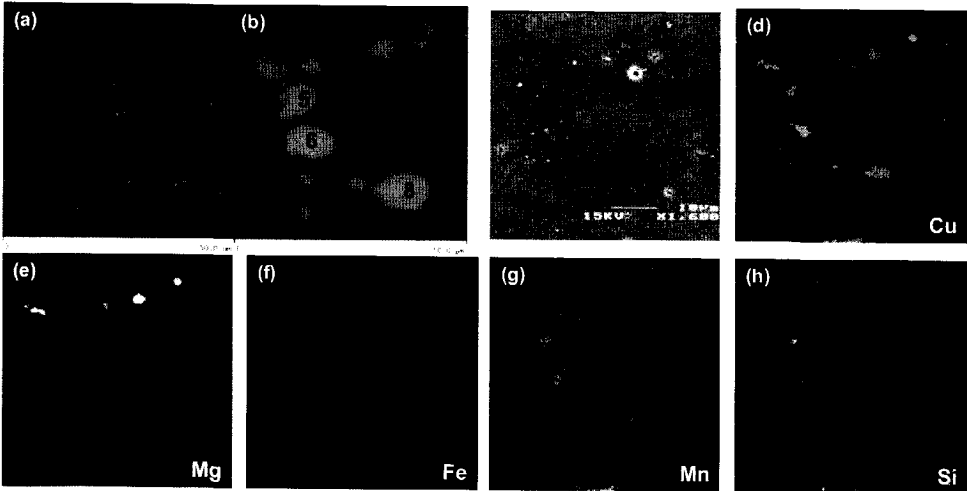


**Figure 8.3:** Topographic image with a height range of 1  $\mu\text{m}$  (a), Volta potential map with a potential range of 0.8 V (b), SEM micrograph (c) and EDS elemental maps (d, e, f, g, h) of the area enclosed in the square given in the potential map of Figure 8.2.

The explanation for this incongruence can be found either in the resolution of the EDS technique or in different variables other than the chemical composition influencing the Volta potential of a metal surface. Indeed, the lateral and depth resolutions of EDS, both in the range of one micrometer, are likely not sufficient to detect variation in chemical composition between the small cathodic areas and the rest of the Al matrix on the most outer layer. Besides, the change in Volta potential could be caused by changes in the structure,

hydratation, etc. of the aluminium oxide film rather than by changes in the chemical composition.

Hughes *et al.* [2] analysed the surface chemistry of 2024-T3 alloy after different times of immersion in the alkaline cleaner Ridoline 53<sup>TM</sup>. These authors on the basis of XPS results claimed that after a few minutes of immersion the surface is covered with an amorphous oxide film, 5-6 nm thick, enriched in magnesium, zinc and silicon. Silicate, which is added to the alkaline cleaner to inhibit the Al etching, is the most likely source of Si, although the alloy itself cannot be excluded as possible source since it contains some Si in solid solution. According to these findings, it may be suggested that the small cathodic spots on the surface, which are not related to intermetallic particles, and the existence of a cathodic region at the periphery of the IMCs are a consequence of inhomogeneities either in the Mg, Zn concentration in the oxide film or in the alumino-silicate part of the passive layer.

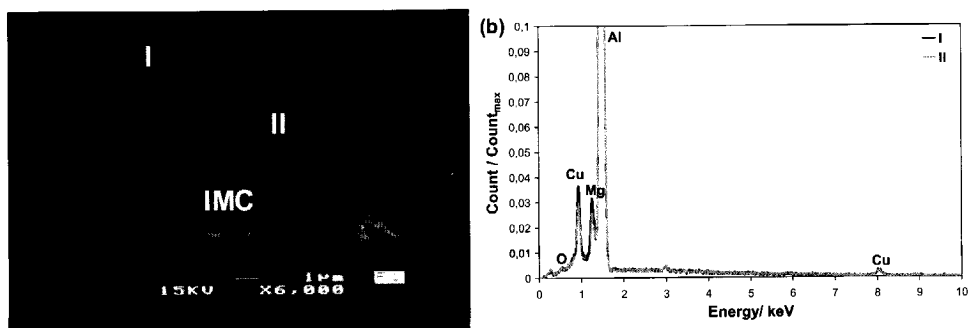


**Figure 8.4:** SEM micrograph (a) and EDS spectra (b) of bare 2024 after mechanical polishing up to 1  $\mu\text{m}$  and 4 minutes of immersion in the alkaline cleaner (Ridoline 53<sup>TM</sup>) at 65°C.

Indeed, the SEM micrograph of Figure 8.4-a shows the presence of small areas (named I), which could be associated with the small cathodic spots of the potential image, being darker in comparison with the rest of the Al matrix (named II). It is interesting to note that also the region at the periphery of the IMC is characterized by a darker colour. The origin of these variations in brightness can be both differences in chemical composition and differences in height, since the micrograph is a secondary electron image. However, the EDS spectra carried out at the location of the dark spots do not show in comparison with those relative to the rest of the Al matrix any appreciable difference in none of the peaks relative to Mg, Zn, O, or Si (Figure 8.4-b). As mentioned before, the EDS technique is not suitable for identifying variations in the chemical composition of the extremely thin aluminium oxide film, due to its poor depth resolution, and within small areas, due to its poor lateral resolution. On the other hand, Auger Electron Spectroscopy could be a valid alternative, since this technique has a much higher lateral and depth resolution, in the order of a few tens of nanometres.

Although the SEM/EDS results do not unequivocally determine the origin of the small cathodic areas, the SKPFM measurements do clearly show their existence in a very reproducible way. The galvanic coupling between these cathodic spots (named I) and the Al matrix (named M) is found by means of section analyses, an example is given in Figure 8.2-

c, to be lower in comparison with that between the intermetallics and the matrix. The former varies from 100 up to 200 mV, whereas the latter ranges between 150 and 350 mV. However, it can not be excluded that this difference is caused only by the smaller size of the cathodic spots with respect to the cathodic regions associated with the IMCs.

It can be concluded that likewise the pickling and the desmutting processes the alkaline cleaning step does not affect either the electrochemical nature of the IMCs, which continue to behave as local cathodes, or the extent of their galvanic coupling with the surrounding matrix. In addition, in agreement with the literature [2], despite the alkaline conditions in the cleaner, the corrosive attack is quite limited and consists of few small and isolated pits and of a minimal etching associated with the intermetallics (Figure 8.4-a). This is likely a consequence of the formation of silicate compounds in the aluminium oxide film that protect the surface from further etching.

- *Ce-based deoxidising (polished surfaces)*

The SEM investigation of the AA2024 surface after 10 minutes of immersion in the Ce-deoxidiser bath shows the occurrence of a strong etching leading to the formation of numerous large pits (Figure 8.5). Most of these pits are the result of a severe localized attack taking place at the periphery of the intermetallics due to the galvanic coupling existing between them and the matrix, which may cause the drop out of the IMC. This is confirmed by the fact that inside several pits a remnant of the original intermetallic can still be observed (Figure 8.5-b).

However, a large percentage of the intermetallic particles is still left on the surface and is characterized by a pronounced dissolution of the surrounding Al matrix (Figure 8.6-a, -b, and -c). In addition, a considerable amount of particles, 0.1-1  $\mu\text{m}$  in size, is present above the matrix, inside the pits and also on top of the IMCs themselves. The EDS analyses show that those particles consist mainly of copper with some traces of oxygen (Figure 8.6-e). This is in agreement with the results of Hughes, Nelson and Miller [3],

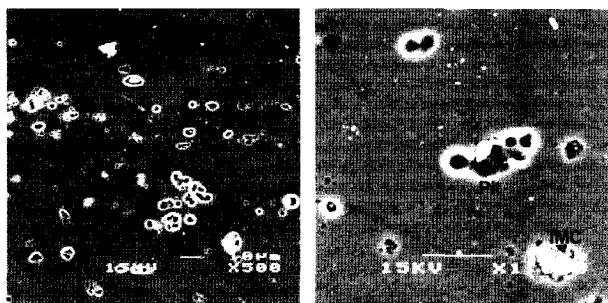


**Figure 8.5:** SEM micrographs of bare 2024 alloy after mechanical polishing up to 1  $\mu\text{m}$ , 4 minutes of immersion in the alkaline cleaner (Ridoline 53<sup>TM</sup>) at 65°C, and 10 minutes of immersion in the Ce-based deoxidiser at 35°C (sample 2DX).

who also observed the formation of small deposits on AA2024 surface as a consequence of the immersion in the Ce-based deoxidiser. On the basis of the value of the  $\text{O } K_{\alpha}/\text{Cu } K_{\alpha}$  intensity ratio obtained with X-ray analysis, which was found to be much lower than the ratio measured on  $\text{Cu}_2\text{O}$  standard, these authors suggested that the particles left on the surface have a metallic core and an oxide shell. Besides, the same research work showed by means of XPS study that the immersion in the Ce-based deoxidiser for few minutes does remove

the oxide film enriched in Mg and Zn left after the alkaline cleaning step, but does not dissolve the silicate compounds.

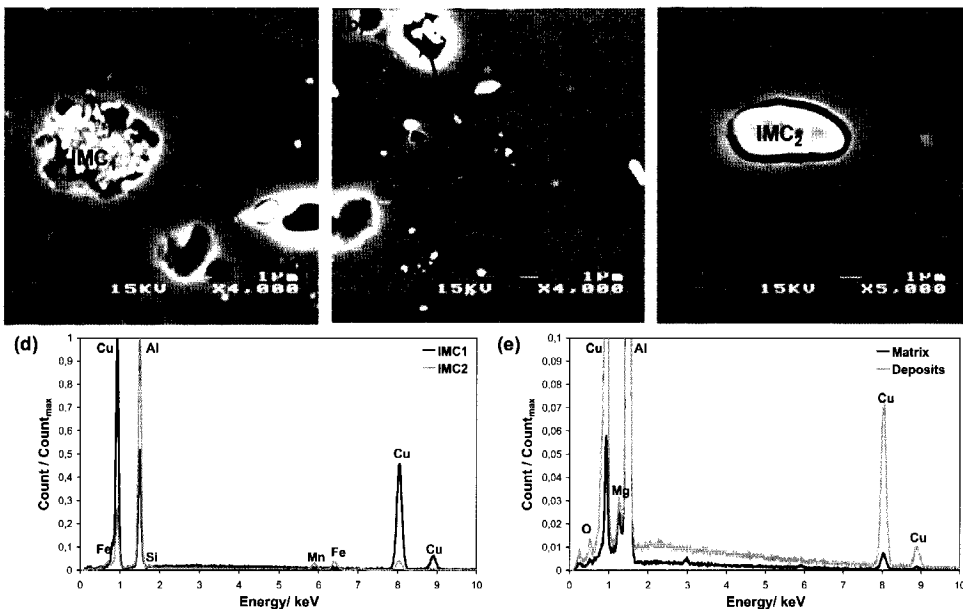


**Figure 8.6:** SEM micrographs (a, b, c) and EDS spectra (d, e) of sample 2DX. Polished sample.

According to our own results and those in the literature, it can be concluded that during the immersion in the Ce-based deoxidiser copper/copper oxide particles deposit on the surface of AA2024, likewise it was observed to occur during the immersion in the acid pickling bath. However, the deoxidising step in comparison with the pickling process leads to a much lower amount of copper particles that are on the other hand bigger in size (Figures 7.4-b and 8.5). This different morphology of the copper deposits caused by the two surface activation treatments is likely due to a different source and mechanism of copper ions realise into solution that afterwards are reduced back and precipitate on the surface in the form of copper/copper oxide particles. In the case of the acid pickling it was observed that the formation of the copper-rich smut is a consequence of the release of copper from the solid solution. On the other hand, in the case of the immersion in the Ce-based deoxidiser it seems that the formation of the copper particles is caused by a selective dissolution of the intermetallics rather than by dissolution of the matrix and consequent redeposition. This is suggested by the higher quantity of copper particles present above the IMCs and inside the pits. Indeed, the spongy structure, which consists of clusters of copper particles, caused by the dissolution of the less noble elements, as Fe, Si, Mn, Al, and Mg, from the intermetallics can either remain at the position of the original intermetallic, i.e. inside the pit, or become electrically isolated from the Al matrix and dissolve into solution as  $\text{Cu}^{2+}$  ions, which in turn can reduce back and deposit at the cathodic sites of the surface, i.e. above the IMCs. The occurrence of selective dissolution of Al, Fe, Mn, and Mg during immersion in the deoxidiser bath is confirmed by the results of the analyses of the bath given in [3].

Figure 8.7 shows the SKPFM measurement carried out on the same area of the SEM micrograph of Figure 8.5-b. Both the pit in the center of the micrograph and the IMC in the bottom right side are clearly recognizable in the topographic image. It can be noted that the strong variation in height at the location of the pit gives rise to some problems during the scan. The cathodic sites, i.e. the brighter areas visible in the potential map, are related not only to the intermetallics but also to the copper deposits, as can be observed in the case of the pit in the central part of the topographic image (Figure 8.7-a) that the SEM investigation has shown to contain some copper particles (Figure 8.5-b).

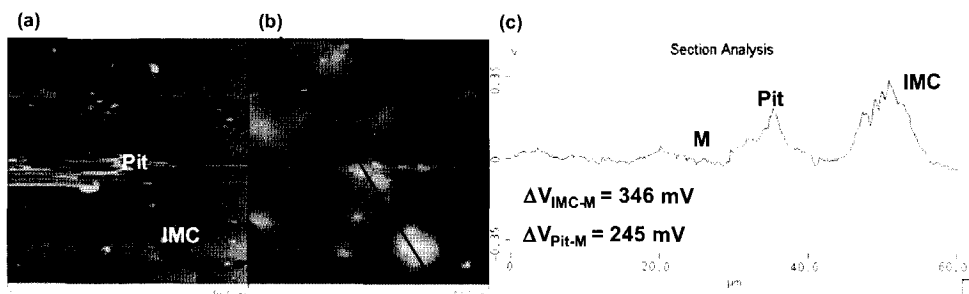


**Figure 8.7:** Topographic image with a height range of  $1 \mu\text{m}$  (a), Volta potential map with a potential range of  $0.8 \text{ V}$  (b), and section analysis along the black line in the potential map (c) of sample 2DX. Polished sample.

The cathodic nature of the copper deposits was already observed in the case of the pickled surface and is expected since copper is a more noble element with respect to aluminium. According to several section analyses across the IMCs and the copper particles (Figure 8.7-c) the galvanic coupling with the Al matrix ranges from  $150$  to  $360 \text{ mV}$  for the intermetallics and from  $100$  to  $270 \text{ mV}$  for the Cu particles. Therefore, similarly to the alkaline cleaning process also the deoxidising step does not affect the extent of the cathodic nature of the intermetallics. On the other hand, it should be noted that the numerous small cathodic areas observed on the alkaline cleaned surface are completely disappeared after the immersion in the Ce-based deoxidiser. This supports the hypothesis that inhomogeneities in the oxide film enriched in Mg and Zn, which is formed during the alkaline cleaning and removed during the deoxidising, are responsible for the appearance of the small cathodic spots on the AA2024 surface after the immersion in the alkaline cleaner.

Finally, the comparison of the SEM study carried out on the bare 2024 alloy after immersion in the nitric-hydrofluoric desmutting solution (Figure 7.9) and in the Ce-based deoxidising bath (Figure 8.5) leads to the conclusion that the etching caused by the former is more severe and as a consequence a higher percentage of intermetallic particles are removed. This is likely related to the different content of hydrofluoric acid in the desmutting and deoxidising bath:  $0.5\text{M}$  and  $0.04\text{M}$ , respectively. The ten times higher concentration of HF seems to overrules the different duration of the two treatments:  $30$  seconds for the desmutting and  $10$  minutes for the Ce-based deoxidiser.

Summing up, the surface preparation procedure consisting of an alkaline cleaning step followed by a deoxidising process in a cerium-containing bath results both in a severe etching of the surface with consequent partial removal of the intermetallics, which occurs however in a more limited extent than in the case of the desmutting treatment discussed in chapter 7, and in the formation of copper deposits, which are however lower in quantity and bigger in size than those formed during the long acid pickling step also discussed in chapter 7.

### 8.3.2 Formation of the cerium-based conversion coating: effect of the intermetallics

This section describes and discusses the results regarding the surface analysis investigation of the bare 2024 alloy directly immersed in the  $\text{CeCl}_3\text{-H}_2\text{O}_2$  solution, i.e. cerate bath, for different times. Since in section 7.3.1 of chapter 7 it has been shown that the surface of AA2024 in the as-received condition while does not present copper deposits, it does contain intermetallics acting as strong local cathodes, this part of the study was aimed to better understand the effect of the cathodic IMCs on the formation of the cerium-based conversion film.

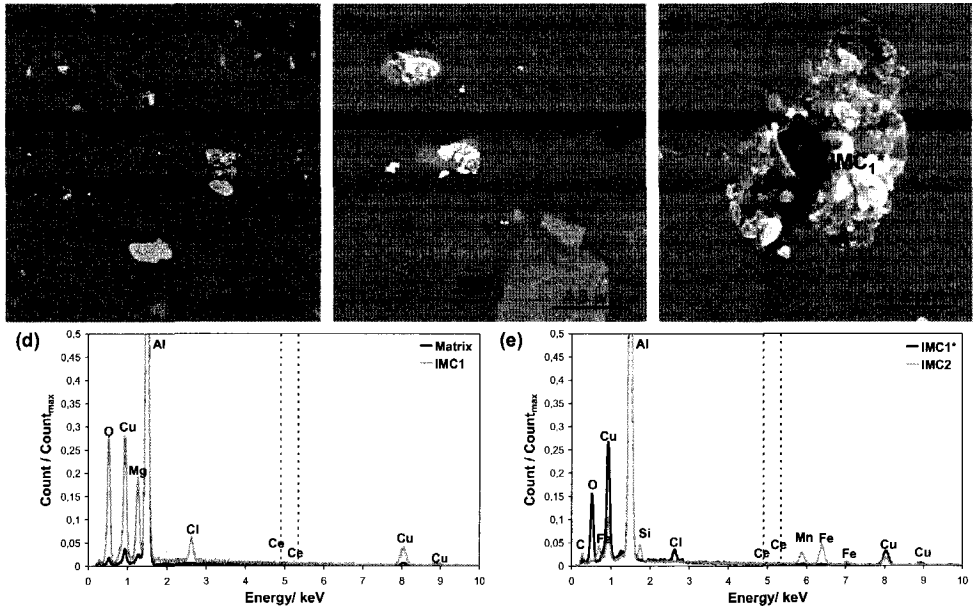


**Figure 8.8:** SEM micrographs (a, b, c) and EDS spectra (d, e) of bare 2024 alloy after mechanical polishing up to  $1\mu\text{m}$  (sample 2AR) and 3 seconds of immersion in the cerate bath.

According to the SEM micrograph of Figure 8.8-a, the immersion for 3 seconds in the cerate bath does not significantly change the morphology of the AA2024 surface. However, when some areas are enlarged (Figure 8.8-b, and -c) the formation of thick deposits is observed above some discrete regions of the surface. The EDS analyses (Figure 8.8-d, and -e) on one hand identify the areas involved in the deposition process as intermetallic particles belonging to the IMC<sub>1</sub>/IMC<sub>1</sub>\* group, i.e. Al-Cu-Mg and Al-Cu intermetallics, on the

other hand show that at these locations the signal relative to oxygen and chloride are very strong and those relative to cerium are completely absent. In addition, none of the several EDS spectra relative to various areas of the surface detect the presence of cerium. Therefore, it can be concluded that the deposits consist of oxide/hydroxide corrosion products enriched in chloride rather than of cerium oxide, which does not precipitate during the short duration of the cerate process or in very low quantity, below the detection limit of the EDS. In the rest of the chapter when mentioning that the cerium oxide is absent it is meant that either it is really completely absent or it is present in such limited amount that cannot be detected by the EDS analyses.

The presence of chloride in these deposits is not surprising since the main component of the cerate solution consists of cerium chloride. The precipitation of oxide/hydroxide compounds on top the Al-Cu-(Mg) intermetallics is likely due to the increase in pH at their location caused by the preferential occurrence of the cathodic reactions, i.e.  $O_2$  and  $H_2O_2$  reduction (equations 3.10-3.12 of chapter 3), which are favoured by the higher potential of these IMCs with respect to the Al matrix.

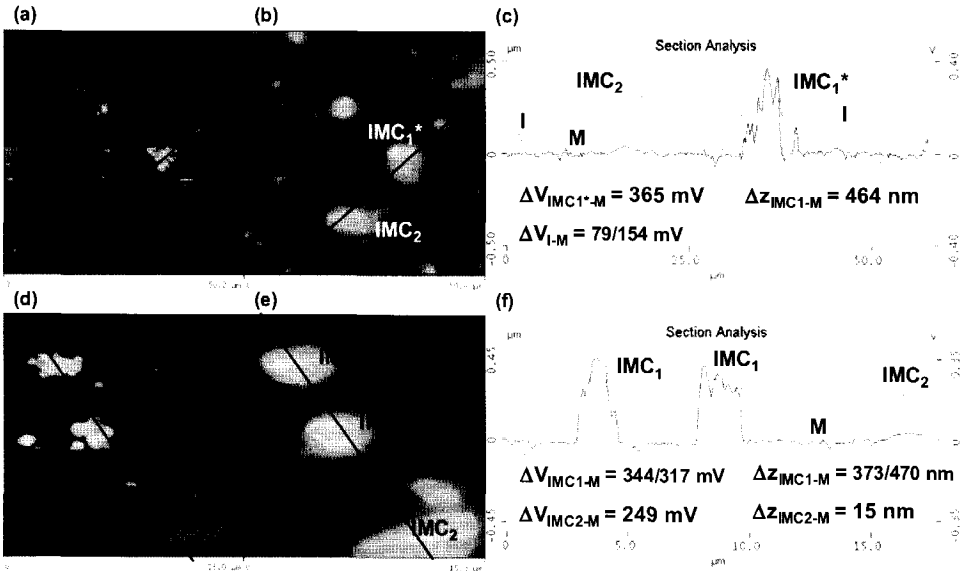


**Figure 8.9:** Topographic images with a height range of 1  $\mu\text{m}$  (a, d), Volta potential maps with a potential range of 0.8 V (b, e), and dual section analyses (c, f) along the black lines in the topographic image (black) and in the potential map (grey) of sample 2AR after 3 seconds of immersion in the cerate bath. Polished sample.

Although, this is likely the case, it is not clear why a similar precipitation phenomenon does not take place also above the Al-Cu-Mn-Fe-(Si) intermetallics, i.e.  $IMC_2$  and  $IMC_2^*$ , which are strong cathodic sites, as well (Figure 7.3 of chapter 7). The morphology of both these IMCs and the Al matrix is not affected by the short contact with the  $CeCl_3-H_2O_2$  solution (Figure 8.8-a, -b, and -c).

The same areas of the SEM micrographs of Figure 8.8-a, and-b have been investigated with the SKPFM technique (top and bottom side of Figure 8.9, respectively). The topographic images (a and d) clearly show the presence of thick deposits in some areas of the surface, which correspond to brighter spots in the potential map (b and e). This appears even more evident when a dual section analysis (c and f), which gives the potential and height profiles along the same line on the surface, is carried out across the intermetallics. The thickness of the oxide/hydroxide deposits is found to be in the order of several hundreds nanometres.

These observations confirm the precipitation of a thick layer of corrosion products at the sites of the cathodic Al-Cu-(Mg) intermetallics, which however seems to no affect the extent of their galvanic coupling with the Al matrix. The lack of influence of the short immersion in the cerate bath on the difference in potential between the matrix and the intermetallics, which still varies in the range of 150-350 mV, is valid also for the Al-Cu-Mn-Fe-(Si) ones. On the other hand, the  $IMC_2/IMC_2^*$  are only slightly visible in the topographic image due to a certain protrusion, which is not a result of the immersion in the  $CeCl_3-H_2O_2$  solution since it is observed also in the sample before any surface treatment (Figure 7.3).

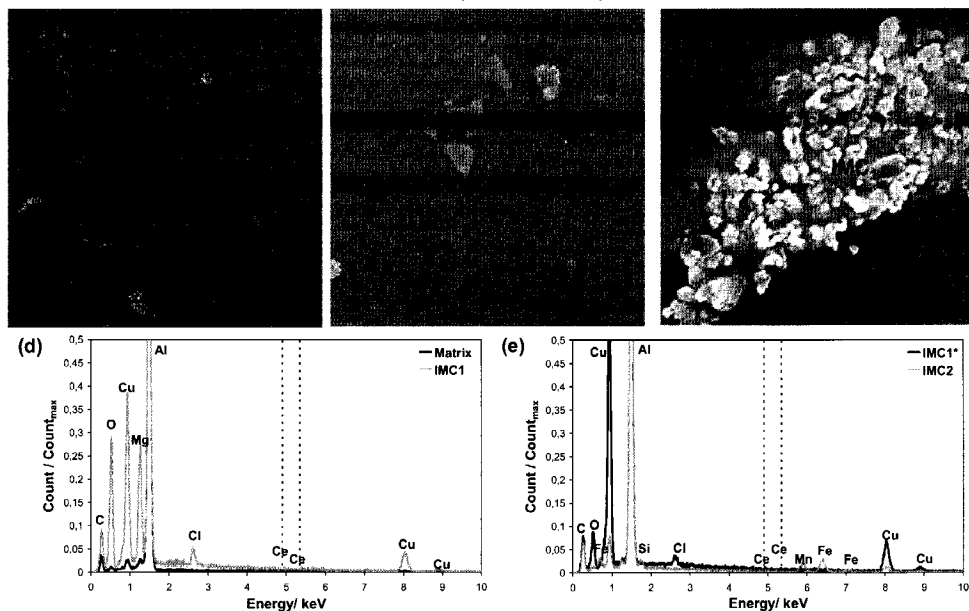


**Figure 8.10:** SEM micrographs (a, b, c) and EDS spectra (d, e) of sample 2AR after 30 seconds of immersion in the cerate bath. Polished sample.

Finally, while the SEM investigation does not show any appreciable modification of the Al matrix as a consequence of the 3 seconds of contact with the cerate bath, the SKPFM study does show the presence of cathodic spots (named I in the dual section analysis of Figure 8.9-c) that are not related with the IMCs. Although the EDS analyses do not detect any difference in chemical composition at these cathodic regions, it is probable that they are



associated with variations in the composition of the aluminium oxide film, likewise for the small cathodic areas observed after the alkaline cleaning process.

In Figure 8.10 some examples of SEM micrographs (a, b, and c) and EDS spectra (d and e) carried out on the surface of AA2024 after 30 seconds of immersion in the cerate bath are given. Likewise after a shorter time of immersion, the Al matrix and the  $IMC_2/IMC_2^*$  are unaffected by the contact with the cerium chloride solution, whereas on top of the Al-Cu-(Mg) intermetallics oxide/hydroxide deposits enriched in chloride are formed. In addition, cerium was not detected in any of the several spots of the surfaces analysed by EDS. This suggests that the increase of the treatment time from 3 to 30 seconds does not lead to any further modification of the AA2024 surface.

The same regions of the surface shown in Figure 8.10-a and -b, have been investigated by means of the SKPFM technique (Figure 8.11). Based on the potential maps (b and e) similar considerations can be made as in the case of the sample immersed for only 3 seconds in the cerate bath (Figure 8.9): the intermetallic particles still behave as local cathodes, even those belonging to the  $IMC_1/IMC_1^*$  group and covered by a thick film of corrosion products, some cathodic spots are present on the surface, which are not related to intermetallics. This confirms the conclusion drawn above that the prolongation of the immersion in the  $CeCl_3-H_2O_2$  bath does not give rise to further variations of the surface.

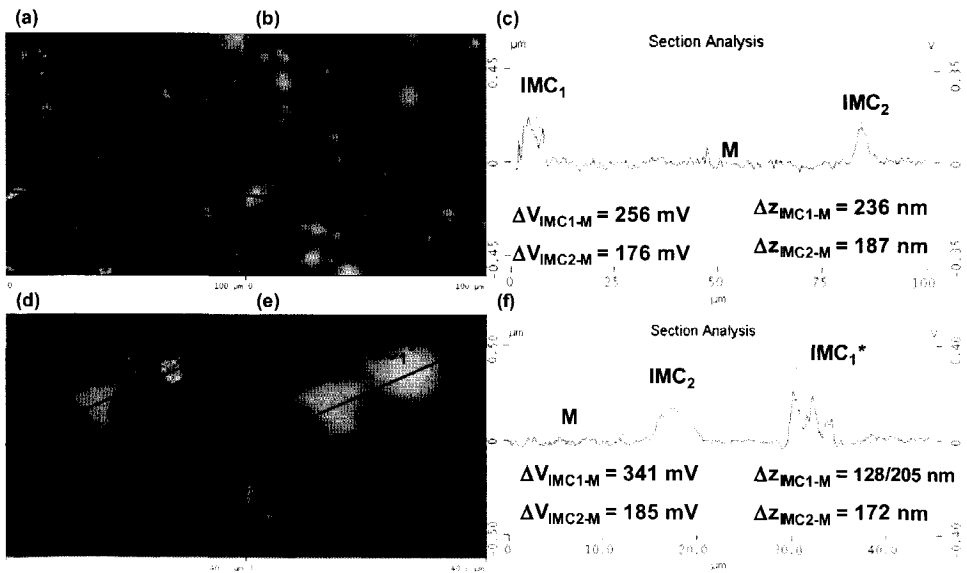


**Figure 8.11:** Topographic images with a height range of 1 μm (a, d), Volta potential maps with a potential range of 0.8 V (b, e), and dual section analyses (c, f) along the black lines in the topographic image (black) and in the potential map (grey) of sample 2AR after 30 seconds of immersion in the cerate bath. Polished sample.

However, the dual section analyses (Figure 8.11-c and f) on one hand prove that the extent of the galvanic coupling existing between the Al matrix and the IMCs is not modified by the increase of the duration of the cerate process, on the other hand highlight a higher

change in height at the sites of the  $IMC_2/IMC_2^*$ , in the order of 100-200 nm. This means that during the immersion in the cerate bath the protrusion of the Al-Cu-Mn-Fe-(Si) intermetallics is enhanced, likely as a result of a more pronounced attack of the Al matrix, which seems anyway to be a general dissolution of the whole surface rather than a localized etching at the periphery of the IMCs.

According to the SEM study of the bare 2024 alloy after a standard, i.e. 2 minutes, duration of the cerate process (Figure 8.12) the Al matrix results to be still almost unchanged

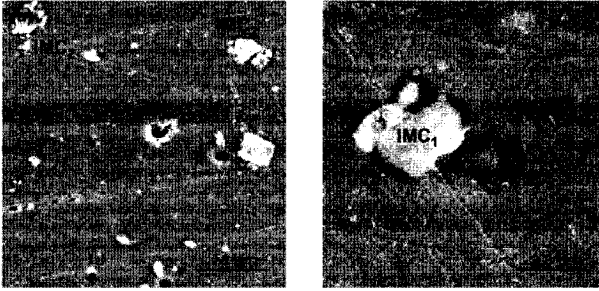


**Figure 8.12:** SEM micrographs of sample 2AR after 2 minutes of immersion in the cerate bath (sample 2ARCe). Polished sample.

except for the appearance of few isolated pits, the protrusion of the Al-Cu-Mn-Fe-(Si) intermetallics is further enhanced, and at the location of the Al-Cu-(Mg) the formation of Cl-rich oxide/hydroxide deposits is still occurring together with a slight local attack of the matrix at their periphery. Therefore, the increase of the exposure time to the cerate bath only

enhances the phenomena observed already after only 3 seconds of immersion. However, while after 3 or even 30 seconds of contact with the cerium chloride solution any trace of cerium oxide on the surface is not detected, after 2 minutes at few spots of the sample the EDS spectra show the presence of the cerium and oxygen peaks (Figure 8.13-c). These areas involved in the cerium oxide/hydroxide precipitation are anyhow very limited in number and are not necessarily associated with IMCs (area named I in the SEM micrograph of Figure 8.13-a, as an example), i.e. the deposition of cerium oxide occurs above a very limited percentage of the intermetallics and not only at their location.

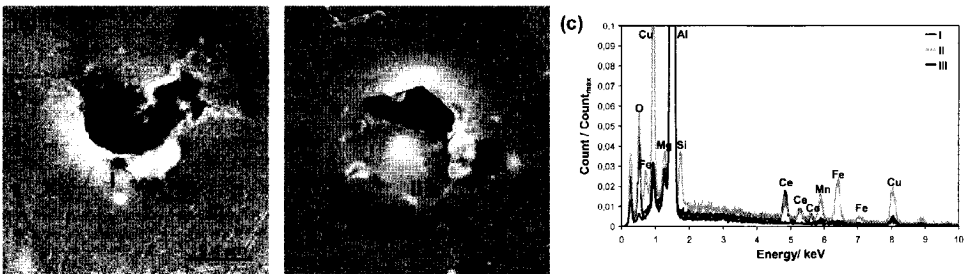


**Figure 8.13:** SEM micrographs (a, b) and EDS spectra (c) of sample 2ARCe. Polished sample.

On the other hand, a common feature is observed at all the sites where the precipitation of the cerate film has taken place: a local attack of the surrounding matrix. This suggests that the electrochemical process leading to the precipitation of the cerium oxide/hydroxide, i.e. cathodic reduction of oxygen and hydrogen peroxide with consequent increase in pH and the anodic dissolution of aluminium, is an extremely localized

phenomenon. The areas involved in the precipitation of cerium oxide shown in the SEM micrographs of Figure 8.13 are enlargements of the locations named I and II in the SEM image of Figure 8.12-a. The topographic and potential scans of this region of the surface are given in Figure 8.14-a and -b, respectively, together with an example of a dual section analysis (Figure 8.14-c). The presence of the pits in the aluminium matrix in proximity of the cerium oxide deposits can be observed in the topographic image and the height profile across one of those (the black line in the dual section analysis of Figure 8.14-c) shows that their depth is quite pronounced, in the order of 500 nm. In addition, the protrusion of the  $\text{IMC}_2/\text{IMC}_2^*$  intermetallics that was observed during the SEM study is also confirmed.

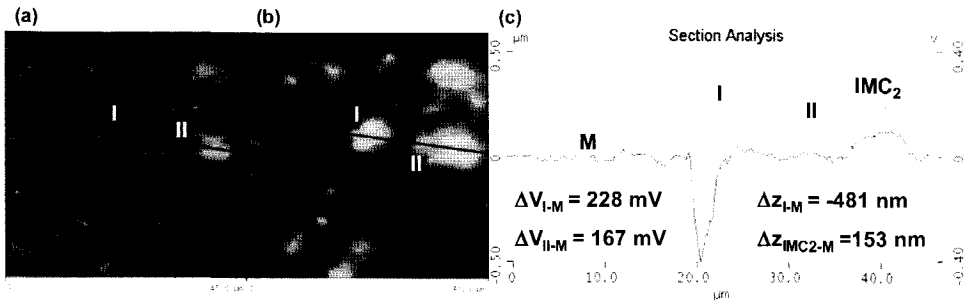


**Figure 8.14:** Topographic image with a height range of 1  $\mu\text{m}$  (a), Volta potential map with a potential range of 0.8 V (b), and dual section analysis (c) along the black lines in the topographic image (black) and in the potential map (grey) of sample 2ARCe. Polished sample.

The comparison of the SEM micrograph (Figure 8.12-a) with the potential map (Figure 8.14-b) leads to the conclusion that not only the IMCs continue to act as cathodic sites but also the areas covered by the cerium oxide (named I and II) has a more noble Volta potential in comparison with the bare Al matrix (named M). This can be easily noted in the dual section analysis made across these regions (the grey line in the diagram of Figure 8.14-c). The few zones of the sample surface, where cerium oxide has precipitated, were characterized by means of the dual section analysis option and their galvanic coupling with the uncoated matrix is found to vary between 100 up to 250 mV. On the other hand, the range of potentials of the IMCs seems to not be influenced by the relatively long immersion in the cerium-based conversion bath.

The absence of the formation of a cerium oxide film on the 2024 aluminium alloy when any surface preparation process is not used could be a consequence of the lack in activation of the surface, which slows down the electrochemical reactions. This would be in agreement with the extremely localized nature of the cerium precipitation and Al dissolution reactions observed after a standard duration of the cerate process, i.e. 2 minutes. Although the formation of the cerium-based conversion coating likely requires the activation of the Al surface, the results discussed above clearly show also that it is not favoured by the presence of the Cu-rich IMCs, which were on the other hand very active towards the chromate formation even in the absence of any surface preparation treatment (section 7.3.2 of chapter 7). Therefore, according to the results of the chromate process the activation of the surface is not a necessary condition for the electrochemical reactions to occur at the location of the

intermetallics. However, in the chromate bath they lead to the formation of a CCC already after 3 seconds of immersion, whereas in the cerate bath they result in the precipitation of Cl-rich products only above the  $IMC_1/IMC_1^*$ . Based on these considerations, it can be concluded that the cathodic nature of the IMCs is not a sufficient condition for the precipitation of the cerium oxide film. On the other hand, our results seem to contradict the results of other authors, who showed the preferential formation of the cerium-based conversion layer on top of the Cu-rich IMCs [4-9]. However, it should be noted that either different cerate treatments, or a surface preparation procedure, or a longer time of immersion in the  $CeCl_3-H_2O_2$  bath were undertaken in these studies, which can affect both the precipitation process and the intermetallics themselves. This is discussed in more details at the end of the next section where a model of the cerium oxide film formation is proposed, which enables to explain not only our own results but also those found in literature.

### 8.3.3 Formation of the cerium-based conversion coating: effect of the Cu-rich smut

This section focuses on the influence of the surface preparation procedure on the nucleation, growth, and final morphology of the cerium-based conversion coating with particular attention to the effect of the presence of copper/copper oxide particles eventually deposited on the surface. The results are described and discussed in six sub-sections. In the first and second part the role of the acid pickling treatment is considered using polished and unpolished AA2024 samples, respectively. Similarly to the study on the CCC the use of polished surfaces was aimed to facilitate the SKPFM measurements, whereas the use of unpolished ones had the purpose of investigating surfaces of practical application. The third and fourth parts of the section deal with the formation of the cerium oxide film on bare 2024 alloy after the deoxidising process and the desmutting step, respectively. Whereas, the fifth subsection reports the results concerning the formation of the film on Alclad 2024 alloy as substrate. The choice of this alloy was made based on the low copper content in the clad layer, which was expected to enable a confirmation of the role played by the Cu-rich smut. Finally, in the sixth part a model of the formation of the Ce-based conversion coating on aluminium alloys is proposed and an attempt to explain according to this model not only our results but also those found in literature is made.

- *Acid pickling (polished surfaces)*

The results of the SEM/EDS investigation of the polished surface of bare 2024 after immersion for 5 minutes in the acid pickling bath ( $H_2SO_4-H_3PO_4$  solution) followed by 3 seconds of contact with the  $CeCl_3-H_2O_2$  solution are illustrate with the examples given in Figure 8.15. Several observations can be made based on the SEM micrographs and EDS spectra. As concern the intermetallics, while those belonging to the  $IMC_2/IMC_2^*$  group are covered by the cerium-based conversion layer, on top of those containing copper and/or magnesium ( $IMC_1/IMC_1^*$ ) either a thick corrosion deposit enriched in chloride ( $IMC_1^*-I$  in the micrographs of Figure 8.15-a and -b) or a cerium oxide film ( $IMC_1^*-II$  in the SEM micrograph of Figure 8.15-a) is formed. In addition, large regions (named II) of the sample surface appears to be covered by a thin film, which is identified by the EDS analyses to consist of cerium oxide/hydroxide (Figure 8.15-e), and in few spots the presence of deposits with a

filiform shape (named III in the micrograph of Figure 8.15-c) are observed and the EDS spectra at their location are characterized by strong oxygen and chloride peaks (Figure 8.15-e). Therefore, the deposition of both the cerium-based conversion layer and the corrosion products enriched in chloride is found to occur not only at the location of the intermetallic particles but also above the Al matrix.

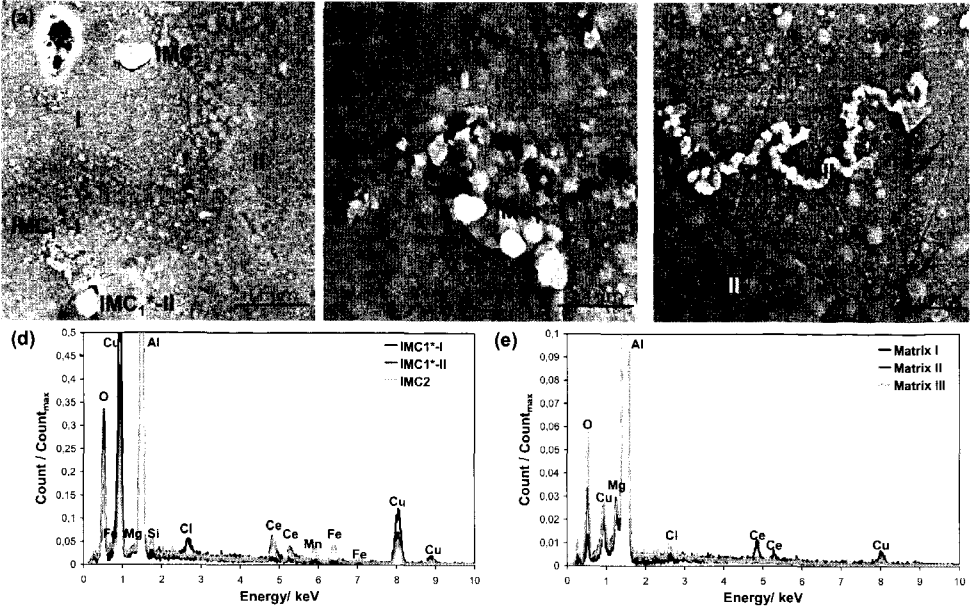


**Figure 8.15:** SEM micrographs (a, b, c) and EDS spectra (d, e) of bare 2024 alloy after mechanical polishing, 5 minutes of immersion in the  $H_3PO_4$ - $H_2SO_4$  solution (sample 2NP), and 3 seconds in the cerate bath.

The SEM study at a high magnification (Figure 8.15-c) suggests that the formation of the thin cerium oxide film takes place through the deposition at evenly distributed sites on the Al surface of isolated and small (less than  $1\ \mu\text{m}$ ) round particles (indicated by arrows), which afterwards coalesce leading to a thin and compact layer. It should be noted that this mechanism of nucleation and growth of the conversion film is in agreement with the

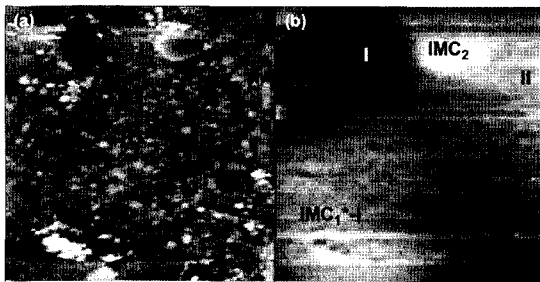


**Figure 8.16:** Topographic image with a height range of  $2\ \mu\text{m}$  (a), Volta potential map with a potential range of  $0.8\ \text{V}$  (b) of sample 2NP after 3 seconds of immersion in the cerate bath. Polished sample.

hypothesis suggested by Li and Thompson [10] that the electrochemical and chemical reactions occurring in the cerate bath result first in a gel precursor followed by the formation of microscopic cerium oxide nuclei on the surface, which in turn act as sites for further deposition.

The precipitation of discrete particles on the surface as initial

stage of the cerium-based conversion coating formation is observed also in the topographic images obtained with the SKPFM technique. In Figure 8.16 the topographic (a) and potential map (b) of the same region shown in Figure 8.15-a are given, as an example. It is interesting to note that although the intermetallics are still visible as brighter spots in the potential scan, the extent of their galvanic coupling with the Al matrix is strongly reduced. On the other hand, a further inhomogeneity in the surface potential is introduced as a consequence of the partial coverage of the matrix with a thin and compact cerium oxide film. Indeed, the areas involved in the precipitation of the film (named II) result to be slightly more noble in comparison with the regions left uncovered (named I).

Figure 8.17 shows some typical SEM micrographs (a, b, and c) and EDS spectra (d and e) of the polished AA2024 surface treated for 20 minutes in the pickling bath prior to immersion for 3 seconds in the cerate solution. It has been found that while the short cerate process affects the intermetallics in a similar way as observed in the case of sample 2NP, the precipitation of cerium oxide on the Al matrix results to be more pronounced. Indeed, the Al-Cu-Mn-Fe-(Si) intermetallics and a portion of the Al-Cu-(Mg) ones ( $IMC_1^*$ -II in the SEM micrograph of Figure 8.17-b) are covered by cerium oxide and the formation of Cl-rich corrosion products occurs at the location of some intermetallic particles belonging to the  $IMC_1/IMC_1^*$  group ( $IMC_1^*$ -I in the SEM micrograph of Figure 8.17-a).

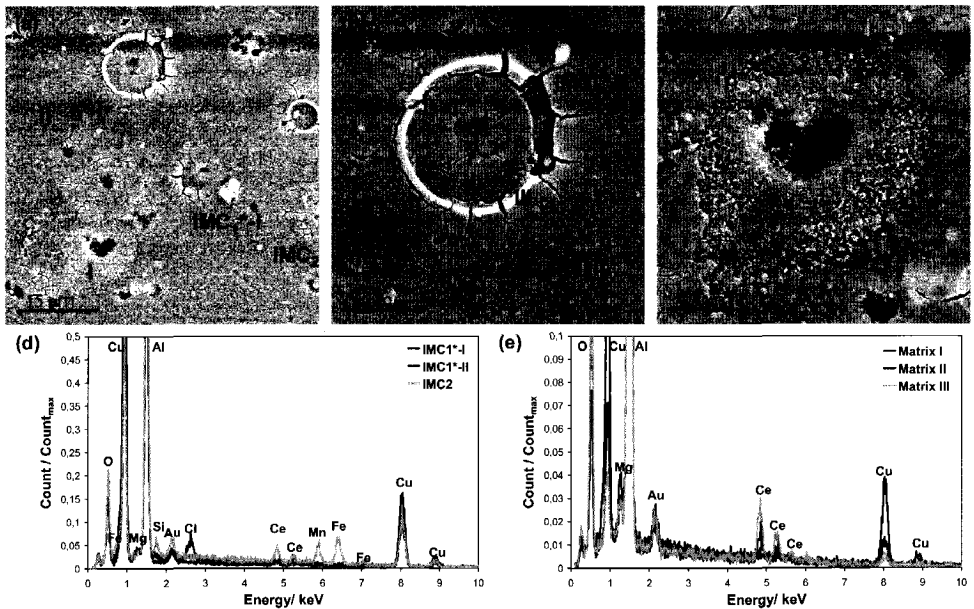


**Figure 8.17:** SEM micrographs (a, b, c) and EDS spectra (d, e) of bare 2024 alloy after mechanical polishing, 20 minutes of immersion in the  $H_3PO_4$ - $H_2SO_4$  solution (sample 2SP), and 3 seconds in the cerate bath.

As concern the Al matrix, only few areas (named I) are not covered by a thin and compact film consisting of cerium oxide. The EDS analyses (Figure 8.17-e) carried out at these locations show not only the absence of the cerium peaks but also strong copper

signals, which suggests that the Cu-rich smut caused by the long immersion in the pickling bath (section 7.3.1 of chapter 7) is not removed by the short contact with the cerium chloride solution. In addition, several circular rings characterized by the presence of a much thicker cerium oxide film, are formed during the short cerate process (area named III in the SEM micrograph of Figure 8.17-b). The formation of such rings may be a consequence of some drops of conversion solution left on the surface after the rinsing step in deionised water, which always follows the immersion in the cerate bath. Indeed, this can enable the cerium oxide deposition to continue at these sites after the removal of the sample from the cerate solution.

Although, on sample 2SP the nucleation and growth of the cerium-based conversion coating has been very fast, in some regions of the surface, especially at the interface between covered and uncovered regions, small round particles, the coalescence of which has led to the formation of the film, are still visible. This suggests that the increase of the duration of the pickling process does accelerate the precipitation of cerium oxide but on the other hand does not change the mechanism of the conversion film formation, which still consists of deposition of discrete small particles evenly distributed on the whole surface that afterwards coalesce resulting in a thin and compact layer.

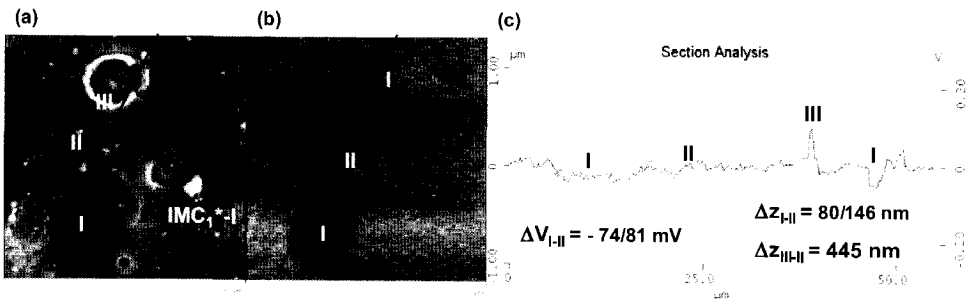


**Figure 8.18:** Topographic image with a height range of 2  $\mu\text{m}$  (a), Volta potential map with a potential range of 0.8 V (b), and dual section analysis (c) along the black line in the topographic image (black) and in the potential map (grey) of sample 2SP after 3 seconds of immersion in the cerate bath. Polished sample.

The potential map (Figure 8.18-b) of the same area of the SEM micrograph of Figure 8.17-a shows that likewise observed for sample 2NP the immersion for 3 seconds in the  $\text{CeCl}_3\text{-H}_2\text{O}_2$  solution leads both to a decrease of the galvanic coupling between the IMCs and the Al matrix and to the creation of a difference in potential between the covered (named II) and uncovered (named I) areas of the sample. However, in the case of sample 2SP the decrease of the galvanic coupling between matrix and intermetallics is such that it is completely eliminated and the position of the IMCs is not anymore recognizable in the potential scan. This is likely a consequence of the formation of the cerium-based conversion coating at both sites, i.e. matrix and IMCs. According to the dual section analysis option carried out at different locations of several SKPFM measurements, an example is given in Figure 8.18-c, the thickness of the cerium oxide film formed on sample 2SP during the 3

seconds of immersion in the cerate solution is in the order of a few tens of nanometres. However, the circular rings (named III) observed in the SEM study and clearly visible also in the topographic images (Figure 8.18-a) can reach thicknesses up to 500 nm, which results in the formation of cracks in the film during the final drying step.

On the basis of the results discussed above, it can be concluded that the nucleation of the cerium-based conversion coating on the pickled AA2024 surface is extremely fast, especially when long times of immersion in the pickling solution are used (sample 2SP), it occurs via deposition and coalescence of discrete particles evenly distributed over the whole surface and not preferentially at the location of the intermetallic particles.

The increase of the time of immersion in the cerate bath from 3 seconds to 2 minutes leads to the formation of a very thick cerium oxide film above the whole surface of sample 2NP, i.e. on top of both the intermetallics and the Al matrix, as can be observed in the SEM micrographs given in Figure 8.19-a and -b. The cerium-based conversion layer is characterized by a crack-mud structure, which is typical for thick conversion film and is a result of the stresses induced in the film during the drying process that always ends the conversion treatment.

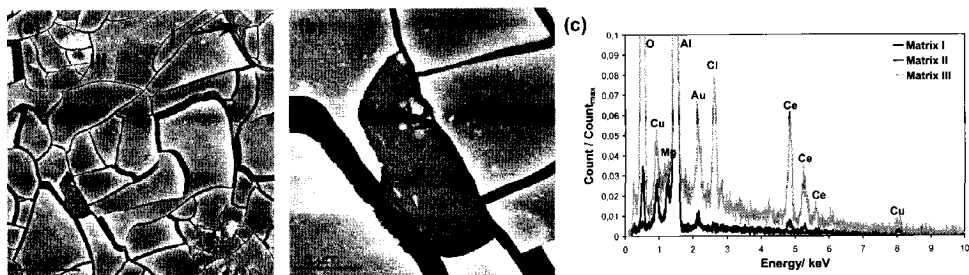


**Figure 8.19:** SEM micrographs (a, b) and EDS spectra (c) of sample 2NP after 2 minutes of immersion in the cerate bath (sample 2NPCe). Polished sample.

The SEM/EDS investigation highlights also the presence of corrosion products enriched in chloride at few spots of the surface, of areas where the film seems absent (named I and II), and of circular rings (named III) where a further precipitation of cerium oxide particles has taken place above the conversion layer. The EDS analyses (Figure 8.19-c) show that amongst the sites where the thick film is absent in some the oxygen and cerium signal are not present (named I) and in others instead these two elements are detected (named II). This means that while at some areas the Al substrate is completely uncovered, at some other sites a thin cerium oxide film is present. The presence of some uncoated areas may indicate that either the conversion film has not been formed or it has been subsequently removed. Similarly, the areas where a thin cerium oxide film is present could result either from a lower film formation rate or from a deposition occurring after the detachment of the thick layer. Although not unequivocally proved by our results, in view of the high reactivity shown by the pickled surface it is more likely that the lost of adhesion is the cause of the uncovered or partially covered sites rather than the lack of precipitation.

The Volta potential measurements, not shown here, confirms that the presence of a thick oxide layer eliminates the potential difference between the matrix and the IMCs, and



that on the other hand the complete detachment of the film at some areas of the surface originates a galvanic coupling between the bare substrate, which acts as anode, and the covered surface, which acts as cathode. Anyhow, this difference in potential is limited at some tens of millivolts.

Also the SKPFM topographic investigation (Figure 8.20) highlights both the detachment of the thick conversion film at discrete sites of the surface and the formation of circular rings of cerium oxide particles, which are likely a results of drops of solution left on the sample after the end of the immersion. When a cross section analysis, i.e. the height

profile along a line in the image, is carried out across the uncovered areas and the annular rings, it is observed that the thickness of either the conversion film or the particles deposited above it

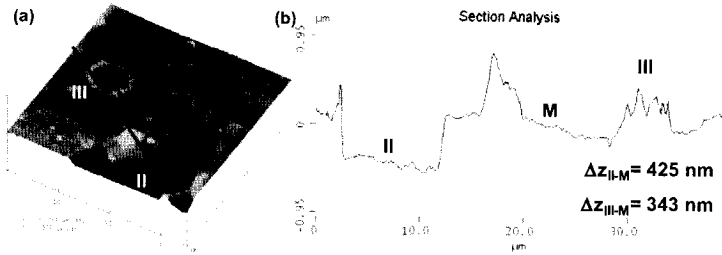


**Figure 8.20:** 3D topographic image (a) and section analysis along the black line in the topographic image (b) of sample 2NPCe. Polished sample.

is relatively high, in the order of few hundreds nanometres.

The SEM/EDS study of sample 2SP after a standard duration (2 minutes) of the cerate process (Figure 8.21) leads to the same conclusions drawn in the case of sample 2NP, i.e. formation of a thick cerium-based conversion coating above either the matrix or the IMCs characterized by a crack-mud morphology, complete absence of the layer at some locations, further deposition of cerium oxide particles above the previously formed thick conversion film in the form of circular rings.

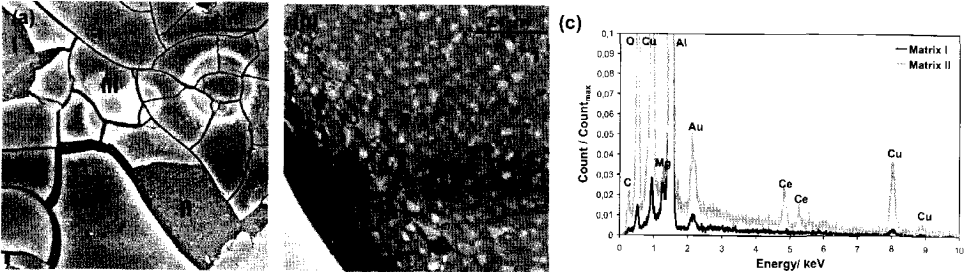


**Figure 8.21:** SEM micrographs (a, b) and EDS spectra (c) of sample 2SP after 2 minutes of immersion in the cerate bath (sample 2SPCe). Polished sample.

In addition, likewise in the case of sample 2NPCe, where the cerium-based conversion layer seems to be absent in some cases the aluminium surface is completely uncovered (zone named I in the SEM micrograph of Figure 8.21-a), whereas in other cases a thin cerium oxide film is present (zone named II in the SEM micrographs of Figure 8.21-a and -b). However, when sample 2SPCe is concerned, below this thin film small particles are present and can be related with the copper deposits formed on the surface as a

consequence of the pickling treatment, since the EDS analyses detect at this location a strong copper signal (Figure 8.21-c). On the other hand, at the sites where the cerium oxide is completely absent also the copper-rich smut is not present. This suggests either that the conversion film did not form or that it has been removed together with the copper smut as a result of a poor adhesion to the substrate. As mentioned previously for sample 2NP, the high reactivity of the pickled surface towards the cerate solution suggests that the uncoated sites are a consequence of the detachment of the layer. This hypothesis is supported also by the fact that the Cu-rich smut was observed to be loosely attached to the aluminium alloy and therefore its presence at the interface Al substrate/conversion coating may be expected to cause a reduction of the film adhesion.

The results of the SKPFM study of sample 2SPCe, not shown here, are similar to those obtained for sample 2NPCe: homogeneous surface potential, except for the areas where the layer has been removed that act as anodic sites, and thickness of the cerium oxide layer being in the order of a few hundreds nanometres. Therefore, it can be claimed that on one hand the increase of the length of the pickling process does strongly accelerate the nucleation and formation of a thin cerium-based conversion layer during the first stages of the film deposition, whereas it does not significantly influence the subsequent growth of the layer.

According to the results of the SEM/EDS and SKPFM studies discussed in this subsection the immersion in the pickling bath, especially for a long time, prior to the cerate process strongly enhances the precipitation rate of the cerium-based conversion coating, which does not occur preferentially in proximity of the intermetallics but involves the whole surface by deposition and coalescence of small cerium oxide particles. In section 7.3.1 of chapter 7 it has been shown that the acid pickling treatment does not completely remove the intermetallics and does not change their cathodic nature but on the other hand it does cause the formation of a copper-rich smut, the amount of which increases with the duration of the treatment. Therefore, the main difference in the morphology of the Al surface in the as-received condition (sample 2AR) and after the acid pickling process (samples 2NP and 2SP) consists of the presence of copper/copper oxide particles evenly distributed on the whole surface. Based on these observations it can be concluded that the presence of the copper-rich smut is the main responsible for the high reactivity of the pickled AA2024 substrate towards the cerate conversion bath rather than the cathodic intermetallic particles. In addition, it should be noted that the activation of the surface caused by the contact with the pickling solution may contribute in enhancing the rate of the electrochemical reactions occurring at the sample surface during the cerate treatment.

- *Acid pickling (unpolished surfaces)*

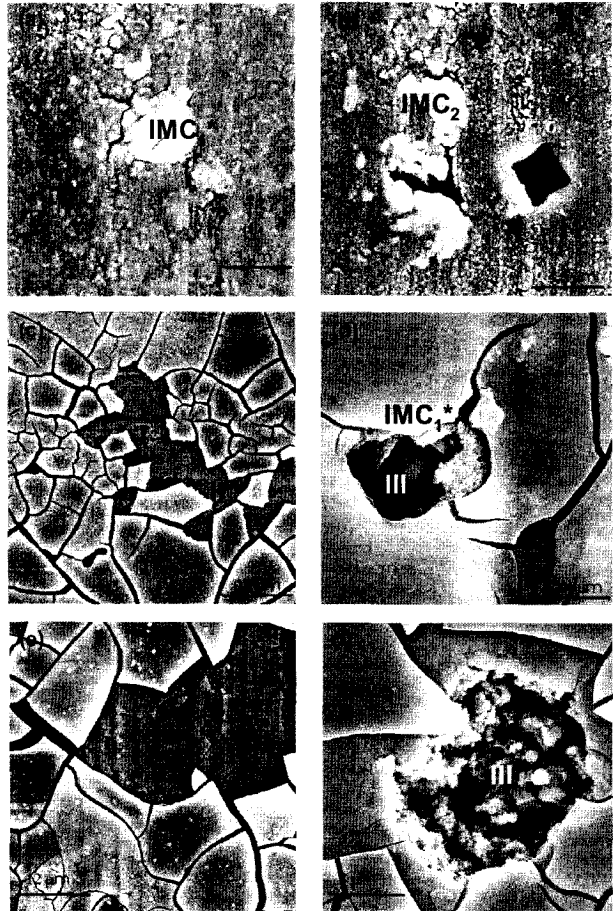
The SEM investigation of the unpolished AA2024 surface after the short (5 minutes) acid pickling treatment and different times of immersion in the cerate bath (Figure 8.22) leads to the same conclusions drawn in the case of the sample that was mechanically polished prior to the surface preparation process. Indeed, after 3 seconds of contact with the  $\text{CeCl}_3\text{-H}_2\text{O}_2$  solution (Figure 8.22-a and -b) a thin film is formed above both the Al matrix and

the intermetallics, as a result of the precipitation and coalescence of small cerium oxide particles. Some areas of the sample (named I) are however still uncovered and at their location discrete particles, which constitute the first stages of the layer formation, can be observed.

The increase of the duration of the cerate process up to 30 seconds (Figure 8.22-c and -d) gives rise to the growth of the conversion film, which becomes relatively thick and contains numerous cracks resulting from the thermal stresses induced by the drying step. Still at some sites of the surface the cerium oxide film is completely absent (areas named I) or very thin (areas named II), as a consequence of either a lack of precipitation or of a poor adhesion. In addition, few pits, which are often but not always associated with intermetallic particles (position named III in the SEM micrograph of Figure 8.22-d) develop on the surface of AA2024 during the contact with the conversion solution. This is a result of the presence of aggressive  $\text{Cl}^-$  ions in the treatment bath, as supported by the EDS investigation that shows the presence of corrosion products being

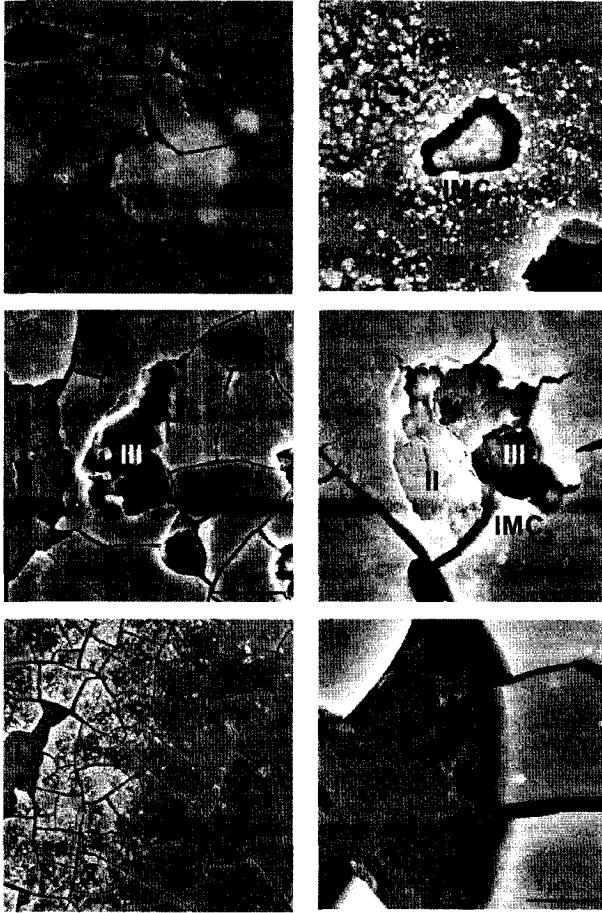
enriched in chloride inside these pits. The further prolongation of the cerate process up to two minutes (Figure 8.22-e and -f) enhances the phenomena already observed after 30 seconds (thickening of the film, formation of some isolated pits, detachment of the layer at some sites) without causing additional modifications to the morphology of the surface.

Figure 8.23 shows the SEM investigation of the conversion film formation as function of the immersion time in the cerate bath when a long (20 minutes) pickling treatment is used as surface preparation procedure (sample 2SP). The increase of the length of the pickling treatment before the cerate process accelerates the initial deposition of the cerium oxide



**Figure 8.22:** SEM micrographs of sample 2NP after 3 seconds (a, b), 30 seconds (c, d) and 2 minutes (e, f) of immersion in the cerate bath. Unpolished sample.

layer; indeed after 3 seconds of exposure to the  $\text{CeCl}_3\text{-H}_2\text{O}_2$  bath (Figure 8.23- a and -b) most of the surface is covered with a film characterized by the presence of cracks, which are indicative of an appreciable thickness. In addition, some sites (named I in the SEM micrograph of Figure 8.23-b) are still not involved in the precipitation process, however they are lower in extension and number in comparison with those observed on sample 2NP.



**Figure 8.23:** SEM micrographs of sample 2SP after 3 seconds (a, b), 30 seconds (c, d) and 2 minutes (e, f) of immersion in the cerate bath. Unpolished sample.

2 minutes of immersion in the  $\text{CeCl}_3\text{-H}_2\text{O}_2$  bath, the precipitation of cerium oxide continues to occur also above the thick conversion film itself (Figure 8.23-e); this suggests that the formation of the cerium-based conversion coating is not a self-limiting process, as the chromate one.

Based on the results discussed in this and the previous section, it can be concluded that the mechanical polishing, carried out prior to the pickling treatment, does not influence the behaviour of the pickled AA2024 surface during the immersion in the cerate bath. The

On the other hand, the growth rate of the cerium-based conversion coating is not affected by the duration of the pickling treatment, as can be observed comparing the SEM micrographs of sample 2SP after either 30 seconds or 2 minutes of immersion in the cerate bath (Figure 8.23-c, -d, -e, and -f) with those relative to sample 2NP (Figure 8.22-c, -d, -e, and -f). Indeed, also for sample 2SP the increase of the duration of the cerate process thickens the layer, which assumes the typical crack-mud structure, causes the formation of isolated pits (position named III in Figure 8.23-c and -d), which are often occurring in proximity of the intermetallics, and leads to the complete or partial removal of the film in some areas (named I and II, respectively, in Figure 8.23), the number and extension of which increase with the duration of the conversion treatment. Besides, during the

investigation using unpolished samples indeed does confirm the accelerating effect of the Cu-rich smut towards the precipitation of the cerium oxide film. In addition, two major problems of the cerate process have been highlighted: the local corrosive attack resulting from the presence of the chloride ions in the conversion bath and the loose of adhesion likely caused by the presence of the Cu-rich smut itself at the interface Al substrate/conversion film.

- *Deoxidising (polished surfaces)*

The immersion for 3 seconds in the  $\text{CeCl}_3\text{-H}_2\text{O}_2$  bath of AA2024 after the alkaline cleaning and the Ce-based deoxidising treatment (sample 2DX) leads to evident modification of the surface, as can be observed from the SEM micrographs given in Figure 8.24-a, -b, and -c.

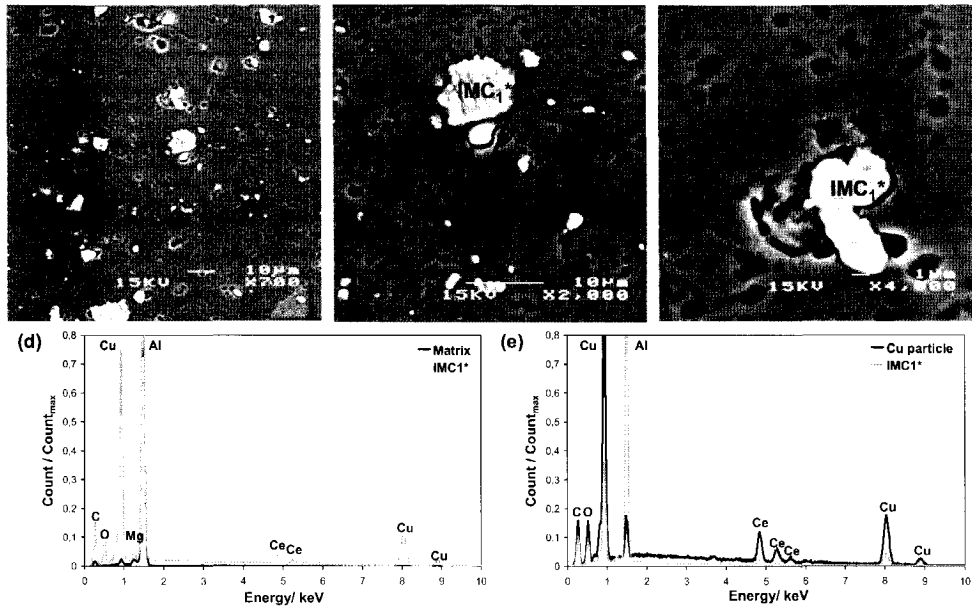


**Figure 8.24:** SEM micrographs (a, b, c) and EDS spectra (d, e) of bare 2024 alloy after mechanical polishing, immersion for 4 minutes in the alkaline non-etching cleaner (Ridoline 53<sup>TM</sup>), 10 minutes in the Ce-based deoxidiser (sample 2DX) and 3 seconds in the cerate bath.

Comparing these SEM micrographs with those relative to sample 2DX prior to the cerate treatment (Figure 8.6-a, -b, and -c) it can be observed that several small pits are formed on the Al matrix as a consequence of the very short cerate process. A local attack at the periphery of both the intermetallics and the Cu particles, which were observed to deposit on the surface during the deoxidising step, has also occurred. In addition, at these locations the EDS analyses detect the presence of cerium and oxygen, whereas above the rest of the surface these elements are completely absent (Figure 8.24-d and -e). This can be seen even more clearly in the elemental maps shown in Figure 8.25, where oxygen and cerium are always related with sites enriched in copper, i.e. either the IMCs or the Cu-rich smut, and further confirms the acceleration effect of copper towards the precipitation of cerium oxide.

The presence both of small pits on the Al matrix and of a film above the intermetallic and the copper particles is also observed in the topographic images obtained with the SKPFM technique. In Figure 8.26-a that relative to the area of the SEM micrograph of Figure 8.24-a is given.

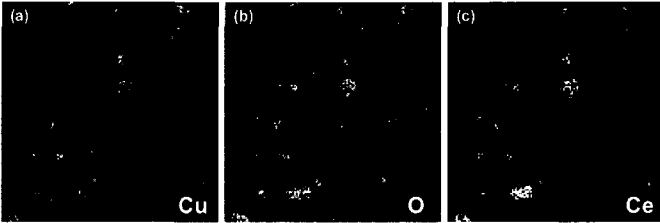


**Figure 8.25:** Elemental maps of sample 2DX after 3 seconds of immersion in the cerate bath. Polished sample.

The comparison with the potential map (Figure 8.26-b) highlights that the areas involved in the deposition of the cerium-based conversion coating act as local cathodes, however the lateral extension of the

cathodic regions appears to be bigger with respect to that of the cerium oxide deposits. This lack of correspondence in size between the areas covered with the conversion layer and those having a more noble Volta potential is more evident in the dual section analysis (Figure 8.26-c), which shows also that both the thickness and the cathodic nature of the cerium oxide film are quite pronounced and can reach values up to 1  $\mu\text{m}$  and 450 mV, respectively. On the other hand, the lateral and depth dimensions of the pits formed on the aluminium matrix are both relatively limited, a few microns for the former and a few hundred nanometres for the latter.

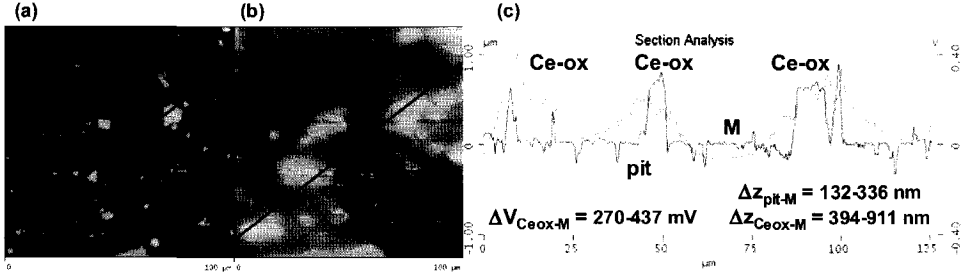


**Figure 8.26:** Topographic image with a height range of 2  $\mu\text{m}$  (a), Volta potential map with a potential range of 0.8 V (b), and dual section analysis (c) along the black line in the topographic image (black) and in the potential map (grey) of sample 2DX after 3 seconds of immersion in the cerate bath. Polished sample.

The lateral extension of the cathodic regions beyond the edges of the cerium oxide deposits does not correspond to any variation in the chemical composition of the surface detectable with the EDS technique. Therefore, similarly to the AA2024 after the immersion in alkaline cleaner, our investigations do not enable to identify the cause of the more noble Volta potential of some areas of the sample surface. However, they do clearly demonstrate the preferential precipitation of cerium oxide/hydroxide at the sites involved in the deposition of the copper particles, either above the Al matrix or above the intermetallics.

The SEM/EDS study (Figure 8.27) shows that the prolongation of the cerate treatment time from 3 seconds to 2 minutes gives rise to the deposition of a thin cerium-based

conversion coating above most of the sample surface. Nevertheless, in the EDS spectra relative to some regions (named I) the cerium peaks are not present, which suggests that either the film has not been formed or it has been subsequently detached (Figure 8.27-e).

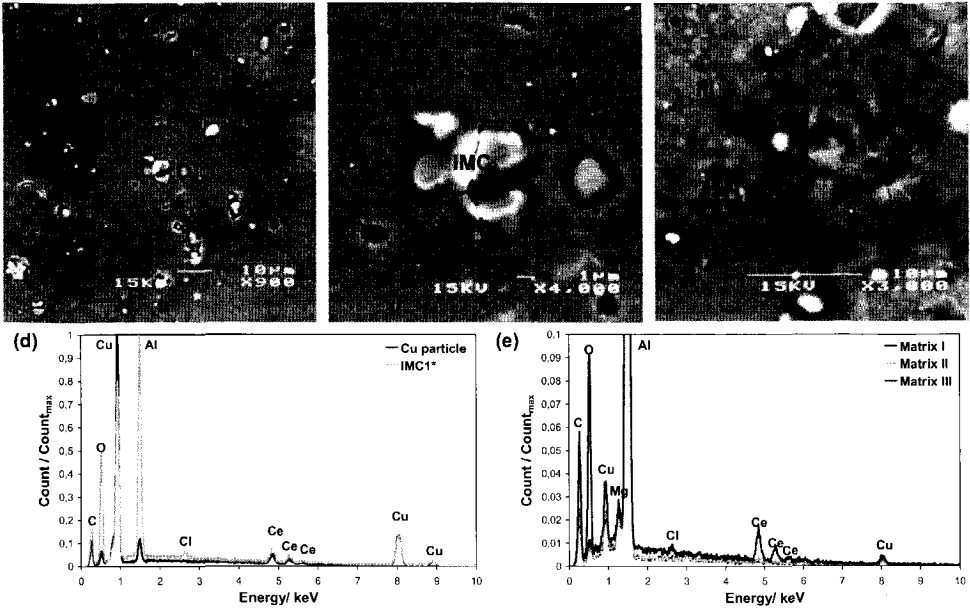


**Figure 8.27:** SEM micrographs (a, b, c) and EDS spectra (d, e) of sample 2DX after 2 minutes of immersion in the cerate bath (sample 2DXCe). Polished sample.

It can be observed that while the layer formed on the Al matrix does not have a crack-mud structure, the film deposited above the IMCs and the Cu particles shows the presence of some cracks. This together with the much weaker Ce signal detected in correspondence of the matrix (note that a lower scale is used in the EDS spectra given in Figure 8.27-e relative to the matrix) leads to the conclusion that a thinner cerium-based conversion coating is formed on the areas of the Al matrix, which are not enriched in copper.

A confirmation is given by the section analyses carried out on several topographic images of sample 2DXCe, an example is given in Figure 8.28. It is found that the thickness of the cerium oxide film formed above the Al matrix ranges from 100 to 220 nm, whereas the layer deposited at the sites of the intermetallics and of the Cu-rich smut reaches thicknesses

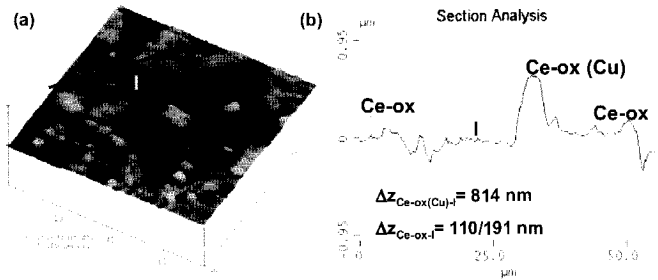


**Figure 8.28:** 3D topographic image (a) and section analysis along the black line in the topographic image (b) of sample 2DXCe. Polished sample.

the layer deposited at the sites of the intermetallics and of the Cu-rich smut reaches thicknesses

of several hundred nanometres and in some cases of more than 1  $\mu\text{m}$ . The limited thickness of the conversion film formed on the matrix, which indicates a low rate of the cerium oxide precipitation at this location, suggests that the most likely cause of the observed uncovered areas (named I) is the lack in cerium oxide deposition rather than the loose of adhesion.

The comparison of the results relative to sample 2DX with those relative to sample 2NP and especially sample 2SP, discussed in the previous sections, suggests that the nucleation and growth of the cerium-based conversion coating on the AA2024 surface after the deoxidising step is slower and more localized than after the acid pickling treatment. Indeed, after 3 seconds of immersion in the  $\text{CeCl}_3\text{-H}_2\text{O}_2$  bath the cerium oxide film on sample 2DX is thicker but also present only at few sites of the surface, whereas on samples 2NP and 2SP it is covering already most of the surface. After a standard time of the cerate treatment, i.e. 2 minutes, while sample 2DX is characterized both by a conversion layer being thin on the Al matrix, extremely thick at some discrete locations, and by the absence of cerium oxide precipitation in large regions of the surface, the pickled surfaces (samples 2NP and 2SP) are covered by a film being quite homogeneous in thickness and having a poor adhesion to the substrate.

These differences in both the formation rate and the morphology of the cerium-based conversion coating formed after these two surface preparation procedures can be explained only considering the different morphology of the copper redeposition caused by the deoxidising treatment in comparison with that arising from the pickling process and assuming valid the acceleration effect that has been previously attributed to the copper particles. Indeed, it was observed that the immersion in the Ce-based deoxidising bath leads to the deposition of a lower amount and more heterogeneously distributed copper particulate matter in comparison with the dipping in the pickling solution. According to the hypothesized speed up of the cerium oxide precipitation caused by the copper, this in turn would lead to a general slower precipitation on the whole sample surface but at the same time to a more pronounced formation of the conversion film at the discrete sites involved in the deposition of the Cu-rich smut. Finally, it should be noted that the deposition of the copper particles on sample 2DX is occurring preferentially above the intermetallics and this is likely the cause of the thick cerium oxide film deposited at their location rather than their intrinsic cathodic nature. In conclusion, the predominant role of the Cu-rich smut with respect to the intermetallics in the nucleation and growth of the cerium-based conversion coating is confirmed by the result concerning the film formation after the Ce-based deoxidising treatment.

- *Desmutting (unpolished surfaces)*

The main results of the investigation of the cerium-based conversion coating formation on the AA2024 surface, which is pickled and desmuted prior to the cerate treatment, are illustrated with the micrographs and EDS spectra given in Figure 8.29 that are relative only to sample 2NPD, i.e the sample immersed for 5 minutes in the pickling solution prior to the desmutting process. However, similar findings were obtained also for sample 2SPD, i.e. the sample treated for 20 minutes in the pickling bath and then immersed in the desmutting one.



This was expected to be the case, since the microstructure of the desmutted AA2024 surface does not depend anymore on the duration of the pickling treatment due to the higher aggressiveness of the nitric/hydrofluoric acid solution, which was found to cause a complete removal of the Cu-rich smut and a partial removal of the intermetallic particles.

After a very short cerate process, i.e. 3 seconds, the precipitation of a cerium oxide film while on the Al matrix occurs in the form of small isolated particles, maximum 1  $\mu\text{m}$  in size, at the location of the few intermetallics left on the surface it leads to the formation of a thin film (Figure 8.29-a and -b). The more pronounced deposition taking place above the IMCs is confirmed by the stronger peaks relative to cerium and oxygen observed in the EDS spectra (Figure 8.29-c).

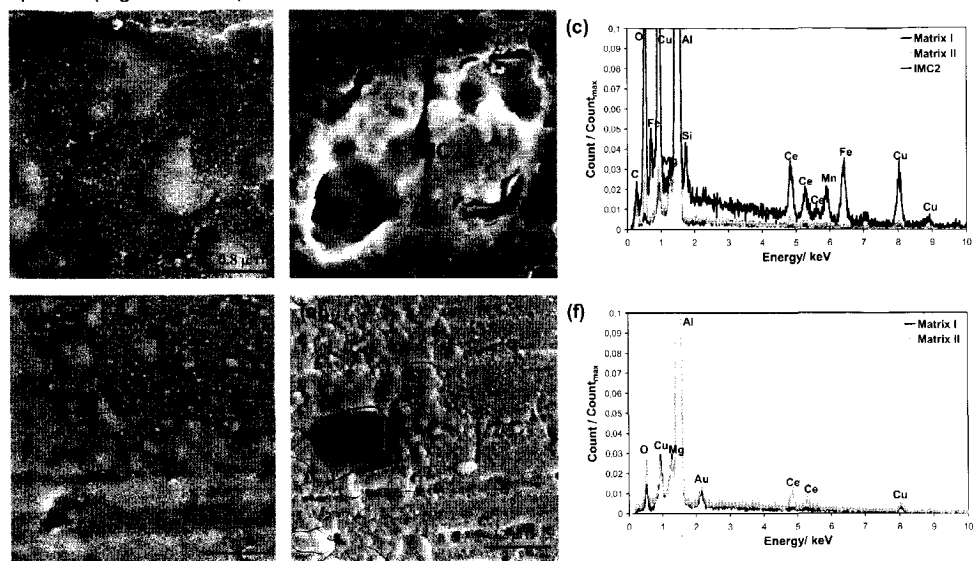


**Figure 8.29:** SEM micrographs (a, b, d, e) and EDS spectra (c, f) of bare 2024 alloy after 5 minutes of immersion in the  $\text{H}_3\text{PO}_4\text{-H}_2\text{SO}_4$  solution and 30 seconds of immersion in the  $\text{HNO}_3\text{-HF}$  solution (samples 2NPD) and different times, 3 seconds (a, b, c), 30 seconds (d), and 2 minutes (e, f) in the cerate bath. Unpolished samples.

Increasing the time of immersion in the  $\text{CeCl}_3\text{-H}_2\text{O}_2$  bath enhances the cerium oxide precipitation on the Al matrix leading in large part of the sample surface, especially after a standard time of the cerate treatment, to the coalescence of the isolated Ce oxide particles and to a film characterized by a crack-mud structure (Figure 8.29-d and -e), which is indicative of an appreciable thickness of the layer. However, also after 2 minutes of immersion large regions (named I) result to be still uncovered, as can be noted by the absence of the Ce signal in the EDS analyses (Figure 8.29-c).

The formation of a cerium oxide film above the intermetallics already after 3 seconds of immersion in the cerate bath could be due to the fact that when the Cu-rich smut is not present on the Al surface the effect of the cathodic nature of the IMCs becomes preponderant and favours the precipitation of the cerium oxide at their location. Although this may be the case, our results show also that the formation of the conversion film above the

rest of the surface does not proceed via the island growth mechanism proposed in literature [11]. Indeed, on the Al matrix the film forms slowly via deposition and coalescence of small Ce oxide particles homogeneously over the whole surface rather than by local film growth at the periphery of the IMCs. A possible explanation of the precipitation of the cerium oxide above the AA2024 surface, which does not present a Cu-rich smut after the surface preparation procedure (samples 2NPD and 2SPD), is that the redeposition of small copper particles takes actually place during the cerate process itself. Although this phenomenon is not proved by the results shown above, it is highly probable due to the strong tendency of copper to dissolve and reduce back to the Al surface in the presence of chloride ions, which was observed to occur even on chromated Alclad 2024 during the impedance measurements carried out in a chloride-containing electrolyte (section 6.3.2 of chapter 6).

Finally, it should be noted that the activation of the Al surface, i.e. thinning of the natural aluminium oxide film, caused by the desmutting step contributes to enhance the reactivity of both the Al matrix and the intermetallics towards the precipitation of the cerium oxide. This would explain the different behaviour of the AA2024 surface directly immersed in the  $\text{CeCl}_3\text{-H}_2\text{O}_2$  (sample 2AR) with respect to that immersed after the desmutting treatment (samples 2NPD and 2SPD). Indeed, although the only morphological difference between the two surfaces is a considerable lower amount of IMCs on the desmuted one, on the former the precipitation of the cerium oxide film is almost negligible, whereas on the later the conversion film is formed on wide areas.

- *Alclad 2024 (unpolished surfaces)*

The SEM/EDS investigation carried out on Alclad 2024 alloy, either pickled for 5 minutes (sample NP) or pickled and then desmuted for 30 seconds (sample NPD), shows that no significant modifications of the surface take place during the short immersion, i.e. 3 seconds and 30 seconds, in the cerate conversion bath. The only phenomenon observed to occur is a further etching of the sample, whereas cerium is not detected either above the Al matrix or above the intermetallics, which are still present in high quantity on sample NP. On the other hand, when the cerate treatment time is increased to 2 minutes on both the pickled and the desmuted surfaces small, less than 1  $\mu\text{m}$  in size, round-shaped particles are formed, which are identified by means of EDS analyses to consist of cerium oxide/hydroxide (Figure 8.30).

Although, on sample NP the precipitation of the conversion film occurs in a larger extent at the location of the intermetallics (Figure 8.30-a and -b), the deposition of cerium oxide on the matrix of this sample and on the surface of sample NPD, where the IMCs are completely removed, does further confirm that the presence of cathodic intermetallics is not a necessary condition for the cerium oxide precipitation on aluminium alloys. On the other hand, the extremely low rate of the conversion film nucleation on Alclad 2024 alloy, which contains only 0.1% of copper and does not undergo the Cu-rich smut formation even during the acid pickling process, does support the hypothesis regarding the acceleration effect of the copper particles towards the cerium oxide precipitation. When the cerate process is prolonged up to 6 minutes, a higher amount of cerium oxide particles precipitate on both samples without however resulting in the formation of a film (Figure 8.31-a and -c).

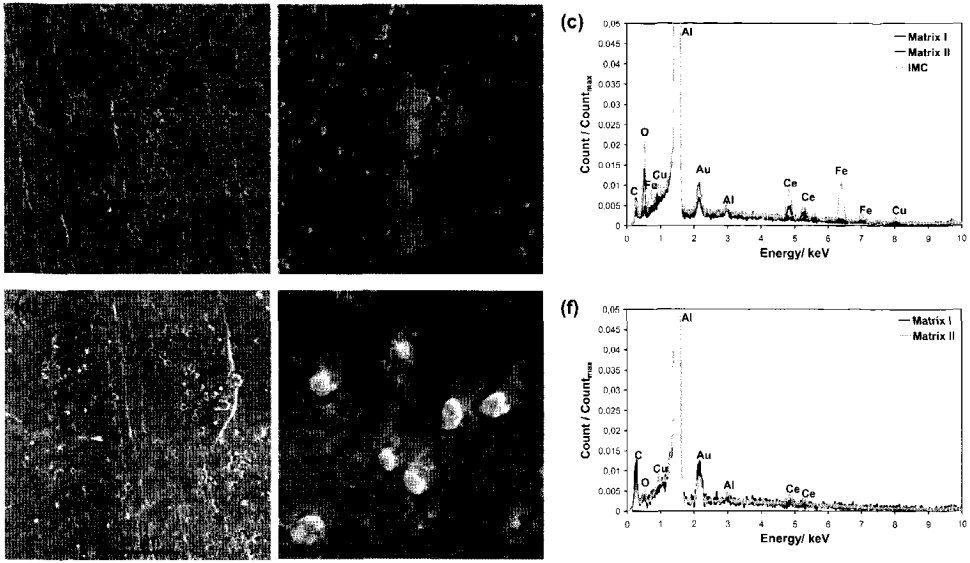


**Figure 8.30:** SEM micrographs (a, b) and EDS spectra (c) of Alclad 2024 alloy after 5 minutes of immersion in the  $H_3PO_4-H_2SO_4$  solution (sample NP) and 2 minutes in the cerate bath. SEM micrographs (d, e) and EDS spectra (f) of Alclad 2024 alloy after 5 minutes of immersion in the  $H_3PO_4-H_2SO_4$  solution, 30 seconds of immersion in the  $HNO_3-HF$  solution (sample NPD) and 2 minutes in the cerate bath (bottom). Unpolished samples.

The further increase of the immersion time in the  $CeCl_3-H_2O_2$  solution to 15 minutes has as main consequence a stronger etching of the aluminium surface rather than the growth of the conversion layer. Therefore, it seems that after the initial slow deposition of discrete particles of cerium oxide the subsequent step of the film formation, i.e. the coalescence of such small particles, does not take place and the corrosive attack of the substrate caused by the aggressive chloride ions present in the conversion bath becomes the preponderant phenomenon occurring at the Al surface.

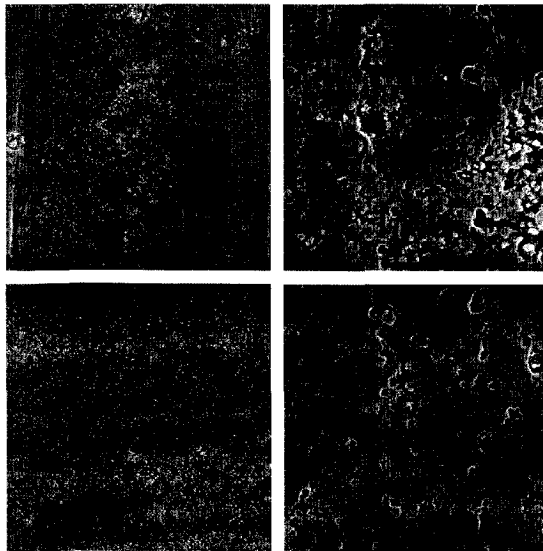


**Figure 8.31:** SEM micrographs of sample NP after 6 (a) and 15 minutes (b) of immersion in the cerate bath and of sample NPD after 6 (c) and 15 minutes (d) of immersion in the cerate bath. Unpolished samples.

The fact that a cerium-based conversion coating does not form on the Alclad 2024 alloy, which has a very low copper content in solid solution, confirms once more that the

presence of some copper particles on the substrate surface is a necessary condition for the deposition of the cerium oxide film.

In conclusion, all the results discussed in these five sub-sections have highlighted the important role played by the presence of copper particles on the aluminium surface on the nucleation and growth of the cerium-based conversion coating. On the basis of these findings, in the next part of the section a model of film formation is proposed and discussed in view also of the results reported in literature.

• Model

The formation of the cerium-based conversion coating on aluminium alloys occurs through different steps. First copper and/or copper oxide particulate matter needs to deposit on the surface of the alloy in order to favour the precipitation of cerium oxide, which takes place in the form of small particles. While the immersion in the cerate bath continues these particles coalesce and lead to the formation of a thin and compact layer. The further duration of the conversion treatment causes a thickening of the film, which can assume a crack-mud structure during the final drying step and may eventually be removed at some sites as a consequence of a poor adhesion to the substrate.

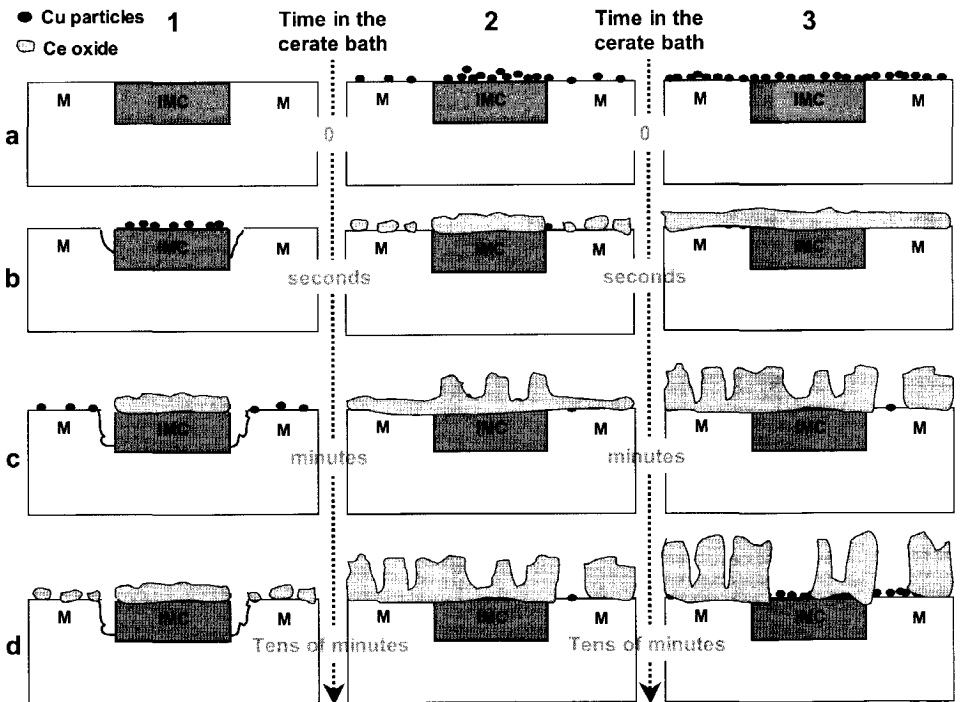


Figure 8.32: Model of the cerium-based conversion coating formation on aluminium alloys.

Although this general mechanism is independent upon the surface preparation procedure, the time necessary to form a relatively thick cerium oxide layer is determined not only by the conversion bath parameters, as temperature and pH, but also by the type of

processes carried out prior to the cerate treatment. Figure 8.32 illustrates three different situations that may be expected to occur:

1. The surface preparation procedure only activates the surface, i.e. dissolves partially or completely the natural aluminium oxide (1-a). At the beginning of the immersion in the cerate bath the cerium oxide precipitation does not take place and the dissolution and redeposition of copper occurs as a result of the selective attack of the intermetallics in the chloride-containing conversion solution. Therefore, the copper particles are formed faster and preferentially at the location of the IMCs (1-b), where then the deposition of the cerium oxide film starts first (1-c). This leads also to a local dissolution of the aluminium matrix at the periphery of the areas involved in the copper particles and cerate film deposition resulting in the formation of pits (1-b and 1-c). Besides, the cathodic nature of the IMCs can, in the absence of the copper-rich smut, play an important role during the early stages of the conversion layer formation enhancing even more the preferential cerium oxide precipitation at their location and the Al matrix dissolution in their proximity (1-c). In the mean time, some copper deposits are created also above the aluminium matrix (1-c) and therefore the precipitation of small cerium oxide particles starts to involve the whole surface (1-d) and can give rise to a thin and compact layer after a relatively long treatment time, which is expected to be inversely dependent on the copper content of the aluminium alloy used as substrate. This is the situation observed in the case of the desmutting process on AA2024 and of the pickling with or without desmutting procedure on Alclad 2024. Obviously, the time required to form the cerium-based conversion film above the whole surface increases when the aluminium alloy is directly immersed in the cerate solution, since an additional period is necessary in order to activate the surface.
2. The surface preparation procedure causes a thinning of the natural aluminium oxide together with the selective dissolution of the intermetallics and subsequent deposition of copper particulate matters above the Al surface and especially at the sites of the IMCs (2-a). During the first stages of the immersion in the cerate bath a thin conversion film precipitates above the IMCs and some small cerium oxide particles form above the Al matrix (2-b). Afterwards, the growth of the film continues as described above, i.e. via coalescence of the particles (2-c) and with the formation of a crack-mud structure (2-d). This leads to the coverage of the complete surface after few minutes of immersion and is the situation observed for AA2024 after the Ce-based deoxidising step.
3. The surface preparation procedure gives rise to an activation of the aluminium surface but also to the formation of a large amount of copper-rich smut homogeneously distributed as a consequence of the dissolution and redeposition of Cu from the solid solution (3-a). Therefore, in the first few seconds of the cerate process a thin and compact film covers most of the surface (3-b) and afterwards grows resulting in a thick cerium oxide layer, which contains numerous cracks (3-c) and is detached in some areas (3-d) as a result of the poor adhesion caused by the presence of the copper-rich smut at the interface with the alloy substrate. This is the situation occurring when the pickling treatment is carried out on AA2024.

The mechanism proposed is based on the fact that the presence of copper and/or copper particles on the aluminium surface has an acceleration effect towards the formation of the cerium oxide conversion layer during the immersion in the cerate bath. Although this effect has been clearly demonstrated by the results discussed in the previous parts of this section, it is not yet clear whether it is simply due to a cathodic activation of the surface, i.e. speed up of the cathodic reduction of  $O_2$  and  $H_2O_2$  with consequent increase in pH that favours the precipitation of cerium oxide/hydroxide, or to a direct involvement of the copper in the reactions occurring in the conversion bath. Another possibility is that the copper particles favour the deposition of the cerate film at their location because they cause a reduction of the activation barrier energy for the cerium oxide precipitation to take place, i.e. they act as heterogeneous nucleation sites. Further investigations are required in order to clarify this point, in particular the chemical nature of the smut, i.e. metallic copper or copper oxide or both, should be first investigated. Nonetheless, the hypothesised important role played by the copper particles is in accordance with and enables to explain not only our own results but also those found in literature:

- ✓ The occurrence of a preferential cerium oxide precipitation at the location of the Cu-containing intermetallics is observed when the aluminium alloy is either directly immersed in the conversion bath [8, 11, 12] or after a surface preparation process that does not cause the formation of copper particles on the surface [6, 12, 13]. The time required for this phenomenon to take place is relatively long and depends on the treatment conditions: in the order of minutes when  $H_2O_2$  is present, of hours when the treatment is carried out in boiling cerium salts solutions, and of days when a NaCl/CeCl<sub>3</sub> solution is used. This findings are consistent with the model proposed above (case 1 of Figure 8.32), which considers as first step of the conversion film formation the redeposition of copper particulate matter occurring preferentially at the IMCs as a consequence of the selective dissolution of the intermetallics themselves. It is important to note that Aldykewicz, Isaacs and Davenport [8] found that the immersion of AA2024-T4 in a NaCl/CeCl<sub>3</sub> electrolyte for 24 hours leads to the deposition of cerium oxide only above the Al-Cu-Mg intermetallics, which are also the only ones showing a localized attack at their location. This further confirms that in order to have the precipitation of cerium oxide above the Cu-containing intermetallics first they need to be selectively attacked.
- ✓ On aluminium alloys with a very low copper content (5xxx and 6xxx series) the precipitation of cerium oxide is observed to occur in higher extent above the cathodic intermetallics [6, 13-15], independently upon the type of cerate treatment. This is however not in contrast with the proposed model of the cerium-based conversion layer formation, since it may be expected that in these alloys the redeposition of copper particles, either during the surface preparation procedure or during the conversion process itself, is quite limited. As a consequence, the cathodic nature of the intermetallics would play a more important role on the cerium oxide precipitation leading to the preferential nucleation and growth of the conversion film at their location.

- ✓ The addition of  $\text{Cu}(\text{glycinate})_2$  in the  $\text{CeCl}_3\text{-H}_2\text{O}_2$  bath is found to strongly speed up the formation of the conversion film on Al alloys poor in copper [7]. This result further supports the acceleration effect attributed to the copper according to our model, since the glycinate compound is supposed to cause a deposition of copper crystallites on the surface.
- ✓ A thin copper film is found to exist at the interface between the cerium-based conversion coating and the Al substrate [7, 16]. This confirms the formation of copper deposits on the surface as a first step of the cerium oxide film formation on aluminium alloys.

## 8.4 Conclusions

A model of the cerium-based conversion coating deposition on aluminium alloys has been developed on the basis of the results of a SEM/EDS investigation in combination with a SKPFM study carried out on both bare and clad AA2024 after different times of immersion in the cerate bath. In order to characterize the role played by different microstructural features, various surface preparation procedures were used prior to the cerate process. The proposed model suggests that the formation of the conversion film takes place through the deposition and subsequent coalescence of small round-shaped cerium oxide particles. First a thin layer is deposited, which during the immersion in the bath can grow leading to a relatively pronounced thickness and to a crack-mud structure. The nucleation of the film formation is strongly accelerated by the presence on the surface of copper particles. The reason for that is not yet clear, although it seems that the effect of the copper particles is more than a simple cathodic activation of the surface. Therefore, the role played by the copper-rich smut on the precipitation of cerium oxide needs to be further investigated taking into consideration the possibility that the copper particles act as preferential nucleation sites as a consequence of favourable energy variations. To do so it is necessary first of all to determine the chemical nature of such particles, i.e. metallic or oxide.

In addition, it has been suggested that the copper-rich smut can either be a result of the surface preparation treatments or be deposited during the early stages of the immersion in the conversion bath. Therefore, the morphology of the cerium oxide film depends upon the amount of the copper particulate mater and its distribution on the surface, i.e. homogeneous or concentrated at the location of the intermetallics. This is in turn determined by both the origin of the Cu particles, i.e. the selective dissolution of the aluminium matrix or of the intermetallics, and the composition of the aluminium alloy substrate. In addition, the cathodic nature of the IMCs becomes important in enhancing the film deposition rate at their location only when the surface preparation conditions and/ or the low copper content in the alloy substrate strongly limit the deposition of the Cu particles on the surface.

The surface analysis investigation showed also the existence of some problems that need to be solved in order to render the cerate process a suitable candidate for the substitution of the chromate one. First of all, the presence of a large quantity of copper-rich smut on the aluminium surface if on one hand has the advantage of resulting in the formation of a thick cerium-based conversion film in a very short time, on the other hand it has the drawback of reducing the adhesion of such film to the substrate. Therefore, it should

be chosen a surface preparation procedure able to cause a moderate copper redeposition, possibly well incorporated in the surface oxide film, in order to optimise at the same time the duration of the process and the adhesion of the conversion layer. In addition, another problem of the cerate process consists of the attack of the aluminium surface caused by the chloride ions present in the conversion bath, which is a phenomenon occurring in competition with the precipitation of the cerium oxide. Therefore, the treatment conditions should be adjusted in order to favour the chemical and electrochemical reactions involved in the formation of the conversion film and to slow down those involved in the corrosive attack. One possible way may be the use of other cerium salts rather than chloride compounds, such as  $\text{Ce}(\text{NO}_3)_3$ , and the increase of the bath pH up to the limit of stability of the cerium salt/hydrogen peroxide solution.

## 8.5 References

- [1] L. Wilson, B.R.W. Hinton, *A Method of Forming a Corrosion Resistant Coating*, Patent WO 88/06639 (1988)
- [2] A.E. Hughes, R.J. Taylor, K.J.H. Nelson, B.R.W. Hinton, L.Wilson, *Mater. Sci. Technol.* 12 (1996) 928
- [3] A.E. Hughes, K.J.H. Nelson, P.R. Miller, *Mater. Sci. Technol.* 15 (1999) 1124
- [4] B.R.W. Hinton, D.R. Arnott, N.E. Ryan, *Mater. Forum* 9 (1986) 162
- [5] D.R. Arnott, N.E. Ryan, B.R.W. Hinton, B.A. Sexton, A.E. Hughes, *Appl. Surf. Sci.* 22/23 (1985) 236
- [6] A.E. Hughes, J. D. Gorman, P.J.K. Paterson, *Corros. Sci.* 38 (1996) 1957
- [7] A.E. Hughes, S.G. Hardin, K.W. Wittel, P.R. Miller, *Proceedings of the NACE meeting: Corrosion/2000, Research topical Symposium: Surface Conversion of Aluminum and Aluminum alloys for Corrosion Protection*, Orlando, US (2000)
- [8] A.J. Aldykewicz Jr., H.W.S. Isaacs, A.J. Davenport, *J. Electrochem. Soc.* 142 (1995) 3342
- [9] A.E. Hughes, R.J. Taylor, B.W.H.R. Hinton, *Surf. Interface Anal.* 25 (1997) 223
- [10] F.-B. Li, G.E. Thompson, *J. Electrochem. Soc.* 146 (1999) 1809
- [11] A.E. Hughes, R.J. Taylor, B.R.W. Hinton, L. Wilson, *Surf. Interface Anal.* 23 (1995) 540
- [12] D.R. Arnott, B.R.W. Hinton, N.E. Ryan, *Mater. Performance* (1987) 42
- [13] M. Dabalà, L. Armelao, A. Buchberger, I. Calliari, *Appl. Surf. Sci.* 172 (2001) 312
- [14] A. Aballe, M. Bethencourt, F.J. Botana, M.A. Cauqui, M. Marcos, J. Pérez, M.A. Rodriguez-Chacon, *Mater. Sci. Forum* 289-292 (1998) 557
- [15] M.A. Arenas, M. Bathencourt, F.J. Botana, J. de Damborenea, M. Marcos, *Corros. Sci.* 43 (2001) 157
- [16] J.D. Gorman, S.T. Johnson, P.N. Johnston, P.J.K. Paterson, A.E. Hughes, *Corros. Sci.* 38 (1996) 1977



## Summary

The surface of aluminium and its alloys, when exposed to air, is always covered by a thin aluminium oxide film, which is amphoteric, i.e. dissolves in strong acid and alkaline media, and contains flaws and defects. Therefore, in many conditions this natural aluminium oxide film needs to be replaced by a more resistant layer, a so-called conversion coating, in order to provide a better corrosion protection to the metal substrate. Up to now most used conversion systems are those based on chromate species, due to their excellent corrosion resistance together with relatively low cost of application.

The corrosion phenomena occurring at the aluminium surface and the formation of the chromate conversion coating, as well, are electrochemically driven processes. As a consequence, the presence of local cathodes and anodes, related to microstructural features, on the surface may be expected to strongly affect not only the type and rate of corrosion but also the nucleation, growth and final properties of the chromate film. Therefore, the development of a method to measure the local electrochemical activity of the aluminium surface would enable a better understanding of these phenomena.

In the last few decades, many authors have attempted to correlate the microstructure and the electrochemical behaviour of the aluminium alloys, especially regarding the corrosion processes. However, controversial theories have been proposed concerning the role played by the intermetallic particles and the alloying elements in both the local corrosive attack of and the formation of the chromate conversion coating on the aluminium alloys surface and further investigations are necessary. To this aim, the present PhD project investigated the influence of microstructural features of 2024 aluminium alloy on the type of corrosion taking place in chloride solution and especially on the formation of the chromate conversion coating. Both scientific and industrial motivations have been at the basis of the choice of the aluminium alloy to be investigated. On one hand, this alloy shows a quite complex microstructure due to the presence of several types of intermetallics and the large content of copper in solid solution, and on the other hand it finds large application in the aerospace industry, where a high level of corrosion resistance is required.

In order to correlate the alloy microstructure both with the mechanisms of corrosion of the un-coated alloy and with the formation and protection of the chromate film, first of all a method was developed to investigate the presence of local cathodic and anodic sites on the alloy surface caused by microstructural features. It was found that the AFM operating in the Kelvin Probe mode (SKPFM) due to its high lateral resolution and when used in combination with SEM and EDS techniques enables to characterize the galvanic coupling existing between the intermetallic particles and the aluminium matrix, between areas covered with the conversion film and the bare alloy, and even between different regions of the same intermetallic. However, the interpretation of the SKPFM results should be made with care,

since limitations arise when measurements made in air are used for understanding phenomena taking place in solution and besides all the factors determining the surface potential measured with this technique are not yet completely understood. Indeed, in addition to the chemical composition of the substrate, the size of the local cathodes or anodes, the topographic features, the adsorption of species on the sample surface, together with the structure, hydration extent, etc. of the oxide film may affect the value of the measured potential. Although this is likely the case, the SKPFM technique has been shown to provide very useful information regarding the distribution of cathodic and anodic areas, which are responsible for the local electrochemistry of the aluminium alloys surface.

To study the influence of the alloy microstructure on its macroscopic electrochemical behaviour two different approaches have been undertaken. In the case of the corrosion of the un-coated AA2024 the microstructure was deliberately changed varying the heat treatment procedure, in particular the time spent in air between the solution treatment and the quenching (quench delay time), whereas in the case of the nucleation and growth of the chromate conversion coating the amount of both the intermetallics and the Cu-rich smut on the surface was significantly modified by using either different surface preparation procedures prior to the conversion process or different alloys as substrate, namely AA2024 bare or clad with commercially pure aluminium (AA1230). These investigations did actually show that the local microscopic features of the surface determine the macroscopic electrochemical response of the aluminium alloy:

- ✓ The changes in the properties of the intermetallic particles caused by the increase of the quench delay time lead to changes in the type of corrosion. Specifically, when this heat treatment parameter exceeds a threshold value, in the order of a few tens of seconds, shell-shaped intermetallics are formed and cause the corrosion to change from general to pitting as a consequence of a very strong and spatially localized galvanic coupling existing between the bulk and the edges of such intermetallics (chapter 4).
- ✓ The presence of intermetallic particles, which serve as cathodic sites, on the aluminium surface causes the nucleation of the chromate conversion coating to change from homogeneous to heterogeneous. Indeed, the reduction of chromate species and the consequent precipitation of chromium hydroxide occur preferentially above the cathodic intermetallics. This, in turn, results in the formation of a conversion film being less homogeneous, less dense, and containing a larger amount of defects often located in proximity of the intermetallics, which are weak spots in the layer although they are covered by the chromate film (chapters 5 and 7).
- ✓ The presence of a Cu-rich smut, which can eventually form during the surface preparation procedure, on the AA2024 surface plays a role as important as the intermetallics in the growth of the chromate film. It causes a lack of adhesion of the chromate film to the aluminium substrate and inhibits the reduction of the chromate species together with the subsequent deposition of the chromium hydroxide (chapter 7).

In addition, with regard to the chromate conversion coating, the modifications in the morphology of the layer caused by the variations in the microstructural features of the

aluminium alloy substrate were expected to strongly affect the corrosion protection provided by the film itself. This has been investigated using two complementary electrochemical techniques, i.e. impedance spectroscopy and noise measurements. The impedance behaviour of the chromate film/aluminium substrate system has been modelled using an equivalent circuit, which was chosen based on a TEM study and on the consistent variation within the different elements rather than on the interpretation of the absolute values related with the physical properties. Nonetheless, we believe that this equivalent network does well represent the impedance behaviour of the chromate film on aluminium alloys in the conditions and especially within the frequency range that were used in the investigation and its validity is supported by the time evolution of the various circuit elements, which is physically meaningful and agrees well with the results of the SEM study carried out on the samples surface after the impedance measurements. In addition, the results of the fit of the EIS data were supported by those obtained with the electrochemical noise technique, which has been shown to be a valid method to study the onset of localized attack. The current and potential time records of the noise measurements were interpreted using a simple and direct evaluation rather than the usual approaches, which are based on analyses either in the time or frequency domains and are, at the moment, argument of controversial discussion in the academic world.

The use of this equivalent circuit, which models the chromate film not as homogeneous and considers the corrosion attack as taking prevalently place inside the defects of the layer rather than all over the exposed area, enabled to gain from the impedance data useful information concerning the local corrosion behaviour of the chromate coated surface. Based on this and on the results of the noise experiments we have suggested that the mechanism of corrosion protection of the chromate conversion coating depends on three main factors: barrier properties, self-healing behaviour, and adhesion to the substrate. According to the proposed mechanism, the presence of intermetallic particles and copper-rich smut on the substrate surface are both deleterious for the resistance towards the corrosive attack of the aluminium alloy coated with the chromate film. Indeed, both microstructural features decrease the barrier and adhesion properties of the chromate layer: the intermetallics due to the formation of large defects at their location, the Cu-rich smut due to a strong reduction of the film thickness and of the chromate film/substrate adhesion.

This approach, based on the consideration of the effects of the microstructural features of the aluminium alloy on its macroscopic electrochemical behaviour, enabled a better understanding of the chromate conversion coating process, which is a prerequisite for the development of chromium-free systems that is becoming a top priority due to the health and environmental problems related to the use of the toxic chromate species. The same approach can indeed be applied for the investigation of alternative conversion processes that involve electrochemical reactions similarly to the chromate one. In particular, within this PhD project the attention was focused on the cerium-based conversion coating since from the literature it was found that it is electrochemically driven and it is one of the most promising chromium-free treatments. The combined use of different surface analyses

techniques (SKPFM, SEM, EDS) has shown that while the intermetallic particles only slightly affect the formation of the cerium oxide film, the presence of the Cu-rich smut is a necessary condition for the precipitation of the cerium-based conversion layer, which occurs via deposition and coalescence of small round-shaped particles. Further investigations are required in order to clarify the exact role played by the copper and/or copper oxide particles in the nucleation and growth of the cerium oxide layer, since several phenomena could be involved in their strong acceleration effect: cathodic activation of the surface, participation to the chemical/electrochemical reactions occurring in the conversion bath, favourable energy variations, etc. In addition, the approach used in this study has highlighted some drawbacks of the cerium-based system, namely lack of adhesion to the substrate and corrosive attack of the aluminium. These problems need to be solved in order to render this conversion process a suitable candidate for the replacement of the chromate conversion coating.

Finally, on the basis of the research work carried out within this PhD project it can be concluded that to develop and/or improve alternative systems for the corrosion protection of aluminium alloys it is first of all necessary to determine whether or not the process is electrochemically driven. If so, then the local electrochemistry related to the microstructural features should be considered as the major parameter in determining the efficiency of the system, related to both the film formation and the corrosion protection provided to the substrate. In addition, this should be done not only for the conversion treatment itself but during the whole process, including all the surface preparation steps.

## Samenvatting

Het oppervlak van aluminium en legeringen is altijd bedekt met een dunne aluminium oxidelaag wanneer deze worden blootgesteld aan de lucht. De oxidelaag is amfoeteer, lost op in sterk zure en alkalische oplossingen en bevat vrijwel altijd defecten. De natuurlijke oxidelaag wordt daarom in veel gevallen vervangen door een meer resistente laag, een zogenoemde conversie coating om voor een betere corrosiebescherming van het substraat te zorgen. De meest gebruikte conversielaag is deze gebaseerd op chromaat vanwege lage kosten en een zeer goede corrosiebescherming.

De corrosieverschijnselen aan het aluminium oppervlak en de vorming van een chromaat conversielaag zijn electrochemisch gedreven processen. De aanwezigheid van lokale kathodes en anodes als gevolg van verschillen in microstructuur zullen daarom niet alleen het type en snelheid van corrosie bepalen maar ook de vorming, groei en uiteindelijke eigenschappen van de chromaat conversielaag. De ontwikkeling van een methode die het mogelijk maakt lokaal de electrochemische activiteit aan het oppervlak te meten kan daarom voor een beter begrip van de verschijnselen zorgen.

In de afgelopen decennia hebben veel onderzoekers geprobeerd om de microstructuur en electrochemische processen van aluminium legeringen aan elkaar te correleren, met name vanuit het oogpunt van corrosieverschijnselen. Er zijn echter controversiële theorieën voorgesteld met betrekking tot de rol die intermetallische deeltjes en legeringselementen spelen in zowel de lokale corrosie aantasting als de vorming van chromaat conversielagen. Verder onderzoek is daarom noodzakelijk. Dit promotieonderzoek heeft zich daarom gericht op de rol van de microstructuur in AA2024 legeringen op het type corrosie dat plaatsvindt in chloorhoudende milieus en met name op de vorming van chromaat conversielagen. Zowel wetenschappelijke als industriële overwegingen hebben een rol gespeeld bij de keuze van de legering. Aan de ene kant laat deze legering een complexe microstructuur vanwege de aanwezigheid van verschillende typen intermetallische deeltjes en het hoge kopergehalte opgelost in de matrix en aan de andere kant wordt deze veelvuldig toegepast in de lucht- en ruimtevaart industrie waar een goede corrosiebestendigheid vereist is.

Om de microstructuur te correleren aan de corrosiemechanismen en aan de vorming en bescherming van de chromaat conversielaag is ten eerste een methode ontwikkeld om de aanwezigheid van verschillen in microstructuur en van lokale kathodische en anodische gebieden te onderzoeken. De AFM in de Kelvin Probe mode (SKPFM) vanwege zijn hoge laterale resolutie, gecombineerd met SEM en EDS maakt het mogelijk om de galvanische koppeling tussen intermetallische deeltjes en de matrix, tussen gebieden wel en niet bedekt met de conversielaag en zelfs tussen gebieden binnen een intermetallisch deeltje te bestuderen. De interpretatie van de meetresultaten moet echter met zorg gedaan worden, omdat er limiteringen zijn bij het gebruiken van metingen gedaan in lucht om verschijnselen

in oplossing te bestuderen. Verder zijn nog niet alle factoren die van invloed zijn op de oppervlaktepotentiaal bekend. Naast de chemische samenstelling van het substraat kunnen ook de grootte van lokale kathodische of anodische gebieden, de topografie, de adsorptie van moleculen op het oppervlak, mate van hydratatie etc. van invloed zijn op de waarde van de gemeten oppervlaktepotentiaal. Ondanks dat dit waarschijnlijk het geval is, is gebleken dat de SKPFM meettechniek waardevolle informatie oplevert met betrekking tot de verdeling van kathodische en anodische gebieden op het oppervlak welke verantwoordelijk zijn voor de lokale electrochemie van het oppervlak van de aluminiumlegering.

Om de invloed van de legeringsmicrostructuur op de macroscopische electrochemische eigenschappen te bepalen zijn twee verschillende benaderingen gevolgd. In het geval van de ongecoate AA2024 is de microstructuur doelbewust gevarieerd door verandering van de warmtebehandeling met in het bijzonder de tijd tussen de tijd in lucht na de oplosbehandeling en het afschrikken in water (quench delay time). In het geval van nucleatie en groei van de chromaat conversielaag is het aantal intermetallische deeltjes en de aanwezigheid van een Cu-rijke smutlaag gevarieerd door een andere oppervlaktebehandeling voor het aanbrengen van de conversielaag en/of het al dan niet aanbrengen van een cladiaag (AA1230) op de 2024 legering. Het onderzoek hieraan liet duidelijk zien dat de lokale microstructuur de macroscopische electrochemische eigenschappen van de legering bepalen:

- ✓ De veranderingen in eigenschappen van de intermetallische deeltjes als gevolg van een toename in de quench delay time leiden tot een verandering in het type corrosie. Als deze warmtebehandelingsparameter een bepaalde waarde overschrijdt (in de orde van enkele tientallen seconden) worden schilvormige intermetallische deeltjes gevormd, die voor een verandering in het type corrosie van algemeen naar putvormige corrosie zorgen. Dit als gevolg van een zeer sterke en locale galvanische koppeling tussen de bulk en de randen van deze intermetallische deeltjes (Hoofdstuk 4).
- ✓ De aanwezigheid van intermetallische deeltjes die als kathodische plaatsen op het aluminium oppervlak fungeren, zorgen ervoor dat de nucleatie van de chromaat conversielaag van homogeen naar heterogeen gaat. De reductie van chromaat deeltjes en de precipitatie van chroomhydroxide vindt bij voorkeur plaats aan het oppervlak van de kathodische intermetallische deeltjes. Dit resulteert in een chromaat conversielaag die minder homogeen, dicht en een groter aantal fouten bevat. Deze fouten zitten vaak in de buurt van intermetallische deeltjes en vormen zwakke plekken hoewel ze bedekt zijn met de chromaatlaag (Hoofdstuk 5 en 7).
- ✓ De aanwezigheid van een Cu-smutlaag die zich tijdens de oppervlaktebehandelingen kan vormen op het AA2024 oppervlak speelt een minstens zo belangrijke rol als de intermetallische deeltjes. Het zorgt ervoor dat de conversielaag zich nauwelijks bindt met het aluminiumsubstraat en voorkomt ook de reductie van chromaat-deeltjes met de hieropvolgende depositie van chroomhydroxide (Hoofdstuk 7).

Hiernaast werd verwacht dat veranderingen in de morfologie van de chromaat conversielaag, veroorzaakt door veranderingen van microstructuur-variaties in de aluminium

legering, een sterke invloed zouden hebben op de corrosiebescherming ervan. Dit is onderzocht met behulp van twee complementaire electrochemische technieken, namelijk impedantiespectroscopie en electrochemische ruismetingen. Het impedantie gedrag van de laag is gemodelleerd met een equivalent circuit dat gebaseerd is op TEM onderzoek en op consistent gedrag van de veranderingen in de parameters in plaats van de interpretatie van de absolute waarden van de fysische eigenschappen. Desalniettemin geloven wij dat dit equivalent netwerk het impedantiegedrag van de chromaat conversielaag onder de bestudeerde omstandigheden goed beschrijft en in het bijzonder in het frequentiegebied dat voor het onderzoek gebruikt is. De geldigheid van het circuit wordt ondersteund door een logisch verloop in de tijd van de verschillende parameters en door SEM onderzoek dat is uitgevoerd aan de monster oppervlakken na afloop van impedantiemetingen. Hiernaast worden de EIS resultaten ook ondersteund door resultaten verkregen met de electrochemische ruis meettechniek waarvan is aangetoond dat het een goede methode is om de start van gelocaliseerde aantasting te onderzoeken. Het stroom- en spanningsverloop is geïnterpreteerd op een eenvoudige en directe manier in plaats van de gebruikelijke benaderingen die zijn gebaseerd op verloop in tijd of in het frequentie domein. Deze methoden zijn momenteel onderwerp van discussie in the academische wereld.

Het gebruik van dit equivalent circuit die de chromaatfilm niet modelleert als een homogeen systeem maar de preferentiële corrosieaantasting in de defecten in ogenschouw neemt maakt het mogelijk om bruikbare informatie met betrekking tot de lokale corrosieaantasting van het gechromateerde oppervlak af te leiden. Hierop en op de electrochemische ruismetingen gebaseerd denken we dat het mechanisme van corrosiebescherming van de chromaat conversielaag is gebaseerd op drie belangrijke factoren: barriere eigenschappen, zelf-reparerend gedrag en hechting aan het substraat. Volgens het voorgestelde mechanisme zorgen de aanwezigheid van precipitaten en de koperrijke smutlaag beiden voor een afname van de corrosiebestendigheid van de aluminiumlegering gecoat met een chromaat conversielaag. Beide microstructureigenschappen zorgen voor een afname van de barriere eigenschappen en hechtingseigenschappen; de intermetallische deeltjes door de vorming van grote defecten in de laag en de Cu-rijke smutlaag door een sterke afname in de dikte en hechting van de conversielaag.

Deze benadering, gebaseerd op het in ogenschouw nemen van de effecten van de microstructuur van de legering op het macroscopisch electrochemische gedrag maakte een beter begrip van het chromaat conversie behandeling mogelijk. Dit is een vereiste voor het ontwikkelen van chroomvrije systemen welke nodig zijn nodig vanwege gezondheids- en milieuproblemen gerelateerd aan het gebruik van de giftige chromaten. Dezelfde benadering kan dan ook worden toegepast voor het onderzoek naar alternatieve conversieprocessen waar electrochemische reacties aan ten grondslag liggen. In het bijzonder is in dit promotiewerk gekeken naar cerium-gebaseerde coatings omdat volgens de literatuur is gebleken dat het aanbrengen hiervan ook electrochemisch gedreven is en verder is het een van de meest veelbelovende chromaat-vrije behandelingen. Het gecombineerde gebruik van verschillende oppervlakte analyse technieken (SKPFM, SEM, EDS) heeft aangetoond dat -

terwijl de intermetallische deeltjes slechts een beperkte invloed hebben op de vorming van de ceriumoxide laag - de aanwezigheid van de Cu-rijke smutlaag is noodzakelijk voor de precipitatie van de cerium-conversielaag welke plaatsvindt via depositie en groei van kleine ronde deeltjes. Verder onderzoek is nodig om de exacte rol van de koper en/of koper-oxide deeltjes in de nucleatie en groei van de ceriumoxide laag te verklaren. Verschillende fenomenen kunnen bijdragen aan hun versnellende rol – kathodische activatie van het oppervlak, deelname aan electrochemische reacties in het conversiebad, preferentiële energie variaties etc. Voorts heeft de benadering in dit promotieonderzoek serieuze tekortkomingen van de cerium gebaseerde conversie lagen laten zien, namelijk gebrek aan hechting met het substraat en corrosieve aantasting van het substraat. Deze problemen dienen eerst opgelost te worden om dit conversieproces een goede kandidaat te maken voor vervanging van de chromaatconversielaag.

Ten slotte kan op basis van het onderzoek in deze promotie geconcludeerd worden, dat om ontwikkeling en/of verbetering van alternatieven mogelijk te maken het allereerst noodzakelijk is om te bepalen of het proces electrochemisch gedreven is. Als dit zo is, dient de lokale electrochemie in relatie tot de microstructuur beschouwd te worden als de belangrijkste parameter voor het bepalen van de efficiëntie van het systeem. Dit is weer bepalend voor zowel de vorming van de film als aan de corrosiebescherming van het substraat. Verder dient dit niet alleen gedaan te worden voor de conversiebehandeling zelf maar ook voor alle voorgaande oppervlaktebehandelingsstappen.



# Acknowledgements

Although during a PhD you are often alone with your own project, many other people apart yourself determine the successful end of this difficult and challenging period of your life. This is the reason why I feel now to say few words of thanks to several people, who have contributed with their support and help to the completion of my PhD, of which this thesis is the final outcome. Before to start I want to assure all the people I will mention below that I am doing this spontaneously and not because it is part of the hundreds roles it is necessary to follow to get a PhD title from TUDelft and that I really feel and think what I will say.

I have decided to thanks people randomly and not by order of importance, since there is not actually such an order because all friends and colleagues have played an important role in my life during these four years even if in different ways. However, I want to thank first my family and especially my parents since without them I would never be what I am now and I would never succeed to reach this important objective of my life. *Cari mamma e papà ancora una volta vorrei ringraziarvi per il vostro aiuto e sostegno e soprattutto per la libertà che mi avete sempre concesso lasciandomi prendere le mie decisioni e lasciandomi inseguire i miei obiettivi, nonostante questi mi abbiano portato fisicamente, ma non con il cuore, lontano da voi.* A big thank is also for my sister Antonella, her husband Enzo, my nephew Gabriele, my niece Anna, my brother Roberto and his girlfriend Monica for the love they always have had for the “crazy” person of the family!

I am greatly indebted to Pier Luigi Bonora from the University of Trento since he is one of the main responsible of my coming in The Netherlands due to his long friendship with my promoter Hans de Wit, to whom I want to say just heartily thank! Hans, I would like to thank you not only for your scientific contribution to the project but also for the motivation you always gave me in the difficult moments and for the friendly relationship you wanted to build with me during these four years. The only regret I have it is your “one-day-per-week” presence in Delft because every meeting with you has been an occasion to learn new things, both from a scientific and a human point of view; then I cannot imagine what I would have learned if I were seeing you everyday. However, at the beginning I had a daily supervision from Huib van Roojen, who supported me in the difficult period of getting started with the PhD and for this I would like to thank you, Huib, and wish you the best for your health. After the leaving of Huib, Erik van Westing took over the supervision of my project. Erik, I believe that your human qualities together with your scientific knowledge make you the “perfect” supervisor. I want to thank you for being always ready to help me and for teaching me a lot about impedance measurements and especially about the “risks” of the fitting procedure...by adding enough resistors and capacitors it is possible to have an equivalent circuit able to model an elephant...

In the draft of this thesis I was greatly supported by Herman Terryn from Vrije Universiteit Brussel, who contributed with useful discussions and comments to make the output of my research more valuable and clearer. Herman, I would like to thank you not only for this but also for your enthusiasm in doing your job, for your friendship (we had great dinners in San Francisco without milk as aperitif!!!), and for allowing me to use the instrumentations of your lab in Brussels. The scientific knowledge I encountered in your group has provided a great contribution to the experimental results and discussions presented in this thesis. I would like also to thank the members of your group, with whom I had very interesting scientific, and not only, conversations during the coffee and beer breaks! Special thanks are due to Tom Schram for his help in carrying out and in the interpretation of the ellipsometric measurements and to Oscar Steenhaut for the AES analyses and for his expertise in the SEM/EDS techniques.

Talking about daily and "unofficial" support, many people from the Corrosie technologie en Elektrochemie (CTE) section of Materiaalkunde are coming to my mind. I would like to start with Francesco and Jeroen, with whom I shared the office during almost all my PhD. Francesco, thanks a lot for being always ready to help me, you are one of the most kind person I never met. Besides, thanks for the conversations in Italian...it is quite relaxing sometimes to speak in your own native language. Jeroen, I would like to thank you for the support in computer problems and with the electrochemical experiments. In both cases you were always giving me useful advises even when surprising and incomprehensible things were happening. Similar thanks are due also to Bart for his technical support not only in the construction of electrochemical cells, in the polishing of samples, in the preparation of electrolytes, but also in fixing my bike! I would like to say a special thank to José, who has an incredible amount of patience and has a particular ability in listening to people! Heartily thank for the hours you spent to talk with me about science, life, work, etc. and especially for discreetly supporting me during one of the more difficult period of my life. I can go on writing a lot about the help I received during these four years from all the members of the lab, but as Herman told me once I should sometimes go against my nature and try to be short, so I just say THANK to all the people I worked with in the CTE group. However, I would like to mention Mae, Xiaolong, Brian, Peter, Saskia, Chris, José, Francesco, and Jeroen, who shared with me the unforgettable experience of the NIMR cluster meetings and congresses!

Arjan Hovestad and Albert Bosch, from TNO Industrie, have given a great contribution to my research on conversion coatings for aluminium alloys. In particular I would like to thank Arjan for being always available in preparing new samples for me in very short time and for helping me in understanding the chemical and electrochemical processes occurring in the conversion baths. I would also like to express my gratitude to John Droog from Corus for his enthusiasm and interest in my work, which was much more than what usually expected from the "industrial partners". Besides, I want to thank all the people who contributed, even if only occasionally, in building the scientific knowledge reported in this thesis carrying out specific experiments and discussing with me the results: Andreas Afseth from Alcan for the TEM investigation (thanks a lot for helping me to do not get crazy in

"fishing" the ultramicrotomed slides), Hans Winter from Corus for the GDOES measurements, Werner van der Weg of the Debey Institute at Utrecht University for the RBS experiments, Anton Suurmond from TNO (Den Helder) for the EIS measurements, and Walter Manfred from Chemetall for the several advises on the cerium-based conversion process.

I would like to take this occasion to thank also Ann Jonker from Corus for giving me the possibility to carry out a stage, which although was not directly related to my PhD project it has been a valuable addition to my scientific and research experience. On this regard, a special thank is due to Koen Lammers for the fruitful discussions about XPS and especially about the organization of research in industry. In addition, I want to express my gratitude to Martin Huisert, who previously was a colleague and especially a very good friend in the CTE group and who during the stage transformed himself in a perfect "chauffeur"...Martin, heartily thank for allowing me to sleep while you were driving, often in the middle of heavy traffic, from Delft to IJmuiden!

And now it is time to thank the numerous friends I met in Delft and those I left in Italy. Dennis, Maria, Stefano, Enrico, Gigi, Sonia, Giordano, thank you a lot for our more than decennial friendship and for making me always feel home when I was shortly, and actually not very often, coming back in Trento. On the other hand, you also should thank me because my come back has been always the occasion for you to get together!

The very good time I had during my four years in Delft is mainly due to the possibility to know and build up friendship with people coming from different countries and belonging to different cultures. However, the first people I met were Italian: Marcello, Arianna, Lucia "the black", Luca (the caravan-man), and Lucia "the blond"...thank you for not letting me feel home sick!!! Theo, thanks a lot for helping me to overcome my lack of self-confidence at the beginning of the PhD and for making me discover the African dance...Bertrand, thank you for often singing "Bella ciao" and for being so patient in teaching me French!!!!...and Nicolas, Frederic, Charles thank you for helping me in improving my spoken French (I can almost forgive you for the final of the European Championship in Rotterdam!) ...Mike, thanks a lot for trying to improve my English pronunciation, however I am afraid I will never loose my Italian accent!!!!...Kay, thank you for your enthusiasm in science and for involving me in the KEN project!!!...Cedric, Marie-Ange, Thib, thanks a lot for the sailing adventures especially that in Marseille where the sun is slightly more present and warmer than in Holland!!!!...Dan, thank you for your music even if you often kept secret the time and place of your performances!!!!...Ramon and all the Spanish community, thank you for the numerous parties at Wolbodo!!!...

Finally, my gratitude is for all of you (even if not all mentioned...sorry...) who have shared with me these four years, or part of them, of Dutch experience with enclosed advantages and drawbacks that I do not need to mention since they have been topics of several and long conversations in front of a biertje!!!



# Curriculum Vitae

## Paola Campestrini

Nationality: Italian

Date of birth: 5 March 1972

Place of birth: Trento-Italy

## Education

### M. Sc. Materials Engineering,

March, 1998

University of Trento (Italy)

- **Thesis Research:** Plasma Nitriding of Cr-Mo Steel Produced by Powder Metallurgy (project leader Prof. Alberto Molinari).
- **Mark:** 110/110 cum laude

### Other Courses

- Technical writing in English (Delft University of Technology, Delft, The Netherlands, February-May 1999)
- Scanning Probe Technique (MSC Research Schools, Ameland, The Netherlands, June 1999)
- Effective Project Management (The Center for Professional Advancement, New Jersey, USA, January 2001)

## Professional Experience

### Post-doc Researcher

August 2002-present

#### Netherlands Institute for Metals Research (NIMR)

- Coaching PhD students
- Improvement of the cerium-based conversion coating

### PhD Researcher

August 1998

July 2002

#### Netherlands Institute for Metals Research (NIMR)

- Surface analysis and electrochemical investigation of conversion coatings on aluminium alloys
- *Better understanding of the mechanism of corrosion protection of chromate conversion coatings*
- Development and improvement of chromium-free conversion coatings

**Practical Training**

October 2001

December 2001

**Research Assistant**

March 1998 to

July 1998

**Corus (IJmuiden-NL)**

- Investigation of metal-polymer adhesion
- Surface analysis of failed systems

**University of Trento (Italy)**

- Tribological studies of different types of steel
- Optimisation of the sintering conditions for steels produced by means of powder metallurgy

# List of Publications

## Journal Papers

- Powder Metallurgy** 42 (1999) 119-125 A.Molinari, T.Bacci, P.Campestrini, M.Pellizzari, B. Tesi  
*Plasma nitriding of Fe-Cr-Mo sintered steels*
- Powder Metallurgy** 42 (1999) 235-241 A. Molinari, G. Straffelini, P.Campestrini  
*Influence of the microstructure on impact and wear behaviour of sintered Cr and Mo steel.*
- Materials and Corrosion** 51 (2000) 616-627 P.Campestrini, H.W. van Rooijen, E.P.M. van Westing, J.H.W. de Wit  
*Influence of the quench delay time on the corrosion behaviour of 2024 aluminium alloy.*
- Corrosion Science** 42 (2000) 1853-1661 P.Campestrini, E.P.M. van Westing, H.W. van Rooijen, J.H.W. de Wit  
*Relation between microstructural aspects of AA2024 and its corrosion behaviour investigated using AFM scanning potential technique*
- Electrochimica Acta** 46 (2001) 2553-2571 P.Campestrini, E.P.M. van Westing, J.H.W. de Wit  
*Influence of surface preparation on performance of chromate conversion coatings on Alclad 2024 aluminium alloy. Part I: Nucleation and growth*
- Electrochimica Acta** 46 (2001) 2631-2647 P.Campestrini, E.P.M. van Westing, J.H.W. de Wit  
*Influence of surface preparation on performance of chromate conversion coatings on Alclad 2024 aluminium alloy. Part II: EIS investigation*
- Electrochimica Acta** 47 (2002) 1097-1113 P.Campestrini, E.P.M. van Westing, J.H.W. de Wit  
*Investigation of the chromate conversion coating on Alclad 2024 aluminium alloy: effect of the pH of the chromate bath*
- Thin Solid Films** 410 (2002) 76-85 P.Campestrini, S. Böhm, T.Schram, H.Terryn, J.H.W. de Wit  
*Investigation of chromate conversion coatings on Alclad 2024 aluminium alloy using spectroscopic ellipsometry*

## Conferences and Proceedings Papers

- Granada, Spain**  
September 22 to 27, 2002  
Oral presentation and proceedings paper at 15<sup>th</sup> International Corrosion Congress  
P.Campestrini, H. Terry, J.H.W. de Wit  
*SEM and SKPFM investigation of the formation of the cerium-based conversion coating on 2024-T3 aluminium alloy.*
- Montreal, Canada**  
August 11 to 15, 2002  
Oral presentation and proceedings paper at the Conference of Metallurgists COM2002  
P.Campestrini, H. Terry, J.H.W. de Wit  
*Investigation of the chromate conversion coating on aluminium alloys: effect of the substrate.*
- London, UK**  
April 9 to 11, 2002  
Poster presentation at the Materials Congress 2002  
P.Campestrini, S. Böhm, T. Schram, H. Terry, J.H.W. de Wit  
*Use of spectroscopic ellipsometry in studying chromate conversion coatings on Alclad 2024 aluminium alloy*
- San Francisco, CA, USA**  
September 2 to 7, 2001  
Oral presentation and proceedings paper at the 200<sup>th</sup> Meeting of the Electrochemical Society  
P.Campestrini, E.P.M. van Westing, J.H.W. de Wit  
*Influence of the microstructure on the nucleation and growth of chromate conversion coatings on Al alloys.*
- Marilleva, Italy**  
June 17 to 22, 2001  
Oral presentation and proceedings paper at the "Electrochemical Impedance Spectroscopy" conference (EIS2001)  
P.Campestrini, E.P.M. van Westing, J.H.W. de Wit  
*EIS investigation of the corrosion protection behaviour of chromate conversion coatings on Alclad 2024 aluminium alloy.*
- Houston, TX, USA**  
March 11 to 16, 2001  
Oral presentation at the NACE Meeting: Corrosion/2000  
P.Campestrini, E.P.M. van Westing, J.H.W. de Wit  
*Assessment of the protective properties of chromate layers on Alclad 2024-T3 aluminium alloy.*
- Budapest, Hungary**  
May 28 to June 1, 2000  
Oral presentation and proceedings paper at the Electrochemical Methods for Corrosion Research conference (EMCR2000)  
P.Campestrini, E.P.M. van Westing, J.H.W. de Wit  
*Use of the Atomic Force Microscopy for the characterization of*



# **Acronyms**

<b>AC</b>	Alternating Current
<b>AES</b>	Auger Electron Spectroscopy
<b>AFM</b>	Atomic Force Microscopy
<b>BL</b>	Barrier Layer
<b>CCC</b>	Chromate Conversion Coating
<b>CCP</b>	Chromate Corrosion Product
<b>CPE</b>	Constant Phase Element
<b>DC</b>	Direct Current
<b>ECI</b>	Electrochemical Interface
<b>EDS</b>	Energy Dispersive Spectroscopy
<b>EIS</b>	Electrochemical Impedance Spectroscopy
<b>EN</b>	Electrochemical Noise
<b>FFT</b>	Fast Fourier Transform
<b>FRA</b>	Frequency Response Analyser
<b>FTIR</b>	Fourier Transform Infrared Spectroscopy
<b>GDOES</b>	Glow Discharge Optical Emission Spectroscopy
<b>IMC</b>	Intermetallic
<b>IR-SE</b>	Infrared Spectroscopic Ellipsometry
<b>MEM</b>	Maximum Entropy Method
<b>MSE</b>	Mean Square Error
<b>OCP</b>	Open Circuit Potential
<b>ORR</b>	Oxygen Reduction Reaction
<b>pH<sub>zc</sub></b>	Ph of Zero Charge
<b>PL</b>	Porous Layer
<b>PSD</b>	Power Spectral Density
<b>RAIRS</b>	Reflection Absorption Infrared Spectroscopy
<b>RBS</b>	Rutherford Backscattering Spectroscopy
<b>SCC</b>	Stress Corrosion Cracking
<b>SCE</b>	Saturated Calomel Electrode
<b>SEM</b>	Scanning Electron Microscopy
<b>SIMS</b>	Secondary Ion Mass Spectrometry
<b>SKPFM</b>	Scanning Kelvin Probe Force Microscopy
<b>TEM</b>	Transmission Electron Microscopy
<b>t<sub>qd</sub></b>	Quench Delay Time
<b>XANES</b>	X-ray Absorption Near Edge Structure
<b>XPS</b>	X-ray Photoelectron Spectroscopy
<b>ZRA</b>	Zero Resistance Ammetry

Code/ Treatment		Alclad AA2024	Bare AA2024	Ultrasonic acetone cleaning 5 min, 25°C	Acid pickling H <sub>2</sub> SO <sub>4</sub> +H <sub>3</sub> PO <sub>4</sub> 60°C	Desmutting HNO <sub>3</sub> +HF 30s, 25°C	Alkaline cleaning Ridoline 53™ 4 min, 65°C	Deoxidising Ce(SO <sub>4</sub> ) <sub>2</sub> +HNO <sub>3</sub> +HF 10 min, 35°C	Chromate process Alodine 1200 3 min, 25°C	Cerate process CeCl <sub>3</sub> +H <sub>2</sub> O <sub>2</sub> 2 min, 25°C
		AR	2AR	X						
		NP	2NP	X	X (5 min)					
		SP	2SP	X	X (20 min)					
		NPD	2NPD	X	X (5 min)	X				
		SPD	2SPD	X	X (20 min)	X				
		-	2DX	X			X	X		
		-	2ARCr	X				X (pH=1.8)		
		NPCr1.8	2NPCr	X	X (5 min)			X (pH=1.8)		
		SPCr1.8	2SPCr	X	X (20 min)			X (pH=1.8)		
		NPDCr1.8	2NPDCr	X	X (5 min)	X		X (pH=1.8)		
		NPDCr1.2	-	X	X (5 min)	X		X (pH=1.2)		
		NPDCr1.4	-	X	X (5 min)	X		X (pH=1.4)		
		NPDCr2.2	-	X	X (5 min)	X		X (pH=2.2)		
		NPDCr2.4	-	X	X (5 min)	X		X (pH=2.4)		
		SPDCr1.8	2SPDCr	X	X (20 min)	X		X (pH=1.8)		
		-	2ARCe	X					X	
		NPCe	2NPCe	X	X (5 min)				X	
		-	2SPCe	X	X (20 min)				X	
		NPDCe	2NPDCe	X	X (5 min)	X			X	
		-	2SPDCe	X	X (20 min)	X			X	
		-	2DXCe	X			X			X

## **Samples Code**

*the electrochemical behaviour of aluminium alloy 2024.*

**Manchester, UK**

May 21 to 24, 2000

Oral presentation and proceedings paper at the 2<sup>nd</sup> Aluminium Surface Science and Technology conference (ASST2000).

P.Campestrini, E.P.M. van Westing, J.H.W. de Wit

*Characterization of chromate conversion coatings on aluminium alloys.*

**Aachen, Germany**

Aug 30 to Sept 2, 1999

Oral presentation at the conference Eurocorr99.

P.Campestrini, H.W. van Rooijen, E.P.M. van Westing, J.H.W. de Wit

*Influence of the quench delay time on the corrosion behaviour of 2024 aluminium alloy.*

